Random Wave Transformation and Sediment Transport Across Barred and Terraced Sand Beaches

by

Mark D. Orzech

and

Nobuhisa Kobayashi

ABSTRACT

Two irregular wave tests were conducted over a permeable fine sand beach in equilibrium, recording time series of the free surface and horizontal velocity at 17 cross-shore locations. The first part of this study supplements the results of Herrman et al. (1997), obtained using a 1:16 impermeable smooth slope. The exponential gamma distribution, with measured mean, standard deviation, and skewness, is shown to be capable of describing the probability distributions of the above data in a unified manner over the beach profiles, in mean water depth $\bar{h} > 1$ cm. In the swash zone, the skewness, s, approaches 2 and the root-mean-square wave height H_{rms} approaches $\sqrt{8}\,\bar{h}$. Cross-shore variations of the mean and standard deviation of mid-depth horizontal velocity are adequately predicted in the shoaling and surf zones using linear long-wave theory locally. In addition to cross-shore data, two velocity profiles were measured and horizontal velocity statistics were shown to be fairly constant over depth. An attempt is also made to synchronize free surface and velocity time series to obtain information about incident and reflected wave spectra in shallow water. Total wave spectra are examined to check for the existence of long period standing waves over the profiles. Finally, sheet flow and energetics-based sediment transport models are used with the measured horizontal velocities to try to predict the equilibrium profiles obtained in this experiment. The energetics model is shown to predict these profiles more accurately than the sheet flow model. In the milder wave conditions of the second test, the energetics model predicts equilibrium

within experimental uncertainty of 1 cm/hr, but both models significantly overpredict bar movement during the more intense wave breaking of the first test. Their shortcomings are examined so as to suggest possible improvements in the models.

ACKNOWLEDGMENTS

TABLE OF CONTENTS

LIST OF FIGURES

ix

LIST OF TABLES

Chapter 1

INTRODUCTION

1.1 The Swash Zone

The swash zone on a beach is located between the surf and backshore zones. It is the area of the beach that is alternately submerged and exposed by wave action. A predictive model for swash dynamics is required in order to model the erosion and recovery of natural and artificial beaches. Swash data has been taken on natural beaches, thereby providing a qualitative understanding of swash dynamics [*e.g.*, Guza and Thornton (1982); Holman and Sallenger (1985); Douglas (1992)]. Yet it is unlikely that simple empirical relationships will be developed from this data because of the limitless possible combinations of different beach profiles and incident wave characteristics. The time-dependent numerical model, based on the finite-amplitude shallow-water equations including bottom friction (Kobayashi and Wurjanto 1992), has been shown to be capable of predicting the swash characteristics on a natural beach within errors of about 20% (Raubenheimer *et al.* 1995). However, this shallow-water model cannot be extended to intermediate water depth. Furthermore, the time-dependent numerical model requires significant computation time to resolve the breaking wave profiles that vary rapidly in time and space. As an alternative to the above procedures, it may be worthwhile to examine possible statistical methods for predicting swash dynamics.

1

1.2 Previous Statistical Work

Time-averaged models in which random waves are represented by the root-mean-square wave height [Battjes and Janssen (1978); Thornton and Guza (1983)] or expressed as the superposition of regular waves [Dally and Dean (1986); Mase and Kobayashi (1991)] are more efficient computationally than time-dependent models. However, they sacrifice detailed temporal information such as the skewness of the wave profile, which was found to be important in predicting cross-shore sediment transport [*e.g.*, Guza and Thornton (1985)]. Furthermore, the existing time-averaged models may considerably underestimate the wave setup and root-mean-square wave height in the swash zone (Cox *et al.* 1994).

In estimating nearshore sediment transport rates, Guza and Thornton (1985) computed the various moments of the fluid velocity field measured on a gently sloping beach. They assumed that time averaging and probabilistic averaging of a random variable were equivalent. Under this assumption, comparisons of the computed moments with monochromatic and linear (Gaussian) random wave models indicated major shortcomings in the monochromatic representation of random waves. The Gaussian model, with given mean and standard deviation, was shown to predict the even moments fairly accurately but to be incapable of predicting the odd moments associated with nonlinearities. For relatively deep water, attempts were made to predict the skewed distribution of the free surface elevation using higher-order expansions [*e.g.*, Longuet-Higgins (1963); Huang and Long (1980); Tayfun (1980)]. In shallow water, Bitner (1980) compared a Gram-Chalier expansion with field data. Still, this higher-order distribution, with measured skewness and kurtosis, predicted the measured free surface probability density functions only slightly better than the Gaussian distribution.

1.3   Previous Work With Beach Profiles and Sediment Transport

At the present time, there are no models capable of accurately predicting the development and final shape of terraced and barred equilibrium beach profiles. Profiles in the form of $d = Ay^{2/3}$, with $d =$ still water depth, $y =$ seaward distance from the shoreline, and $A =$ sediment scale parameter, have been shown to represent typical profiles of natural beaches [$e.g.$, Dean (1991)]. Perturbations of these equilibrium profiles in the form of barred and terraced beaches have also been observed. However, the processes involved in the creation of these perturbed beach profiles are not presently well understood. Trowbridge and Young (1989) developed a sheet flow sand transport model based on the bottom shear stress and showed that this model could explain the measured onshore movement of a nearshore bar in Duck, North Carolina during the mild wave conditions between February and August, 1982. Thornton et $al.$ (1996) used an energetics-based sediment transport model to explain the offshore movement of a bar on the same beach during storms in October, 1990. Yet no existing model can predict both onshore and offshore bar migrations satisfactorily.

1.4   Objectives and Overview

In recent years the probabilistic approach has been neglected in favor of time-dependent numerical modeling, probably for lack of a reasonably simple skewed distribution. The following study is in part an attempt to test the accuracy of one such distribution and to provide experimental data for the construction of a time-averaged model. In this respect, it is a continuation of work begun by Herrman et $al.$ (1997).

In their work and in this research, the exponential gamma distribution [$e.g.$, Gran (1992)] with given mean, standard deviation, and skewness is adopted to describe the probability density function of the free surface elevation from outside the surf zone through the swash zone. This distribution allows skewness, s, to range

between $s = 0$ and $s = 2$. The skewness determines the shape of the distribution, which becomes Gaussian for $s = 0$ and exponential for $s = 2$. The Gaussian distribution may be appropriate in relatively deep water, far seaward of the breaker zone, where local nonlinearity may be negligible. The exponential distribution may be a good approximation in the swash zone, where the lower limit of the free surface elevation is determined by the elevation of the bottom. As there has been no theoretical justification for the adopted exponential gamma distribution, Herrman conducted experiments on a uniform 1:16 slope to evaluate its applicability, as well as to examine the cross-shore variations of the mean, standard deviation, and skewness of the free surface elevation from outside the surf zone to the swash zone. The fixed 1:16 slope eliminated the uncertainty of the bottom elevation but did not represent typical concave beach profiles.

This study conducts similar tests with a concave fine-sand beach, on one barred and one terraced equilibrium profile. It compares the predictions of the exponential gamma distribution to surface elevation and cross-shore velocity data and examines the cross-shore variation of free surface and velocity statistics across these irregular profiles. Velocity statistics over the depth are also examined at two cross-shore locations to determine the degree of vertical variation of the velocity in the region above the bottom boundary layer and below the wave trough level.

The second major objective of this study is to explore the shortcomings of existing sediment transport theories in predicting perturbed equilibrium profiles. The sheet flow and energetics-based models discussed in section 1.3 are applied to the equilibrium profiles obtained in the two tests in order to examine the reasons why existing sand transport models cannot predict these equilibrium profiles of no net cross-shore sediment transport. The measured free surface elevations and velocities are analyzed to obtain the free surface and velocity statistics included in these models. The sheet flow model is only capable of predicting onshore sediment

transport and does not include the effects of undertow. The energetics-based model has been shown to predict only offshore bar movement and growth due to strong undertow and longshore currents. Suggestions will be made for the development of an improved model to explain the observed equilibrium profiles.

The following chapter introduces the exponential gamma distribution and corresponding predictions for free surface parameters in the swash zone. Chapter 3 provides an overview of the laboratory experiments, including initial testing of the fine beach sand and establishment and measurement of the equilibrium profiles. It also discusses the wave gauge and velocimeter probe locations and provides a basic description of the two wave tests. Chapters 4 and 5 present an analysis of measured free surface elevations and velocities respectively, obtaining the probability distributions of these variables and comparing velocity results to the predictions of linear wave theory. This data is then supplied to the sheet flow and energetics sediment transport models in Chapter 6. The deviations of these model predictions from the observed zero net transport may provide a guide to developing more accurate predictions of cross-shore sediment transport.

Chapter 2

EXPONENTIAL GAMMA DISTRIBUTION

This chapter develops the theory of the exponential gamma distribution and describes some of its implications for basic wave parameters in the lower swash zone, which remains wet during wave uprush and downrush. It is assumed in this study that the time series of the free surface elevation, η, above the still water level (SWL) is a stochastic process satisfying the conditions of stationality and ergodicity [$e.g.$, Goda (1985)]. The time and probabilistic averaging of the stochastic variable can then be regarded to be equivalent, and they will thus both be denoted by an overbar in the following. The probability density function of η is assumed to be expressed by the exponential gamma distribution [$e.g.$, Gran (1992)]. The mean, standard deviation, and skewness coefficient of η are denoted by $\bar{\eta}$, σ, and s, respectively. It is assumed that $0 \leq s \leq 2$ on the basis of available field and laboratory data [Bitner (1980); Huang and Long (1980); Goda (1985); Mase and Kobayashi (1991); Raubenheimer et $al.$ (1995)].

2.1 Form of the Exponential Gamma Distribution

The normalized free surface elevation, η_*, is defined as $\eta_* = (\eta - \bar{\eta})/\sigma$ and thus has mean and standard deviation equal to zero and unity, respectively. The skewness, s, of η_* is the same as the skewness of η. The exponential gamma distribution for η_* can be shown to be expressed as

$$f(\eta_*) = [\Gamma(a)]^{-1}\sqrt{\psi'(a)}\,e^{-ay}\exp\left(-e^{-y}\right) \qquad (2.1)$$

6

with

$$y = \sqrt{\psi'(a)}\,\eta_* - \psi(a) \tag{2.2}$$

in which a = shape parameter; Γ = gamma function; ψ = digamma function; and ψ' = trigamma function. The relationship between s and a is given by

$$s = -\psi''(a)\,[\psi'(a)]^{-1.5} \tag{2.3}$$

in which ψ'' = tetragamma function. The kurtosis, K, of η_* and η is given by

$$K = \psi'''(a)\,[\psi'(a)]^{-2} + 3 \tag{2.4}$$

in which ψ''' = pentagamma function.

The gamma and related functions are explained in Abramowitz and Stegun (1972) and tabulated by Gran (1992). The values of $\Gamma(a)$, $\psi(a)$, $\psi'(a)$, $\psi''(a)$, and $\psi'''(a)$ for given a can be found using *Mathematica* (Wolfram 1991). The value of a for given s can be obtained by solving (2.3) using an iteration method (Gran 1992). Figure 2.1 shows the variations of a and $(K-3)$ with respect to s. For $s < 0.4$, a can be described approximately by $a = (0.5 + s^{-2})$ (Gran 1992). The shape parameter, a, decreases from infinity at $s = 0$ to zero at $s = 2$. The kurtosis, K, increases from $K = 3$ at $s = 0$ to $K = 9$ at $s = 2$.

2.2 Limits of the Exponential Gamma Distribution

In deep water, skewness approaches zero and equation (2.1) reduces to the Gaussian distribution:

$$f(\eta_*) = \frac{1}{\sqrt{2\pi}}\exp\left(-\frac{\eta_*^2}{2}\right) \qquad \text{for} \ \ s = 0 \tag{2.5}$$

In the wet lower swash zone, skewness approaches two and equation (2.1) becomes the exponential distribution:

$$f(\eta_*) = e^{-(\eta_*+1)} \qquad \text{for} \ \ s = 2 \tag{2.6}$$

7
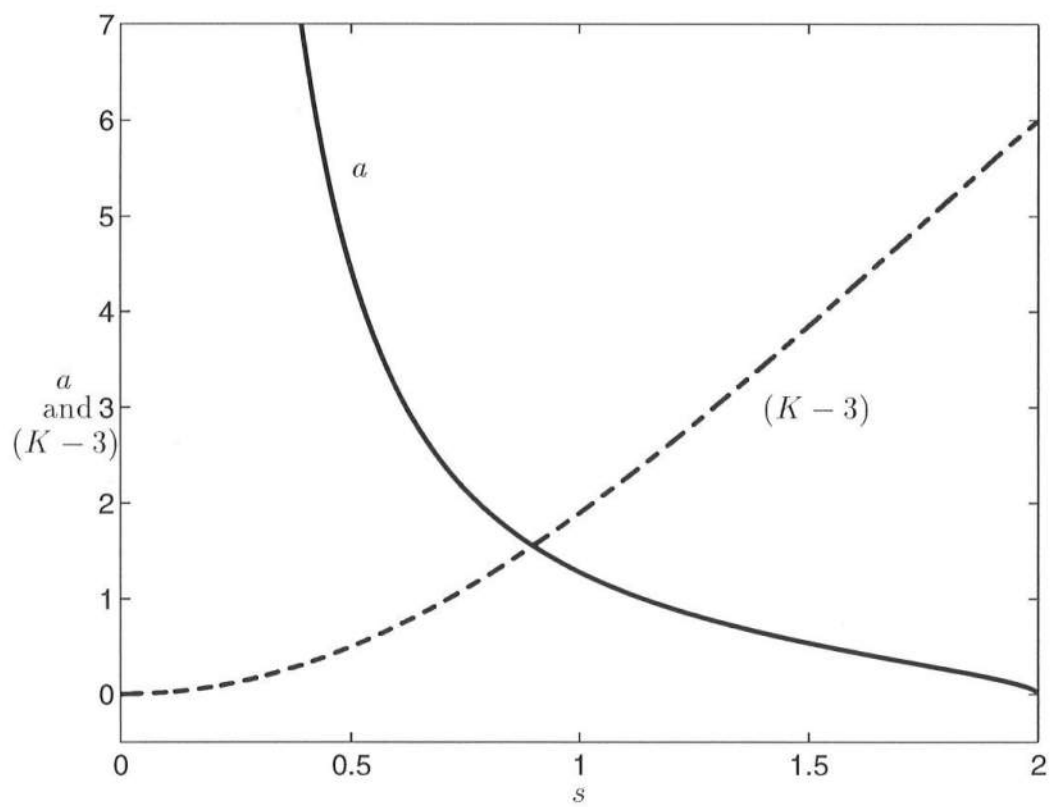
Figure 2.1: Shape Parameter, a, and Kurtosis, K, as a Function of Skewness, s

This exponential distribution is limited to the range $\eta_* = [(\eta - \bar{\eta})/\sigma] \geq -1$. This lower limit may be interpreted in terms of the instantaneous water depth, $h = (\eta - z_b)$, where $z_b =$ a bottom elevation which is taken to be positive above SWL. Here, the bottom elevation is assumed to be in equilibrium and to remain unchanged in each test. It is required that $h \geq 0$ and hence that $\eta \geq z_b$. The lower limit of η for $s = 2$ may be assumed to be imposed by z_b, resulting in $(\bar{\eta} - \sigma) = z_b$. Since the mean water depth $\bar{h}$ is given by $\bar{h} = (\bar{\eta} - z_b)$, this intuitive assumption requires that the mean depth approach the standard deviation in the swash zone:

$$\bar{h} = \sigma \quad \text{for} \ s = 2 \tag{2.7}$$

2.3 Trends of Available Data

As in Herrman $et\ al.$ (1997), one objective of this study is to investigate whether equations (2.6) and (2.7) hold in the swash zone. Previous research has been inconclusive and sometimes contradictory. Earlier surf zone laboratory data [$e.g.$, Mase and Kobayashi (1991)] indicated a landward decrease in skewness, s, toward the still water shoreline. Raubenheimer $et\ al.$ (1995) measured the free surface oscillations using runup wires placed parallel to a natural beach face and obtained small, negative values of s for the sea swell frequency range. However, the data of Herrman $et\ al.$ (1997) showed that the skewness did indeed increase landward of the still water shoreline and approach a value close to two in the swash as predicted above. This study will provide further evidence in support of (2.6) and (2.7). Note that, as in Herrman $et\ al.$ (1997), the swash zone free surface elevation, η, used below corresponds to that measured by a vertical gauge with its lower limit on the fixed beach face.

The root-mean-square wave height, H_{rms}, is defined in this study using the standard deviation, σ, [Thornton and Guza (1983); Battjes and Stive (1985)]

$$H_{\text{rms}} = \sqrt{8}\sigma \tag{2.8}$$

9

If equation (2.7) holds in the swash zone, then $H_{\mathrm{rms}}/\bar{h} = \sqrt{8}$, which is much larger than the result $H_{\mathrm{rms}}/\bar{h} \simeq 0.42$, measured in the inner surf zone of a natural beach by Thornton and Guza (1982). On the other hand, the free surface elevation time series measured by vertical capacitance wave gauges buried partially in the sand beach in the SUPERTANK Project (Kriebel 1994) indicated that $H_{mo}/\bar{\eta}$ ranges between 3 and 4 at the still water shoreline, where H_{mo} = zero-moment wave height, given by $H_{mo} = 4\sigma$. Since $z_b = 0$ and $\bar{h} = \bar{\eta}$ at the still water shoreline, this observed range corresponds to $H_{\mathrm{rms}}/\bar{h} = 2.1$ to 2.8. This suggests that equation (2.7) may be reasonable in the swash zone and that the value of $H_{\mathrm{rms}}/\bar{h}$ may increase appreciably from the inner surf zone to the swash zone. The data of Herrman *et al.* (1997) on a 1:16 impermeable slope also indicated that $H_{\mathrm{rms}}/\bar{h}$ approached a value near 3 in the swash zone. This study will provide additional support for these results.

Chapter 3

EXPERIMENTAL PROCEDURES

Because velocity statistics were measured in multiple positions in this study using a single velocimeter, it was necessary to run the same random wave set repeatedly over an unchanging equilibrium profile, repositioning the velocimeter between runs. For this reason, it was important both to achieve an equilibrium beach profile with the fine sand used in the experiment and to obtain repeatable sets of waves. In order to predict the beach profile shape, it was necessary to obtain further information about characteristics of the sediment. Special techniques were required for the calibration and processing of swash wave gauges to ensure accurate measurement of relatively small water depth above the sand bottom. This chapter will review these experimental procedures, summarize their results, and describe the experimental setup.

3.1 Sediment Characteristics

Approximately 6 m^3 of fine white quarry sand was used in the construction of an initially 1:12 beach slope. To anticipate better the shape of the equilibrium profiles that would be established from this initial slope and to facilitate later analysis of sediment transport, several tests were conducted to determine basic characteristics of the fine sand. These tests measured density, specific gravity, porosity, grain size distribution, and fall velocity.

Density, specific gravity, and porosity were estimated using standard testing procedures (Al Khafaji and Andersland 1992). Bulk density was measured by determining the weight of a known volume of lightly compacted sand. To find the specific gravity this measured quantity of sand was then added to a known volume and weight of water in a flask, while maintaining the same total volume in the flask. It was then heated for ten minutes to remove trapped air, and then weighed. The specific gravity of the sand was defined as the ratio of the immersed sand weight to that of the pure water. Sand water content was determined to be insignificant. Using specific gravity and water content data, porosity was calculated as the volume of voids divided by the gross volume of the sand. The bulk density of the sand was found to be $\rho = 1.7$ kg/m^3. Specific gravity was determined to be $s = 2.66$, indicating somewhat silty sand. Porosity was measured as $n_p = 0.4$.

3.1.1   Grain Size

Grain size was measured using a sieve test procedure with seven different sieve sizes. The numerical results of three sieve tests are are shown graphically in Figure 3.1 and summarized in Table 3.1. Sample sizes with total mass (M_T) ranging from 206.1 g to 499.2 g were agitated for 15-25 minutes. The relative steepness of the three curves in Figure 3.1 indicates that the sand is of fairly uniform size and thus will establish an equilibrium profile with little or no variation of sand size along the wave tank. As shown in the figure, mean diameter, d_{50}, was determined by linear interpolation of the portions of the three curves between sieve sizes 0.150 mm and 0.212 mm. In each case, d_{50} was found to be 0.18 mm.
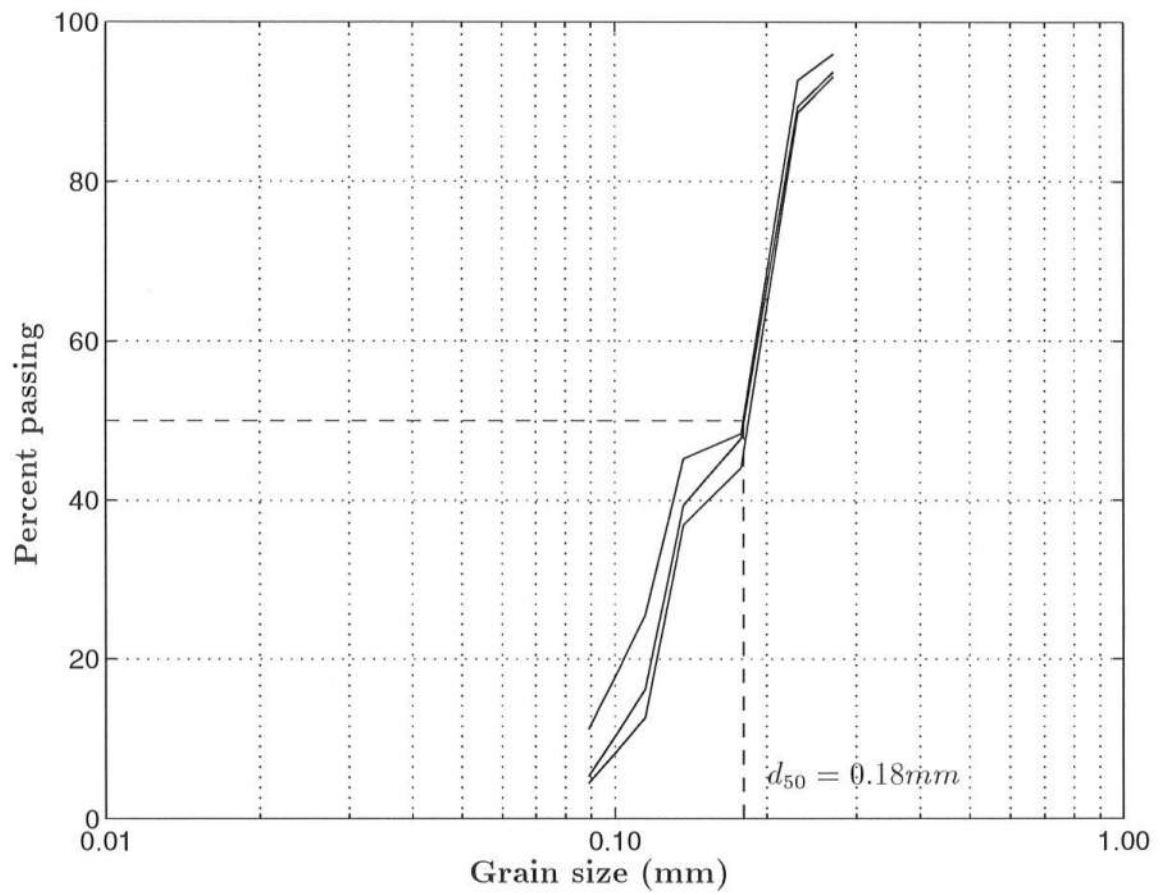
Figure 3.1: Fine White Sand Grain Size Analyses, 1/96 and 10/96

13

Table 3.1: Summary of Sieve Test Data

Sieve	Sand captured(I)			Sand captured(II)			Sand captured(III)		
Sieve	Mass	Percent	Percent	Mass	Percent	Percent	Mass	Percent	Percent
Size(mm)	(g)	of M_T	Passing	(g)	of M_T	Passing	(g)	of M_T	Passing
0.250	33.4	6.87	93.13	12.9	6.26	93.74	20.1	4.03	95.97
0.212	21.8	4.48	88.65	8.9	4.32	89.42	16.2	3.25	92.72
0.150	216.5	44.53	44.12	85.8	41.63	47.79	221.3	44.33	48.39
0.125	35.1	7.22	36.90	17.4	8.44	39.35	15.8	3.17	45.22
0.106	117.9	24.25	12.65	47.7	23.14	16.21	98.2	19.67	25.55
0.075	39.9	8.21	4.44	22.5	10.92	5.29	71.6	14.34	11.22
(Pan)	21.6	4.44	0.00	10.9	5.29	0.00	99.2	11.22	0.00
TOTALS	486.2g	100.00	–	206.1g	100.00	–	499.2g	100.00	–

3.1.2 Fall Velocity

By equating the drag and the submerged weight of a spherical particle falling in quiet water, one obtains the relation

$$\frac{w}{\sqrt{g(s-1)d}} = \sqrt{\frac{4}{3C_D}} \tag{3.1}$$

in which w = particle terminal fall velocity, g = gravitational constant = 9.81 m/s^2, s = particle specific gravity, d = particle diameter, and C_D = drag coefficient. Average fall velocity for the fine sand was calculated by substituting $s = 2.66$ and $d_{50} = 0.18$ mm into equation (3.1), along with an empirical value of C_D for a sphere [*e.g.*, Yalin (1976)]. It was estimated that $w = 1.89$ cm/s for the spherical particle.

Fall velocity was also determined experimentally. A few grains from each size group in the first sieve test were allowed to fall through a clear plastic cylinder filled with water, and their motion was visually timed for a distance of one meter. Ten fall times were recorded for each size group and then averaged to obtain a mean fall velocity for each group. Results are summarized in Table 3.2. When these results were averaged with weighting proportional to each group's percent of the total mass,

14

Table 3.2: Fall Velocity Measurement Results

Sieve Number	Effective Diameter	Percent of M_{total}	Measured w
60	0.27mm	6.26%	5.2 cm/s
70	0.230	4.32	3.0
100	0.178	41.63	2.1
120	0.137	8.44	1.6
140	0.115	23.14	1.3
200	0.089	10.92	1.0
Pan	—	5.29	0.67

it was found that $w_{avg} = 1.9$ cm/s, practically the same as the 1.89 cm/s predicted for the sphere of diameter $d_{50} = 0.18$ mm.

3.2 Experimental Setup

The experiments were conducted in a wave tank that was 30 m long, 2.44 m wide, and 1.5 m high with a constant water depth of 61.0 cm. Repeatable irregular waves, based on the TMA spectrum (Bouws *et al.* 1985) using linear wave theory and random phases, were generated with a piston-type wave paddle. The experimental setup is shown in Figure 3.2. A rock beach with a 1:8 slope was located at the far end of the tank to absorb waves propagating outside of the experimental area. The previously constructed divider wall along the center line in the tank was again used to enclose the beach, and a rear wall was added to support the upper beach berm area. As mentioned above, the fine sand beach was built with an initial slope of 1:12. Ten capacitance wave gauges were used to measure the temporal variations of free surface elevations. An Acoustic-Doppler Velocimeter (ADV) (Kraus *et al.* 1994) was employed to measure the temporal variations of fluid velocities. The sampling rate for the free surface and fluid velocity measurements was 20 Hz. Two tests were conducted on two different sand profiles after equilibrium had been established

PROFILE VIEW

PLAN VIEW
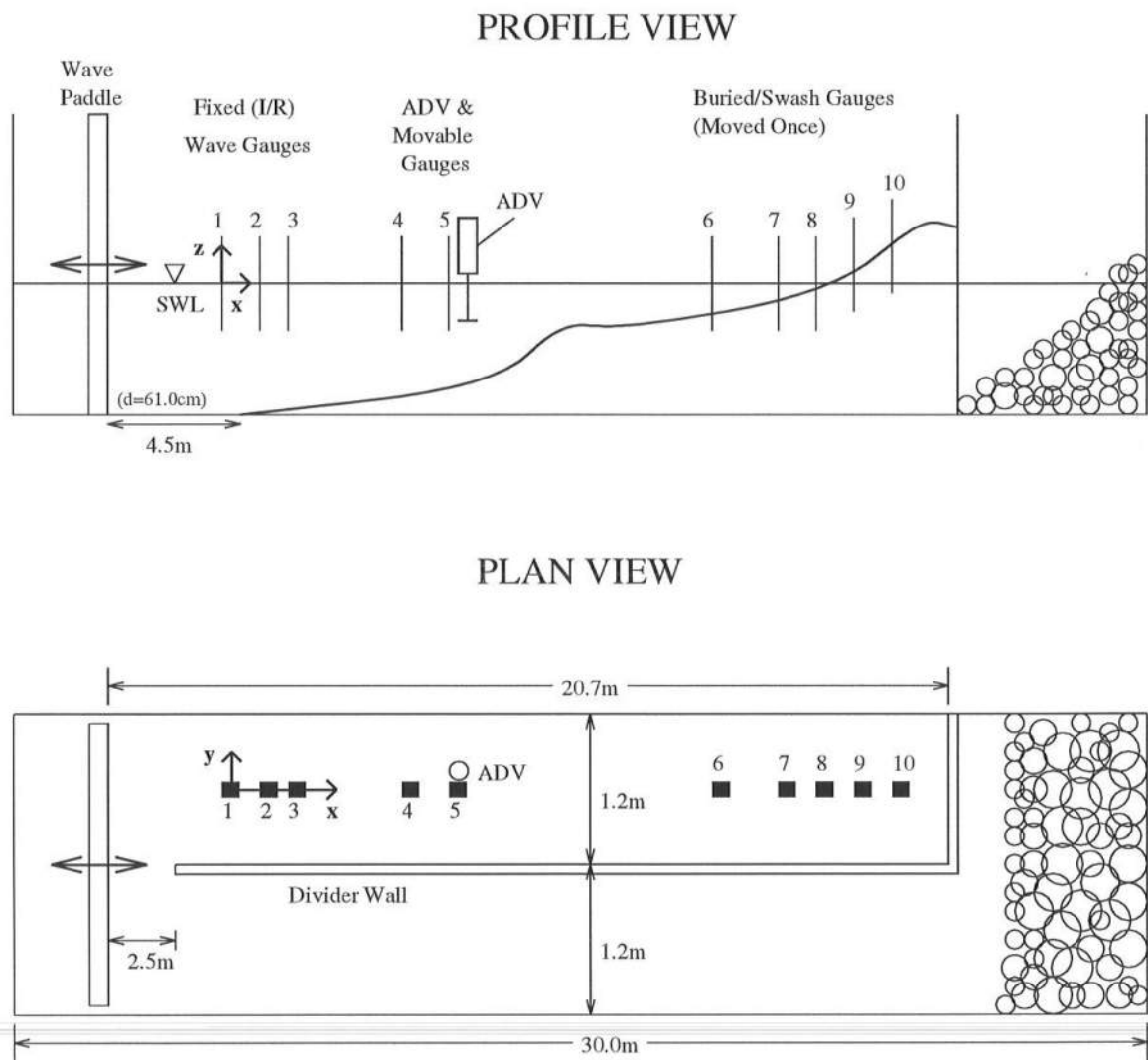
Figure 3.2: Wave Tank Experimental Setup

under the specified random wave action. The wave paddle motion, controlled by a computer, was approximately identical for all the runs in each test.

3.3 Establishing Equilibrium Profiles

To estimate whether acceptable equilibrium profiles would be attained for the given sand beach and incident waves, use was made of the simple profile shape equation introduced by Bruun (1954):

$$d = Ay^{2/3} \tag{3.2}$$

where d = still water depth to profile (m), y = distance offshore from still water shoreline (m), and A = sediment scale parameter based on the mean diameter of the sand. It is noted that d is used in this study for both sediment diameter and still water depth, in accordance with their customary notations. For sand with d_{50} = 0.18mm it was estimated that $A = 0.094$ m$^{1/3}$ (Dean et $al.$ 1994).

Initial attempts to predict onshore/offshore sand transport in this study made use of the profile parameter for random waves in the field (Kraus and Mason 1993):

$$P_s = \frac{gH_{s,o}^2}{w^3 T_p} \tag{3.3}$$

where $g = 9.81$ m/s^2, $H_{s,o}$ = significant wave height in deep water (m), w = sediment fall velocity = 0.019 m/s in this experiment, and T_p = peak period of incident random waves. For values of $P_s \geq 26{,}500$, data generally shows offshore transport and the creation of bars in the field. For the random wave sets chosen to be used in tests 1 and 2, the incident wave spectral peak periods were $T_p = 2.8$ s and 1.6 s and the significant wave heights were $H_{s,o} = 0.21$ m and 0.18 m, respectively. For these wave conditions, the corresponding profile parameters were determined to be approximately 22,000 and 29,000. This implied empirically that there would be a tendency for onshore transport with the formation of a berm in test 1 and offshore transport with the creation of a bar in test 2.

17

Before each of the two tests was begun, the random wave set preselected for each test was run repeatedly for several days, and the beach was allowed to shape itself into a stable equilibrium profile. Testing commenced only after the profile shape was observed to remain nearly constant for approximately one day of wave action. A comparison of the two final equilibrium profiles for tests 1 and 2 is shown in Figure 3.3, along with a plot of the predicted $Ay^{2/3}$ profile shape. While the
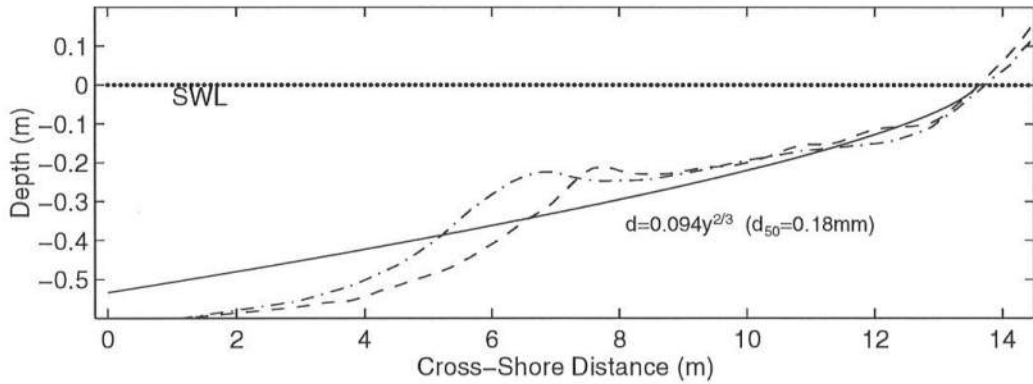
Figure 3.3: Final Equilibrium Profiles (- - Test 1; -.- Test 2) and $d = Ay^{2/3}$

$Ay^{2/3}$ profile follows the general trend of the two equilibrium profiles, it does not account for the significant perturbations in the region of the bars. The steeper slope further offshore is partly a result of the initial 1:12 slope which is steeper than typical offshore slopes. In partial agreement with the predictions of the profile parameter, the test 1 profile stabilized as a terrace, with only minor evidence of a bar and trough. A larger and more visible bar and trough developed on the test 2 profile, after a period of offshore transport.

3.4   Measurement of Equilibrium Profiles

During each of the two tests detailed measurements were made of the beach profile using a manual vernier pointer in the swash zone and a Panametrics 22DLHP ultrasonic depth gauge in deeper water. To ensure that longshore profile variation

18

was negligible, the profile was measured along three cross-shore transects separated by 28 cm in the longshore direction, with the center transect running down the center of the experimental beach area. Each transect included 77 measurement points spaced at 16 cm. For test 1, three-transect profiles were taken before the test began, in the middle of the test, and after the test was complete. For test 2, because of complications with the ultrasonic depth gauge, it was only possible to take a two-transect profile before the test and a three-transect profile after the test.

As shown in Figures 3.4 – 3.8, longshore variation in the raw profile data was generally small, especially in the swash zone. The cross-shore distance in these figures corresponds to the shoreward distance from the coordinate origin at the location of wave gauge 1, as shown in Figure 3.2. The greatest variation occurred slightly offshore of the swash zone and amounted to about 10% of the water depth. In both tests fairly uniform ripples were established in the regions offshore of the bar and along the terrace between the bar and the swash zone. These ripples were approximately 1–3 cm in height and 10–15 cm in length and were observed to shift their position slightly during runs. The representative profile for each measurement set was obtained by first smoothing the three transects with a three-point smoothing routine and then averaging the resulting profiles. The final equilibrium profile for test 1 was obtained by averaging the pre-test, mid-test, and post-test smoothed profiles. The final equilibrium profile for test 2 was an average of the pre-test and post-test smoothed profiles only. The smoothed profiles for each date are shown in Figures 3.9 and 3.10. The small profile shifts that occurred over several hours of testing are represented by the differences between these lines. Such insignificant change after several hours of wave attack confirms that the profiles were essentially in equilibrium. The final profiles for tests 1 and 2 were plotted earlier in Figure 3.3.
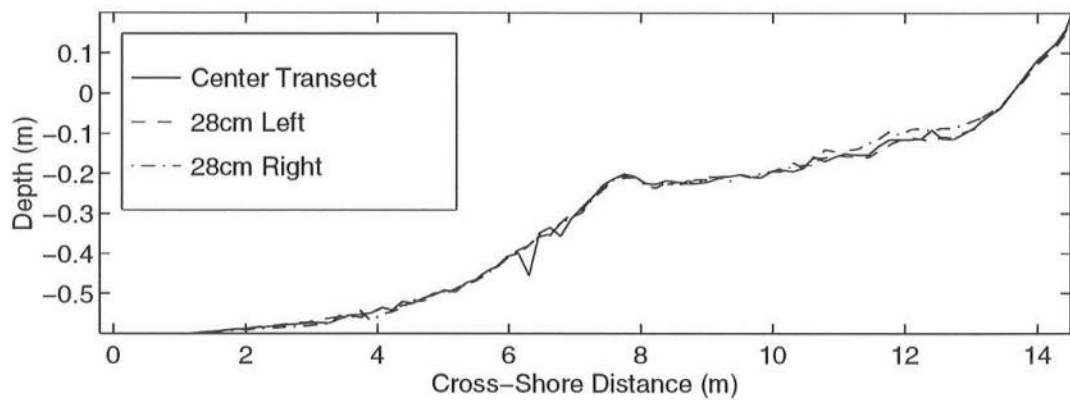
Figure 3.4: Unsmoothed Profiles at Three Transects, 3/7/97 (Pre-Test 1)
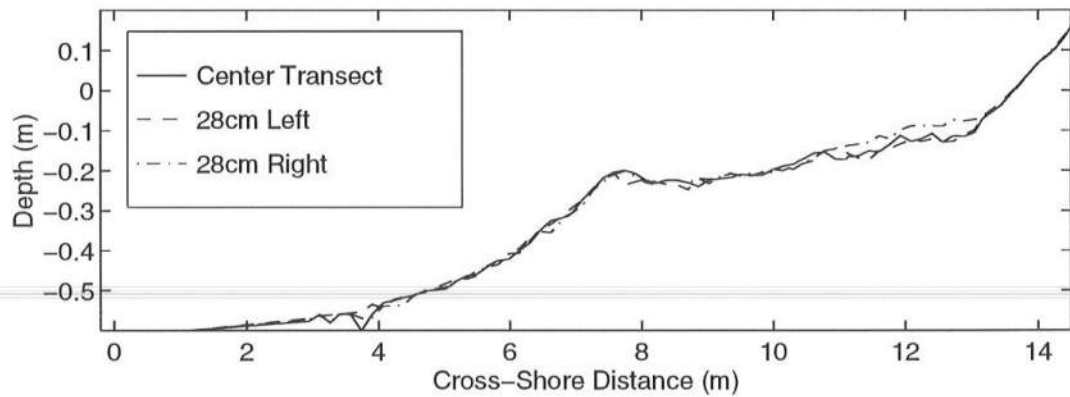
Figure 3.5: Unsmoothed Profiles at Three Transects, 3/11/97 (Mid-Test 1)
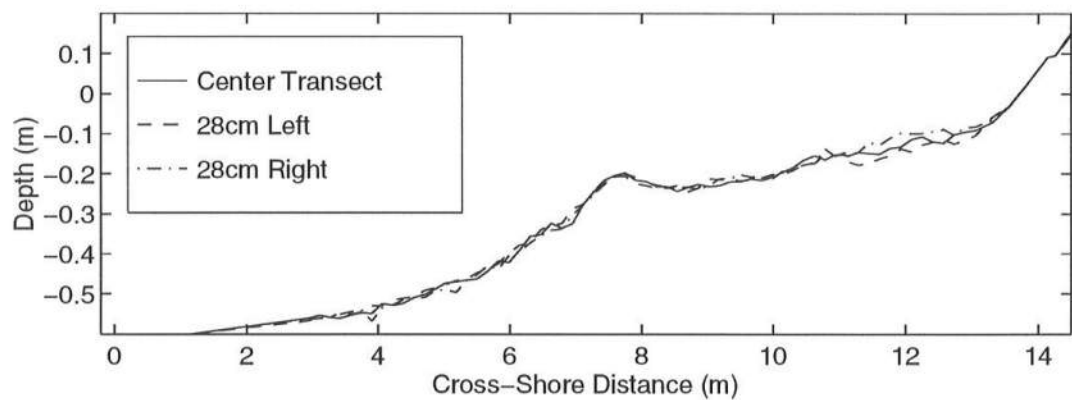
Figure 3.6: Unsmoothed Profiles at Three Transects, 3/13/97 (Post-Test 1)
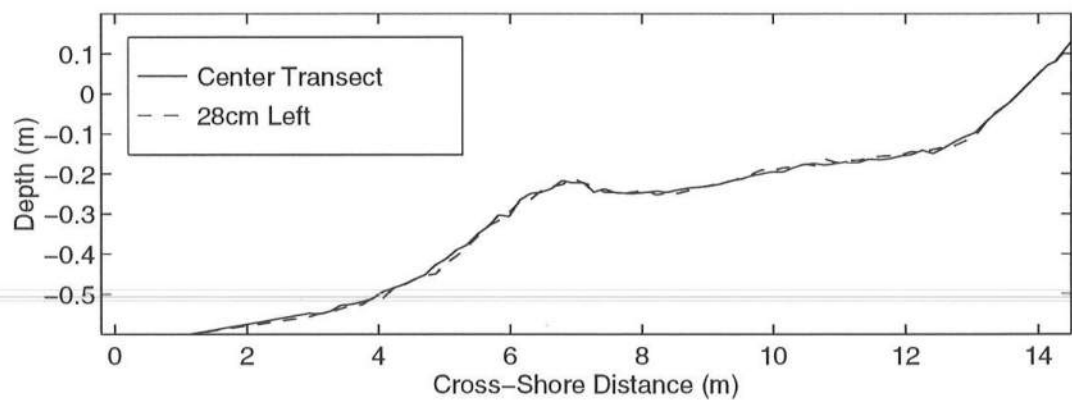
Figure 3.7: Unsmoothed Profiles at Two Transects, 5/2/97 (Pre-Test 2)

21
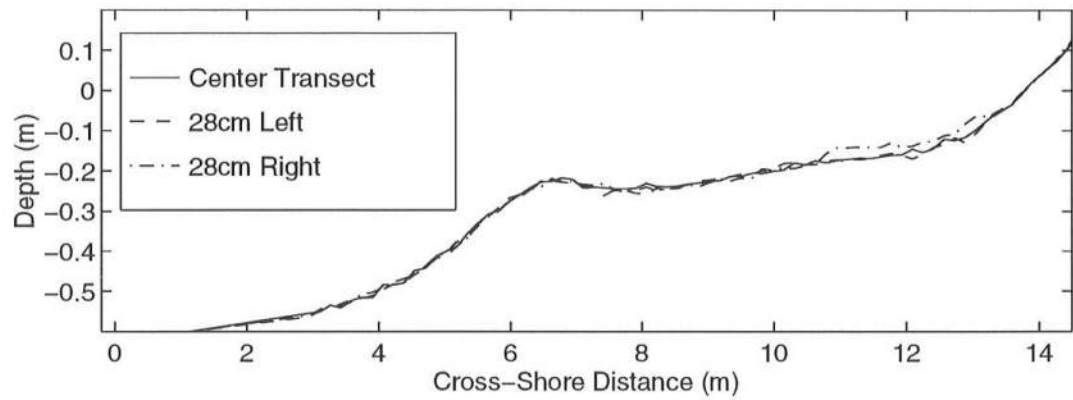
Figure 3.8: Unsmoothed Profiles at Three Transects, 5/30/97 (Post-Test 2)
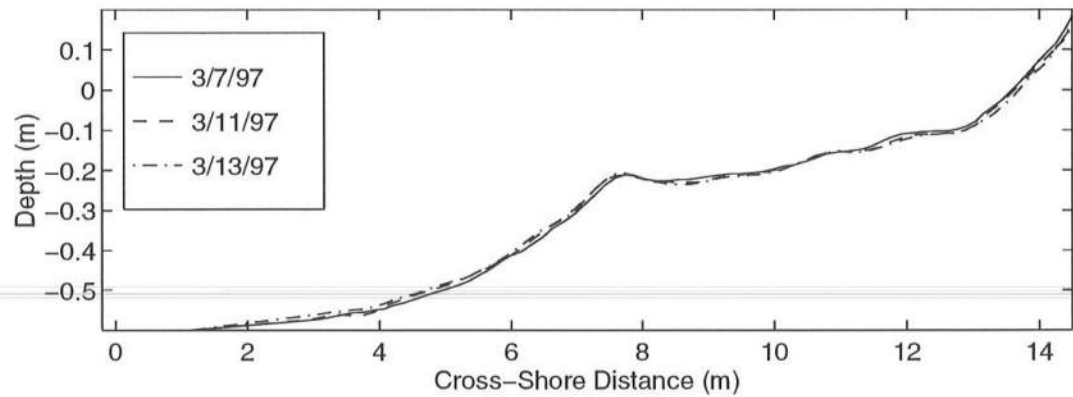
Figure 3.9: Smoothed Average Profiles, 3/7/97, 3/11/97, and 3/13/97 (Test 1)

22
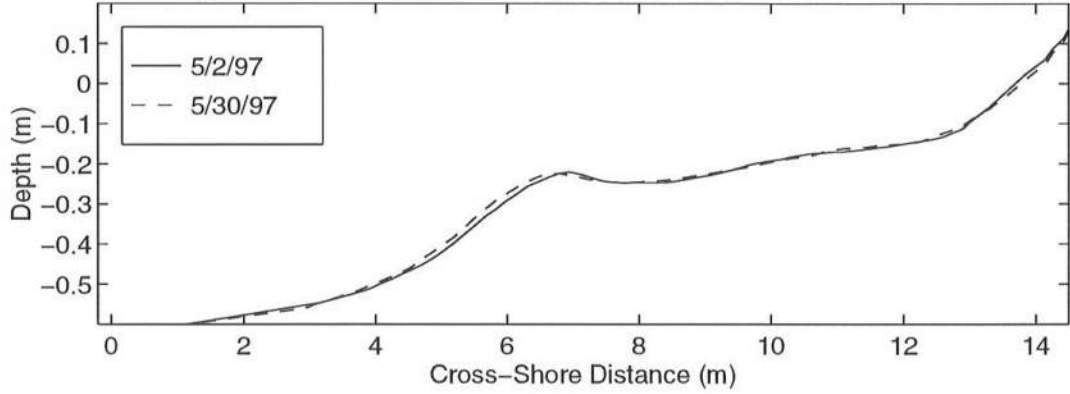
Figure 3.10: Smoothed Average Profiles, 5/2/97, 5/30/97 (Test 2)

3.5 Gauge Measurement Positions

Each test consisted of 21 runs performed for the free surface measurements along the center line of the beach profile. Velocity measurements were made at a location approximately 10 cm to one side of the center line (see Figure 3.2). The duration of each run was 400 s, from which the initial transient duration of 75 s was removed. The remaining 325 s of each time series was used for the subsequent data analyses. The runs from each test were numbered 1 through 21.

3.5.1 Wave Gauge Positions

The cross-shore locations of all wave gauge measurement positions are shown in Figure 3.11, over the two final equilibrium profiles. Wave gauges 1, 2, and 3 were fixed for each test and employed to separate the incident and reflected waves using the procedure described by Kobayashi and Raichle (1994). The gauges were located at the water depth $d = 60.0$ cm below SWL for both tests. In accordance with the procedure of Herrman et $al.$ (1997), the horizontal coordinate x in this paper is taken to be positive landward with $x = 0$ at the location of gauge 1. For both tests, wave gauges 2 and 3 were located at $x = 0.38$ m and $x = 0.50$ m, respectively.

23
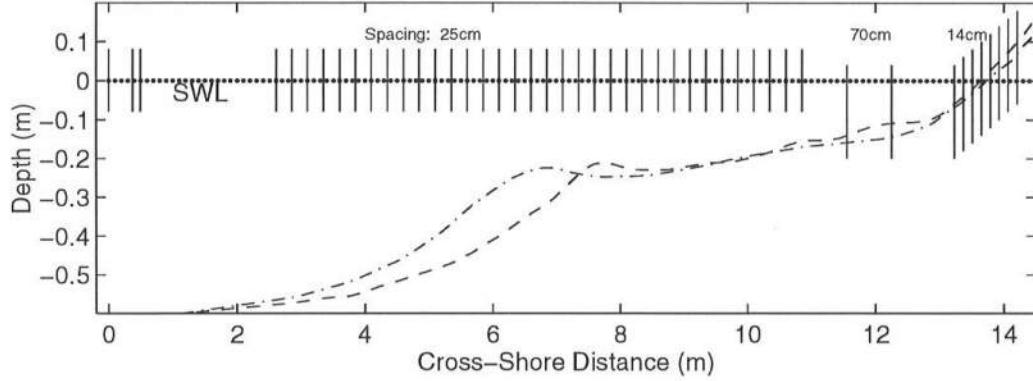
Figure 3.11: Cross-Shore Positions of Wave Gauge Measurements Over Final Profiles (- - Test 1, -.- Test 2)

As indicated in Figure 3.2, wave gauges 4 and 5 were attached to a movable carriage along with the ADV. They were repositioned 17 times during each test. Measurements made by these wave gauges were spaced at 0.25 m and covered a region from $x = 2.60$ m to 10.85 m, with corresponding depth range $d = 15$–58 cm for test 1 and $d = 17$–57 cm test 2. The ADV and gauge 5 were at the same cross-shore position during each run in order to allow for synchronized measurements of surface elevation and cross-shore velocity. Gauges 6 through 10 were partially buried in the sand and were moved only once, between runs 12 and 13 for test 1 and between runs 10 and 11 for test 2. The two positions of gauge 6 were spaced 0.70 m apart, while the swash measurements of gauges 7-10 were spaced at 0.14 m. Water depths at gauges 4-10 for the two tests are listed in Tables 3.3 and 3.4. Note that the water depth d is used for gauges 4–6, whereas the bottom elevation $z_b = -d$ is given for gauges 7–10 to avoid implying a negative water depth in the swash zone, where $d < 0$. The bottom elevations at gauges 7–10 were measured by a manual vernier pointer for each run because the relatively small water depth at these gauge locations was significantly affected by the minor bottom elevation change during runs.

24

Table 3.3: Depth of Water at each Gauge Position for Free Surface Test 1

Run	Water Depth, d (cm)			Bottom Elevation, z_b (cm)			
	Gauge 4	Gauge 5	Gauge 6	Gauge 7	Gauge 8	Gauge 9	Gauge 10
1-1	58	58	14	-6.6	-3.4	2.1	7.4
1-2	57	56	14	-6.7	-3.4	2.0	7.4
1-3	56	55	14	-6.6	-3.4	1.9	7.3
1-4	54	53	14	-6.5	-3.4	1.8	7.2
1-5	51	50	14	-6.6	-3.4	1.7	7.1
1-6	49	47	14	-6.7	-3.5	1.6	7.0
1-7	45	43	14	-6.8	-3.4	1.7	7.1
1-8	40	37	14	-6.9	-3.3	1.7	7.1
1-9	34	32	14	-6.9	-3.4	1.6	7.0
1-10	28	24	14	-6.8	-3.5	1.5	7.0
1-11	28	24	14	-6.7	-3.5	1.4	6.9
1-12	28	24	14	-6.8	-3.6	1.4	6.8
1-13	21	21	11	-6.5	-2.3	4.0	10.0
1-14	22	23	11	-6.5	-2.4	3.8	9.9
1-15	23	23	11	-6.3	-2.3	3.6	9.8
1-16	22	21	11	-6.1	-2.3	3.6	9.8
1-17	21	21	11	-6.2	-2.3	3.5	9.6
1-18	21	21	11	-6.1	-2.4	3.5	9.5
1-19	21	21	11	-5.9	-2.5	3.4	9.4
1-20	20	18	11	-6.3	-2.4	3.2	9.3
1-21	17	15	11	-6.6	-2.6	3.1	9.2

Table 3.4: Depth of Water at each Gauge Position for Free Surface Test 2

Run	Water Depth, d (cm)			Bottom Elevation, Z_b (cm)			
	Gauge 4	Gauge 5	Gauge 6	Gauge 7	Gauge 8	Gauge 9	Gauge 10
2-1	57	57	16	-8.8	-4.9	0.4	4.9
2-2	55	54	16	-9.8	-4.6	0.5	5.0
2-3	53	51	16	-7.7	-4.9	0.0	4.5
2-4	50	48	16	-7.3	-5.2	0.0	4.6
2-5	46	44	16	-9.7	-4.7	0.4	5.0
2-6	41	38	16	-9.5	-4.8	0.4	5.1
2-7	35	31	16	-9.5	-4.9	0.4	5.0
2-8	28	26	16	-8.0	-4.7	0.2	4.7
2-9	24	22	16	-7.9	-4.9	0.1	4.7
2-10	22	24	16	-7.7	-4.9	0.0	4.5
2-11	22	24	14	-5.0	-3.1	2.0	6.4
2-12	22	24	14	-5.0	-3.0	2.0	6.3
2-13	25	25	14	-5.3	-3.0	1.1	6.2
2-14	25	25	14	-5.6	-3.0	2.0	6.2
2-15	24	23	14	-5.6	-3.1	2.0	6.2
2-16	23	22	14	-5.5	-3.1	1.9	6.2
2-17	21	20	14	-5.5	-3.1	2.0	6.2
2-18	21	20	14	-5.5	-3.0	1.9	6.1
2-19	21	20	14	-5.6	-3.0	1.9	6.1
2-20	19	18	14	-5.7	-3.1	1.9	6.1
2-21	18	17	14	-5.8	-3.1	2.0	6.1

Wave gauges 6 through 10 were partially buried in the sand beach, as illustrated in Figure 3.2. Gauges 7 through 10 were located within the swash zone, while gauge 6 was in water that was too shallow to allow operation of an ordinary capacitance gauge. Figure 3.12 depicts the special design of these swash gauges, intended to minimize scour around the point of contact between gauge and sand. The gauge ground was connected to a flat steel plate and attached to the divider wall shown in Figure 3.2, while the active end of the gauge consisted only of a thin insulated rod.
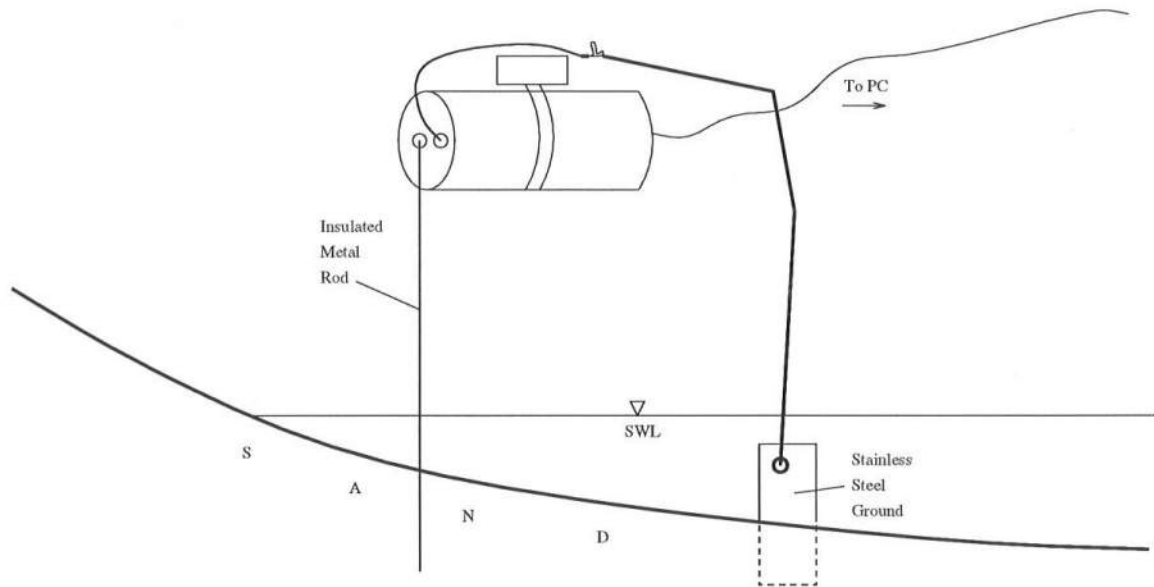
Figure 3.12: Swash Wave Gauge Design

3.5.2   Wave Gauge Calibration

Wave gauges were calibrated before and in the middle of each of the two tests. Calibrations were conducted by raising the level of water in the tank until the sand at gauge 10 was at least 5 cm under water, then gradually draining the tank and recording gauge voltage readings for every 1 cm change in the water surface. For every calibration 25 different readings were recorded for each of the ten gauges. For the pre-test calibrations the water level was initially raised to +13 cm relative to the normal still water level, while for the mid-test calibrations the water level was initially raised to +15 cm. This level was then allowed to drop by 24 cm to -11 cm (pre-test) or -9 cm (mid-test). The higher initial water level for the mid-test calibration was necessary to obtain a sufficient number of gauge 10 calibration points after that gauge was moved to its highest position.

27
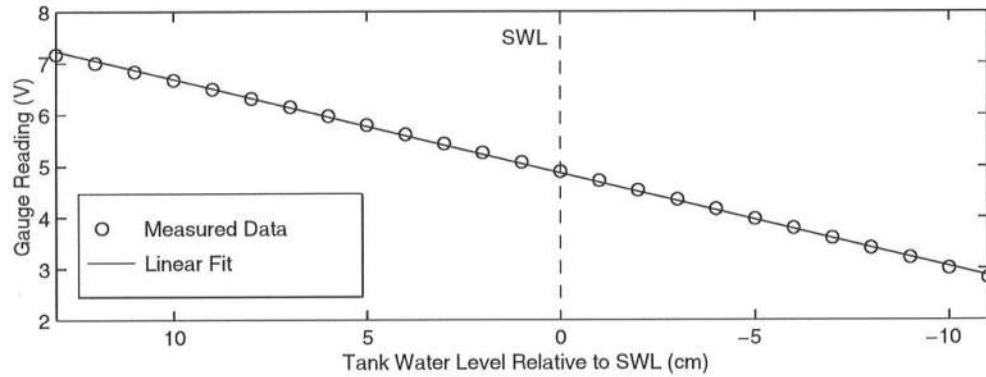
Figure 3.13: Calibration Points and Linear Fit, Gauge 1, Pre-Test 1

For gauges 1–5 calibration data generally followed a straight line, as illustrated for gauge 1 in Figure 3.13. For these gauges the conversion factor was obtained from the best fit slope to all of the data points. This slope is shown in Figure 3.13 as a solid line. The vertical dashed line in the figure represents the elevation of the normal still water level during the wave tests. For the buried gauges 6–10 the sand bottom was eventually exposed by the falling water level in the tank during the calibration. At this point readings from each gauge became more erratic and strayed from the straight line slope, as shown for a gauge 9 calibration in Figure 3.14. In this plot the voltage readings follow the linear fit quite well while the water level is above the sand. However, they immediately depart from the straight line once the falling water exposes the sand (indicated here by the vertical dashed line). This departure is partly due to a delayed drop of the water table in the sand as compared to the water level in the tank. It is also likely that gauge readings are distorted in the partially saturated sand because of the different capacitance of the material. Because of such irregular effects in partially saturated sand, it was decided to obtain conversion factors for the buried gauges by using only the slope of the linear fit to the data above the sand level. Such a slope is shown by the solid

28
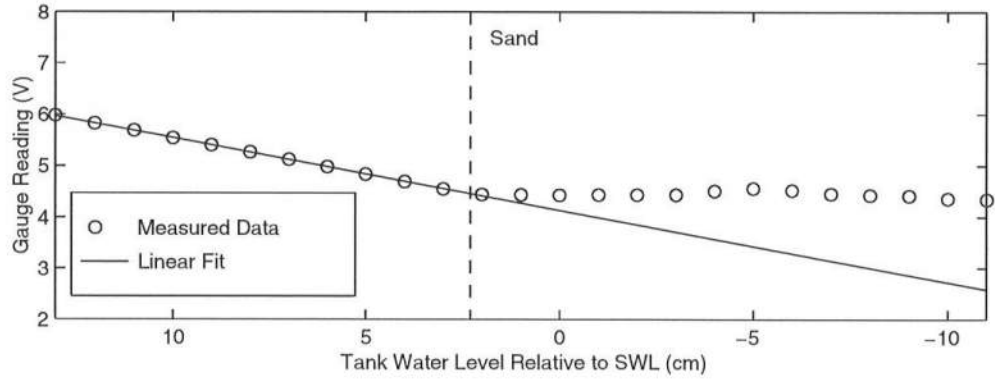
Figure 3.14: Calibration Points and Linear Fit, Gauge 9, Pre-Test 1

line in Figure 3.14. In order to obtain at least five linear points above the sand at the highest position of gauge 10, $z_b = 10$ cm, it was necessary to raise the water in the tank to its highest level, 15 cm above SWL.

Following test 1, it was determined that readings for gauge 7 were erratic in both calibrations. Significant variation had occurred even before the falling water level had exposed the sand at that gauge. Figure 3.15 shows an example of this irregular behavior between the two vertical dashed lines, which here represent still water level and sand level, respectively. Because such irregularity would have resulted in additional errors of up to 3 cm in free surface measurements, it was decided to discard all gauge 7 records from the data analyzed in test 1. The first twelve runs for gauge 8 in test 1 were also discarded for the same reason. For test 2, no such calibration irregularities were observed. However, it was necessary to discard one record each for gauge 5 at $x = 10.35$ m and gauge 6 at $x = 12.25$ m in run 20 of the second test because they exhibited large and unrealistic deviations from all other wave records in the test.

29
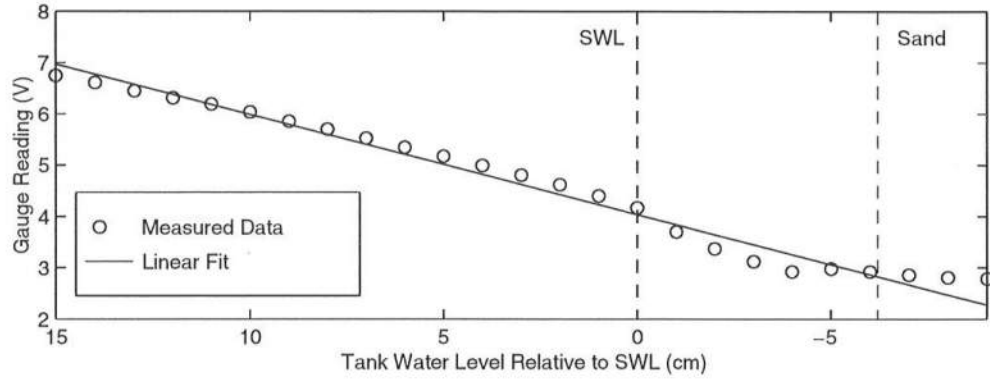
Figure 3.15: Calibration Points and Linear Fit, Gauge 7, Mid-Test 1

3.5.3 Velocity Gauge Positions

A 2D side-looking probe was attached to the acoustic Doppler velocimeter cylinder at the end of a steel rod 40 cm in length, allowing for measurement of cross-shore and longshore water velocities. Longshore velocities associated with three-dimensional turbulence were small compared with cross-shore velocities, which were dominated by waves and wave-induced currents. The 3D side-looking probe, which could also measure vertical velocities, was not used because it was more easily exposed above wave troughs in shallower water. Thus, as in Herrman *et al.* (1997), only cross-shore velocities were analyzed in these tests.

Horizontal and vertical locations of the 21 ADV measurement positions are illustrated in Figure 3.16. The 2D probe was positioned at 17 different cross-shore locations with a horizontal spacing of 0.50 m. At two of these positions ($x = 7.35$ m and $x = 9.85$ m) it was adjusted vertically to obtain three-point profiles of the cross-shore velocity over depth. At the remaining positions the probe was located as close as possible to mid-depth. However, the deep water probe positions were generally above mid-depth to avoid impacts of wave crests on the ADV cylinder. This problem could have been avoided by use of a longer rod connecting the probe

30
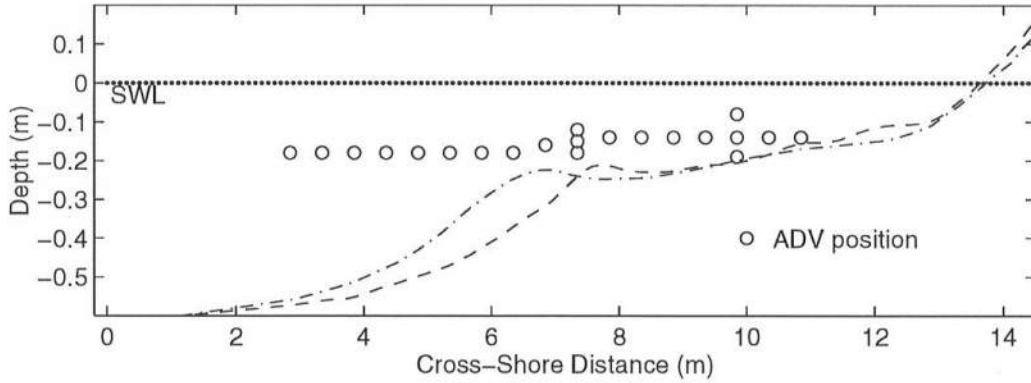
Figure 3.16: Velocimeter Probe Measurement Positions Over Final Profiles
(- - Test 1; -.- Test 2)

and the ADV cylinder, but the longer rod might then have resulted in excessive vibration of the probe. The shallow water probe positions were below mid-depth to avoid exposure of the probe to air above wave troughs.

3.6 Repeatability of Tests

After completing the 21 runs for the free surface and velocity measurements for the two tests, the repeatability of the incident and reflected waves was checked for each test. The separated incident and reflected wave spectra at the location of wave gauge 1 were plotted together for the 21 runs, as shown in Figure 3.17. The plotted 21 spectra for the incident and reflected waves in tests 1 and 2 were almost identical.

Comparisons were also made of the spectral parameters, such as the incident wave spectral peak period, T_p, the spectral estimate of the incident significant wave height, $H_{mo} = 4\sqrt{m_0}$, with m_0 = zero-moment of the incident wave spectrum, and the average reflection coefficient, $R = \sqrt{(m_0)_r/m_0}$, with $(m_0)_r$ = zero-moment of the reflected wave spectrum. In addition, the separated incident wave time series were analyzed using a zero-upcrossing method to obtain the time series parameters, such

31
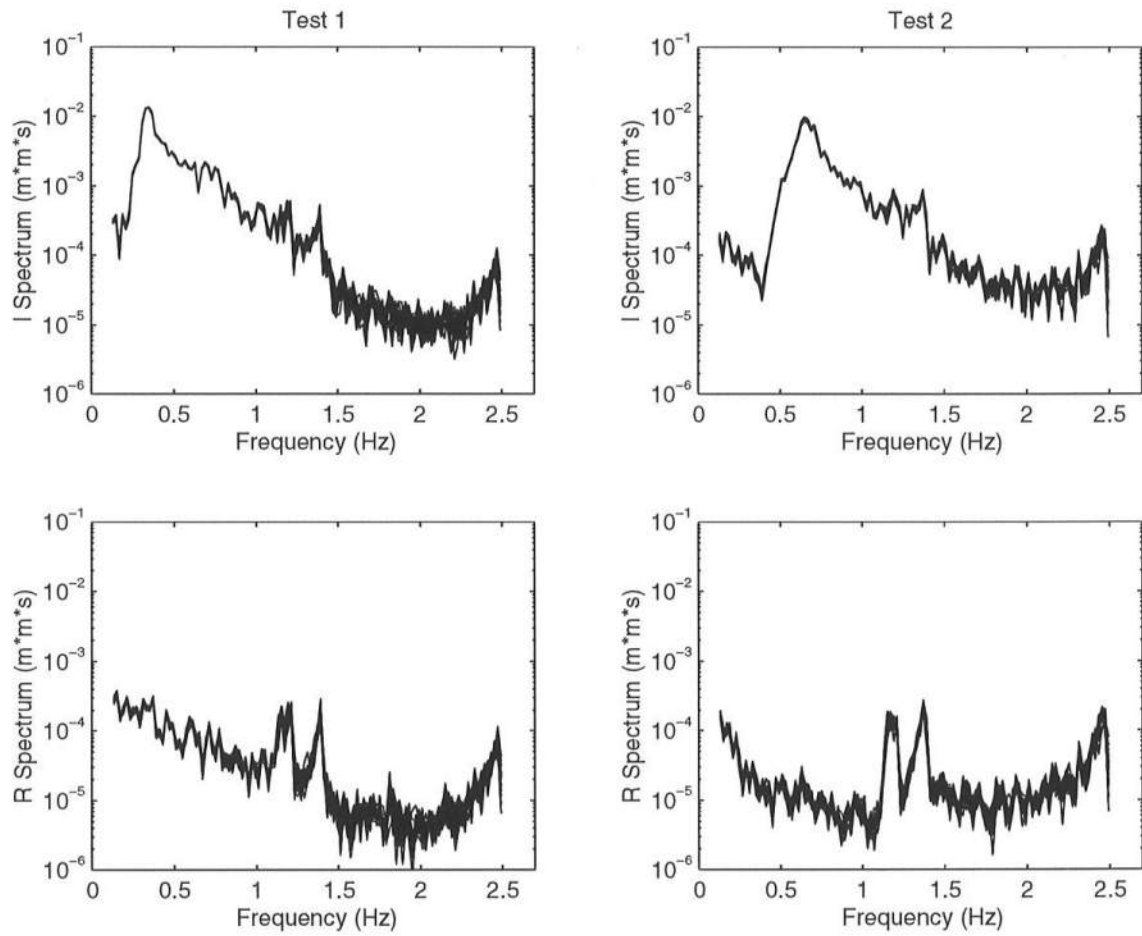
Figure 3.17: Smoothed Power Density Spectra of Incident (I) and Reflected (R) Waves for Test 1 and 2

Table 3.5: Incident Wave Characteristics for Two Tests

Test	T_s (s)	H_s (cm)	T_p (s)	H_{mo} (cm)	H_{rms} (cm)	R
1	2.5	20.7	2.8	20.3	14.3	0.25
2	1.4	18.5	1.6	18.2	12.6	0.19

as the significant wave period, T_s, and the significant wave height, H_s. Table 3.5 lists the average values of T_s, H_s, T_p, H_{mo}, H_{rms}, and R for the 21 runs for both tests. Here, H_{rms} is defined by (2.8). In Tables 3.6 and 3.7, average wave parameters are shown for each of the 21 runs in tests 1 and 2, respectively.

The deviations from the average values of T_s, H_s, T_p, H_{rms}, and H_{mo} in the 21 runs were generally less than 1% and did not exceed 4%. The reflection coefficient, R, varied less than for Herrman *et al.* (1997), with a nearly constant value of $R = 0.25$ for test 1 and a range of $R = 0.18$–0.19 for test 2. The waves in test 1 plunged intensely in a small region slightly shoreward of the terrace edge, creating a large amount of suspended sediment. Spilling breakers were more common in test 2, and breaking occurred more continuously over the bar and in shallower water up to the swash zone. Visual estimates of the extent of breaker and swash zones are shown over the final equilibrium profiles in Figures 3.18 and 3.19.

The values for wave setup, $\bar{\eta}$, root-mean-square wave height, H_{rms}, skewness, and kurtosis were also compared for gauges 1–3 in each run of both tests. These values, shown in Tables 3.8 – 3.11, are consistent through each test and generally within small percentage points of error. It may thus be concluded that the runs of tests 1 and 2 were acceptably repeatable.

Table 3.6: Time Series and Spectral Parameters for Test 1

| Run | Time Series | | Spectral | | |
	$T_s(s)$	$H_s(cm)$	$H_{mo}(cm)$	$H_{rms}(cm)$	R
1-1	2.5	20.6	20.1	14.3	0.25
1-2	2.6	20.8	20.2	14.3	0.25
1-3	2.5	20.8	20.2	14.3	0.25
1-4	2.5	20.4	20.2	14.3	0.25
1-5	2.6	20.9	20.3	14.3	0.25
1-6	2.6	20.6	20.2	14.3	0.25
1-7	2.6	21.0	20.2	14.3	0.25
1-8	2.5	20.6	20.3	14.3	0.25
1-9	2.6	20.6	20.2	14.3	0.25
1-10	2.6	20.9	20.2	14.3	0.25
1-11	2.5	20.2	20.3	14.3	0.25
1-12	2.5	20.4	20.3	14.4	0.25
1-13	2.6	20.8	20.4	14.4	0.25
1-14	2.6	21.1	20.4	14.4	0.25
1-15	2.5	20.4	20.4	14.4	0.25
1-16	2.5	20.6	20.4	14.4	0.25
1-17	2.5	20.8	20.5	14.4	0.25
1-18	2.6	20.8	20.4	14.4	0.25
1-19	2.5	21.1	20.5	14.4	0.25
1-20	2.6	21.1	20.5	14.4	0.25
1-21	2.5	20.6	20.4	14.4	0.25
Mean	2.5	20.7	20.3	14.3	0.25
Max	2.6	21.1	20.5	14.4	0.25
Min	2.5	20.2	20.1	14.3	0.25

Table 3.7: Time Series and Spectral Parameters for Test 2

	Time Series		Spectral		
Run	$T_s(s)$	$H_s(cm)$	$H_{mo}(cm)$	$H_{rms}(cm)$	R
2-1	1.4	18.4	18.2	12.6	0.19
2-2	1.4	18.5	18.2	12.6	0.19
2-3	1.4	18.0	17.6	12.3	0.19
2-4	1.4	18.4	18.1	12.6	0.19
2-5	1.4	18.5	18.1	12.5	0.19
2-6	1.4	18.4	18.1	12.6	0.19
2-7	1.4	18.4	18.1	12.5	0.19
2-8	1.4	18.3	18.0	12.5	0.19
2-9	1.4	18.4	18.0	12.5	0.19
2-10	1.4	18.2	18.0	12.5	0.19
2-11	1.4	18.7	18.5	12.8	0.19
2-12	1.4	18.8	18.5	12.8	0.19
2-13	1.4	18.7	18.5	12.8	0.19
2-14	1.4	18.8	18.4	12.8	0.19
2-15	1.4	18.7	18.5	12.8	0.19
2-16	1.4	18.7	18.4	12.8	0.19
2-17	1.4	18.9	18.4	12.8	0.18
2-18	1.4	18.6	18.4	12.8	0.19
2-19	1.4	18.6	18.3	12.7	0.19
2-20	1.4	18.7	18.3	12.7	0.18
2-21	1.4	18.7	18.4	12.7	0.19
Mean	1.4	18.5	18.2	12.6	0.19
Max	1.4	18.9	18.5	12.8	0.19
Min	1.4	18.0	17.6	12.3	0.18
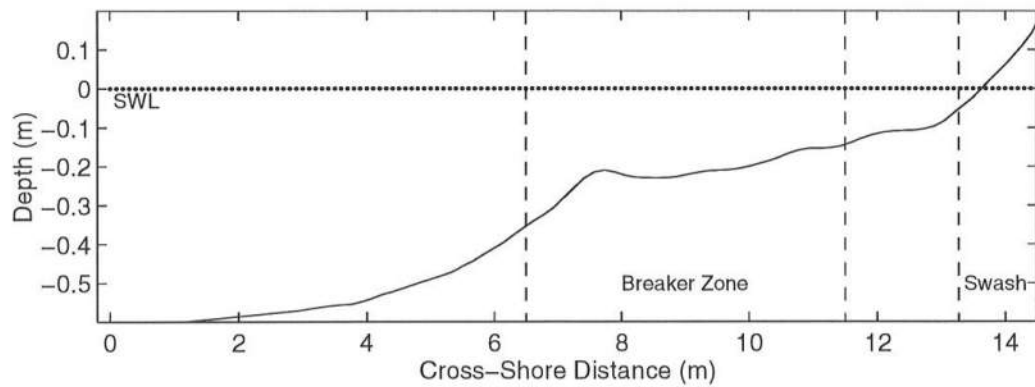
Figure 3.18: Breaker and Swash Zones During Test 1
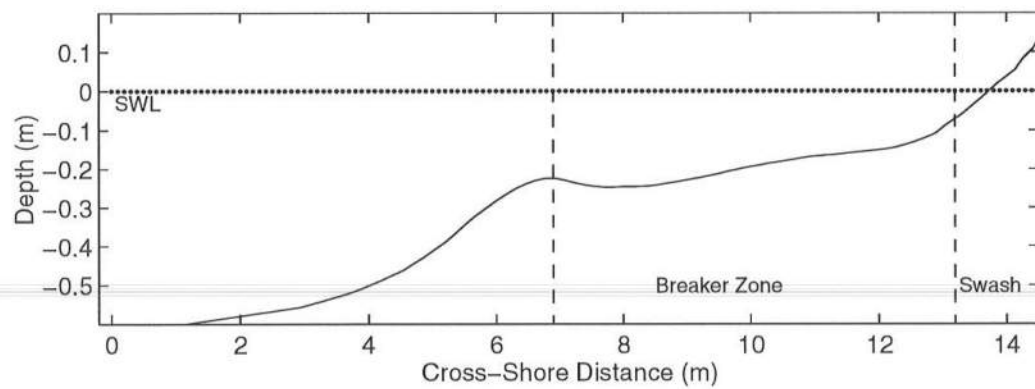
Figure 3.19: Breaker and Swash Zones During Test 2

36

Table 3.8: $\overline{\eta}$ and H_{rms} for Test 1

Run	Setup, $\overline{\eta}\,(cm)$			$H_{rms}\,(cm)$		
	Gauge 1	Gauge 2	Gauge 3	Gauge 1	Gauge 2	Gauge 3
1-1	-0.14	-0.16	-0.22	14.49	14.14	14.19
1-2	0.11	-0.06	-0.06	14.51	14.17	14.18
1-3	-0.02	-0.15	-0.25	14.54	14.12	14.15
1-4	-0.12	-0.05	-0.08	14.52	14.14	14.17
1-5	-0.18	-0.06	-0.02	14.57	14.19	14.22
1-6	-0.47	-0.46	-0.36	14.46	14.14	14.17
1-7	-0.17	-0.24	-0.29	14.52	14.15	14.21
1-8	-0.04	-0.17	-0.17	14.54	14.23	14.25
1-9	-0.06	-0.08	-0.17	14.48	14.16	14.19
1-10	-0.16	-0.14	-0.28	14.52	14.17	14.21
1-11	0.04	0.08	-0.11	14.54	14.22	14.25
1-12	0.06	-0.12	-0.25	14.55	14.26	14.25
1-13	-0.27	-0.27	-0.42	14.66	14.21	14.26
1-14	-0.27	-0.16	-0.22	14.66	14.26	14.29
1-15	-0.05	-0.10	-0.22	14.65	14.25	14.32
1-16	-0.08	-0.22	-0.26	14.68	14.23	14.30
1-17	-0.19	-0.29	-0.37	14.71	14.25	14.33
1-18	0.01	-0.10	-0.20	14.66	14.23	14.26
1-19	-0.41	-0.55	-0.58	14.70	14.25	14.31
1-20	-0.03	-0.06	-0.09	14.69	14.27	14.33
1-21	-0.15	-0.27	-0.33	14.69	14.24	14.29
Mean	-0.12	-0.17	-0.24	14.59	14.20	14.24

Table 3.9: Skewness and Kurtosis for Test 1

Run	Skewness, s			Kurtosis, K		
	Gauge 1	Gauge 2	Gauge 3	Gauge 1	Gauge 2	Gauge 3
1-1	0.66	0.62	0.62	3.86	3.73	3.67
1-2	0.68	0.63	0.62	3.88	3.73	3.65
1-3	0.68	0.62	0.61	3.94	3.69	3.62
1-4	0.69	0.62	0.63	3.94	3.73	3.66
1-5	0.67	0.64	0.63	3.94	3.74	3.65
1-6	0.66	0.63	0.63	3.91	3.72	3.67
1-7	0.68	0.63	0.62	3.92	3.73	3.65
1-8	0.67	0.64	0.64	3.89	3.78	3.70
1-9	0.66	0.62	0.62	3.90	3.74	3.66
1-10	0.67	0.62	0.61	3.91	3.71	3.64
1-11	0.67	0.64	0.64	3.91	3.79	3.72
1-12	0.65	0.64	0.62	3.86	3.74	3.64
1-13	0.66	0.63	0.59	3.86	3.71	3.57
1-14	0.66	0.64	0.60	3.88	3.76	3.63
1-15	0.65	0.63	0.60	3.87	3.75	3.65
1-16	0.65	0.62	0.60	3.86	3.72	3.61
1-17	0.67	0.63	0.62	3.92	3.75	3.65
1-18	0.66	0.63	0.59	3.90	3.73	3.59
1-19	0.65	0.62	0.60	3.93	3.74	3.62
1-20	0.66	0.62	0.60	3.94	3.70	3.59
1-21	0.67	0.61	0.59	3.95	3.69	3.59
Mean	0.67	0.63	0.61	3.90	3.73	3.64

Table 3.10: $\overline{\eta}$ and H_{rms} for Test 2

Run	Setup, $\overline{\eta}(cm)$			$H_{rms}(cm)$		
	Gauge 1	Gauge 2	Gauge 3	Gauge 1	Gauge 2	Gauge 3
2-1	-0.23	-0.22	-0.30	12.78	12.62	12.50
2-2	-0.08	-0.18	-0.12	12.77	12.57	12.49
2-3	-0.15	-0.11	-0.14	12.44	12.23	12.13
2-4	-0.18	-0.10	-0.25	12.72	12.53	12.43
2-5	-0.02	-0.07	-0.04	12.73	12.50	12.41
2-6	-0.10	-0.08	-0.16	12.73	12.53	12.44
2-7	-0.12	-0.05	-0.12	12.71	12.51	12.40
2-8	-0.13	-0.05	-0.14	12.68	12.46	12.38
2-9	-0.14	-0.11	-0.12	12.66	12.55	12.37
2-10	-0.12	-0.06	-0.10	12.62	12.49	12.35
2-11	-0.27	-0.25	-0.11	12.96	12.72	12.71
2-12	-0.17	-0.18	-0.24	12.98	12.74	12.75
2-13	-0.13	-0.16	-0.19	12.96	12.67	12.69
2-14	-0.14	-0.08	-0.19	12.92	12.67	12.69
2-15	-0.18	-0.09	-0.11	12.97	12.75	12.76
2-16	-0.12	-0.12	-0.15	12.92	12.64	12.69
2-17	-0.19	-0.14	-0.14	12.96	12.64	12.70
2-18	-0.18	-0.03	-0.21	12.93	12.64	12.70
2-19	-0.17	-0.08	-0.21	12.84	12.65	12.63
2-20	-0.09	-0.10	-0.19	12.85	12.64	12.64
2-21	-0.18	-0.14	-0.19	12.90	12.64	12.65
Mean	-0.15	-0.11	-0.16	12.81	12.59	12.55

Table 3.11: Skewness and Kurtosis for Test 2

Run	Skewness, s			Kurtosis, K		
	Gauge 1	Gauge 2	Gauge 3	Gauge 1	Gauge 2	Gauge 3
2-1	0.38	0.36	0.34	3.10	3.06	3.01
2-2	0.38	0.37	0.35	3.14	3.09	3.03
2-3	0.40	0.37	0.36	3.26	3.16	3.12
2-4	0.39	0.36	0.36	3.20	3.10	3.05
2-5	0.40	0.37	0.35	3.22	3.09	3.06
2-6	0.40	0.36	0.36	3.16	3.07	3.03
2-7	0.40	0.37	0.35	3.20	3.12	3.04
2-8	0.38	0.35	0.35	3.23	3.10	3.08
2-9	0.41	0.36	0.36	3.23	3.12	3.07
2-10	0.41	0.37	0.35	3.24	3.15	3.07
2-11	0.37	0.36	0.34	3.08	3.04	3.01
2-12	0.40	0.37	0.34	3.17	3.11	3.06
2-13	0.38	0.36	0.34	3.17	3.10	3.05
2-14	0.42	0.37	0.35	3.22	3.10	3.06
2-15	0.38	0.37	0.34	3.15	3.11	3.03
2-16	0.39	0.37	0.35	3.17	3.11	3.05
2-17	0.39	0.36	0.34	3.19	3.07	3.05
2-18	0.39	0.35	0.34	3.17	3.09	3.05
2-19	0.37	0.38	0.35	3.15	3.17	3.07
2-20	0.38	0.36	0.33	3.19	3.14	3.06
2-21	0.39	0.37	0.34	3.22	3.12	3.06
Mean	0.39	0.36	0.35	3.18	3.11	3.05

Chapter 4

FREE SURFACE ELEVATIONS

In this chapter, cross-shore surface elevation statistics will be summarized and used to evaluate the applicability of the exponential gamma distribution in the surf and swash zones. The wave setup, $\bar{\eta}$, the standard deviation, σ, the skewness, s, and the kurtosis, K for each of the measured time series of the free surface elevation, η, are computed under the assumption of equivalency of probabilistic and time averaging, as was done by Herrman $et\ al.$ (1997). These 325 s time series, sampled at the rate of 20 Hz, include the effects of reflected waves. The root-mean-square wave height, H_{rms}, is determined using equation (2.8). The normalized free surface elevation, $\eta_* = (\eta - \bar{\eta})/\sigma$, is then calculated using the measured values of $\bar{\eta}$ and σ. For each of the time series of η_*, the probability density function, $f(\eta_*)$, is computed using 20 bins in the range determined by the measured maximum and minimum values of η_*.

4.1 Probability Density Functions for Gauges 1–3 for Tests 1 and 2

Figure 4.1 shows the measured probability density functions at wave gauges 1–3 for the 21 runs in the two tests. The exponential gamma distribution, $f(\eta_*)$, given by equation (2.1) is also plotted in Figure 4.1 for the measured minimum and maximum values of s for each test. The ordinate for the figures plotted for $f(\eta_*)$ is the normalized free surface elevation, η_*, varying vertically. Figure 4.1 may be used as an indicator of the high degree of repeatability for the 21 runs in each test, as the different runs are almost indistinguishable. The exponential gamma distribution

41
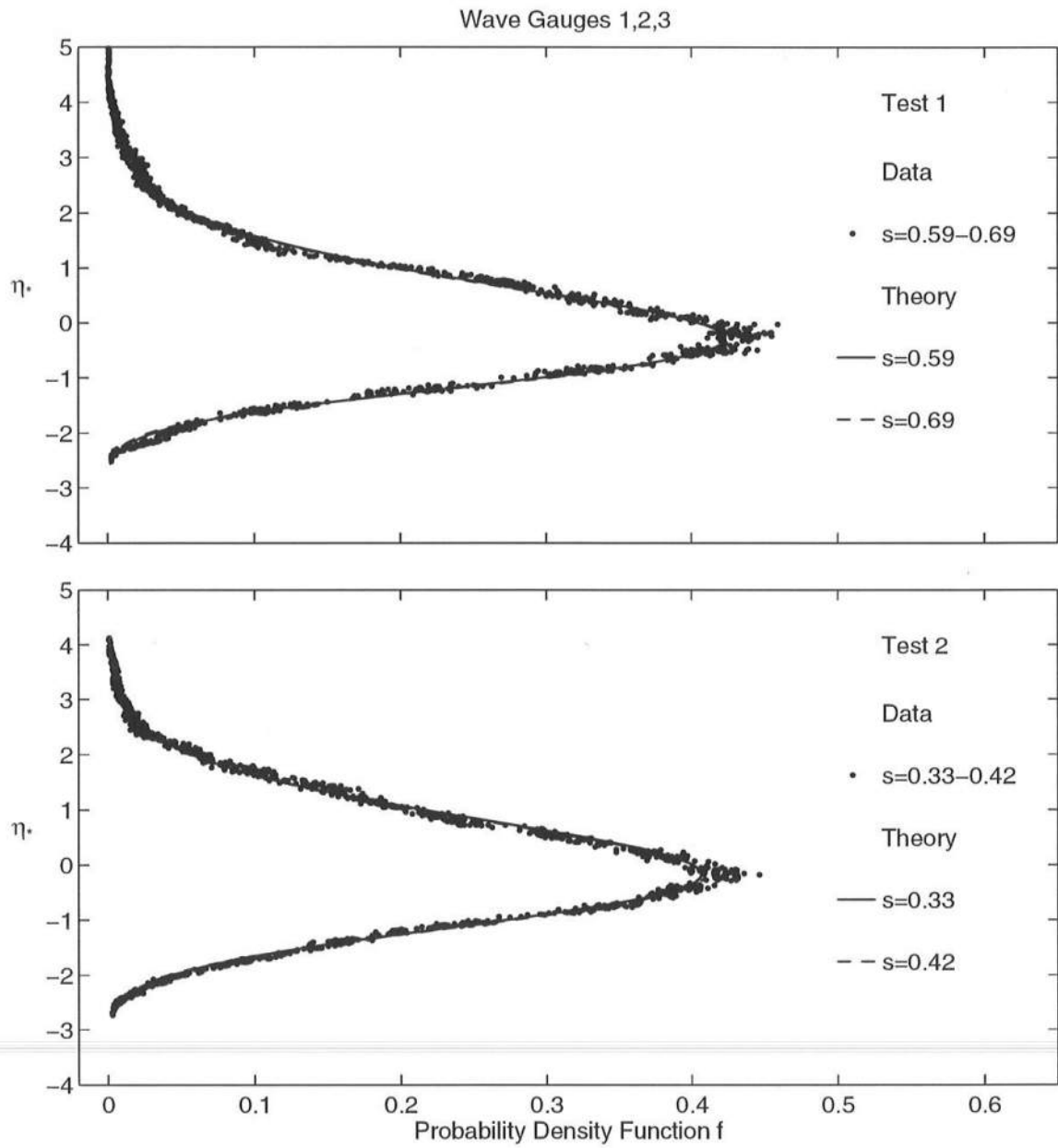
Figure 4.1: Measured and Computed Probability Distributions for 21 Runs at Wave Gauges 1–3 for Tests 1 and 2

changes little for the measured range of s for each test and is in good agreement with the measured distributions, except for the scatter of data points at the peak of $f(\eta_*)$. Gauges 1–3 are located in relatively deep water ($d = 60$ cm), and the distributions are approximately Gaussian, as expected.

4.2   Spatial Variations in Statistical Values of Free Surface Elevations

The measured cross-shore variations of $\bar{\eta}$, H_{rms}, $H_{\mathrm{rms}}/\bar{h}$, and s for tests 1 and 2 are shown in Figures 4.2 and 4.3. The cross-shore coordinate origin, $x = 0$, is located at gauge 1. The mean water depth $\bar{h}$ is given by $\bar{h} = (\bar{\eta} - z_b)$ where z_b is the bottom elevation. The values of $\bar{\eta}$, H_{rms}, $H_{\mathrm{rms}}/\bar{h}$ and s at the locations of wave gauges 1–3 are plotted for all 21 runs in each test. The swash zones of the final equilibrium profiles are shown as solid lines in the upper two plots of each figure. As explained in Section 3.5.2, all the runs for gauge 7 and the first twelve runs for gauge 8 in test 1 were discarded due to calibration uncertainties. Also, values of H_{rms} and $H_{\mathrm{rms}}/\bar{h}$ have been removed for the first twelve runs for gauge 4 in test 1 because the gauge's vertical position shifted after calibration. The data from the repeated measurements at the locations of the buried gauges 6–10 are plotted individually without averaging in order to indicate that the visible scatter of data points is largely limited to the swash zone, as was also seen in Herrman *et al.* (1997).

As expected, the wave setup, $\bar{\eta}$, gradually increases as waves move shoreward in shallower water, becoming tangential to the beach slope in the swash zone. Some variation is visible in swash zone measurements of $\bar{\eta}$. It will be noted that the most shoreward measurement of $\bar{\eta}$ on the top plot of Figure 4.3 appears to be below the average equilibrium sand level explained in Section 3.4. This is likely due to experimental limitations on the precise measurement of the sand bottom position in shallow water, as explained in Section 3.5.1. The actual bottom elevation in the swash zone during each test varied less than 1 cm as listed in Tables 3.3 and 3.4. The statistical analysis also becomes less reliable in regions of extremely small depth

43
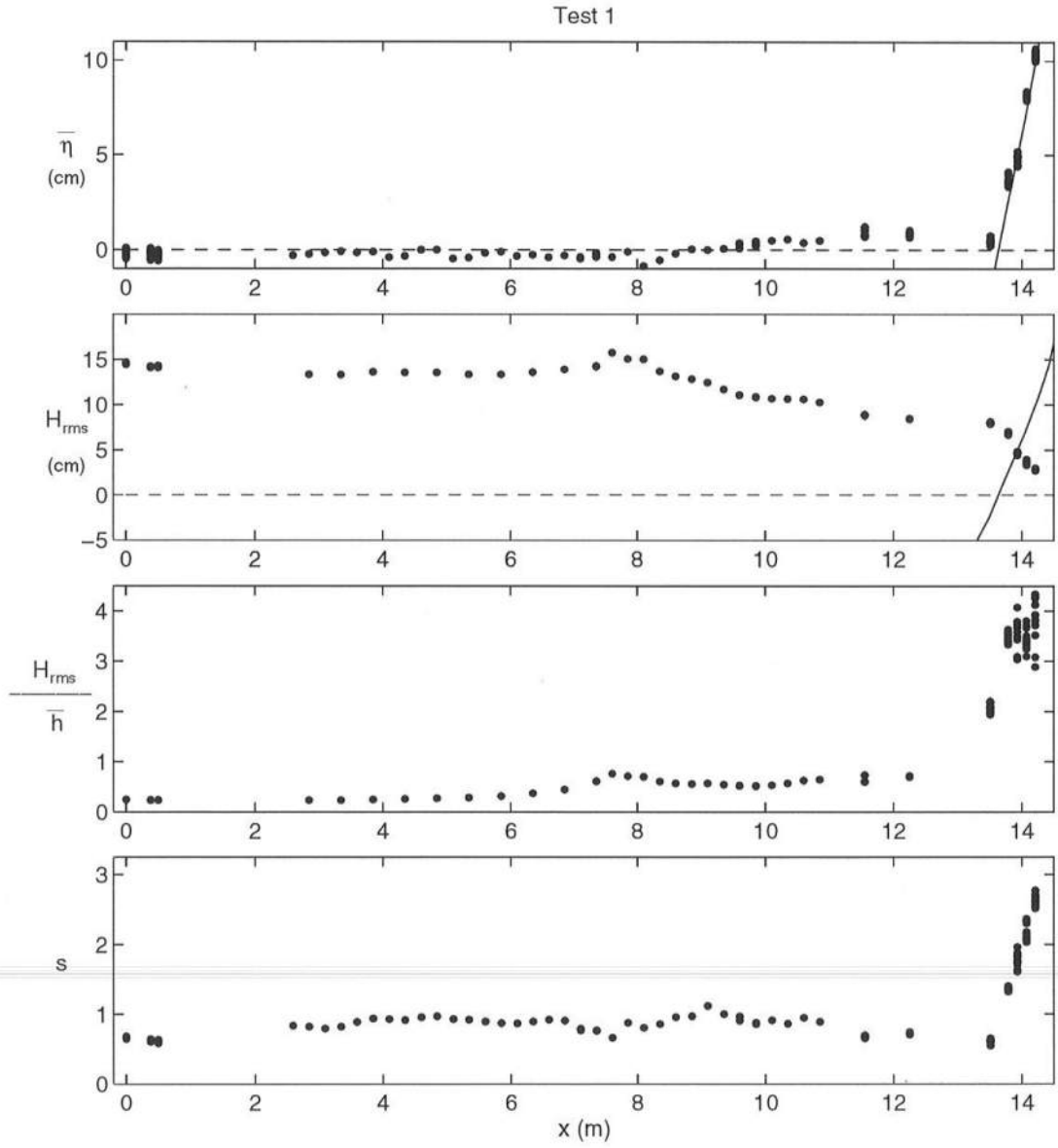
Figure 4.2: Measured Cross-Shore Variations of $\overline{\eta}$, H_{rms}, $H_{\mathrm{rms}}/\overline{h}$, and s for Test 1

44
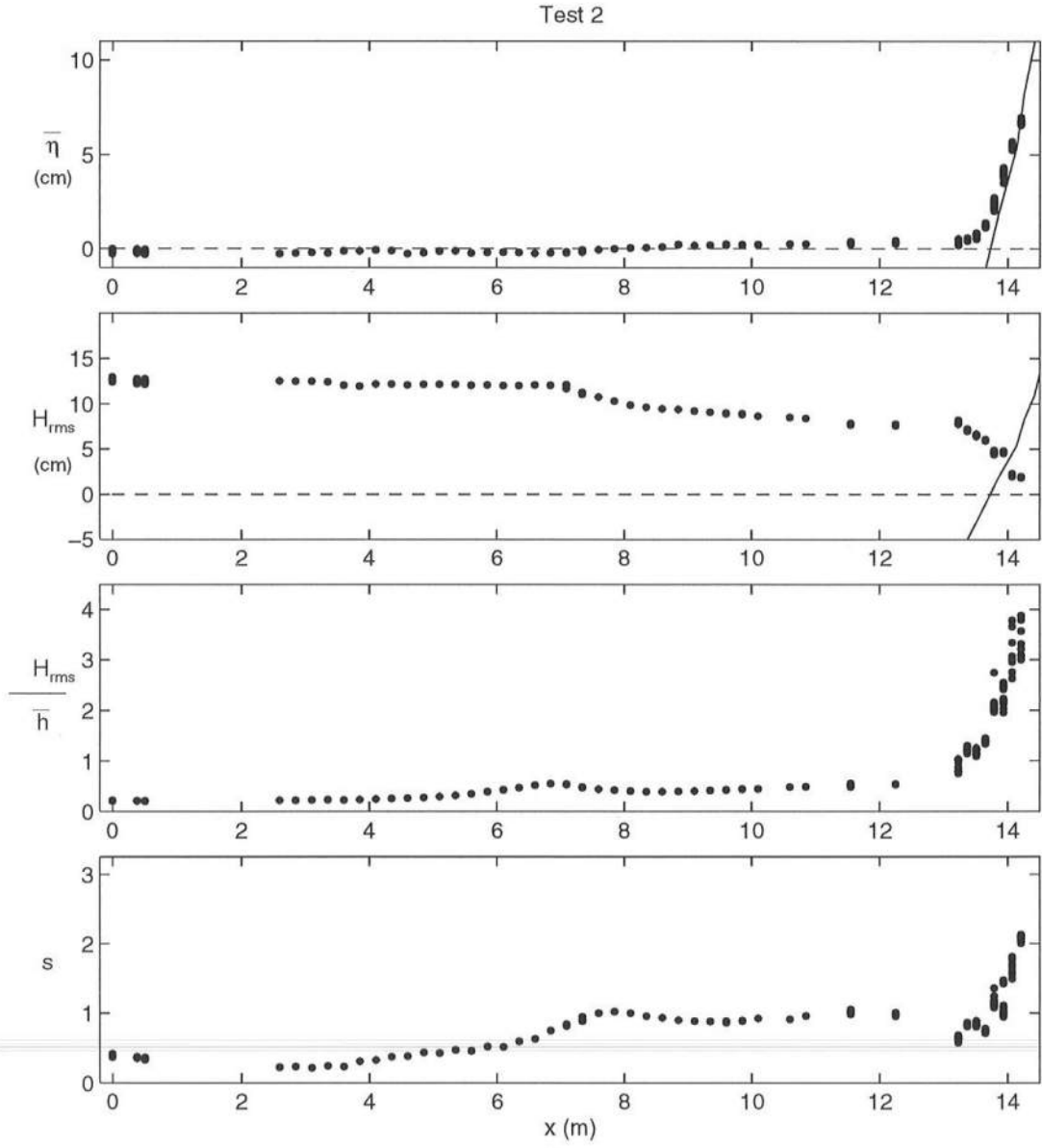
Figure 4.3: Measured Cross-Shore Variations of $\overline{\eta}$, H_{rms}, $H_{\mathrm{rms}}/\overline{h}$, and s for Test 2

45

affected by infrequent wave uprush and downrush. Because of these uncertainties, the present data analysis is limited to the region of mean water depth $\overline{h} \gtrsim 1.0$ cm. In the region of shallower depth, $\overline{h} \lesssim 1.0$ cm, it may be necessary to account for the probability of occurrence of dry periods of zero depth, but it will be extremely difficult to measure very small depths above a movable bottom.

The measured values of H_{rms} are approximately constant in the region seaward of the bar/terrace. They reach a slight peak after passing onto the terrace, then decrease steadily in the surf zone and more rapidly in the swash zone. The sand surface is again represented by a solid line on these plots, to illustrate the abrupt decline in H_{rms} that begins near the still water shoreline. There was relatively intense breaking at the edge of the terrace in test 1, though it is not very apparent from the relatively constant values of H_{rms} seaward of the surf zone. The slightly smaller and shorter waves of test 2 actually show a decline of H_{rms} as they approach the breaker zone. The incident wave conditions have been listed in Table 3.5.

The measured values of $H_{\text{rms}}/\overline{h}$ in Figures 4.2 and 4.3 reflect the beach profile fairly strongly in deeper water, then begin to rise rapidly as they approach the still water shoreline. The landward increase of $H_{\text{rms}}/\overline{h}$ is mostly caused by the landward decrease of $\overline{h}$. The decrease of H_{rms} after the bar is rapid enough to produce a slight decrease in $H_{\text{rms}}/\overline{h}$ in the breaker region for both tests. The measured values of $H_{\text{rms}}/\overline{h}$ in the inner surf zone are more constant than the 1:16 slope data of Herrman et $al.$ (1997) and more similar to the field data on gently sloping concave beaches obtained by Thornton and Guza (1982, 1983). The measured values of $H_{\text{rms}}/\overline{h}$ approach a value close to the intuitive upper limit of $H_{\text{rms}}/\overline{h} = \sqrt{8}$ in the swash zone, as predicted by equation (2.7) with (2.8). The exact upper limit is again difficult to pinpoint because of the rapid increase and scatter of $H_{\text{rms}}/\overline{h}$ as $\overline{h}$ approaches zero, although the scatter shown in these two tests is less than that seen by Herrman et $al.$ (1997). These results imply that the landward decrease of H_{rms}

is more gradual than that of $\overline{h}$ in the swash zone.

Figure 4.3 shows that the skewness, s, increased landward and then decreased toward the still water shoreline, in accordance with available data [*e.g.*, Mase and Kobayashi (1991); Raubenheimer *et al.* (1995)]. However, skewness results in test 1 appear to have been significantly influenced by the intense breaking, which may have produced the dip in s recorded near the edge of the terrace. In comparison with the 1:16 slope data of Herrman *et al.* (1997), the cross-shore variation of s over the barred and terraced beaches is less pronounced, indicating the effect of the beach profile on the irregular wave transformation. In both tests the skewness decreases somewhat as waves approach the swash zone, then increases again in the swash and approaches an upper limit slightly above the value $s = 2$ predicted by the exponential distribution given in equation (2.6). The upper limit of $s = 2$ seems to be accurate to within about 20%, however. This trend in s confirms that the probability distribution of the free surface elevation is strongly affected by the bottom elevation, as was the case with the 1:16 slope data of Herrman *et al.* (1997). The free surface statistical data shown in Figures 4.2 and 4.3 are listed in Tables 4.1 and 4.2 in Section 4.6.

4.3 Measured and Theoretical Probability Density Functions

For each of the measurement locations, the measured probability density function of η_* was compared with the exponential gamma distribution given by equation (2.1) together with the measured skewness, s. Figures 4.4 and 4.5 show the degree of overall agreement for tests 1 and 2, respectively. The comparisons are separated into four zones for each test on the basis of the wave transformation processes indicated in Figures 3.18 and 3.19 as well as the cross-shore variations of s shown in Figures 4.2 and 4.3. The four zones correspond roughly to the "shoaling zone" with little wave breaking, the "surf zone" with intense wave breaking, the "transition zone" between surf and swash, and the "swash zone" above the still

47
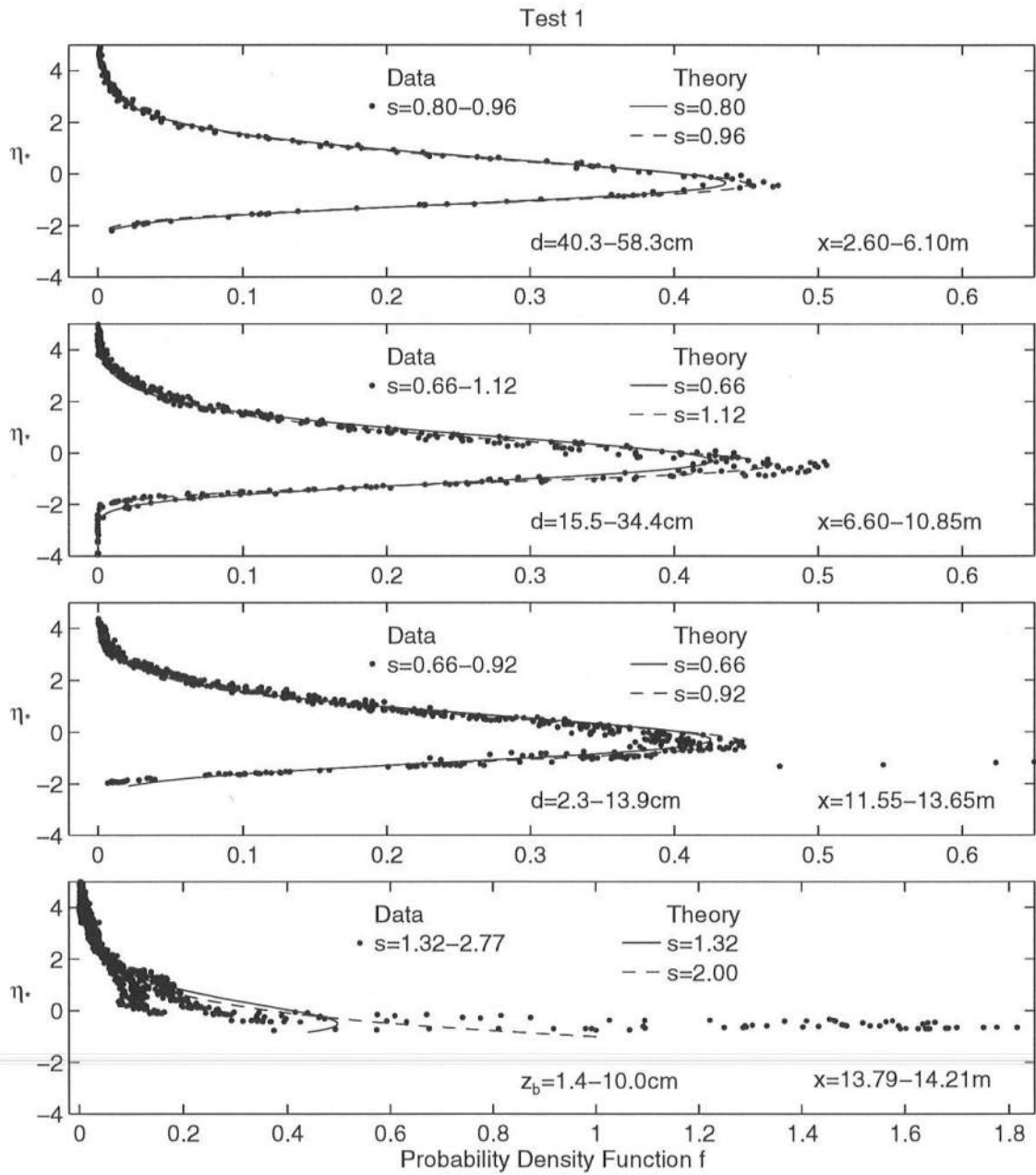
Figure 4.4: Measured and Computed Probability Distributions in Four Zones for Test 1
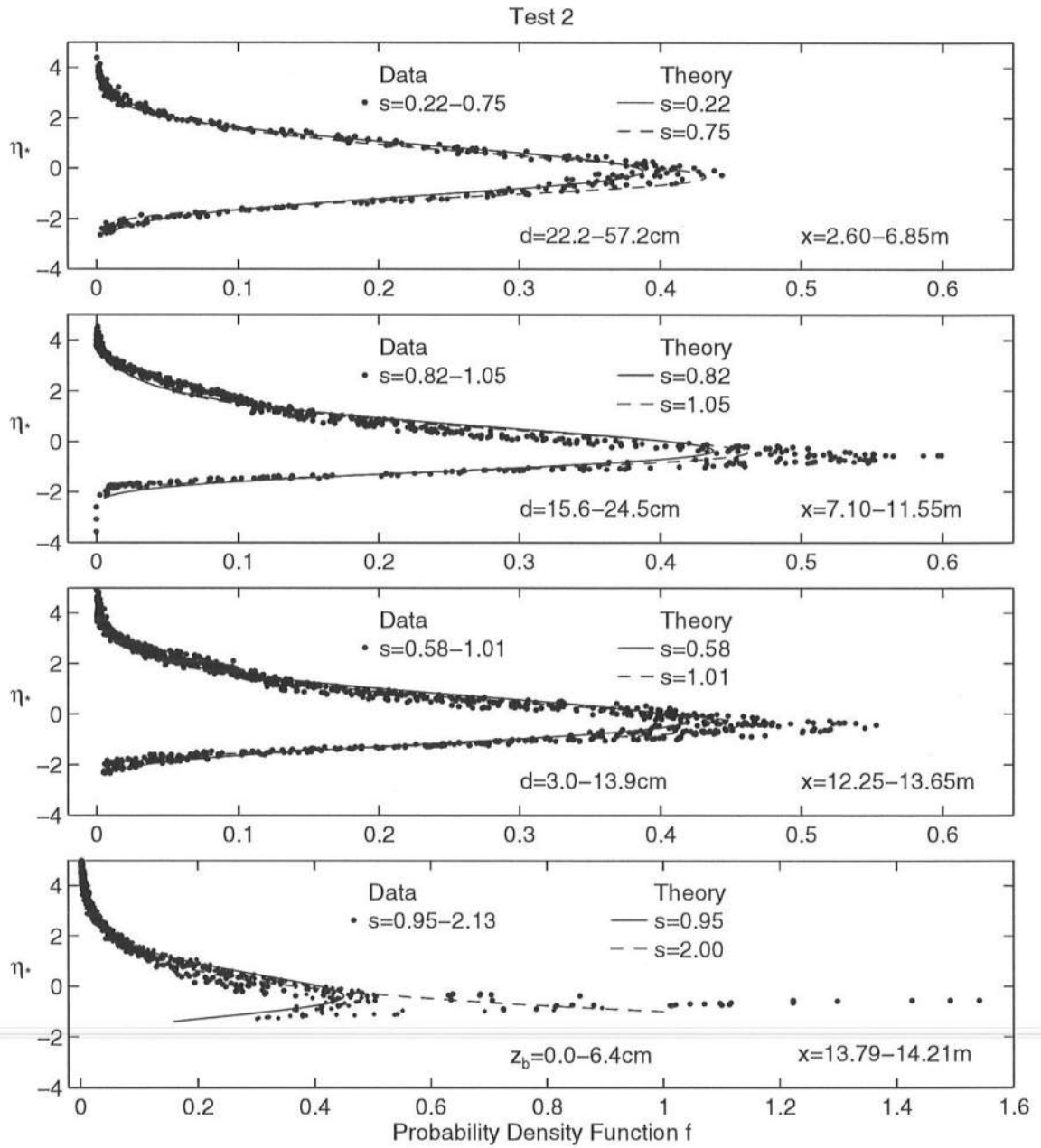
Figure 4.5: Measured and Computed Probability Distributions in Four Zones for Test 2

water line. The agreement was good in the shoaling zone, and fair in the surf, transition, and swash zones.

The measured minimum and maximum values of s in each zone are indicated in these figures. The exponential gamma distributions based on these minima and maxima are plotted for each zone so that the data points would fall between the two theoretical curves if the agreement were perfect. In the shoaling and surf zones, experimental and theoretical curves maintain a roughly Gaussian shape, except that the distribution here is slightly skewed and more peaked. For the Gaussian distribution $f(\eta_*) = 0.004$ at $\eta_* = \pm 3$ and $f(\eta_*) = 0.4$ at $\eta_* = 0$ using equation (2.5). An anomalous data spike appears in the transition zone of Figure 4.4; this is likely due to uncertainties involved in the measurement of the small water depth and sand bottom, which will be discussed in more detail in the following section. In the swash zone, the exponential gamma distribution becomes exponential with $s = 2$ given by equation (2.6). The agreement is better for the large values of η_*, which correspond to the large free surface elevations. This is partially because the theoretical distributions for the large values of η_* are not very sensitive to the skewness, s.

Separate figures for each wave gauge position are plotted in Figures 4.13 – 4.34 in Section 4.7 to show that Figures 4.4 and 4.5 indeed represent the overall agreement for tests 1 and 2, respectively. The overall agreement is very similar to the 1:16 slope data of Herrman et $al.$ (1997).

Finally, the measured values of the kurtosis, K, are compared with the theoretical values of K based on equation (2.4). As discussed in Section 2.1, equation (2.4) together with equation (2.3) may be used to derive a theoretical relationship between K and s. This relationship has been illustrated in Figure 2.1 and is now redrawn as the solid line in Figure 4.6. This figure shows all measured values of
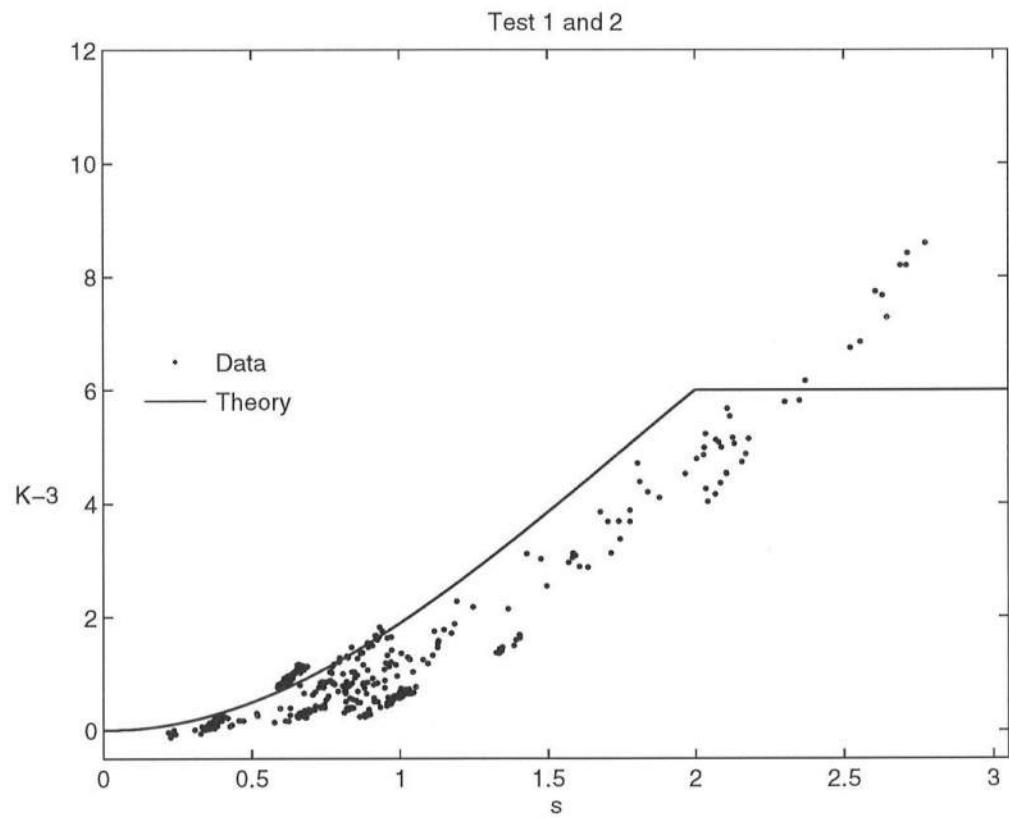
Figure 4.6: Measured and Computed Kurtosis, K, as a Function of Skewness, s

$(K-3)$ as a function of s in comparison to the theoretical curve, where it is assumed here that $(K-3)=6$ for $s>2$. As was also found by Herrman *et al.* (1997), the relation between K and s based on the exponential gamma distribution tends to overpredict K somewhat for $s<2$ and can not explain the increase of K for $s>2$. This suggests that there may be a need for an empirical fit to data to describe this relationship for practical applications.

4.4 Measurements and Uncertainties of Swash Zone Bottom Location

To determine the elevation of the sand surface at each swash gauge as accurately as possible, the bottom elevation at each gauge was measured with a vernier scaled pointer gauge for all runs of each test. Bottom elevations at three longshore positions corresponding to the profile transect locations discussed in Section 3.4 were recorded for gauges 7–10 following each run. These were then averaged to obtain a single value for each run at each gauge, which was used in calculations of the mean water depth, $\overline{h}$, and other statistical parameters. This averaging is consistent with the average equilibrium profile discussed in Section 3.4.

Although there was significant motion of the sand particles *during* each 400 s wave run, the surface measured *before* and *after* runs varied little. The variations in the bottom depth or elevation at gauges 7–10 over tests 1 and 2, tabulated earlier in Tables 3.3 and 3.4, are now shown in Figure 4.7. Average bottom elevation at the four gauges varied by less than 1 cm over the entire course of test 1, excluding the repositioning of these gauges between runs 12 and 13. This variation was greater at gauge 7 during test 2, which initially was located slightly below the swash zone and on the edge of a region of ripples. Except for this irregularity, the average bottom elevation measured at each swash gauge over test 2 also varied by less than 1 cm, excluding the repositioning of the gauges between runs 10 and 11. The longshore deviations from these averages were less than 0.6 cm.
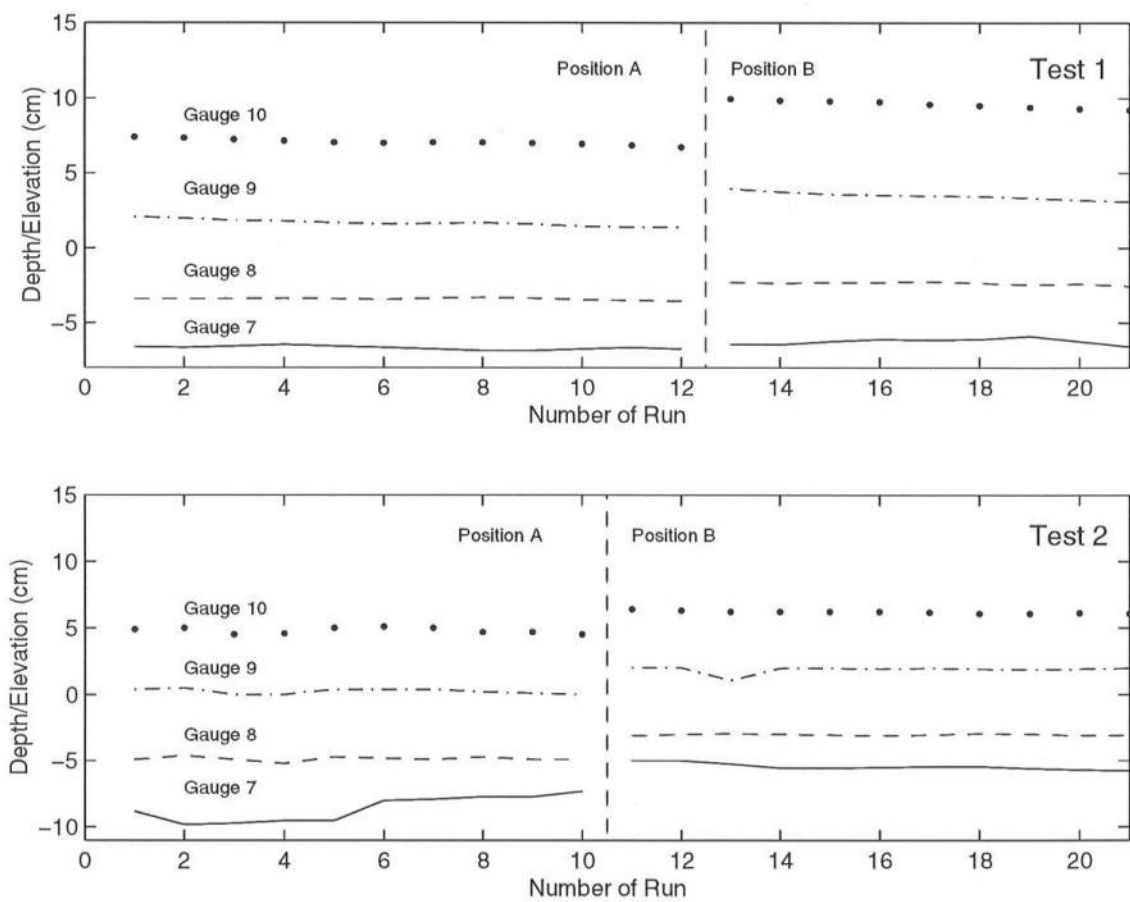
Figure 4.7: Measured Depth/Elevation of Sand Bottom at Gauges 7–10 During Tests 1 and 2
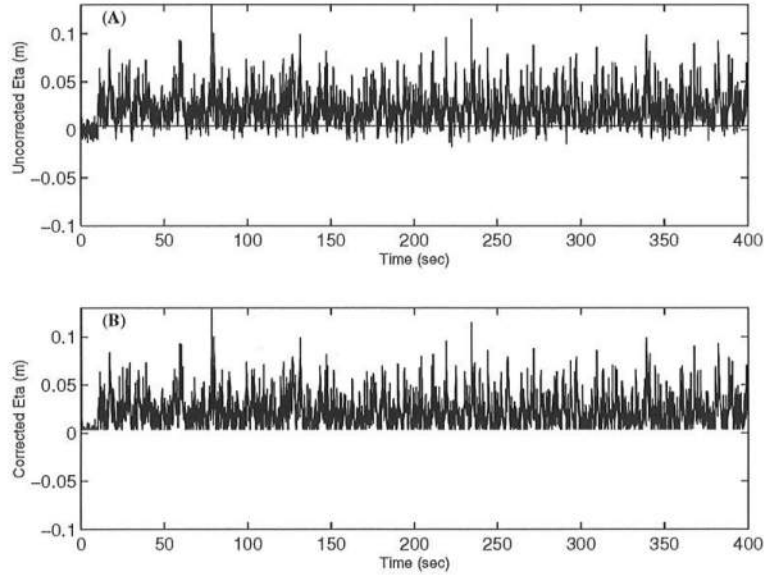
Figure 4.8: **(A)** Uncorrected Time Series of Free Surface at Swash Gauge 9 for Run 5 of Test 2; **(B)** Corrected Time Series

The bottom elevation, z_b, in the swash zone directly affects the instantaneous water depth $h = (\eta - z_b)$, where the free surface elevation η was measured by the swash gauges. In the swash zone, h can be very small and the small variation of z_b influences the value of h significantly. When the sand surface was exposed at a given swash gauge, the gauge reading would correspond to the bottom elevation, z_b, only if the sand were completely saturated. Otherwise the reading would drop below this value to reflect the lower water level beneath the sand surface. Because of uncertainty about how the gauge capacitance would be affected by partially saturated sand, it was decided not to attempt to measure the water level below the sand surface. In the time series of surface elevations in the swash zone, all gauge readings below the measured sand bottom value were set equal to that value. This "cutoff" procedure is shown for a typical swash gauge time series in Figure 4.8.

In Figure 4.8(A) the measured sand bottom, z_b, is indicated by the horizontal line drawn at 0.004 m. The gauge readings in this 400 s time series fall below the

54

sand bottom many times, occasionally by distances approaching 2 cm. Analysis of time series such as this required that all values below this line be reassigned the measured value of z_b, as shown in Figure 4.8(B). The adjusted time series of this form were then analyzed to obtain the swash zone statistical values presented in this chapter.

Several factors may have contributed to the difference between measured bottom position and minimum swash gauge readings illustrated in Figure 4.8. The suspension of large quantities of sediment during wave uprush and downrush in the swash zone lowers the apparent bottom elevation. The water was consistently very cloudy during the runs, and it was not possible to measure sand elevations under flowing water. Since the swash gauges were calibrated under quiescent water, it is not certain whether gauge readings exactly corresponded to the water elevation. Additionally, because of some longshore variation of the beach profile the three-point averaged z_b values did not always reflect the exact bottom elevation at the location of each gauge. However, this difference was generally less than 0.3 cm. In light of these uncertainties, the measurement of water depths, h, less than about 1 cm may not have been very accurate.

The probability distributions shown in Figure 4.4 included an anomalous group of data points in the third plot, corresponding to approximately $\eta_* = -1.5$. These values, which can also be seen clearly in Figure 4.22, imply that the very small water depth occurred more often than predicted by the exponential gamma distribution. Lowering the specified bottom elevation, z_b, would increase the water depth, h, and could eliminate the anomalous data points. This change is *not* made herein, in order to clearly indicate the uncertainties and difficulties in measuring the small water depth above the movable bed. Similar spikes also appear in the fourth plot of Figures 4.4 and 4.5, but these appear to be an extension of the exponential distribution for $s = 2$. The uncertainties in bottom elevation and the cutoff line

discussed above directly affect the position of these spikes in each figure. The value $\eta_* = -1$ for the exponential distribution corresponds to $\eta = z_b$, as explained in relation to equation (2.6). Consequently, the measured probability distributions in the vicinity of $\eta_* = -1$ for the swash zone may not be very accurate.

4.5 Wave Spectral Transformation in Cross-Shore Direction

A preliminary examination was conducted into the transformation of the total (incident + reflected) wave spectra recorded at different cross-shore locations. The object of this examination was to detect evidence of the existence of standing waves over the terrace region in test 1 or test 2. The first mode of such a standing wave, illustrated for test 1 in the bottom diagram of Figure 4.9, would have a node located over the edge of the terrace with antinodes located both offshore and near the still water shoreline. The wavelength of such a standing wave would be approximately $L \simeq 4l$, where $l \simeq 5.66$ m is the distance from the terrace edge to the still water shoreline in test 1. Thus for test 1, $L_1 \simeq 22.64$ m. For test 2, with $l \simeq 6.91$ m, we find $L_1 \simeq 27.64$ m.

Figures 4.9 and 4.10 show wave spectra measured in the vicinity of: (1) the offshore antinode position; (2) the node position; (3) a mid-terrace location; and (4) the shoreline antinode position for a first mode standing wave in test 1 and test 2, respectively. Were such a standing wave present, it would be identifiable as a peak in spectra for positions (1) and (4) and a trough in the spectrum at position (2), all occurring at the same low frequency. Such consistent low frequency peaks and troughs are not apparent in either of these two figures.

Mode frequencies are estimated by the simple relationship

$$f_i = \frac{C}{L_i} = \frac{\sqrt{g\overline{h}_t}}{4l/(2i-1)} \qquad \text{for} \ \ i = 1, 2, \ldots \qquad (4.1)$$

where $\overline{h}_t =$ mean depth on the terrace $\simeq 23$ cm, and linear long wave theory is applied since $L_i > 25\overline{h}_t \simeq 6$ m when $i = 1$ or 2. From equation (4.1), we find that

56
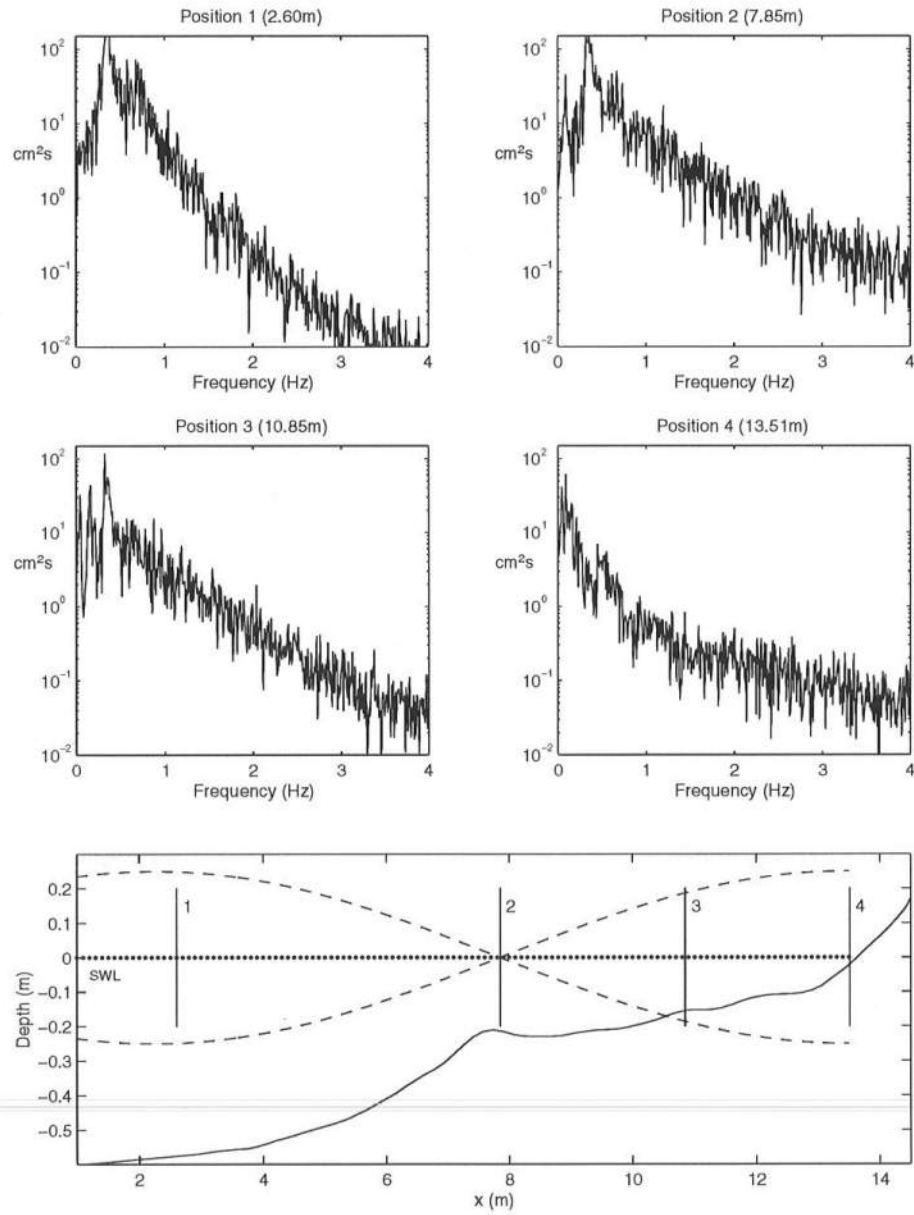
Figure 4.9: Unsmoothed Wave Spectra at Four Cross-Shore Locations Near Nodes and Antinodes of First Mode Standing Wave, Test 1
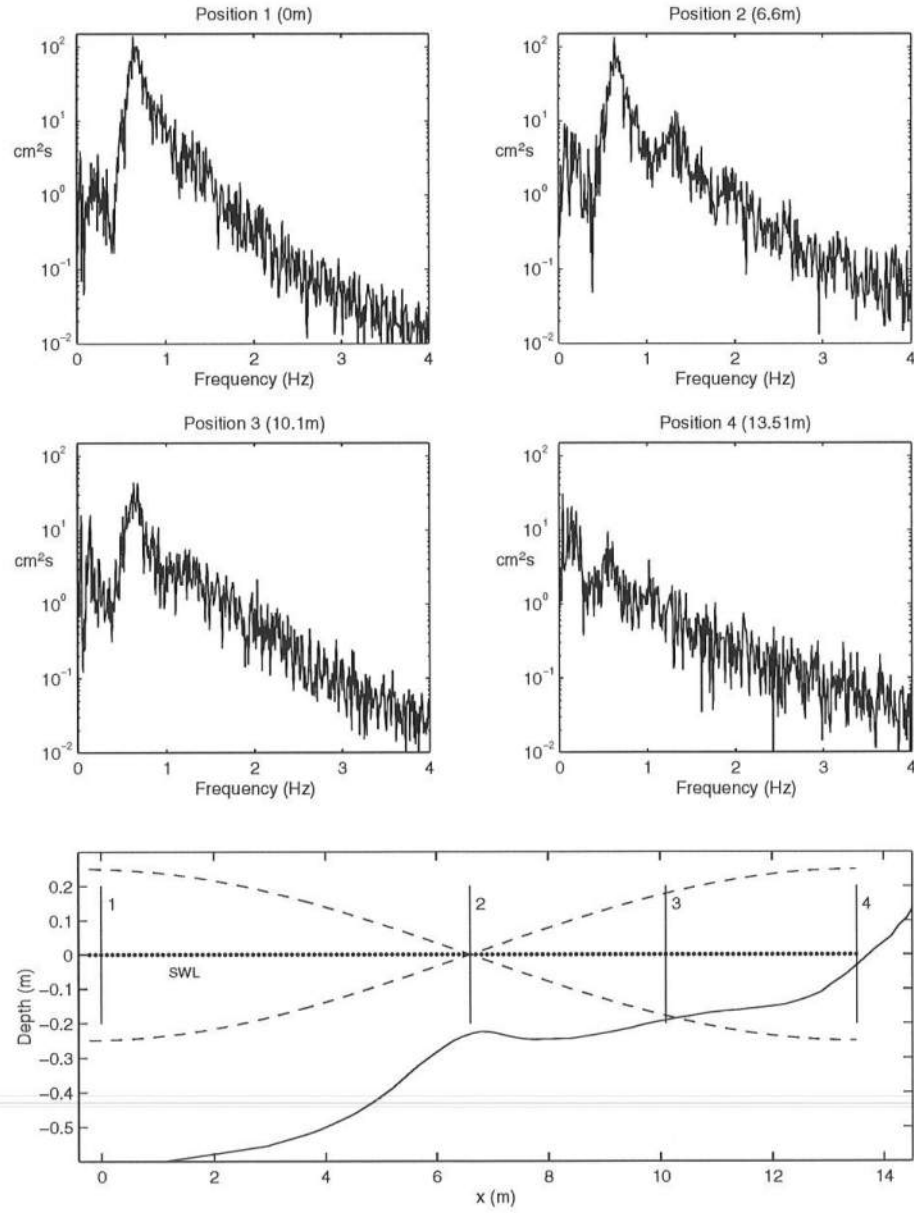
Figure 4.10: Unsmoothed Wave Spectra at Four Cross-Shore Locations Near Nodes and Antinodes of First Mode Standing Wave, Test 2

for test 1, $f_1 = 0.07$ Hz and $f_2 = 0.20$ Hz, while for test 2, $f_1 = 0.05$ Hz and $f_2 = 0.16$ Hz.

In the top half of Figures 4.11 and 4.12 the wave spectra at position (4) from tests 1 and 2 are expanded to examine more closely the locations of spectral peaks at the respective shorelines. Two vertical dashed lines have been added to each spectral plot in order to indicate the standing wave frequencies for the first (f_1) and second (f_2) modes. The envelopes of both modes are displayed with the corresponding equilibrium beach profile in the lower half of each figure. Although there is a localized peak around the second mode frequency in Figures 4.11 and 4.12, these standing waves are not dominant. The lack of clear evidence of standing waves of the first or second mode in either test indicates that the barred and terraced profiles in test 1 and 2 are not caused by standing waves.
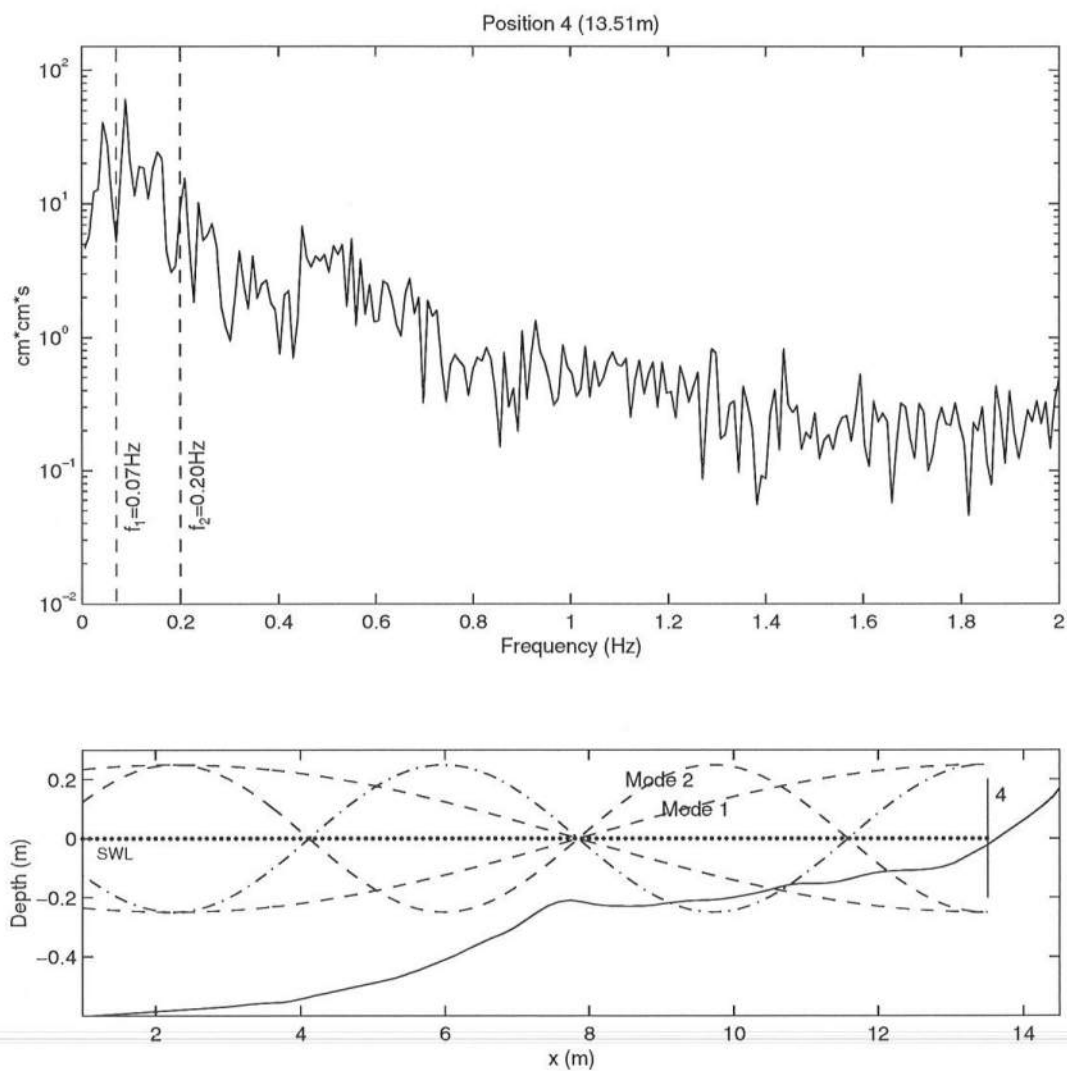
Figure 4.11: Expanded Wave Spectrum at Still Water Shoreline, Test 1 (Standing Wave First Mode Frequency $f_1 \simeq 0.07$ Hz, Second Mode Frequency $f_2 \simeq 0.20$ Hz)
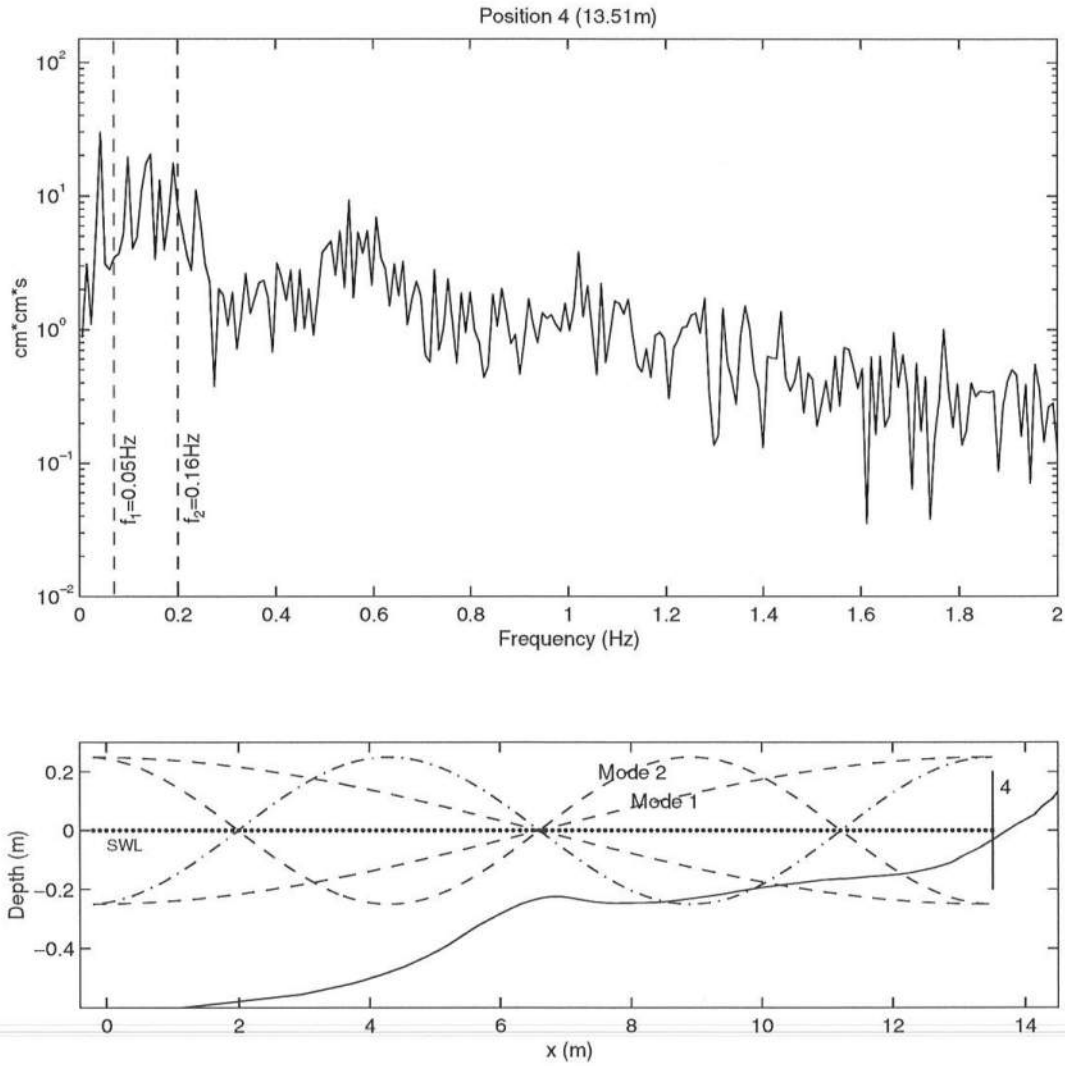
Figure 4.12: Expanded Wave Spectrum at Still Water Shoreline, Test 2 (Standing Wave First Mode Frequency $f_1 \simeq 0.05$ Hz, Second Mode Frequency $f_2 \simeq 0.16$ Hz)

61

4.6 Complete Free Surface Statistical Data For Tests 1 and 2

Complete free surface statistical data is given below for each gauge location for tests 1 and 2. Each gauge is indexed by its x position and the corresponding water depth, where $z_b = -d$. For gauges 1, 2, and 3 located at $x = 0$, 0.38, and 0.50 m, respectively, the measured values of $\bar{\eta}$, H_{rms}, s, and K for the 21 runs have been listed in Tables 3.8 – 3.11. The values listed in Tables 4.1 and 4.2 are the average values for these three gauges over the 21 runs.

Table 4.1: Test 1 Gauge Data

x (m)	z_b (cm)	$\bar{\eta}$ (cm)	$\bar{h}$ (cm)	H_{rms} (cm)	s	Kurtosis, K data	theory
0.00	-60.0	-0.12	59.88	14.59	0.67	3.90	3.87
0.38	-60.0	-0.17	59.83	14.20	0.63	3.73	3.78
0.50	-60.0	-0.24	59.76	14.24	0.61	3.64	3.74
2.60	-58.3	-0.31	57.99	——	0.84	4.31	4.35
2.85	-58.1	-0.23	57.87	13.36	0.82	4.14	4.32
3.10	-57.1	-0.16	56.94	——	0.80	4.09	4.23
3.35	-56.4	-0.09	56.31	13.33	0.82	4.14	4.30
3.60	-56.0	-0.16	55.84	——	0.89	4.42	4.53
3.85	-55.5	-0.11	55.39	13.65	0.94	4.65	4.69
4.10	-54.1	-0.40	53.70	——	0.93	4.68	4.66
4.35	-52.8	-0.32	52.48	13.55	0.92	4.52	4.61
4.60	-51.4	0.00	51.40	——	0.96	4.49	4.75
4.85	-50.1	0.00	50.10	13.56	0.97	4.52	4.79
5.10	-48.7	-0.48	48.22	——	0.93	4.47	4.65
5.35	-47.2	-0.42	46.78	13.37	0.92	4.47	4.62
5.60	-45.1	-0.18	44.92	——	0.90	4.28	4.55
5.85	-42.6	-0.12	42.48	13.36	0.87	4.18	4.47
6.10	-40.3	-0.33	39.97	——	0.87	4.22	4.45
6.35	-37.5	-0.26	37.24	13.62	0.89	4.34	4.53
6.60	-34.4	-0.40	34.00	——	0.92	4.39	4.63
6.85	-31.7	-0.30	31.40	13.94	0.91	4.31	4.58

x (m)	z_b (cm)	$\overline{\eta}$ (cm)	$\overline{h}$ (cm)	H_{rms} (cm)	s	Kurtosis, K	
						data	theory
7.10	-27.7	-0.38	27.32	——	0.77	3.97	4.16
7.10	-27.7	-0.42	27.28	——	0.78	4.02	4.18
7.10	-27.7	-0.46	27.24	——	0.79	4.04	4.23
7.35	-23.6	-0.26	23.34	14.23	0.76	3.88	4.14
7.35	-23.6	-0.19	23.41	14.30	0.77	3.86	4.15
7.35	-23.6	-0.38	23.22	14.27	0.77	3.87	4.15
7.60	-21.1	-0.38	20.76	15.79	0.66	3.70	3.86
7.85	-21.3	-0.11	21.23	15.06	0.88	4.04	4.48
8.10	-22.5	-0.87	21.62	15.05	0.81	3.83	4.27
8.35	-23.1	-0.56	22.50	13.71	0.86	3.98	4.42
8.60	-23.3	-0.21	23.07	13.15	0.96	4.03	4.75
8.85	-23.1	0.03	23.10	12.86	0.97	4.10	4.80
9.10	-22.2	-0.02	22.13	12.49	1.12	4.59	5.31
9.35	-21.4	0.06	21.45	11.73	1.00	4.12	4.91
9.60	-21.1	0.29	21.39	11.07	0.91	3.70	4.58
9.60	-21.1	0.35	21.45	11.12	0.96	3.95	4.77
9.60	-21.1	0.08	21.18	11.09	0.97	4.02	4.79
9.85	-20.7	0.46	21.16	10.87	0.87	3.67	4.47
9.85	-20.7	0.42	21.12	10.82	0.86	3.50	4.42
9.85	-20.7	0.23	20.93	10.90	0.88	3.59	4.49
10.10	-19.7	0.49	20.21	10.71	0.91	3.62	4.59
10.35	-18.3	0.55	18.87	10.65	0.86	3.35	4.44
10.60	-16.6	0.37	16.96	10.60	0.95	3.74	4.72
10.85	-15.5	0.48	15.98	10.30	0.89	3.64	4.53
11.55	-13.9	0.98	14.88	8.86	0.69	3.19	3.95
11.55	-13.9	1.07	14.97	8.82	0.66	3.09	3.85
11.55	-13.9	0.76	14.66	8.80	0.67	3.11	3.90
11.55	-13.9	0.68	14.58	8.86	0.68	3.19	3.91
11.55	-13.9	1.15	15.05	8.87	0.68	3.11	3.91
11.55	-13.9	1.23	15.13	8.92	0.69	3.18	3.95
11.55	-13.9	0.80	14.70	8.91	0.70	3.21	3.96
11.55	-13.9	0.79	14.69	8.83	0.66	3.09	3.85
11.55	-13.9	0.70	14.60	8.81	0.67	3.15	3.88

Table 4.1, continued

x (m)	z_b (cm)	$\overline{\eta}$ (cm)	$\overline{h}$ (cm)	H_{rms} (cm)	s	Kurtosis, K data	Kurtosis, K theory
11.55	-13.9	0.81	14.71	8.81	0.69	3.27	3.94
11.55	-13.9	0.81	14.71	8.81	0.66	3.14	3.86
11.55	-13.9	1.07	14.97	8.89	0.67	3.16	3.89
12.25	-11.2	1.02	12.22	8.49	0.71	3.36	4.00
12.25	-11.2	0.65	11.85	8.50	0.74	3.37	4.08
12.25	-11.2	0.94	12.14	8.50	0.73	3.36	4.05
12.25	-11.2	0.68	11.88	8.51	0.75	3.36	4.09
12.25	-11.2	0.84	12.04	8.49	0.73	3.34	4.05
12.25	-11.2	0.90	12.10	8.45	0.74	3.41	4.08
12.25	-11.2	0.80	12.00	8.44	0.70	3.30	3.98
12.25	-11.2	0.84	12.04	8.42	0.71	3.31	3.99
12.25	-11.2	0.83	12.03	8.40	0.71	3.31	4.00
13.65	-2.3	1.27	3.57	6.91	0.68	3.32	3.90
13.65	-2.4	0.67	3.07	6.71	0.83	3.51	4.33
13.65	-2.3	1.10	3.40	6.87	0.70	3.31	3.98
13.65	-2.3	0.56	2.86	6.67	0.88	3.55	4.48
13.65	-2.3	0.54	2.84	6.73	0.92	3.55	4.64
13.65	-2.4	0.56	2.96	6.73	0.82	3.37	4.29
13.65	-2.5	0.73	3.23	6.85	0.79	3.41	4.22
13.65	-2.4	0.74	3.14	6.80	0.76	3.28	4.12
13.65	-2.6	0.43	3.03	6.79	0.81	3.39	4.28
13.79	2.1	4.11	2.01	6.71	1.40	4.54	6.45
13.79	2.0	3.97	1.97	6.67	1.40	4.52	6.45
13.79	1.9	3.74	1.84	6.78	1.38	4.32	6.37
13.79	1.8	3.71	1.91	6.75	1.39	4.45	6.40
13.79	1.7	3.76	2.06	6.94	1.34	4.33	6.20
13.79	1.6	3.44	1.84	6.69	1.40	4.50	6.45
13.79	1.7	3.69	1.99	6.96	1.35	4.34	6.21
13.79	1.7	3.74	2.04	6.95	1.34	4.32	6.20
13.79	1.6	3.63	2.03	6.94	1.32	4.25	6.13
13.79	1.5	3.49	1.99	7.03	1.34	4.25	6.17
13.79	1.4	3.40	2.00	7.03	1.34	4.23	6.18
13.79	1.4	3.33	1.93	6.89	1.34	4.26	6.21

Table 4.1, continued

| x | z_b | $\overline{\eta}$ | $\overline{h}$ | H_{rms} | s | Kurtosis, K | |
(m)	(cm)	(cm)	(cm)	(cm)		data	theory
13.93	4.0	5.21	1.21	4.64	1.88	6.97	8.48
13.93	3.8	4.84	1.04	4.45	1.97	7.39	8.85
13.93	3.6	4.99	1.39	4.75	1.78	6.73	8.05
13.93	3.6	4.88	1.28	4.76	1.84	7.08	8.31
13.93	3.5	5.08	1.58	4.80	1.74	6.66	7.88
13.93	3.5	4.67	1.17	4.56	1.74	6.24	7.90
13.93	3.4	4.91	1.51	4.83	1.61	5.86	7.31
13.93	3.2	4.41	1.21	4.60	1.71	5.99	7.77
13.93	3.1	4.46	1.36	4.75	1.63	5.83	7.43
14.07	7.4	8.31	0.91	3.37	2.37	8.88	9.00
14.07	7.4	8.37	0.97	3.35	2.35	8.65	9.00
14.07	7.3	8.22	0.92	3.55	2.30	8.56	9.00
14.07	7.2	8.20	1.00	3.69	2.18	7.90	9.00
14.07	7.1	8.11	1.01	3.64	2.16	7.49	9.00
14.07	7.0	8.12	1.12	3.68	2.17	7.68	9.00
14.07	7.1	8.03	0.93	3.75	2.10	7.16	9.00
14.07	7.1	8.18	1.08	3.79	2.04	6.78	9.00
14.07	7.0	8.23	1.23	3.80	2.08	7.18	9.00
14.07	7.0	8.06	1.06	3.76	2.07	6.96	9.00
14.07	6.9	8.04	1.14	3.87	2.10	7.40	9.00
14.07	6.8	7.89	1.09	3.97	2.04	6.99	9.00
14.21	10.0	10.64	0.64	2.72	2.61	10.34	9.00
14.21	9.9	10.49	0.59	2.74	2.71	10.86	9.00
14.21	9.8	10.48	0.68	2.81	2.71	10.97	9.00
14.21	9.8	10.50	0.70	2.79	2.69	10.94	9.00
14.21	9.6	10.40	0.80	2.83	2.63	10.45	9.00
14.21	9.5	10.13	0.63	2.74	2.77	11.30	9.00
14.21	9.4	10.35	0.95	2.92	2.56	9.92	9.00
14.21	9.3	10.30	1.00	2.90	2.64	10.58	9.00
14.21	9.2	9.98	0.78	2.99	2.52	9.60	9.00

Table 4.2: Test 2 Gauge Data

x	z_b	$\overline{\eta}$	$\overline{h}$	H_{rms}	s	Kurtosis, K	
(m)	(cm)	(cm)	(cm)	(cm)		data	theory
0.00	-60.0	-0.15	59.85	12.81	0.39	3.18	3.31
0.38	-60.0	-0.11	59.89	12.59	0.36	3.11	3.26
0.50	-60.0	-0.16	59.84	12.55	0.35	3.05	3.24
2.60	-57.2	-0.27	56.89	12.53	0.23	2.88	3.10
2.85	-56.9	-0.23	56.70	12.50	0.23	2.95	3.11
3.10	-55.0	-0.21	54.82	12.51	0.22	2.97	3.09
3.35	-54.0	-0.24	53.73	12.40	0.24	2.93	3.12
3.60	-52.8	-0.13	52.71	12.06	0.24	3.00	3.11
3.85	-51.5	-0.12	51.34	11.96	0.31	3.01	3.19
4.10	-49.8	-0.06	49.75	12.17	0.33	2.94	3.21
4.35	-48.0	-0.11	47.94	12.19	0.37	3.04	3.28
4.60	-46.1	-0.26	45.88	12.08	0.38	3.08	3.29
4.85	-44.0	-0.22	43.81	12.13	0.43	3.09	3.37
5.10	-41.4	-0.14	41.23	12.14	0.43	3.07	3.36
5.35	-38.3	-0.13	38.15	12.14	0.47	3.16	3.44
5.60	-34.7	-0.25	34.50	12.03	0.46	3.18	3.42
5.85	-31.3	-0.20	31.08	12.07	0.52	3.26	3.54
6.10	-28.2	-0.18	27.98	12.02	0.52	3.30	3.53
6.35	-25.6	-0.20	25.38	12.02	0.60	3.39	3.70
6.60	-23.6	-0.25	23.32	12.08	0.63	3.39	3.78
6.85	-22.2	-0.23	21.94	12.05	0.75	3.55	4.10
7.10	-22.3	-0.21	22.09	11.69	0.83	3.58	4.34
7.10	-22.3	-0.17	22.13	12.11	0.84	3.55	4.37
7.10	-22.3	-0.23	22.07	12.05	0.82	3.51	4.29
7.35	-23.6	-0.09	23.51	11.06	0.95	3.75	4.72
7.35	-23.6	-0.07	23.53	11.23	0.91	3.58	4.60
7.35	-23.6	-0.18	23.42	11.24	0.89	3.65	4.51

Table 4.2, continued

| x | z_b | $\overline{\eta}$ | $\overline{h}$ | H_{rms} | s | Kurtosis, K | |
(m)	(cm)	(cm)	(cm)	(cm)		data	theory
7.60	-24.5	-0.05	24.43	10.75	1.00	3.74	4.91
7.85	-24.5	-0.01	24.50	10.32	1.02	3.72	4.97
8.10	-24.5	0.04	24.52	9.88	1.00	3.68	4.89
8.35	-24.5	0.06	24.57	9.65	0.96	3.44	4.74
8.60	-24.0	0.09	24.13	9.47	0.93	3.41	4.67
8.85	-23.4	0.21	23.59	9.38	0.90	3.28	4.56
9.10	-22.6	0.17	22.79	9.22	0.89	3.25	4.51
9.35	-21.8	0.19	22.02	9.09	0.88	3.24	4.50
9.60	-20.9	0.24	21.14	8.93	0.86	3.24	4.44
9.60	-20.9	0.23	21.13	8.97	0.88	3.28	4.49
9.60	-20.9	0.19	21.09	8.93	0.89	3.29	4.51
9.85	-19.9	0.18	20.08	8.82	0.90	3.37	4.54
9.85	-19.9	0.19	20.09	8.91	0.89	3.26	4.51
9.85	-19.9	0.21	20.11	8.85	0.90	3.30	4.54
10.10	-19.2	0.22	19.38	8.65	0.93	3.50	4.64
10.60	-17.5	0.26	17.74	8.52	0.91	3.51	4.60
10.85	-16.9	0.25	17.18	8.43	0.96	3.58	4.76
11.55	-15.6	0.38	15.98	7.86	1.03	3.66	5.00
11.55	-15.6	0.34	15.94	7.88	1.03	3.65	5.00
11.55	-15.6	0.31	15.91	7.78	1.03	3.73	5.00
11.55	-15.6	0.25	15.85	7.78	1.05	3.77	5.08
11.55	-15.6	0.38	15.98	7.68	1.01	3.66	4.93
11.55	-15.6	0.34	15.94	7.73	0.98	3.61	4.84
11.55	-15.6	0.26	15.86	7.76	1.01	3.67	4.92
11.55	-15.6	0.23	15.83	7.73	1.02	3.65	4.97
11.55	-15.6	0.24	15.84	7.80	1.04	3.65	5.04
11.55	-15.6	0.27	15.87	7.88	1.05	3.67	5.06

Table 4.2, continued

x (m)	z_b (cm)	$\overline{\eta}$ (cm)	$\overline{h}$ (cm)	H_{rms} (cm)	s	Kurtosis, K	
						data	theory
12.25	-13.9	0.39	14.29	7.66	0.98	3.54	4.82
12.25	-13.9	0.35	14.25	7.69	1.00	3.57	4.88
12.25	-13.9	0.41	14.31	7.61	0.98	3.60	4.81
12.25	-13.9	0.29	14.19	7.73	1.00	3.57	4.89
12.25	-13.9	0.43	14.33	7.67	0.97	3.53	4.79
12.25	-13.9	0.27	14.17	7.61	0.96	3.49	4.75
12.25	-13.9	0.27	14.17	7.68	0.97	3.46	4.79
12.25	-13.9	0.41	14.31	7.68	0.97	3.54	4.78
12.25	-13.9	0.33	14.23	7.70	0.97	3.55	4.78
12.25	-13.9	0.40	14.30	7.76	1.01	3.60	4.92
13.23	-8.8	0.32	9.12	7.90	0.65	3.26	3.84
13.23	-9.8	0.53	10.33	7.80	0.63	3.27	3.78
13.23	-7.7	0.48	8.18	7.83	0.68	3.22	3.92
13.23	-7.3	0.34	7.64	7.86	0.66	3.30	3.86
13.23	-9.7	0.36	10.06	7.85	0.67	3.30	3.88
13.23	-9.5	0.35	9.85	7.83	0.66	3.31	3.87
13.23	-9.5	0.38	9.88	7.77	0.68	3.31	3.91
13.23	-8.0	0.35	8.35	8.18	0.61	3.17	3.74
13.23	-7.9	0.18	8.08	8.20	0.62	3.16	3.77
13.23	-7.7	0.22	7.92	8.22	0.58	3.14	3.66
13.37	-5.0	0.49	5.49	6.96	0.86	3.49	4.42
13.37	-5.0	0.42	5.42	7.04	0.83	3.40	4.33
13.37	-5.3	0.57	5.87	7.01	0.85	3.53	4.40
13.37	-5.6	0.41	6.01	7.08	0.83	3.40	4.35
13.37	-5.6	0.56	6.16	7.12	0.83	3.39	4.35
13.37	-5.5	0.51	6.01	7.14	0.81	3.32	4.28
13.37	-5.5	0.47	5.97	7.15	0.84	3.40	4.37
13.37	-5.5	0.48	5.98	7.25	0.86	3.50	4.44
13.37	-5.6	0.46	6.06	7.19	0.82	3.39	4.31
13.37	-5.7	0.50	6.20	7.23	0.84	3.39	4.37
13.37	-5.8	0.49	6.29	7.17	0.83	3.37	4.32

x (m)	z_b (cm)	$\overline{\eta}$ (cm)	$\overline{h}$ (cm)	H_{rms} (cm)	s	Kurtosis, K	
						data	theory
13.51	-4.9	0.65	5.55	6.41	0.84	4.03	4.36
13.51	-4.6	0.79	5.39	6.51	0.81	3.78	4.27
13.51	-4.9	0.84	5.74	6.44	0.85	3.94	4.39
13.51	-5.2	0.72	5.92	6.48	0.85	4.03	4.38
13.51	-4.7	0.52	5.22	6.57	0.89	4.07	4.53
13.51	-4.8	0.58	5.38	6.66	0.82	3.81	4.30
13.51	-4.9	0.52	5.42	6.66	0.82	3.86	4.30
13.51	-4.7	0.74	5.44	6.50	0.86	3.98	4.41
13.51	-4.9	0.80	5.70	6.56	0.82	3.74	4.30
13.51	-4.9	0.79	5.69	6.47	0.84	3.84	4.36
13.65	-3.1	1.20	4.30	5.96	0.76	3.86	4.11
13.65	-3.0	1.32	4.32	5.97	0.77	3.85	4.17
13.65	-3.0	1.31	4.31	5.95	0.78	3.81	4.18
13.65	-3.0	1.26	4.26	5.94	0.73	3.84	4.05
13.65	-3.1	1.22	4.32	6.01	0.73	3.76	4.03
13.65	-3.1	1.14	4.24	6.07	0.77	3.88	4.14
13.65	-3.1	1.20	4.30	5.99	0.74	3.76	4.08
13.65	-3.0	1.24	4.24	6.08	0.74	3.86	4.07
13.65	-3.0	1.31	4.31	5.99	0.75	3.85	4.10
13.65	-3.1	1.37	4.47	6.00	0.71	3.68	4.00
13.65	-3.1	1.31	4.41	5.99	0.77	3.83	4.17
13.79	0.4	2.73	2.33	4.57	1.13	4.58	5.36
13.79	0.5	2.64	2.14	4.62	1.13	4.54	5.36
13.79	0.0	2.31	2.31	4.59	1.08	4.25	5.17
13.79	0.0	2.18	2.18	4.54	1.25	5.18	5.82
13.79	0.4	2.64	2.24	4.63	1.15	4.78	5.44
13.79	0.4	2.64	2.24	4.69	1.18	4.88	5.57
13.79	0.4	2.00	1.60	4.39	1.36	5.15	6.29
13.79	0.2	2.54	2.34	4.76	1.13	4.46	5.35
13.79	0.1	2.36	2.26	4.72	1.19	5.28	5.60
13.79	0.0	2.42	2.42	4.89	1.17	4.71	5.53

x (m)	z_b (cm)	$\overline{\eta}$ (cm)	$\overline{h}$ (cm)	H_{rms} (cm)	s	Kurtosis, K	
						data	theory
13.93	2.0	4.34	2.34	4.74	0.95	4.08	4.71
13.93	2.0	4.26	2.26	4.79	1.03	4.29	4.99
13.93	1.1	3.51	2.41	4.82	0.95	4.19	4.73
13.93	2.0	4.09	2.09	4.67	0.99	4.16	4.84
13.93	2.0	3.74	1.74	4.55	1.09	4.18	5.23
13.93	1.9	3.76	1.86	4.61	1.04	4.04	5.05
13.93	2.0	4.13	2.13	4.81	1.03	4.25	5.01
13.93	1.9	3.83	1.93	4.69	1.11	4.33	5.29
13.93	1.9	3.95	2.05	4.68	0.99	3.96	4.86
13.93	1.9	3.78	1.88	4.54	1.48	6.03	6.75
13.93	2.0	4.02	2.02	4.55	1.43	6.12	6.56
14.07	4.9	5.42	0.52	1.97	1.78	6.68	8.04
14.07	5.0	5.68	0.68	2.02	1.59	6.09	7.25
14.07	4.5	5.25	0.75	2.08	1.80	7.71	8.16
14.07	4.6	5.40	0.80	2.10	1.58	6.05	7.21
14.07	5.0	5.69	0.69	2.07	1.57	5.96	7.15
14.07	5.1	5.64	0.54	1.98	1.81	7.38	8.19
14.07	5.0	5.61	0.61	2.03	1.70	6.68	7.72
14.07	4.7	5.40	0.70	2.15	1.68	6.85	7.61
14.07	4.7	5.44	0.74	2.18	1.50	5.55	6.83
14.07	4.5	5.37	0.87	2.27	1.58	6.13	7.21
14.21	6.4	6.96	0.56	1.80	2.09	7.99	9.00
14.21	6.3	6.78	0.48	1.83	2.13	8.16	9.00
14.21	6.2	6.75	0.55	1.83	2.08	8.08	9.00
14.21	6.2	6.67	0.47	1.81	2.13	8.05	9.00
14.21	6.2	6.82	0.62	1.85	2.03	7.98	9.00
14.21	6.2	6.83	0.63	1.94	2.07	8.12	9.00
14.21	6.2	6.78	0.58	1.94	2.00	7.79	9.00
14.21	6.1	6.68	0.58	1.88	2.03	8.22	9.00
14.21	6.1	6.62	0.52	1.85	2.12	8.53	9.00
14.21	6.1	6.74	0.64	1.92	2.03	7.86	9.00
14.21	6.1	6.57	0.47	1.85	2.11	8.67	9.00

4.7 Measured and Computed Probability Distributions at Each Gauge Position

On the following pages Figures 4.13 – 4.34 show individual plots of measured versus computed probability distributions of the free surface at each measurement position for tests 1 and 2, excluding the distributions at gauges 1–3, which were already shown in Figure 4.1. Note that repeated measurements at a single location for the gauges buried in the sand and for multiple measurements at velocity profile locations are plotted together.

Figure 4.13: Measured and Computed Probability Distributions at Positions $x = 2.60,\ 2.85,\ 3.10,$ and 3.35 m for Test 1
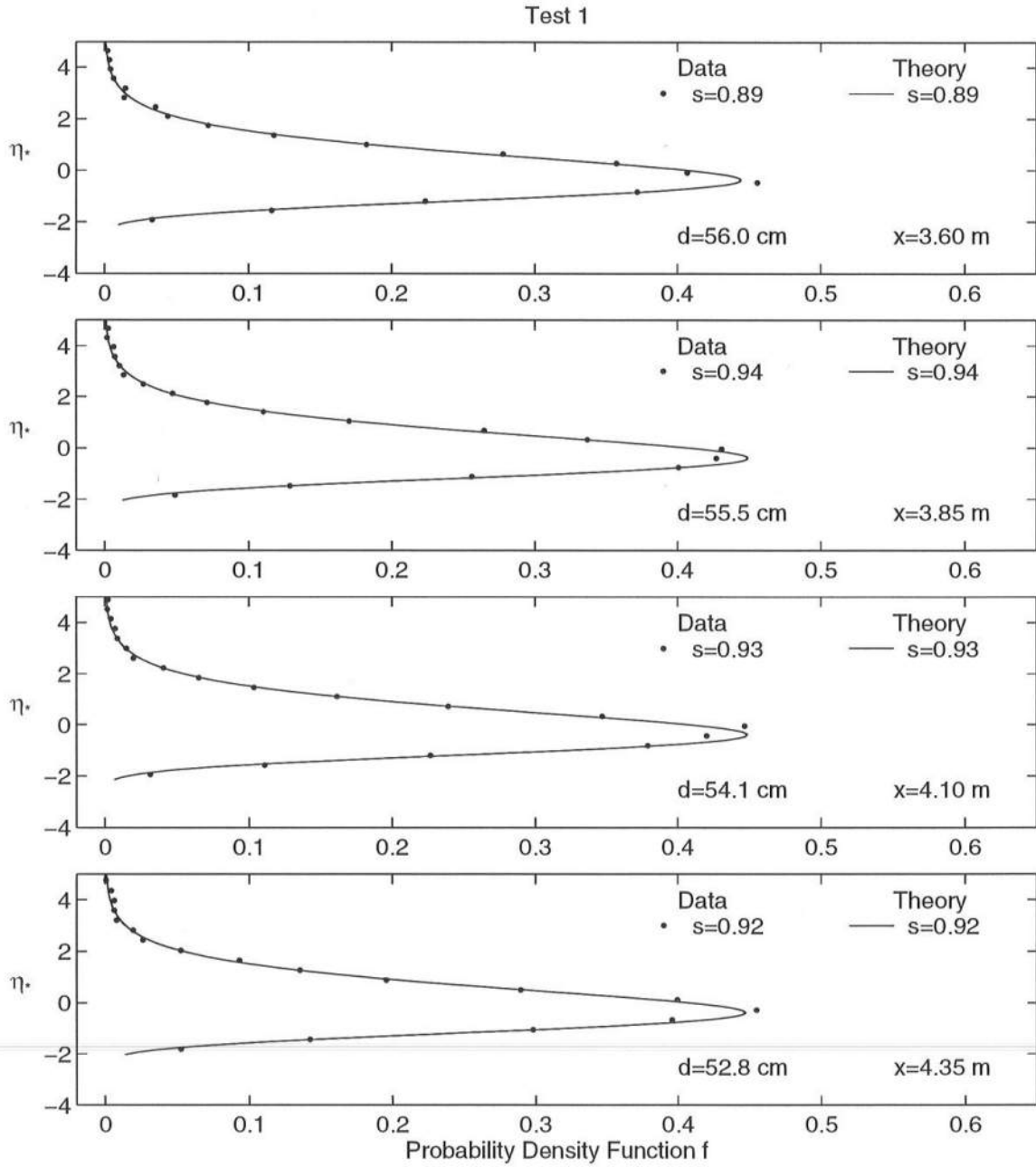
Figure 4.14: Measured and Computed Probability Distributions at Positions $x = 3.60, 3.85, 4.10,$ and 4.35 m for Test 1
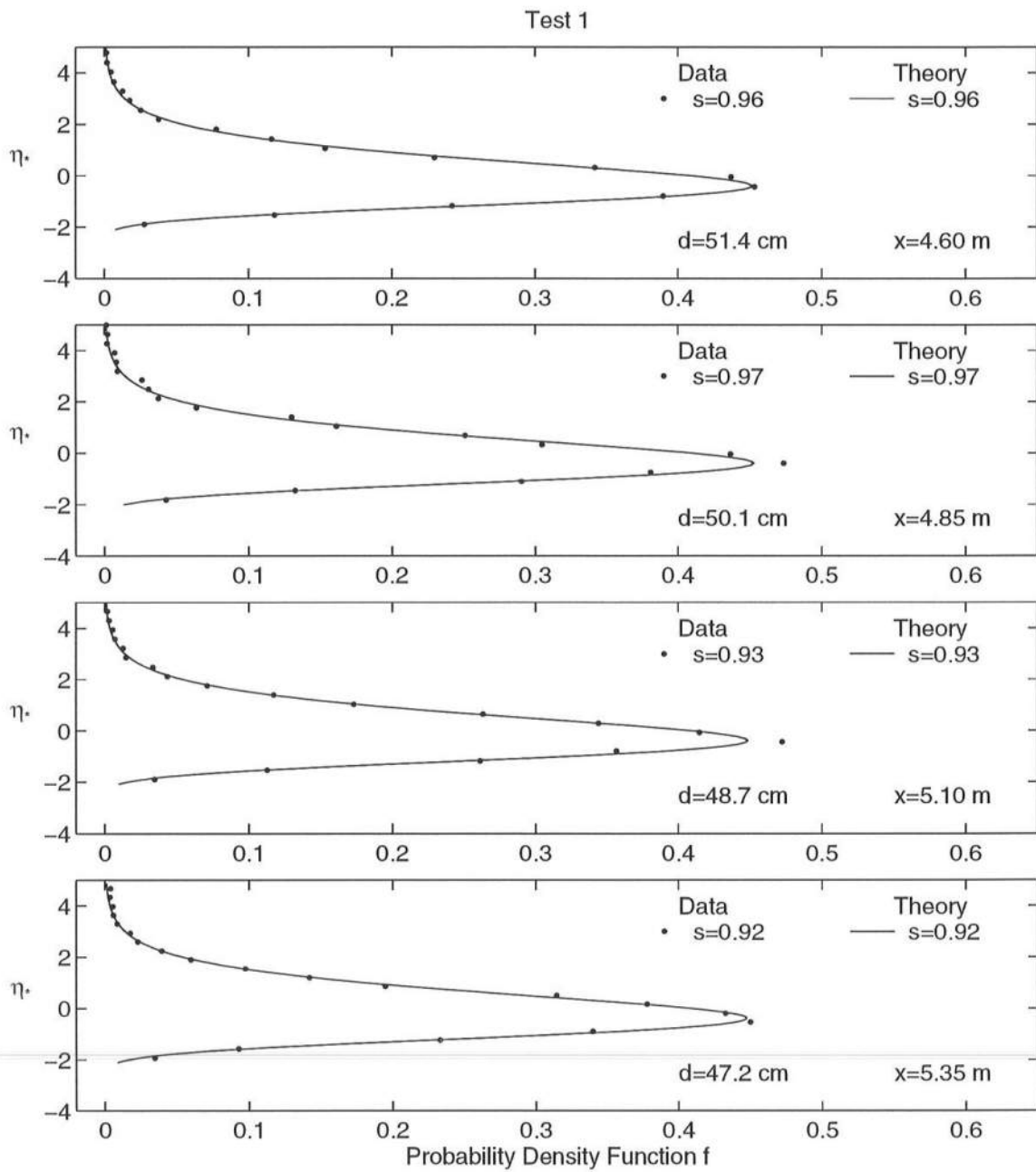
Figure 4.15: Measured and Computed Probability Distributions at Positions $x = 4.60$, 4.85, 5.10, and 5.35 m for Test 1
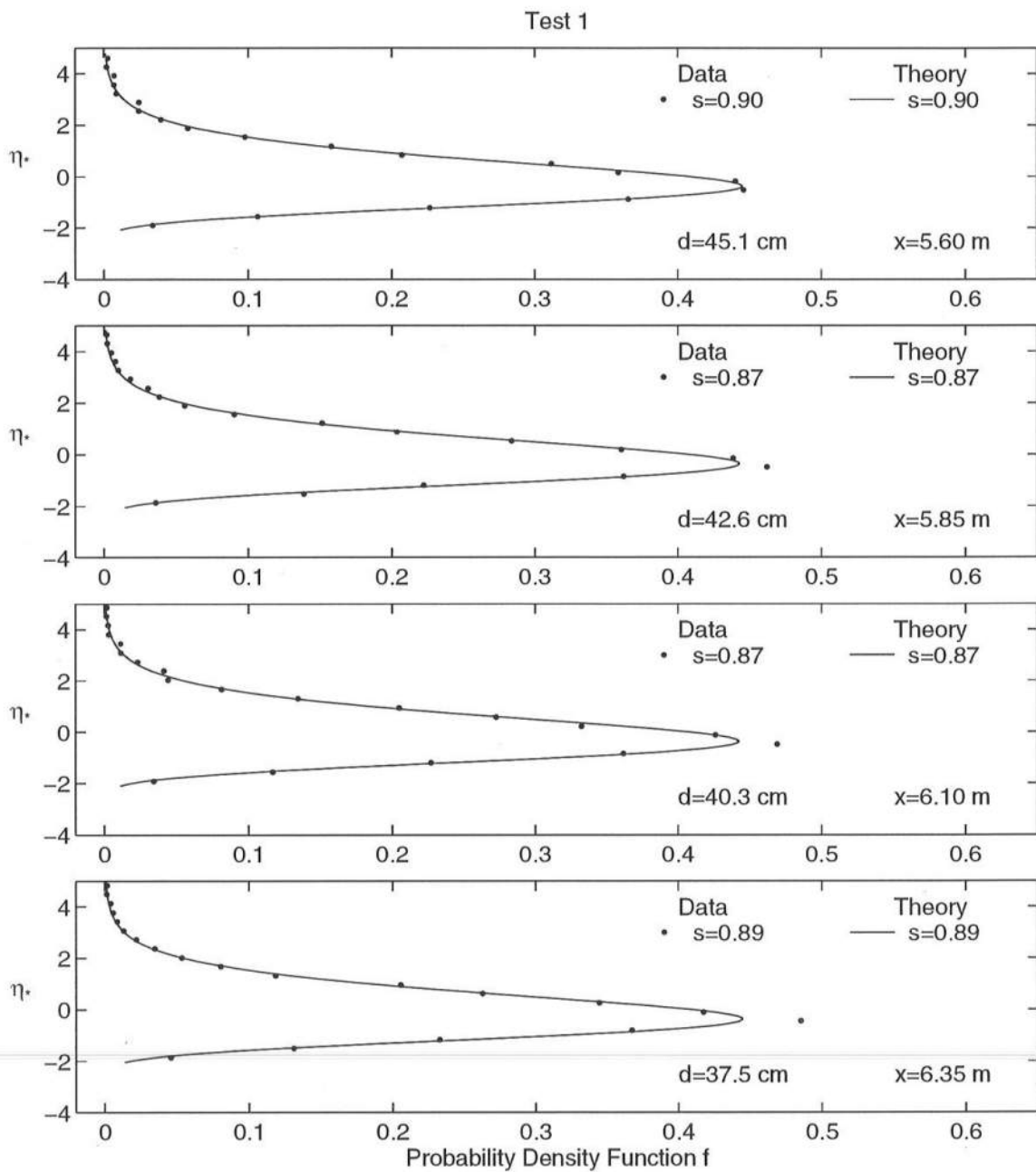
Figure 4.16: Measured and Computed Probability Distributions at Positions $x = 5.60$, 5.85, 6.10, and 6.35 m for Test 1
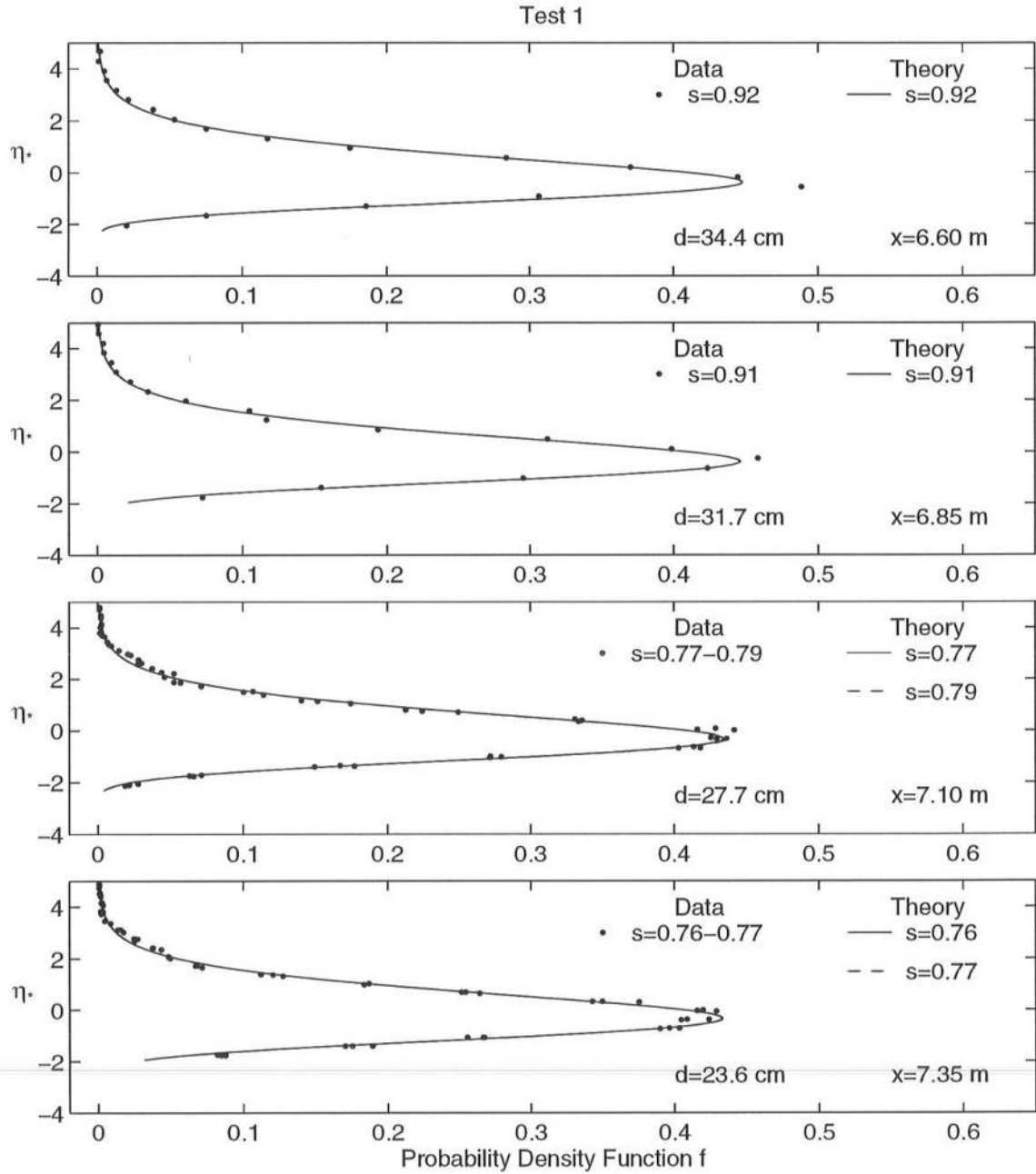
Figure 4.17: Measured and Computed Probability Distributions at Positions $x = 6.60$, 6.85, 7.10, and 7.35 m for Test 1 ($x = 7.10$ and $x = 7.35$ are Velocity Profile Locations)
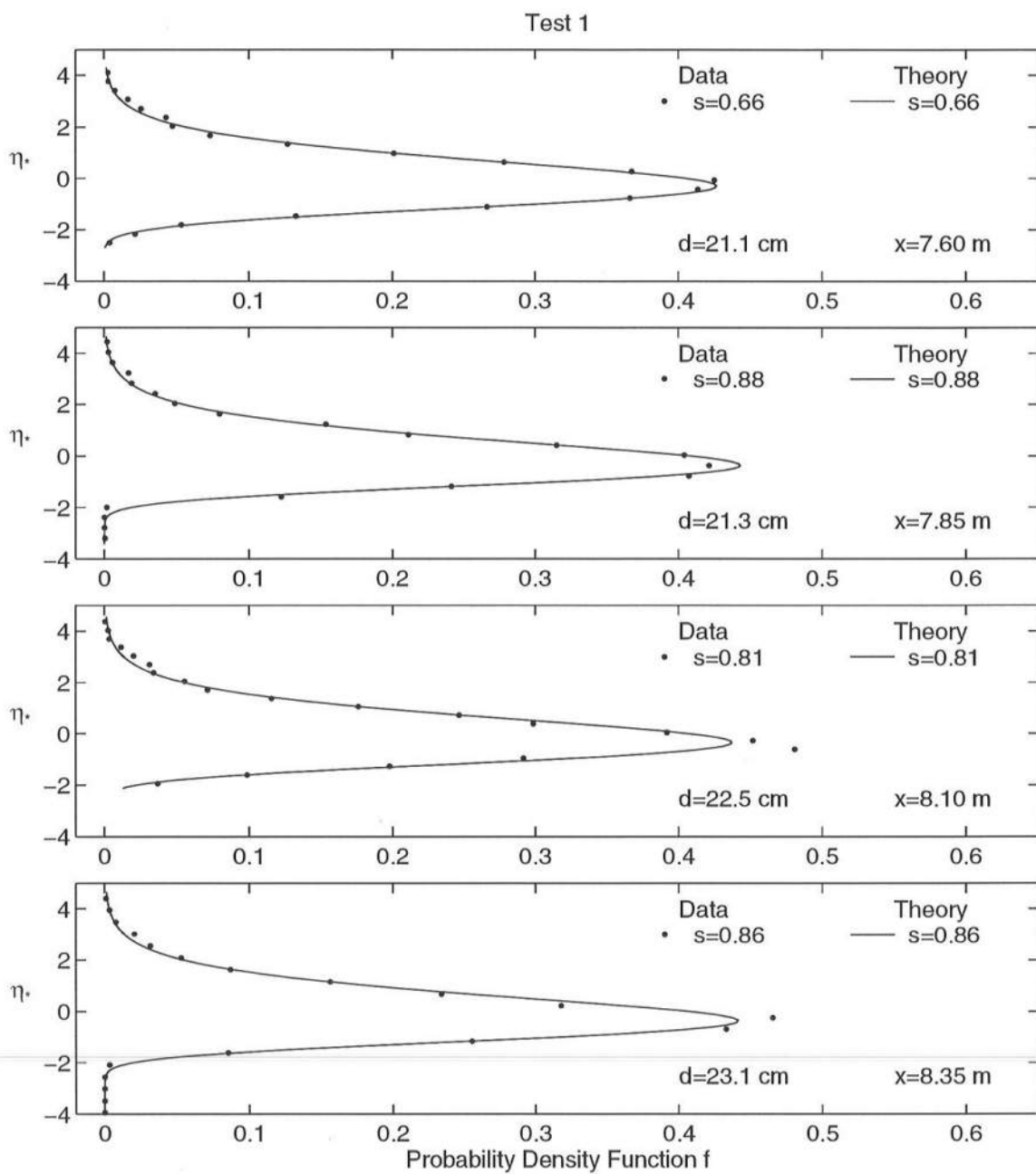
Figure 4.18: Measured and Computed Probability Distributions at Positions $x = 7.60, 7.85, 8.10$, and 8.35 m for Test 1
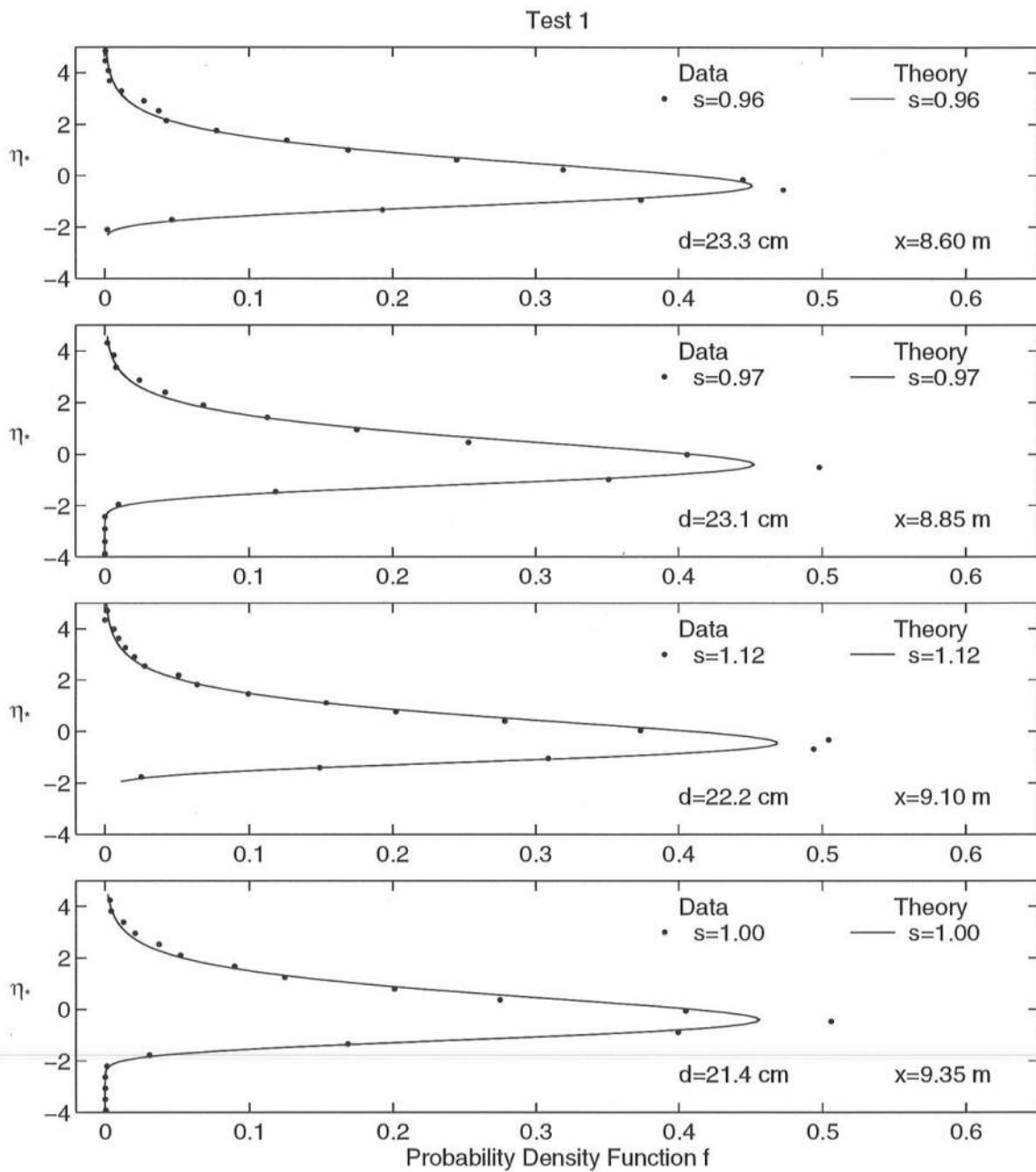
Figure 4.19: Measured and Computed Probability Distributions at Positions $x = 8.60$, 8.85, 9.10, and 9.35 m for Test 1
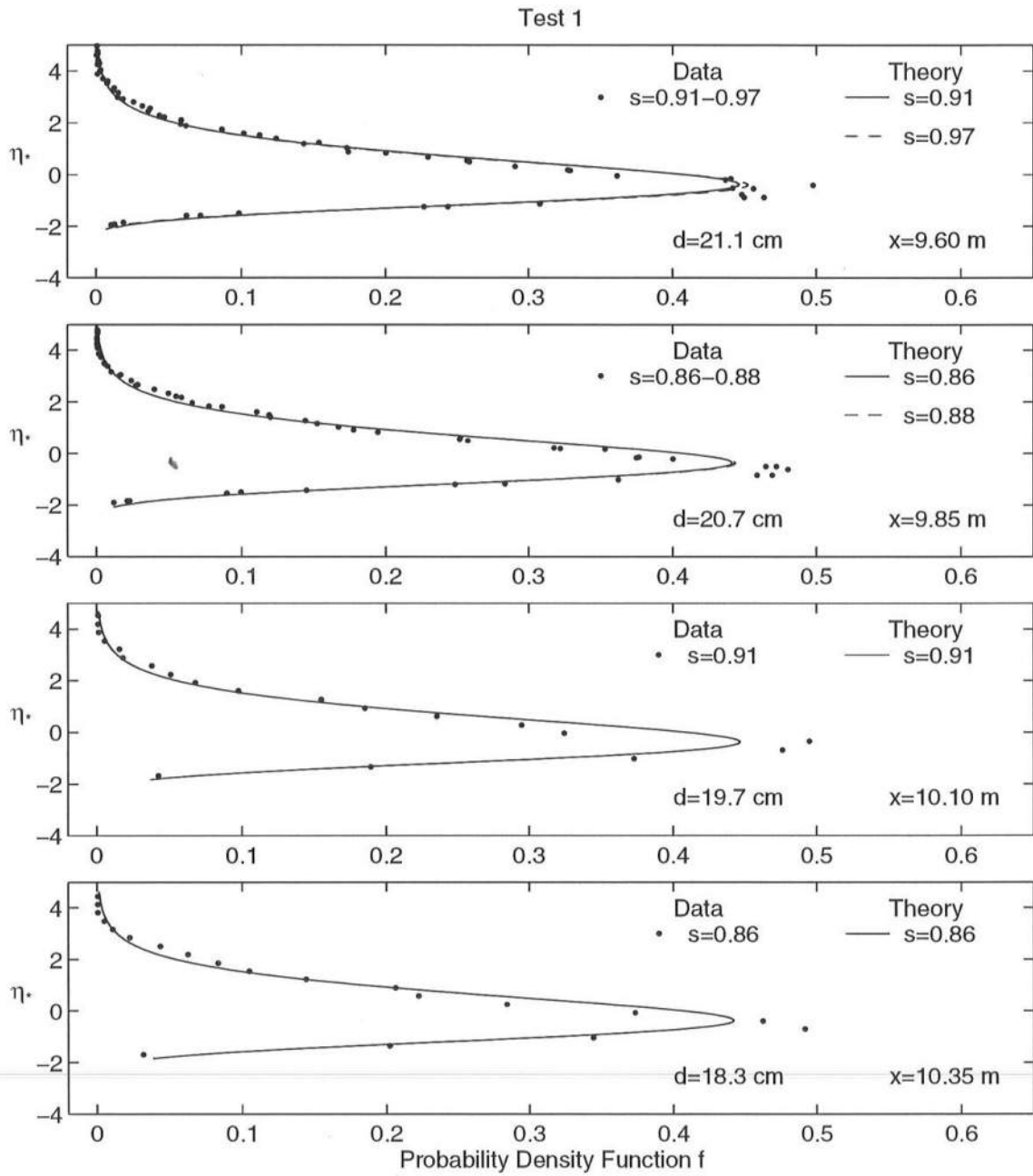
Figure 4.20: Measured and Computed Probability Distributions at Positions $x = 9.60$, 9.85, 10.10, and 10.35 m for Test 1 ($x = 9.60$ and $x = 9.85$ are Velocity Profile Locations)

79
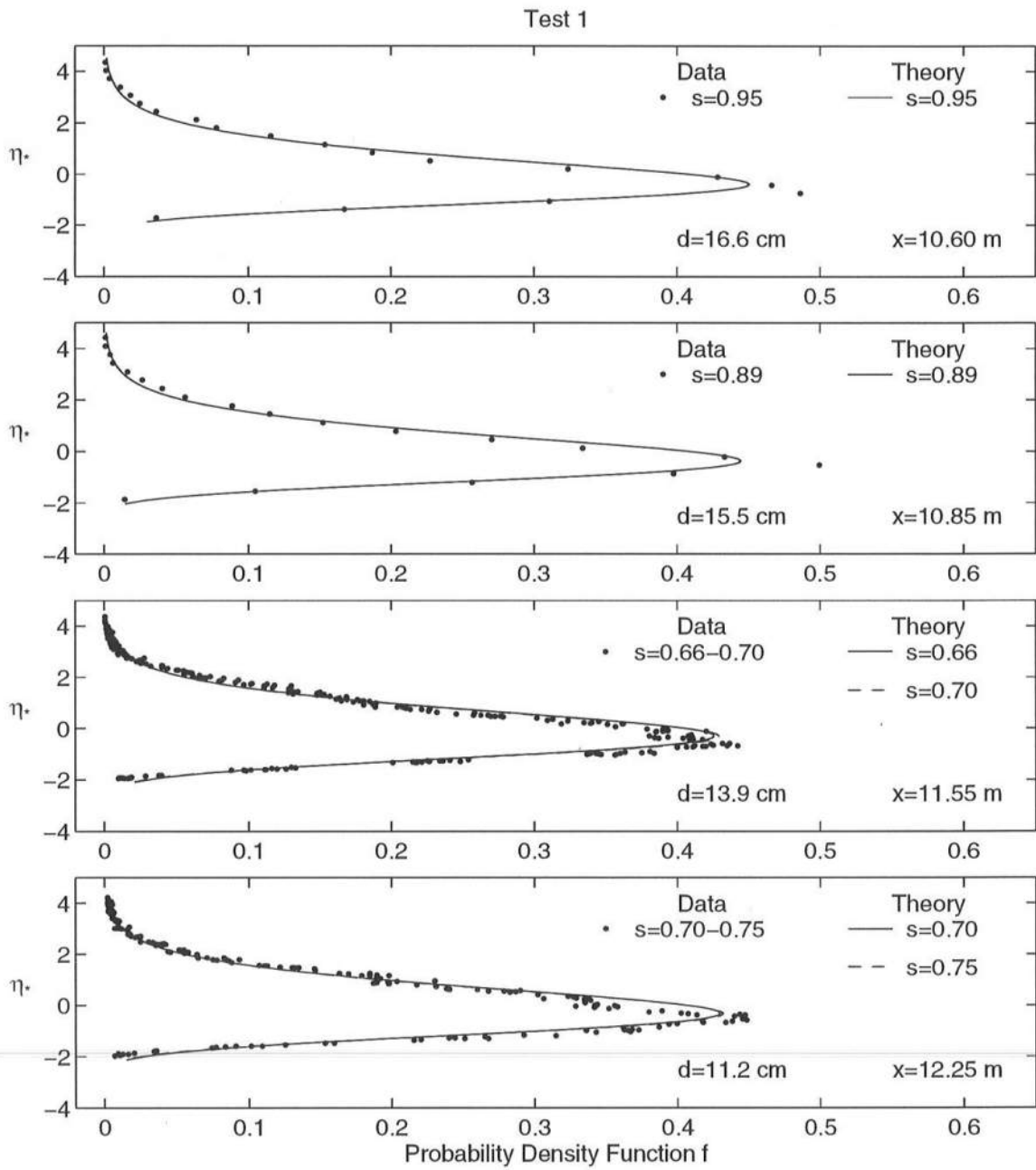
Figure 4.21: Measured and Computed Probability Distributions at Positions $x = 10.60$, 10.85, 11.55, and 12.25 m for Test 1
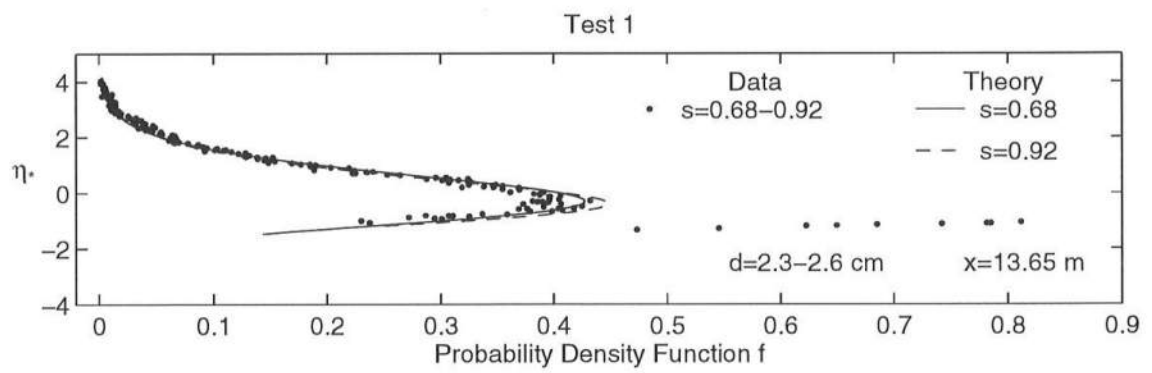
Figure 4.22: Measured and Computed Probability Distributions at Position $x = 13.65$ m for Test 1 (Positions $x = 13.23$, 13.37, and 13.51 were discarded)
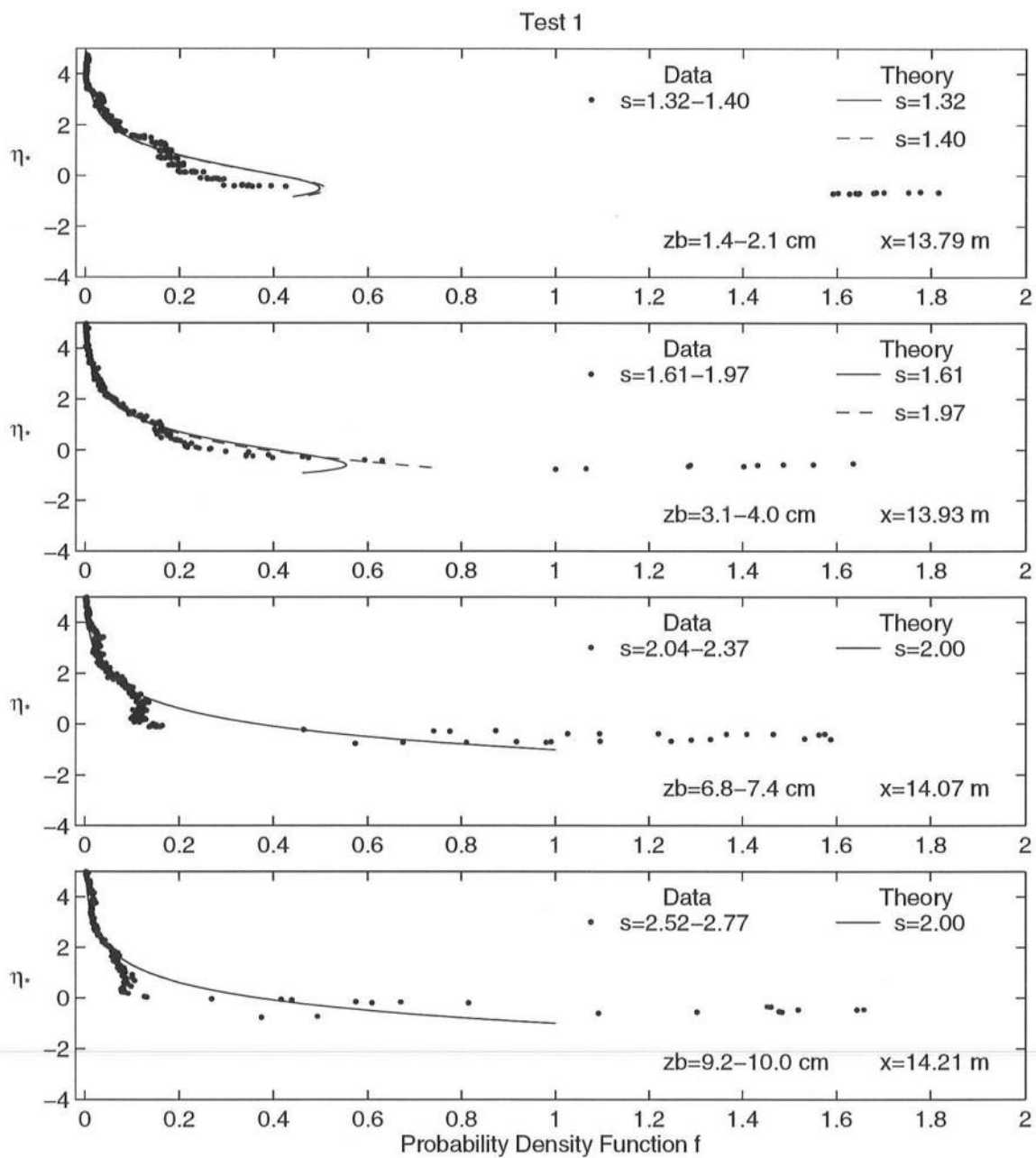
Figure 4.23: Measured and Computed Probability Distributions at Positions $x = 13.79$, 13.93, 14.07, and 14.21 m for Test 1
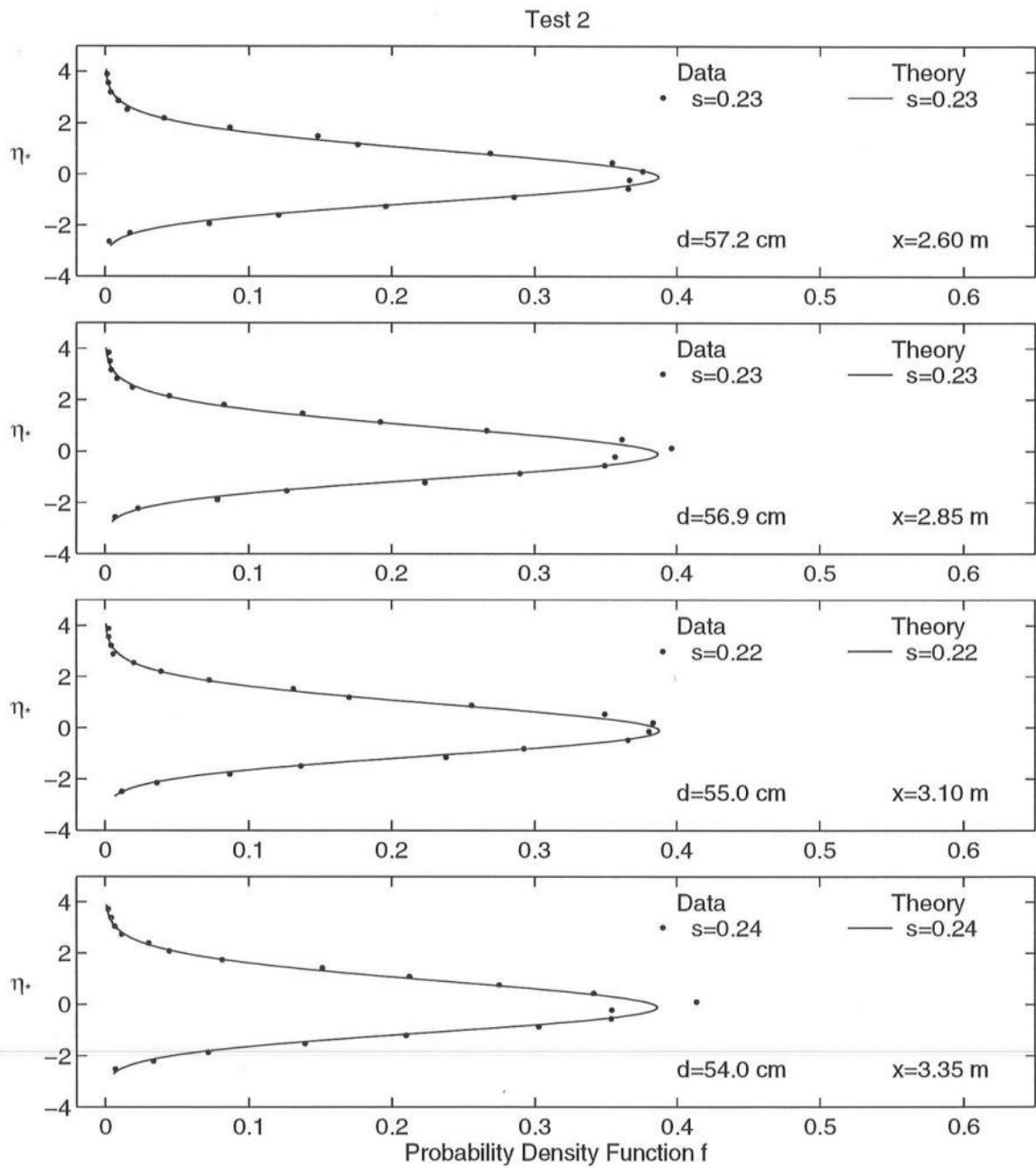
Figure 4.24: Measured and Computed Probability Distributions at Positions $x = 2.60, 2.85, 3.10,$ and 3.35 m for Test 2
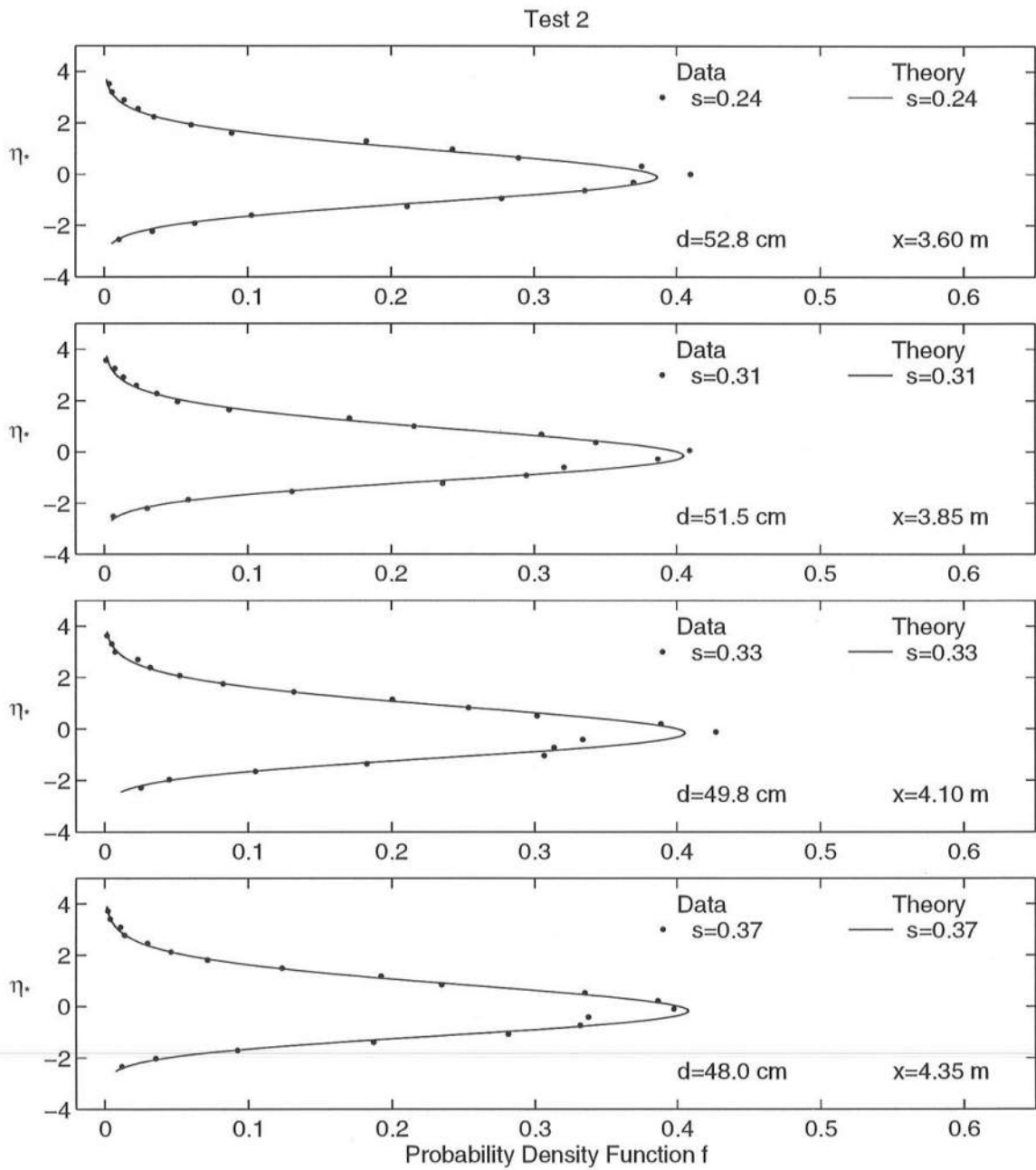
Figure 4.25: Measured and Computed Probability Distributions at Positions $x = 3.60, 3.85, 4.10,$ and 4.35 m for Test 2
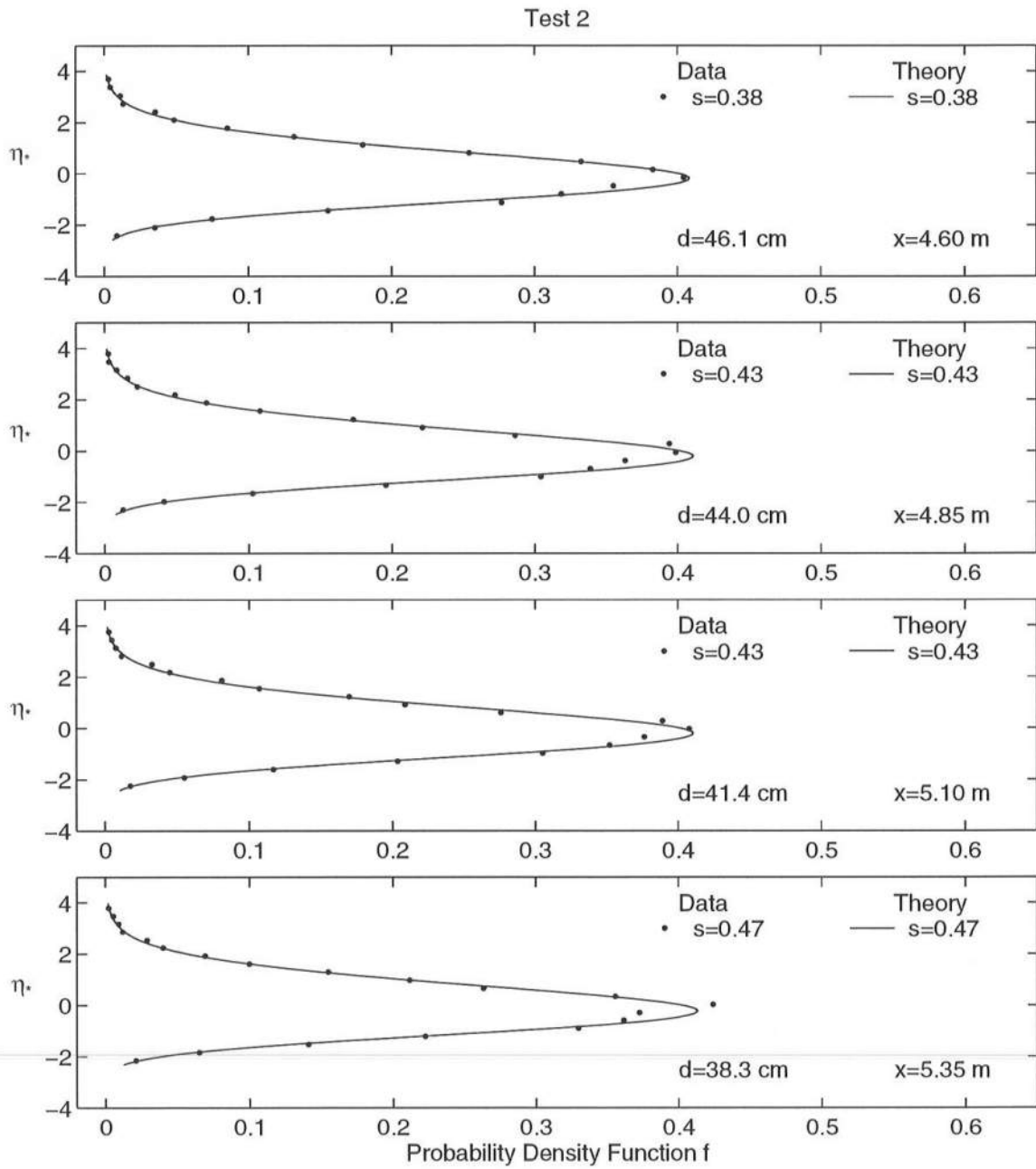
Figure 4.26: Measured and Computed Probability Distributions at Positions $x = 4.60, 4.85, 5.10$, and 5.35 m for Test 2
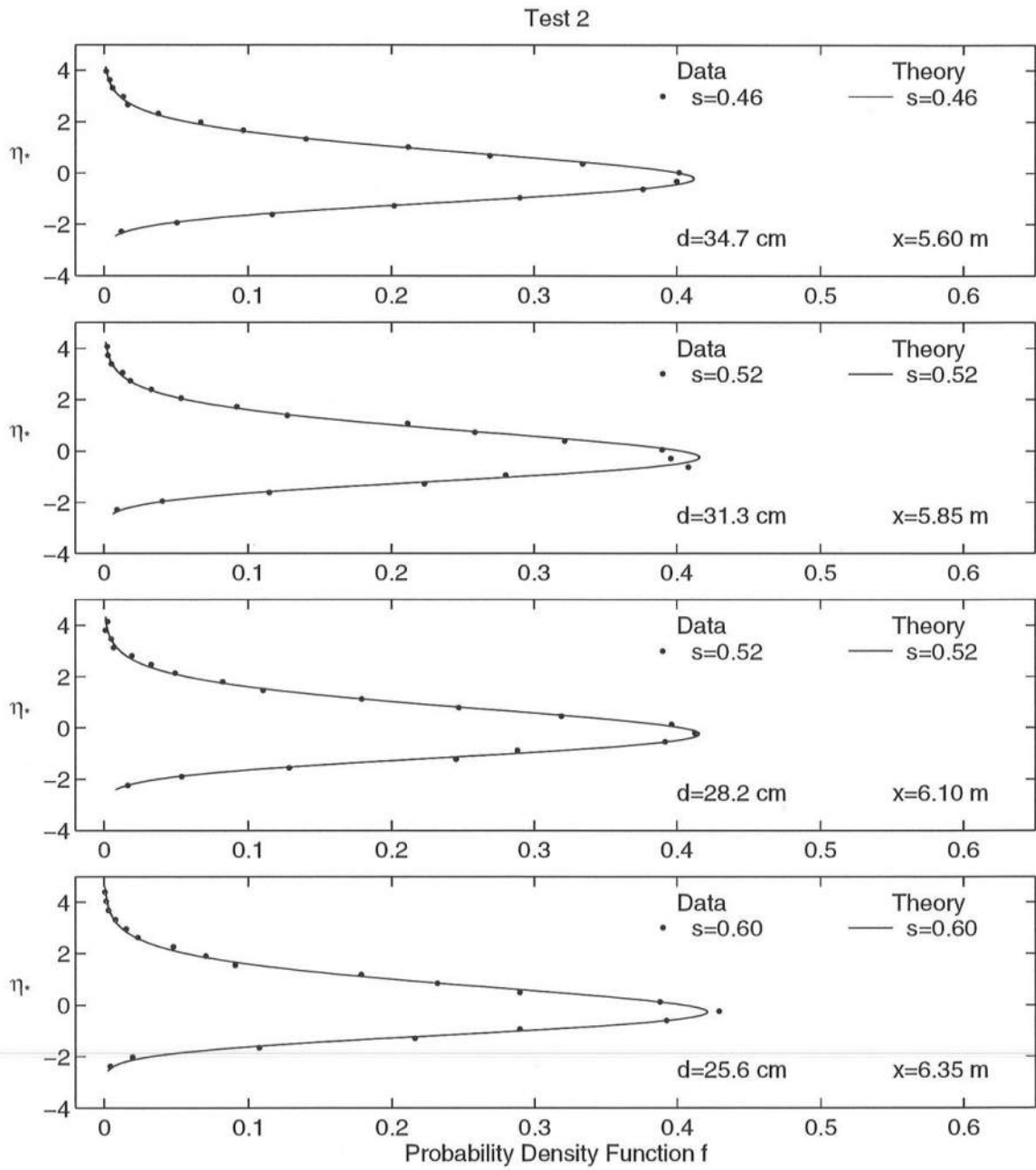
Figure 4.27: Measured and Computed Probability Distributions at Positions $x = 5.60, 5.85, 6.10$, and 6.35 m for Test 2
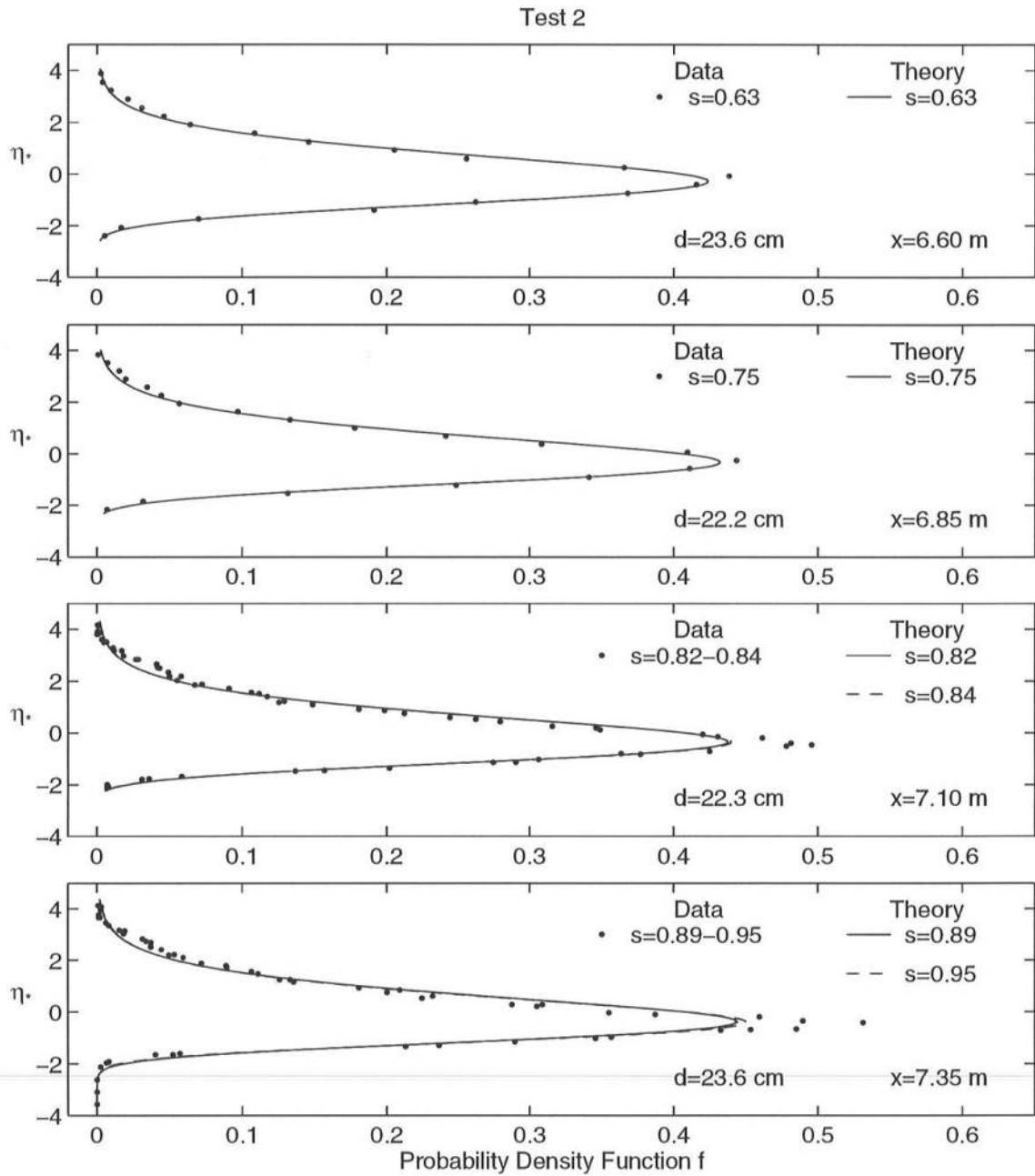
Figure 4.28: Measured and Computed Probability Distributions at Positions $x = 6.60$, 6.85, 7.10, and 7.35 m for Test 2 ($x = 7.10$ and $x = 7.35$ are Velocity Profile Locations)
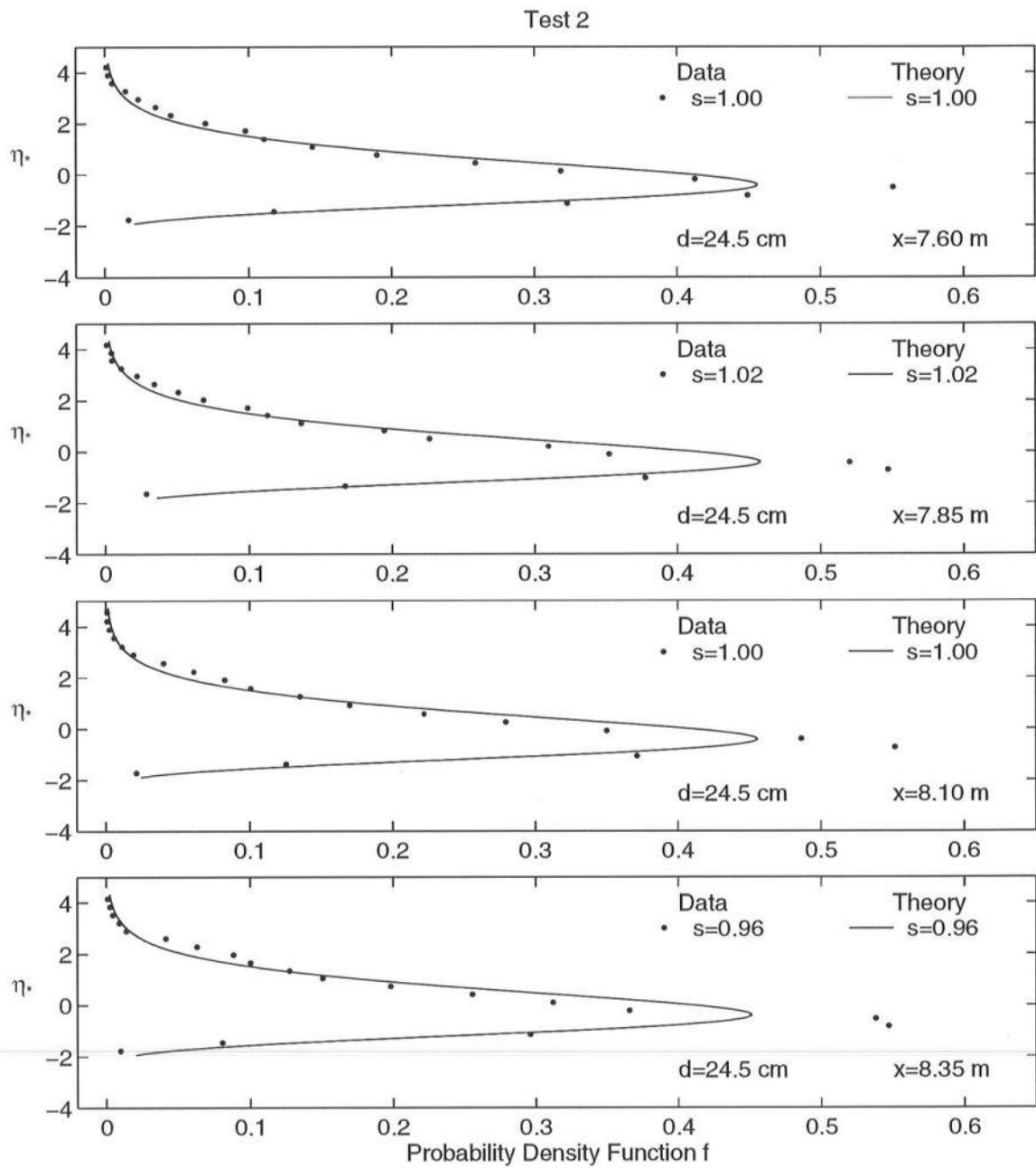
Figure 4.29: Measured and Computed Probability Distributions at Positions $x = 7.60,\ 7.85,\ 8.10,$ and 8.35 m for Test 2
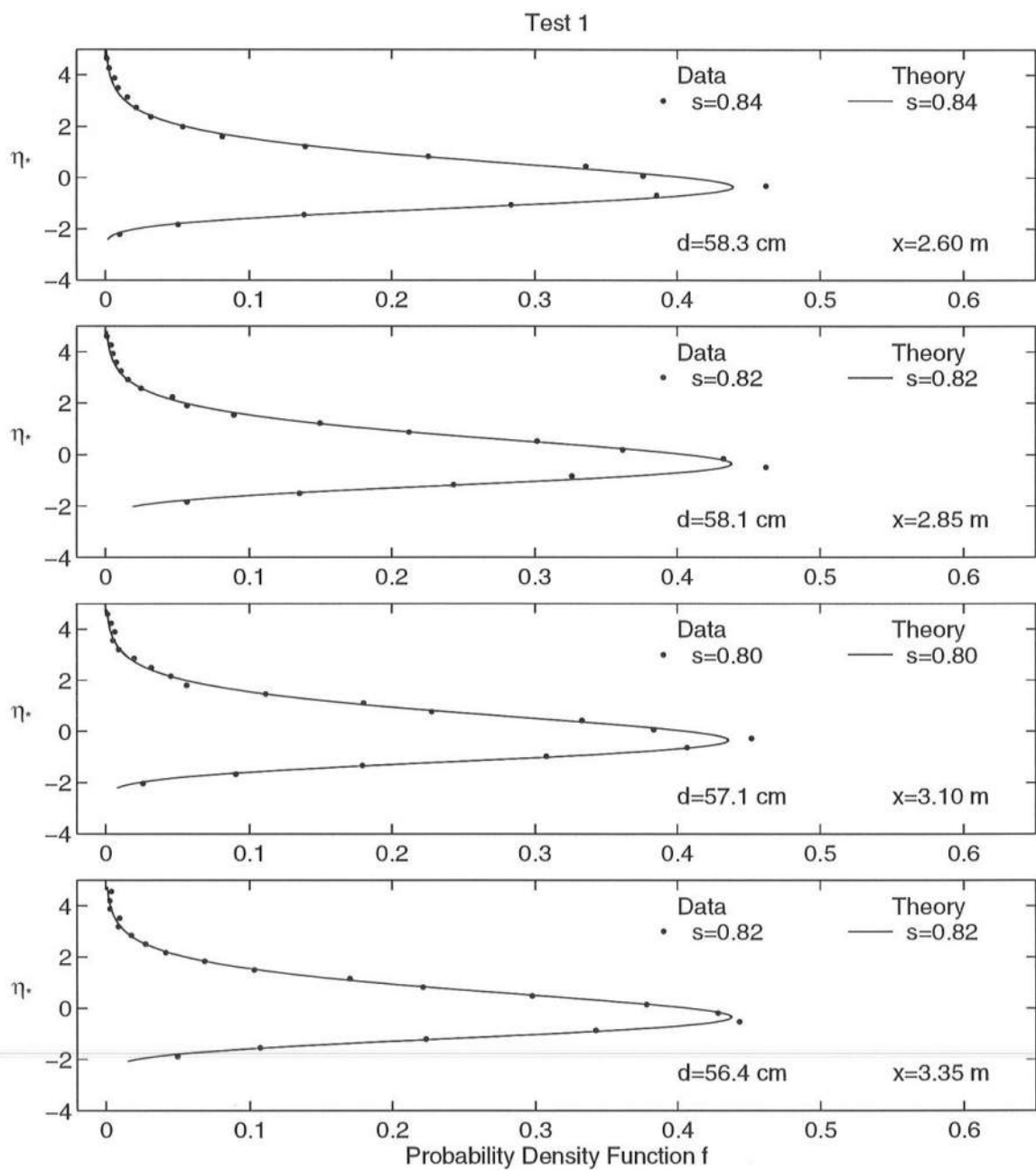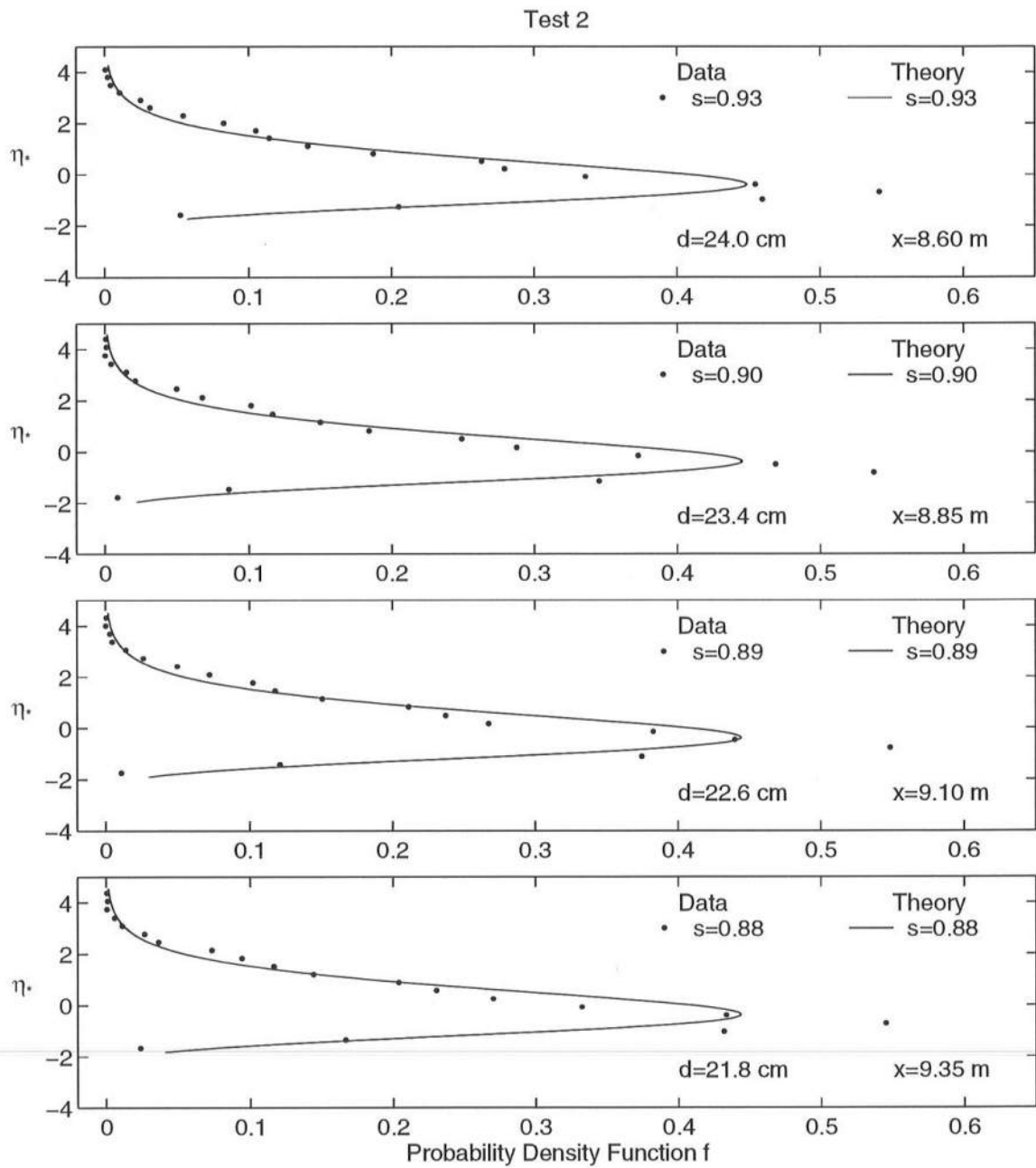
Figure 4.30: Measured and Computed Probability Distributions at Positions $x = 8.60,\ 8.85,\ 9.10,$ and 9.35 m for Test 2
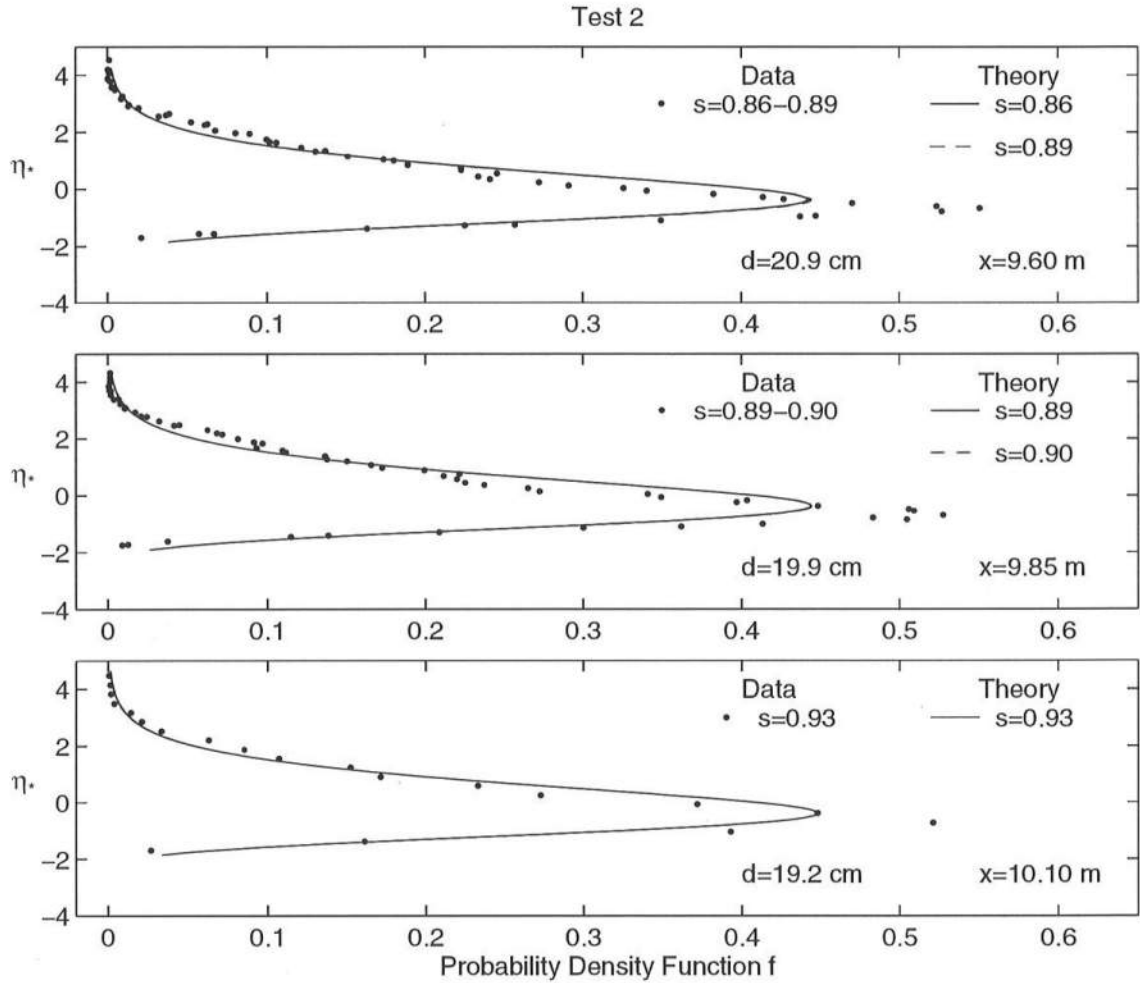
Figure 4.31: Measured and Computed Probability Distributions at Positions $x = 9.60$, 9.85, and 10.10 cm for Test 2 ($x = 9.60$ and $x = 9.85$ are Velocity Profile Locations; Data at $x = 10.35$ was discarded)
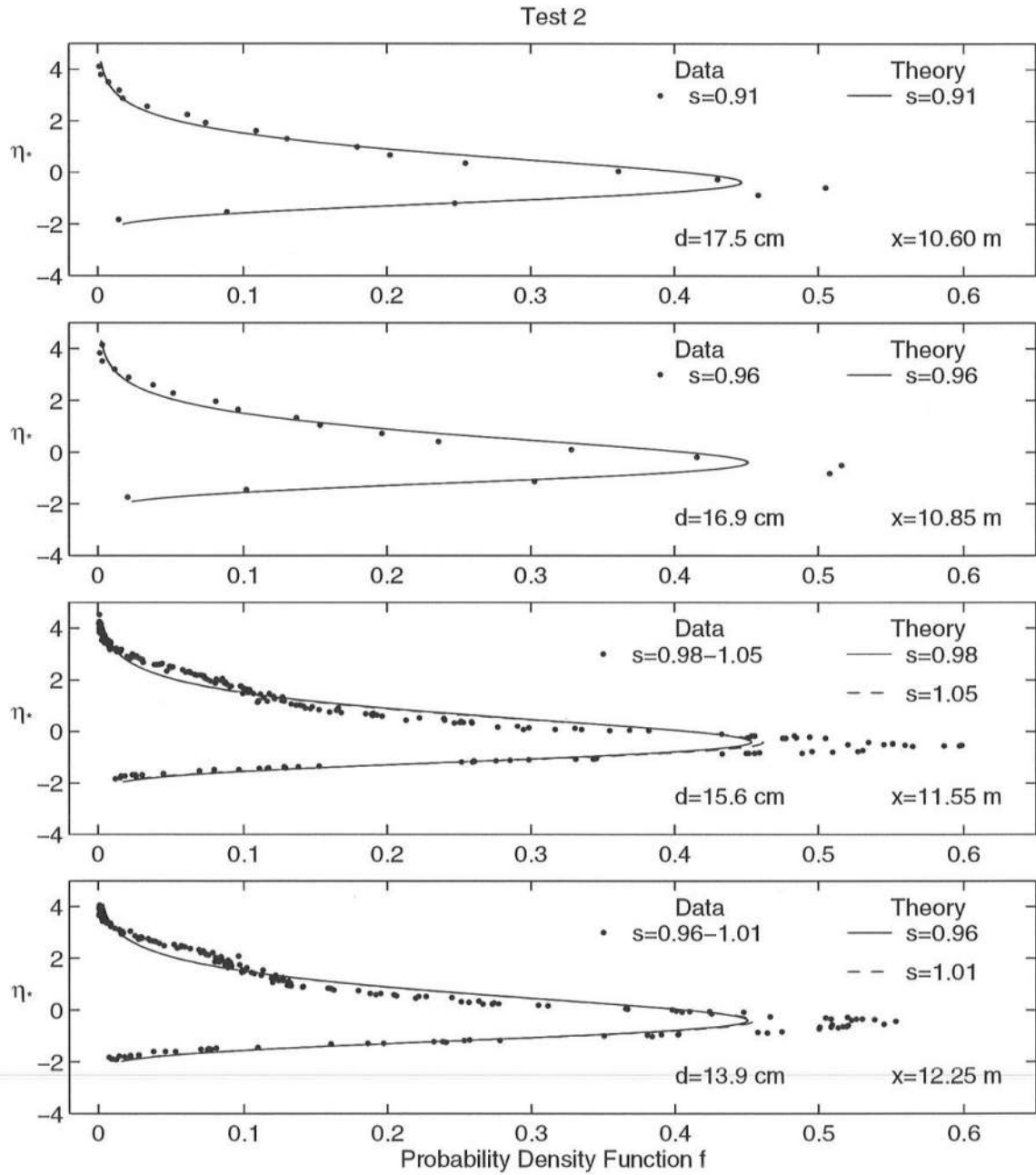
Figure 4.32: Measured and Computed Probability Distributions at Positions $x = 10.60$, 10.85, 11.55, and 12.25 m for Test 2 (Run 20 for gauge 6 at $x = 12.25$ m was discarded)

91
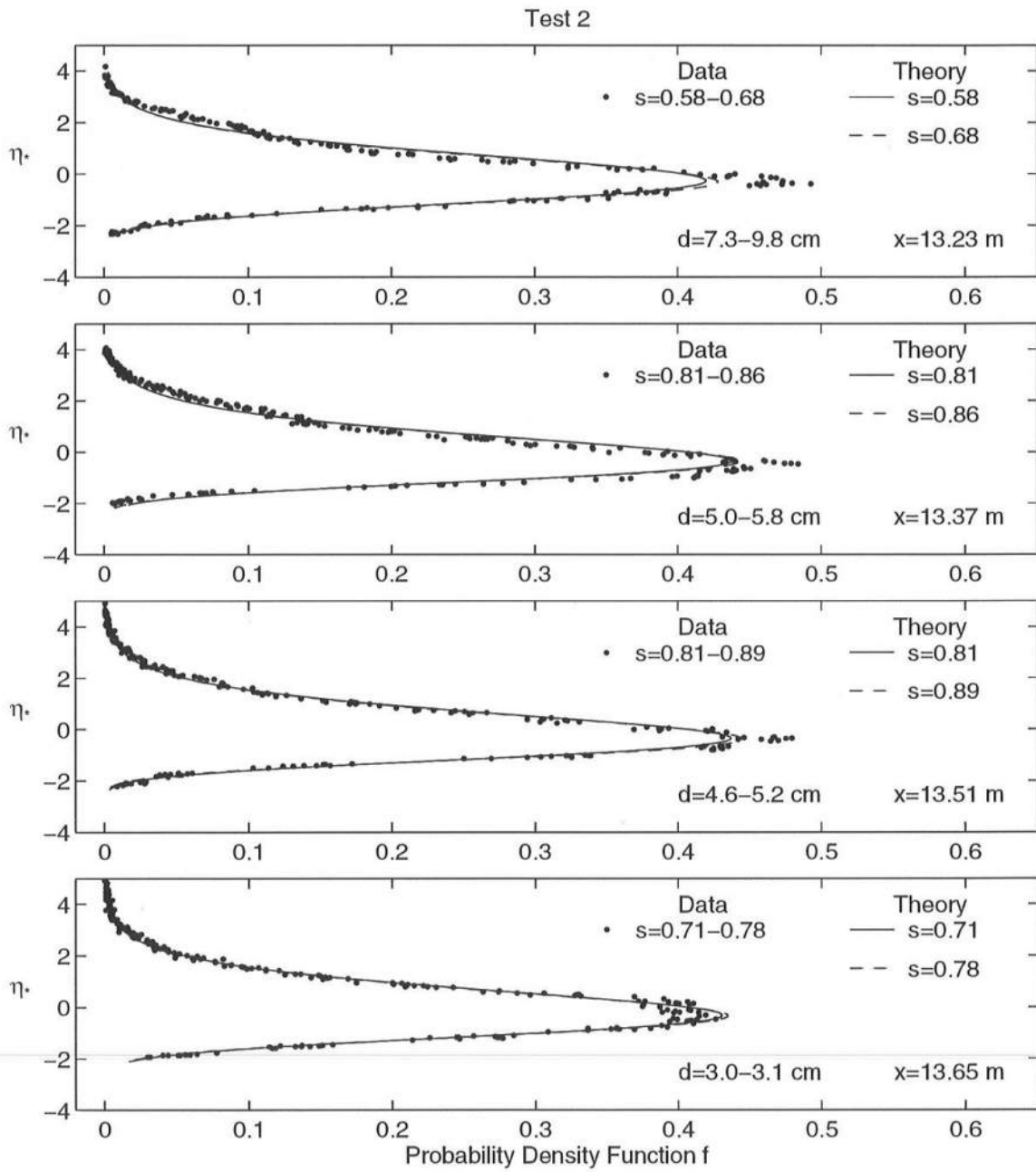
Figure 4.33: Measured and Computed Probability Distributions at Positions $x = 13.23$, 13.37, 13.51, and 13.65 m for Test 2

92
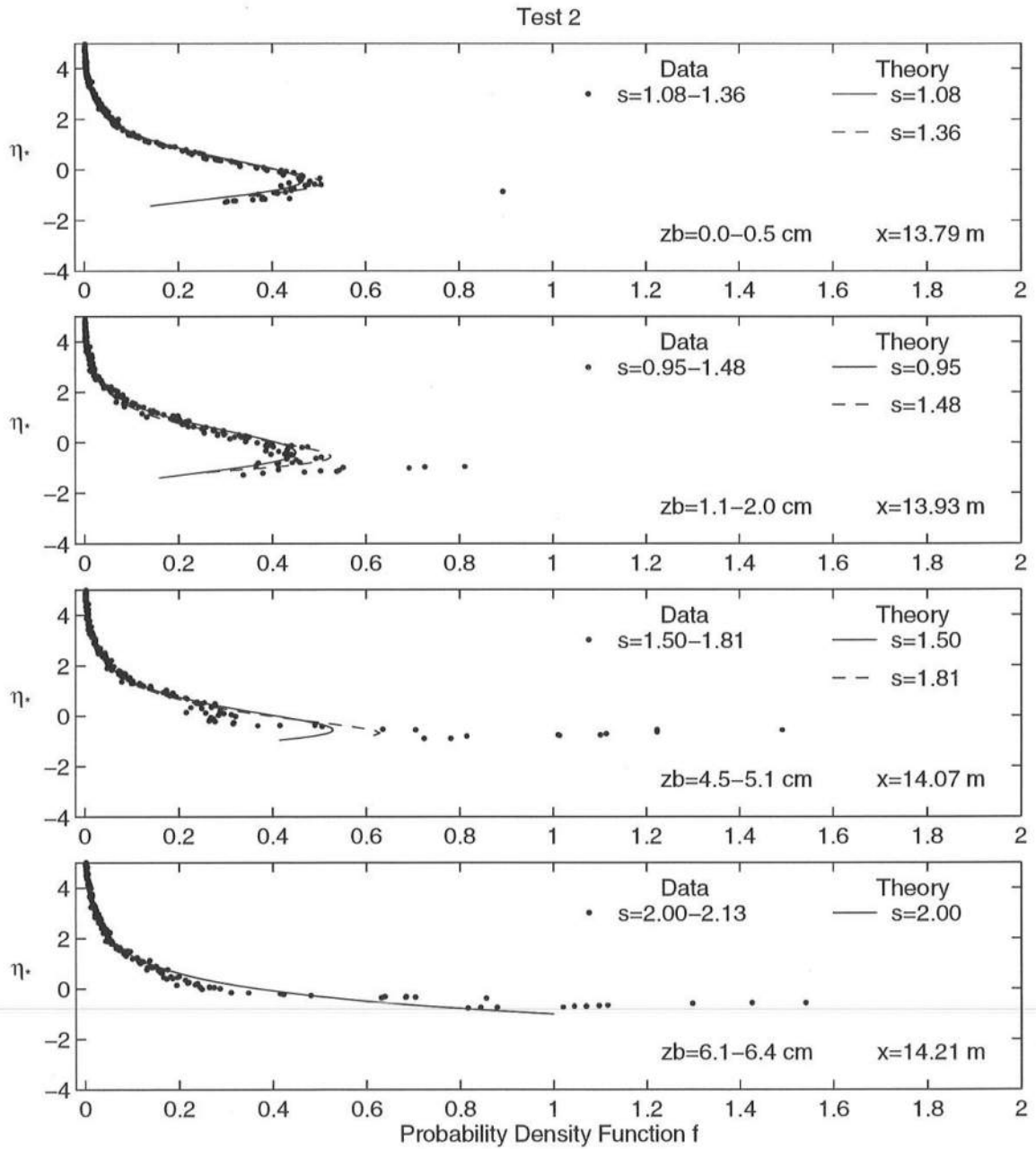
Figure 4.34: Measured and Computed Probability Distributions at Positions $x = 13.79$, 13.93, 14.07, and 14.21 m for Test 2

Chapter 5

CROSS-SHORE HORIZONTAL VELOCITIES

In the present chapter, cross-shore velocity statistics will be summarized and compared to the predictions of the exponential gamma distribution in surf and swash zones, as was done for free surface elevations in chapter 4. Also included in this analysis will be an examination of the variation of these statistics over depth and an attempt to synchronize free surface and velocity time series. Velocity measurements were made at 17 cross-shore locations, with two 3-point vertical profiles taken at $x = 7.35$ m and $x = 9.85$ m. The mean velocity, $\overline{u}$, the standard deviation, σ_u, the skewness, s_u, and the kurtosis, K_u, are calculated for each time series of the cross-shore velocity, u, measured at the approximate mid-depth below SWL. These are computed under the assumption of equivalency of the probabilistic and time averaging, in the same manner as Herrman *et al.* (1997). The horizontal velocity, u, is taken as positive landward, so that the undertow velocity, $\overline{u}$, is negative. The normalized horizontal velocity, $u_* = (u - \overline{u})/\sigma_u$, is then calculated using the measured values of $\overline{u}$ and σ_u. The probability density function, $f(u_*)$, for each time series of u_* is determined and compared with the exponential gamma distribution. The theoretical distribution is given by equations (2.1) – (2.3), where η_* and s must be replaced by u_* and s_u, respectively. Skewness and kurtosis values for u are the same as those for u_*.

94

5.1 Horizontal Velocity and Linear Theory

In obtaining approximate relationships between the free surface and horizontal velocity statistics, local nonlinearity is neglected and linear progressive long-wave theory is assumed to be approximately valid locally even inside surf zones [e.g., Guza and Thornton (1980)]. The oscillatory components of the horizontal velocity and free surface elevation are then related as follows:

$$(u - \overline{u}) \simeq \sqrt{\frac{g}{\overline{h}}} (\eta - \overline{\eta}) \tag{5.1}$$

Here g = gravitational acceleration and $\overline{h}$ = mean water depth, given by $\overline{h} = (d + \overline{\eta})$ with d = still water depth. If equation (5.1) holds, the following relationships can be derived as well:

$$\sigma_u \simeq \sqrt{\frac{g}{\overline{h}}}\sigma \quad ; \quad s_u \simeq s \quad ; \quad K_u \simeq K \tag{5.2}$$

in which σ, s and K are the standard deviation, skewness, and kurtosis of the free surface elevation, η. Furthermore, the probability density functions of $u_* = (u - \overline{u})/\sigma_u$ and $\eta_* = (\eta - \overline{\eta})/\sigma$ become approximately the same because $u_* \simeq \eta_*$ under the assumption of (5.1), with $\sigma_u \simeq (\sqrt{g/\overline{h}})\sigma$.

To estimate the undertow velocity, $\overline{u}$, the horizontal velocity, u, at the approximate mid-depth is assumed to be represented by the depth-averaged velocity, U. For an impermeable beach, the time-averaged continuity equation, $\overline{hU} = 0$, yields:

$$\overline{U} = -\left(\overline{h}\right)^{-1} \overline{(\eta - \overline{\eta})\left(U - \overline{U}\right)} \tag{5.3}$$

in which $\overline{h} = (d + \overline{\eta})$ (Kobayashi *et al.* 1989). Substitution of $u \simeq U$ and equation (5.1) into (5.3) yields:

$$\overline{u} \simeq -\sqrt{g\overline{h}} \left(\frac{\sigma}{\overline{h}}\right)^2 = -\frac{\sqrt{g\overline{h}}}{8} \left(\frac{H_{\text{rms}}}{\overline{h}}\right)^2 \tag{5.4}$$

This study will compare predictions of equations (5.2) and (5.4) to velocity statistics obtained from tests 1 and 2.

5.2 Cross-Shore Variations in Statistical Values of Horizontal Velocity

Figures 5.1 and 5.2 show the cross-shore variations of the measured values of $\bar{u}$, σ_u, s_u and K_u in the still water depth $d = 15$–58 cm for test 1 and $d = 17$–57 cm for test 2. The three data points at cross-shore locations $x = 7.35$ m and $x = 9.85$ m for the repeated velocity measurements made in vertical velocity profiles are represented by the middle point at each location to be consistent with the other data points in these figures. The depth range was limited due to difficulties measuring undertow velocity, $\bar{u}$, in the shallow water. The computed values of $\bar{u}$, σ_u, s_u, and K_u at each cross-shore location are also shown in Figures 5.1 and 5.2. These were obtained from equations (5.2) and (5.4), making use of the corresponding measured values of $\bar{h} = (d + \bar{\eta})$, σ, s, and K.

The measured and computed undertow, $\bar{u}$, agree well in deeper water in both tests. However, there is some underprediction of the magnitude of $\bar{u}$ in the surf zone. This may be explained by the fact that equation (5.4), which is based on linear long wave theory, does not account for the additional water volume flux due to a roller. This roller effect increases the magnitude of $\bar{u}$, as shown by Svendsen (1984) for regular waves. This underprediction was also visible in Tests 2 and 3 of Herrman *et al.* (1997). The measured undertow velocity fields are shown over the corresponding profiles in Figure 5.3. Undertow is strong over most of the terrace region in both tests, leading one to expect offshore transport. This will be examined further in Chapter 6.

There is good agreement (within about 10%) between the measured and computed standard deviation, σ_u, for test 1, as shown in Figure 5.1. Figure 5.2 shows only fair agreement (usually within 30%) in test 2. These results compare well to the level of agreement predicted by Guza and Thornton (1980) from field data intercomparisons. It should be noted, however, that Guza and Thornton (1980) focused their analysis on wind wave frequencies, while in this study the measured,

96
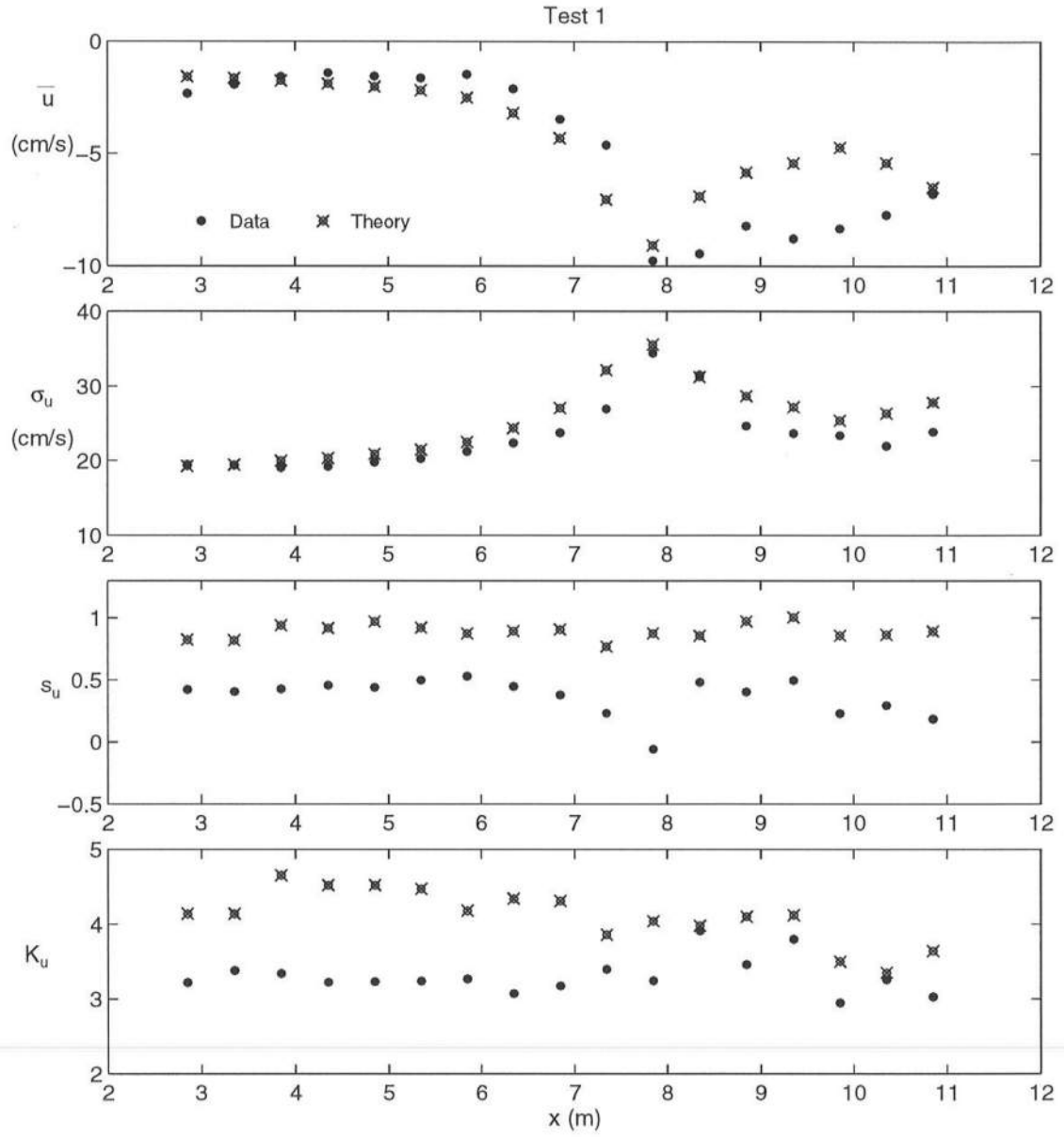
Figure 5.1: Measured and Computed Cross-Shore Variations of $\overline{u}$, σ_u, s_u, and K_u for Test 1
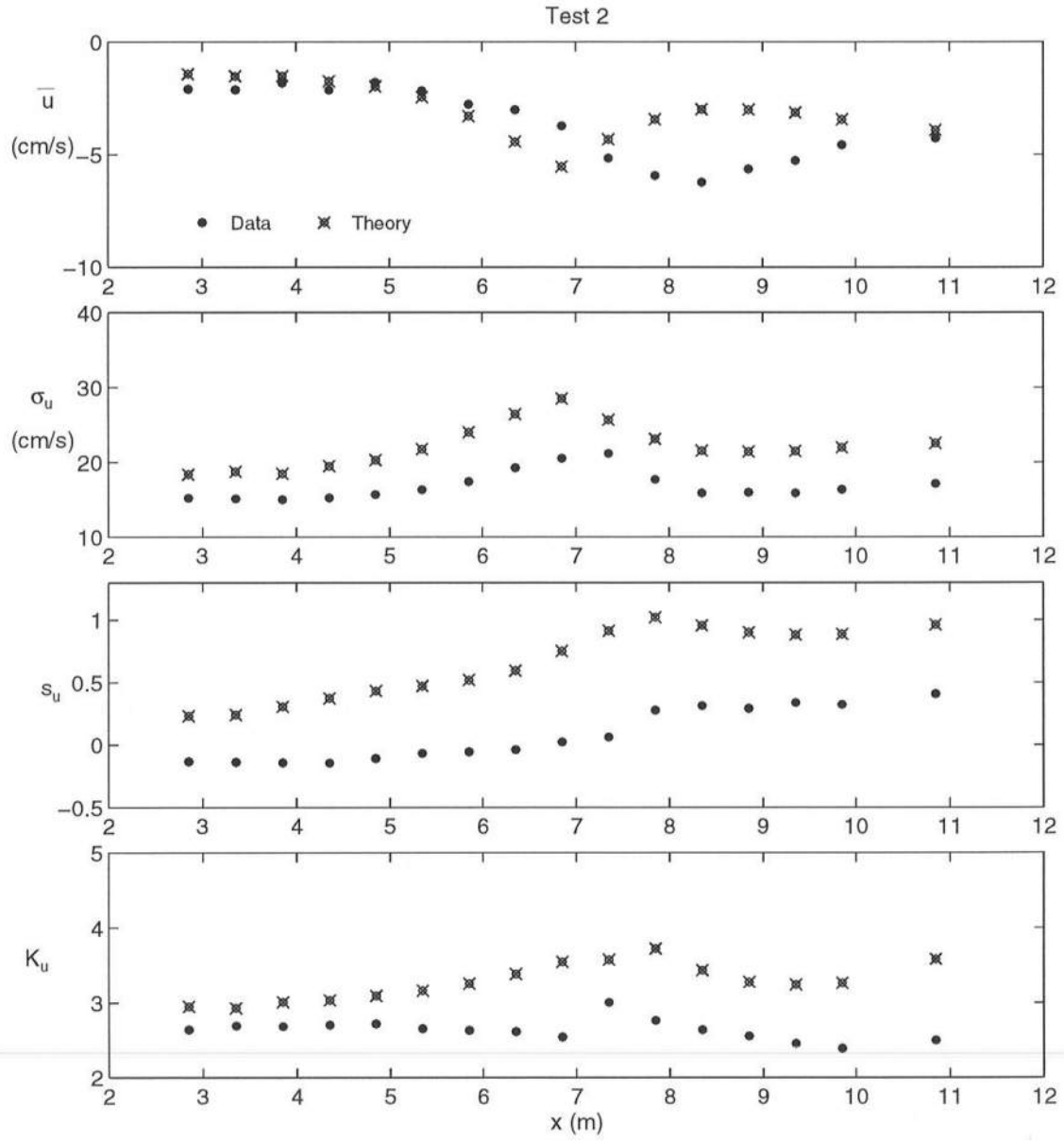
Figure 5.2: Measured and Computed Cross-Shore Variations of $\overline{u}$, σ_u, s_u, and K_u for Test 2

98
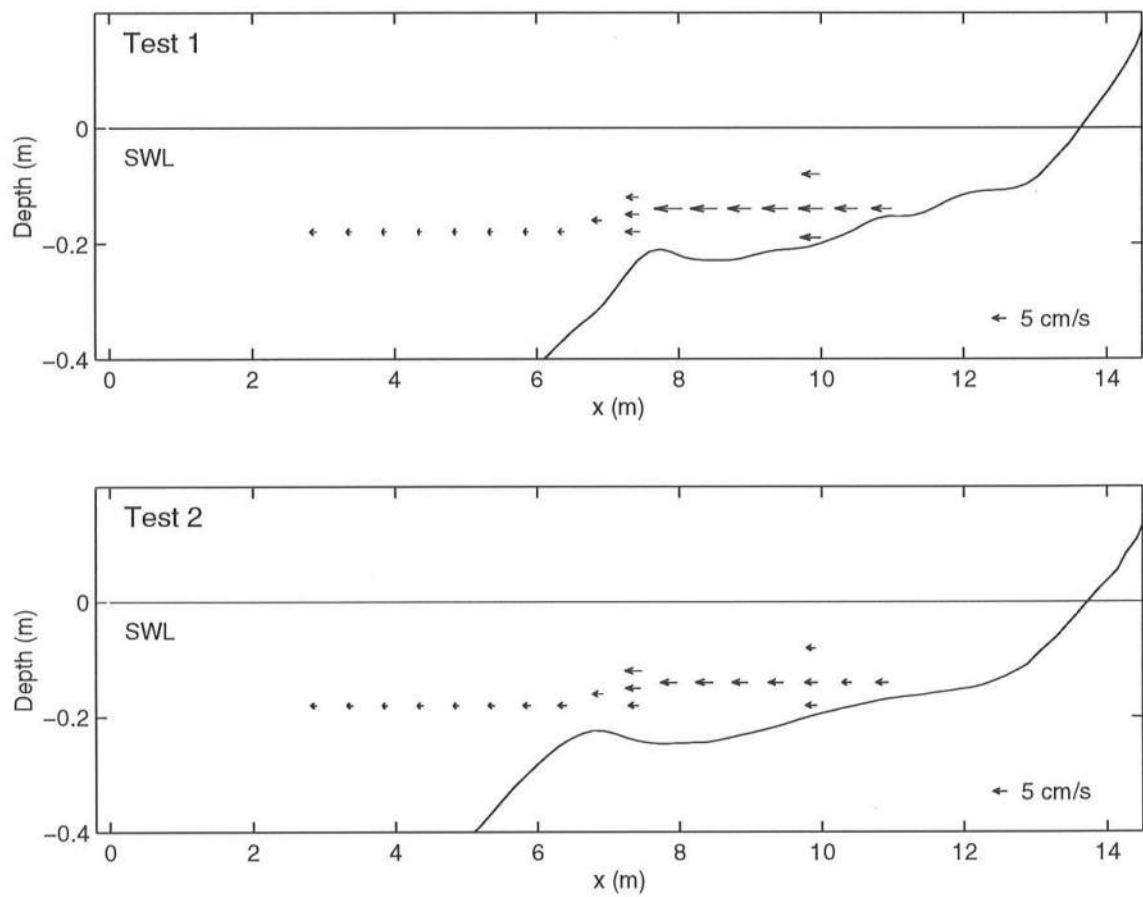
Figure 5.3: Undertow Velocity Fields for Tests 1 and 2

99
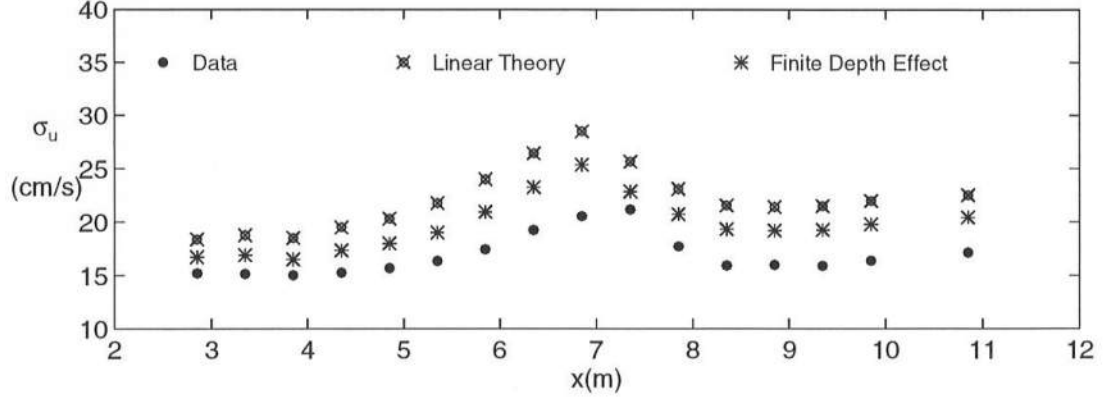
Figure 5.4: Comparison of Linear Theory and Finite Depth Theory Predictions of Standard Deviation, σ_u, for Test 2

unfiltered time series are used because of difficulty separating wind wave and low-frequency components for practical applications. The merely fair agreement shown in test 2 of this study might be explained by examination of the values of $L_p/\bar{h}$, where L_p = linear wavelength based on T_p and T_p = 2.8 and 1.6 s for tests 1 and 2, respectively, as listed in Table 3.5. For depths ranging from 15 to 58 cm, $L_p/\bar{h}$ ranged from 11 to 22 in test 1 but only from 6 to 12 in test 2. This suggests that the linear long-wave assumption may not be appropriate for test 2. Indeed, when the standard deviation, σ_u, is calculated for test 2 using linear finite-depth theory based on the peak period T_p, there is better agreement between theory and data. This is illustrated in Figure 5.4.

The values of $|\bar{u}|$ and σ_u initially increase landward in Figures 5.1 and 5.2, consistent with values based on the depth-averaged velocity, U, computed by Kobayashi and Karjadi (1996) using the finite-amplitude shallow-water equations. However, unlike the 1:16 slope data of Herrman *et al.* (1997), both $|\bar{u}|$ and σ_u decrease landward after a peak near the location of the terrace edge. The intense breaking at the bar crest in test 1 appears to have caused the sharp decrease of $|\bar{u}|$ and σ_u in Figure 5.1. In summary, Figures 5.1 and 5.2 indicate that the local application

100

of linear long-wave theory is a reasonable first approximation for $\bar{u}$ and σ_u in the shoaling and surf zones.

On the other hand, these figures generally indicate that the skewness and kurtosis (the third and fourth moments) are not well predicted by linear long-wave theory. The skewness, s_u, of the horizontal velocity, u, at the approximate mid-depth is always less than the skewness, s, of the free surface elevation, η. Also, s_u drops steeply at the point of intense breaking in test 1. Milder declines in s_u due to wave breaking were measured by Herrman $et\ al.$ (1997) in their tests 2 and 3. The comparison between s and s_u suggests that nonlinearity decreases downward from the free surface. The difference $(s - s_u)$ tends to fluctuate, with an average value on the order of 0.5. The measured values of s_u differ noticeably in the two tests. While s_u in test 1 seems to have been drastically affected by breaking at the terrace edge, the shoreward increase of s_u for test 2 is only slightly perturbed by breaking over the bar. The skewness, s_u, in the shoaling region for test 2 is small and slightly negative, which implies that the cross-shore velocities are skewed somewhat seaward.

The kurtosis, K_u, of the mid-depth horizontal velocity, u, is generally over-predicted by the kurtosis, K, of the free surface elevation, η, in both tests 1 and 2. For test 1, the largest differences between the data and the linear theory occur in the shoaling zone in deeper water. In the surf zone, kurtosis values show greater variability for test 1, again reflecting the intense breaking that took place in that test. For test 2, K_u is less than K at all locations, with only a small shift in values to mark the surf zone. Both tests here indicate closer agreement than the kurtosis comparison by Herrman $et\ al.$ (1997).

The values plotted in Figures 5.1 and 5.2 are also listed in Tables 5.1 and 5.2, where x_u and z_u are the horizontal and vertical coordinates of the ADV probe. The coordinate system used herein has been defined in Figure 3.2.

Table 5.1: Velocity Data for Test 1

Run	z_b (cm)	x_u (m)	z_u (cm)	$\overline{u}$ (cm/s)		σ_u (cm/s)		Skewness		Kurtosis	
				Data	Theory	Data	Theory	s_u	s_η	K_u	K_η
1-1	-58.1	2.85	-0.18	-2.33	-1.59	19.46	19.26	0.42	0.82	3.22	4.14
1-2	-56.4	3.35	-0.18	-1.94	-1.65	19.36	19.41	0.41	0.82	3.38	4.14
1-3	-55.5	3.85	-0.18	-1.58	-1.77	19.04	19.95	0.43	0.94	3.34	4.65
1-4	-52.8	4.35	-0.18	-1.41	-1.89	19.21	20.33	0.46	0.92	3.23	4.52
1-5	-50.1	4.85	-0.18	-1.56	-2.03	19.76	20.85	0.44	0.97	3.23	4.52
1-6	-47.2	5.35	-0.18	-1.64	-2.19	20.26	21.44	0.50	0.92	3.24	4.47
1-7	-42.6	5.85	-0.18	-1.48	-2.53	21.21	22.45	0.53	0.87	3.27	4.18
1-8	-37.5	6.35	-0.18	-2.13	-3.20	22.35	24.34	0.45	0.89	3.07	4.34
1-9	-31.7	6.85	-0.16	-3.48	-4.32	23.69	27.05	0.38	0.91	3.18	4.31
1-10	-23.6	7.35	-0.12	-4.06	-7.01	27.75	31.93	0.29	0.76	3.40	3.88
1-11	-23.6	7.35	-0.15	-4.62	-7.05	26.94	32.14	0.23	0.77	3.40	3.86
1-12	-23.6	7.35	-0.18	-4.84	-7.10	25.91	32.21	0.27	0.77	3.38	3.87
1-13	-21.3	7.85	-0.14	-9.75	-9.08	34.43	35.55	-0.06	0.88	3.25	4.04
1-14	-23.1	8.35	-0.14	-9.44	-6.90	31.53	31.23	0.48	0.86	3.91	3.98
1-15	-23.1	8.85	-0.14	-8.22	-5.83	24.64	28.68	0.40	0.97	3.46	4.10
1-16	-21.4	9.35	-0.14	-8.78	-5.42	23.62	27.18	0.50	1.00	3.80	4.12
1-17	-20.7	9.85	-0.08	-5.99	-4.76	25.19	25.41	0.62	0.87	4.24	3.67
1-18	-20.7	9.85	-0.14	-8.34	-4.73	23.34	25.36	0.23	0.86	3.95	3.50
1-19	-20.7	9.85	-0.19	-7.14	-4.86	23.50	25.62	0.38	0.88	3.24	3.59
1-20	-18.3	10.35	-0.14	-7.74	-5.41	21.94	26.32	0.29	0.86	3.26	3.35
1-21	-15.5	10.85	-0.14	-6.80	-6.50	23.84	27.82	0.19	0.89	3.02	3.64

Table 5.2: Velocity Data for Test 2

Run	z_b (cm)	x_u (m)	z_u (cm)	$\overline{u}$ (cm/s)		σ_u (cm/s)		Skewness		Kurtosis	
				Data	Theory	Data	Theory	s_u	s_η	K_u	K_η
2-1	-56.9	2.85	-0.18	-2.10	-1.43	15.21	18.39	-0.13	0.23	2.64	2.95
2-2	-54.0	3.35	-0.18	-2.12	-1.53	15.13	18.76	-0.14	0.24	2.69	2.93
2-3	-51.5	3.85	-0.18	-1.83	-1.52	15.03	18.49	-0.14	0.31	2.68	3.01
2-4	-48.0	4.35	-0.18	-2.14	-1.75	15.25	19.50	-0.14	0.37	2.70	3.04
2-5	-44.0	4.85	-0.18	-1.81	-1.99	15.68	20.30	-0.11	0.43	2.72	3.09
2-6	-38.3	5.35	-0.18	-2.16	-2.45	16.34	21.76	-0.07	0.47	2.65	3.16
2-7	-31.3	5.85	-0.18	-2.76	-3.29	17.43	23.99	-0.05	0.52	2.63	3.26
2-8	-25.6	6.35	-0.18	-3.01	-4.43	19.26	26.42	-0.04	0.60	2.61	3.39
2-9	-22.2	6.85	-0.16	-3.72	-5.54	20.53	28.49	0.02	0.75	2.54	3.55
2-10	-23.6	7.35	-0.12	-5.75	-4.20	21.23	25.26	0.20	0.95	2.89	3.75
2-11	-23.6	7.35	-0.15	-5.15	-4.32	21.15	25.63	0.06	0.91	3.01	3.58
2-12	-23.6	7.35	-0.18	-3.40	-4.37	21.31	25.76	0.10	0.89	3.01	3.65
2-13	-24.5	7.85	-0.14	-5.93	-3.44	17.71	23.10	0.28	1.02	2.77	3.72
2-14	-24.5	8.35	-0.14	-6.22	-2.99	15.92	21.55	0.31	0.96	2.64	3.44
2-15	-23.4	8.85	-0.14	-5.64	-3.01	15.97	21.41	0.29	0.90	2.56	3.28
2-16	-21.8	9.35	-0.14	-5.26	-3.13	15.91	21.49	0.34	0.88	2.46	3.24
2-17	-19.9	9.85	-0.08	-3.16	-3.38	16.97	21.79	0.38	0.90	2.49	3.37
2-18	-19.9	9.85	-0.14	-4.56	-3.44	16.38	21.99	0.32	0.89	2.39	3.26
2-19	-19.9	9.85	-0.18	-4.01	-3.39	16.17	21.84	0.32	0.90	2.43	3.30
2-20	-18.3	10.35	-0.14	-3.27	——	16.55	——	0.34	——	2.45	——
2-21	-16.9	10.85	-0.14	-4.28	-3.90	17.13	22.52	0.41	0.96	2.50	3.58

5.3 Vertical Variations of Velocity Statistics at Two Cross-Shore Locations

Vertical profiles of the cross-shore velocity were taken at $x = 7.35$ m and 9.85 m to examine the variation of $\overline{u}$, σ_u, s_u, and K_u over depth. At $x = 7.35$ m velocity time series were recorded at elevations $z_u = $ -12, -15, and -18 cm below SWL for both tests. At $x = 9.85$ m data was taken at $z_u = $ -8, -14, and -19 cm below SWL for test 1 and $z_u = $ -8, -14, and -18 cm below SWL for test 2. These results have already been listed in Tables 5.1 and 5.2. In this section they will be presented graphically. Figures 5.5 and 5.6 show profiles of $\overline{u}$, σ_u, s_u, and K_u at the two locations for tests 1 and 2, respectively. The locations of these velocity profiles with respect to the equilibrium beach profiles may be viewed in Figure 5.3.

In general, the results indicate that the mean velocity and standard deviation remain relatively constant over the depth ranges measured. Measured undertow, $\overline{u}$, is within 20% of its middepth value for all profiles. The vertical variation of undertow $\overline{u}$ for irregular waves appears to be less than that for regular waves (Cox and Kobayashi 1997). Standard deviation, σ_u, remains within 5% of the value calculated at middepth for both tests.

Figures 5.5 and 5.6 also show relatively uniform values for the higher moments, s_u and K_u, over the depth. There is greater variability in these results at $x = 9.85$ m for test 1, however, which might be explained as a consequence of the intense wave breaking. Variability may also be due to instrument error in measuring the velocity, especially at the shallowest depth, $z_u = $ -8 cm. Except for this one position, skewness s_u varied less than 4 % from its middepth value, and kurtosis, K_u, remained within 3% of its middepth value in all other tests. The vertical profiles of cross-shore velocity and its moments are important in predicting the cross-shore sediment transport using the measured velocity at a single elevation, as will be discussed in Chapter 6.
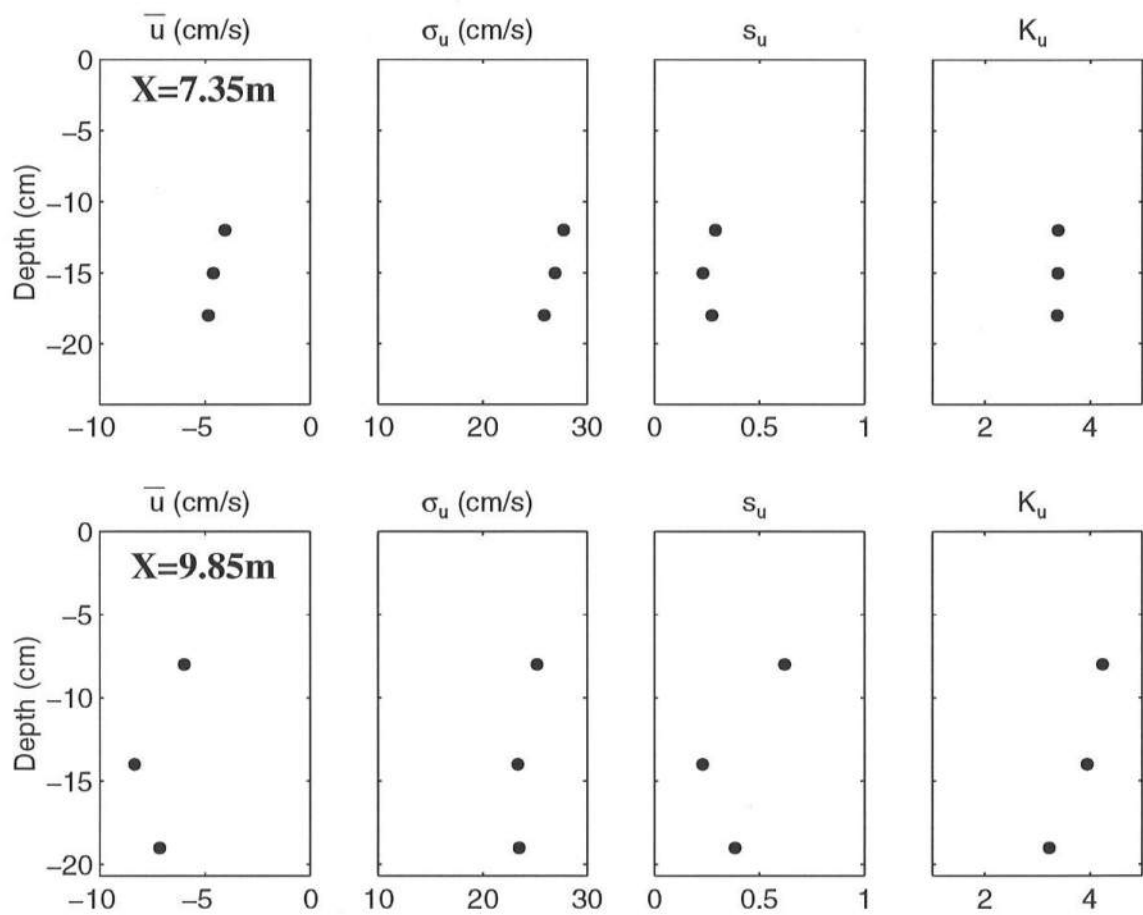
Figure 5.5: Velocity Profile Statistics for Test 1
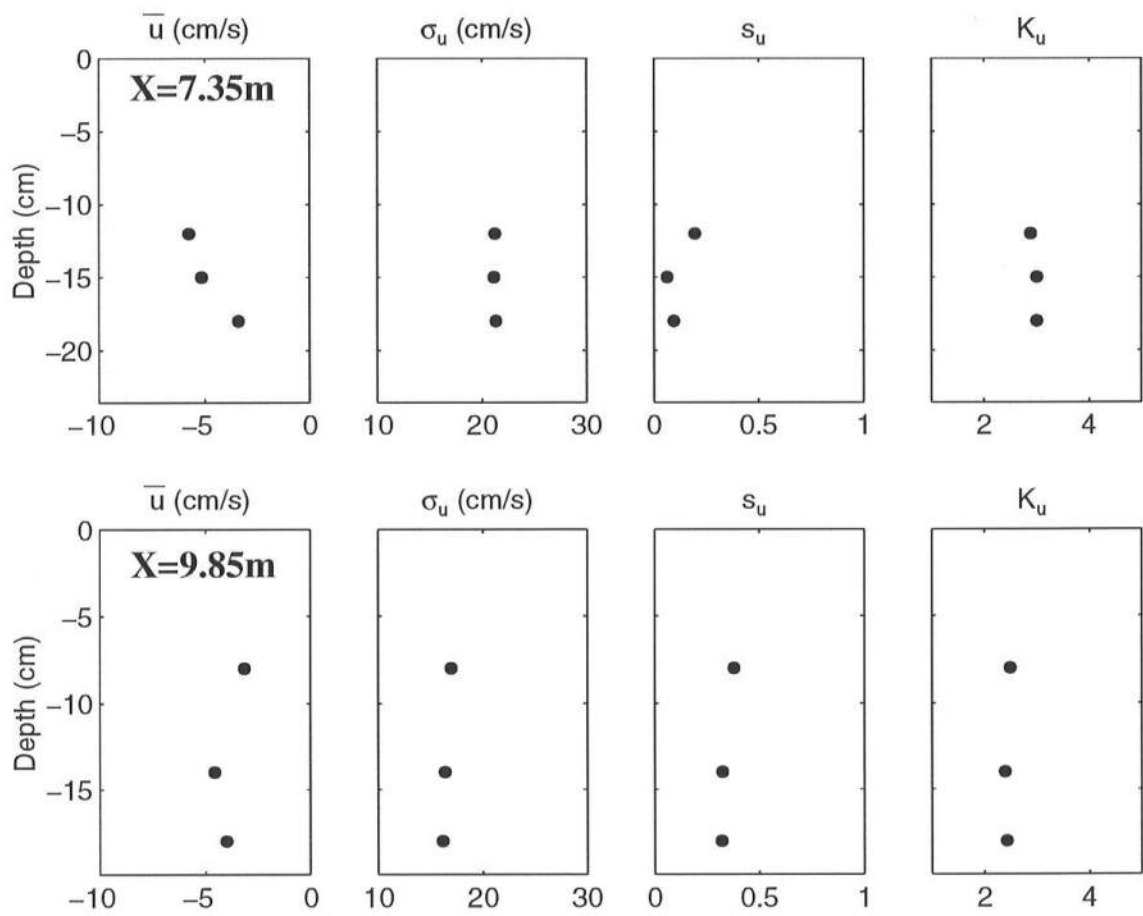
Figure 5.6: Velocity Profile Statistics for Test 2

5.4 Measured and Theoretical Probability Density Functions

In this section the measured probability density function, $f(u_*)$, is compared with the exponential gamma distribution based on the measured skewness, s_u. The agreement is good in test 1 except for slight deviations at the peaks of $f(u_*)$; these deviations are somewhat larger in the results for test 2. To show the degree of the overall agreement for tests 1 and 2 together, the combined measured distributions are separated into two groups on the basis of the measured skewness, s_u. Figure 5.7 shows the measured distributions with $s_u = (-0.14) - 0.29$ in comparison with the exponential gamma distributions with $s_u = 0$ and $s_u = 0.29$, where $s_u \geq 0$ must be assumed to be consistent with the assumption of $s \geq 0$ made in (2.1). Data falling outside the theoretical curves most often corresponded to values of $s_u \leq 0$. In the lower plot, the measured distributions with $s_u = 0.31 - 0.62$ are compared with the exponential gamma distributions with $s_u = 0.31$ and 0.62. These exponential gamma distributions deviate somewhat more within the specified range of s_u. Figure 5.7 indicates that most of the data points fall between these two theoretical curves, apart from the scatter near the peak of $f(u_*)$. The agreement is similar to those shown in Figures 4.4 and 4.5 for the free surface elevations. Lack of sufficient data precludes determining whether the exponential gamma distribution is applicable to horizontal velocities near the still water shoreline. For completeness, the full set of individual comparisons is shown in Section 5.6 in Figures 5.11 – 5.22.

5.5 Synchronization of Velocity and Free Surface Time Series

As depicted in Figure 3.2, the acoustic Doppler velocimeter (ADV) and wave gauge 5 were positioned at the same cross-shore location for each run of each test in order to measure simultaneous velocity and free surface time series at each point. Such a synchronization would enable the separation of incident and reflected waves in shallow water without using multiple wave gauges. Unfortunately, attempts at
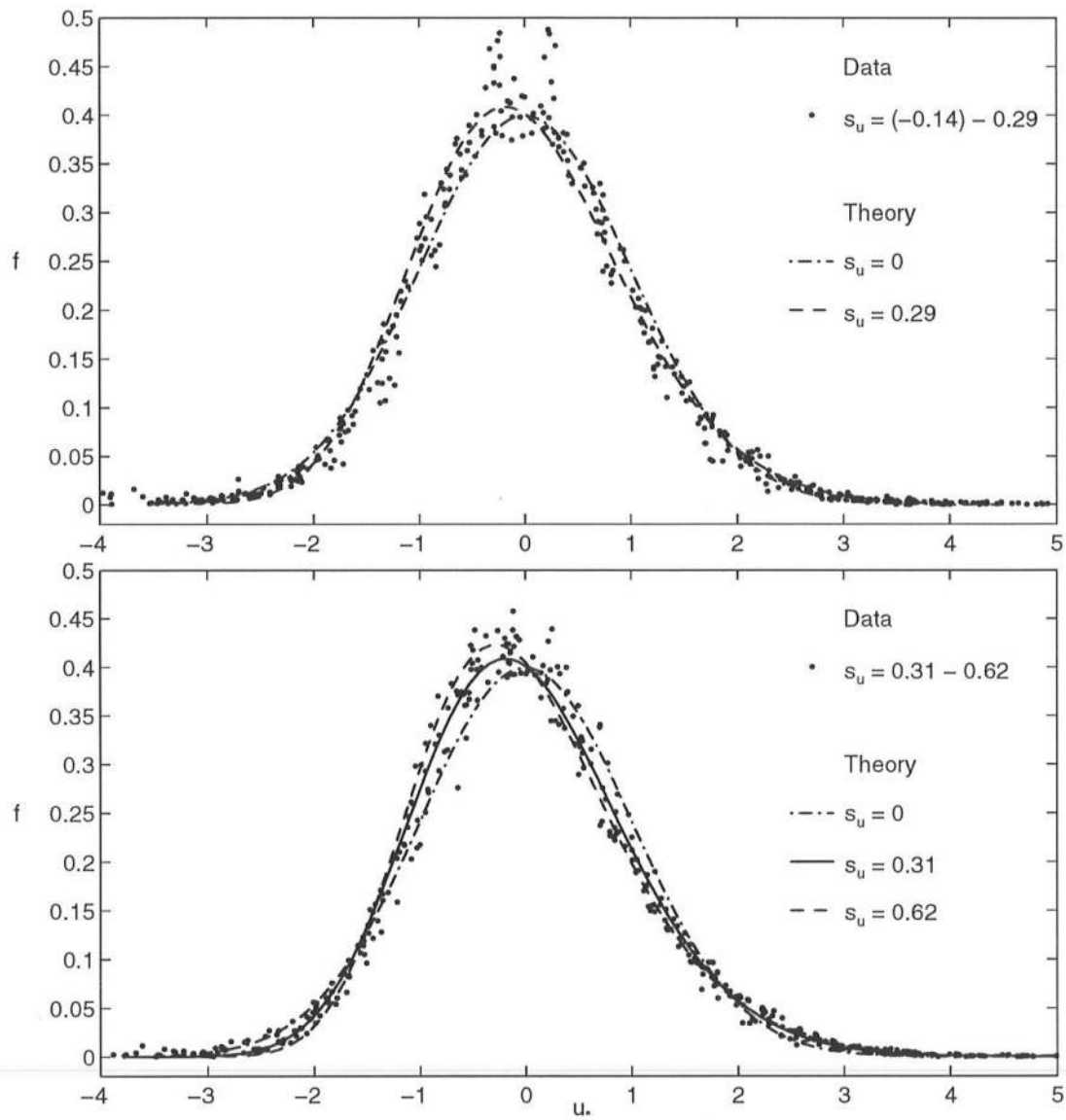
Figure 5.7: Measured and Computed Probability Distributions of Horizontal Velocities for Tests 1 and 2 in Two Separate Skewness Ranges

synchronization were ultimately unsuccessful. Proper synchronization was hampered by the need for two separate computers to run the ADV and the wave gauges. Different clock and program speeds on the two computers introduced slight phase shifts into the data so that after 400 s of testing, velocity and free surface time series that were initially synchronized had shifted by approximately 0.33 s. The development of such a phase shift is illustrated in Figure 5.8.

The figure shows the 400 s time series of the normalized free surface elevation, $\eta_* = (\eta - \bar{\eta})/\sigma$, and the normalized cross-shore velocity $u_* = (u - \bar{u})/\sigma_u$, for the first run of test 1 in three segments, where $\bar{\eta}$, σ, $\bar{u}$, and σ_u are the measured values for this run. The first 25 s of both time series are presented in expanded form in the top panel to illustrate the close synchronization of the initial measurements. In the second panel, the next 325 s of the two time series are displayed in a compacted form. Careful examination of this panel reveals increasing evidence of the phase shift as one moves from left to right. The third and final panel displays the remaining 25 s of the time series in expanded form to show clearly the phase shift that has developed. Figure 5.9 shows a plot of the individual measurement points of u_* vs.those of η_* for the same run as above. The general trend of the data points follows the line $u_* = \eta_*$, corresponding to equation (5.1) based on local linear progressive long-wave theory.

It was initially suspected that the phase shift may have been due primarily to the effects of reflected waves. However, more careful testing revealed the computer speeds to be almost entirely responsible for the time series difference. A more accurate measure of the phase shift was obtained by running the ADV and wave gauge data programs simultaneously for 3 hours. After this time the ADV computer time reading was lagging behind that of the wave gauge computer by 9 seconds. The phase shift rate implied by this time difference, 0.33 s per 400 s, was used to adjust time series of η_*, as illustrated in Figure 5.8; given this adjustment, very close
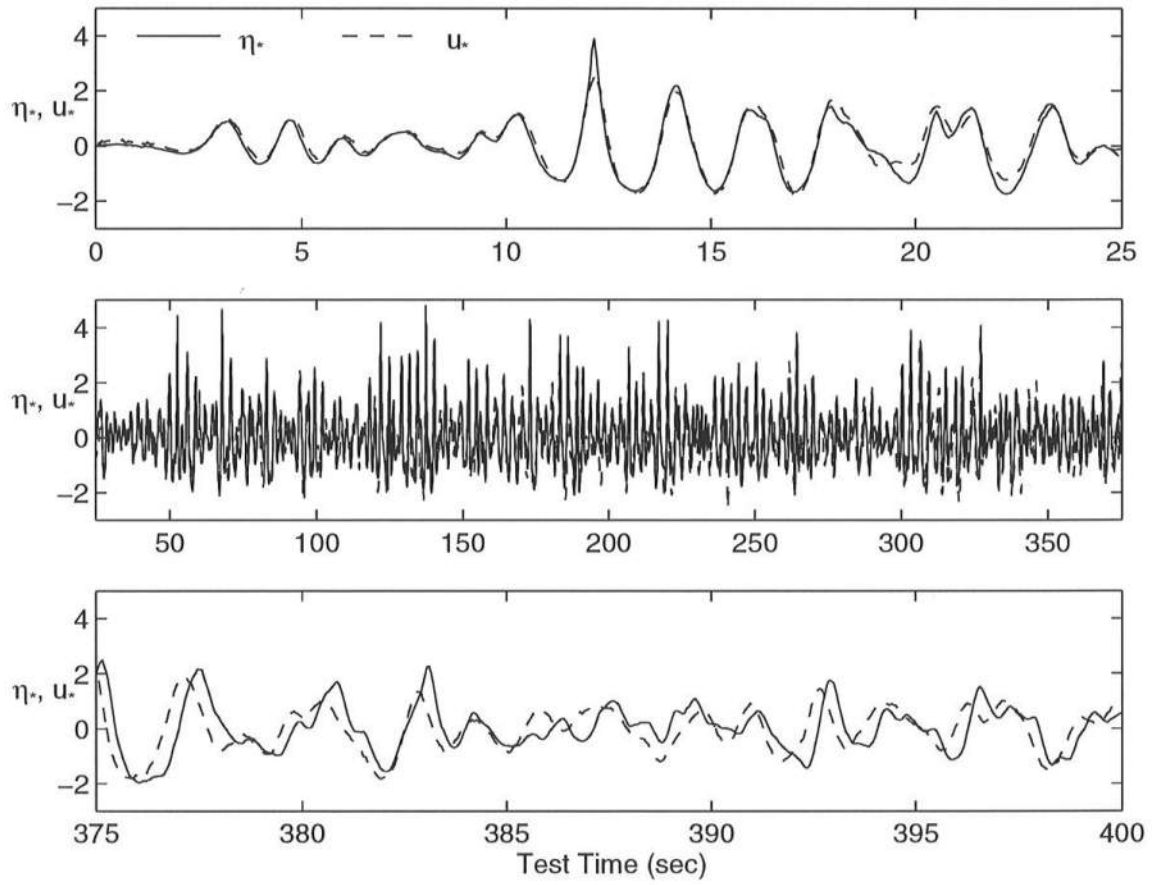
Figure 5.8: Uncorrected Simultaneous Time Series of Normalized Free Surface, η_*, and Normalized Velocity, u_*, Run 1 of Test 1
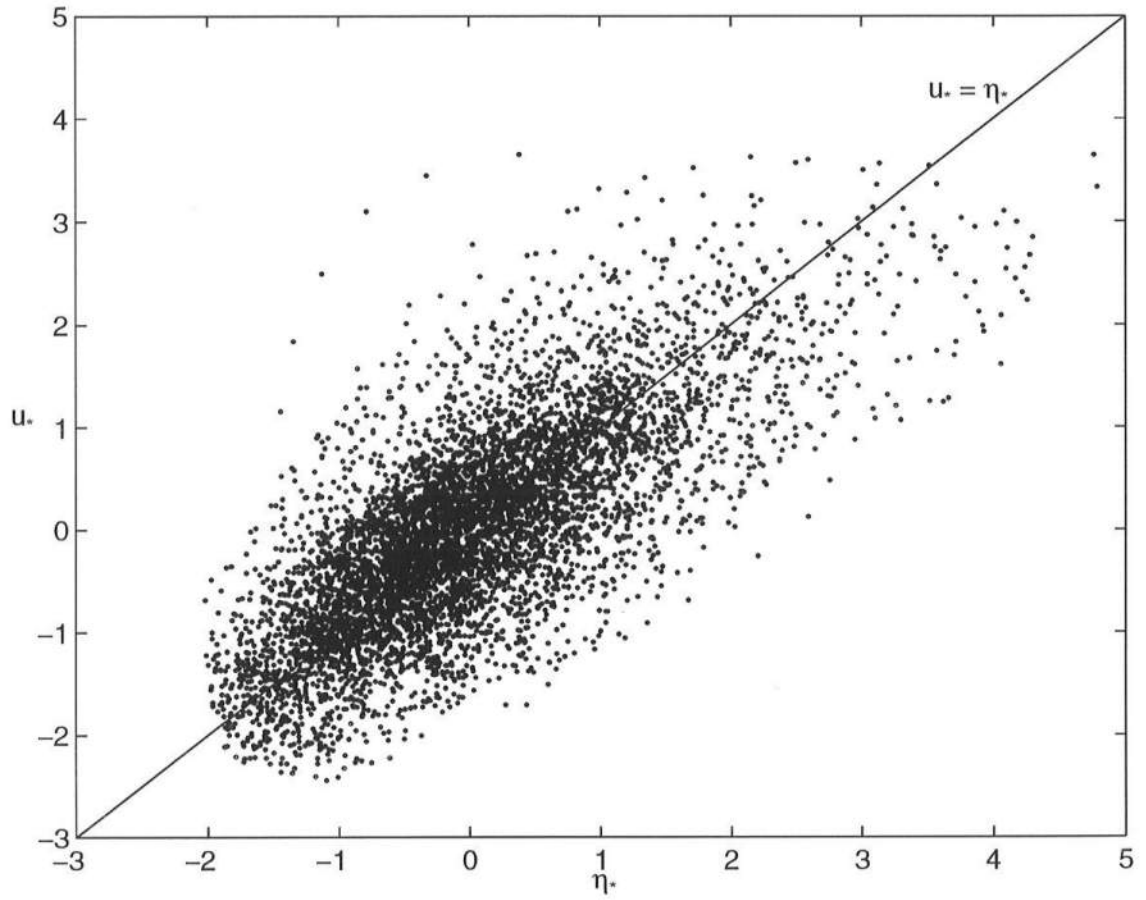
Figure 5.9: Comparison of Uncorrected Normalized Velocity, u_*, and Normalized Free Surface, η_*, Run 1 of Test 1 (Solid line indicates $u_* = \eta_*$)

sychronicity of the time series was obtained. The corrected version of the above time series of η_* is replotted with the original time series of u_* in Figure 5.10. The final 25 s of the time series still do not show a perfect match between u_* and η_*. These additional irregularities are most likely due to the reflected waves which had reached the gauge position by that time but were not present for the initial 25 s of measurements.

It would be possible to correct the actual time series data using the phase shift determined above. This would require the use of a point-by-point interpolation program to shift each of the 8000 points of the η_* or u_* time series by the appropriate amount, based on its location in the series. However, the validity of such an adjustment would be questionable. It might not be possible to verify the accuracy of the estimated 0.33 s shift, and any errors in this measurement would propagate through the analysis. For these reasons it was decided not to continue with efforts to synchronize the free surface and velocity time series.
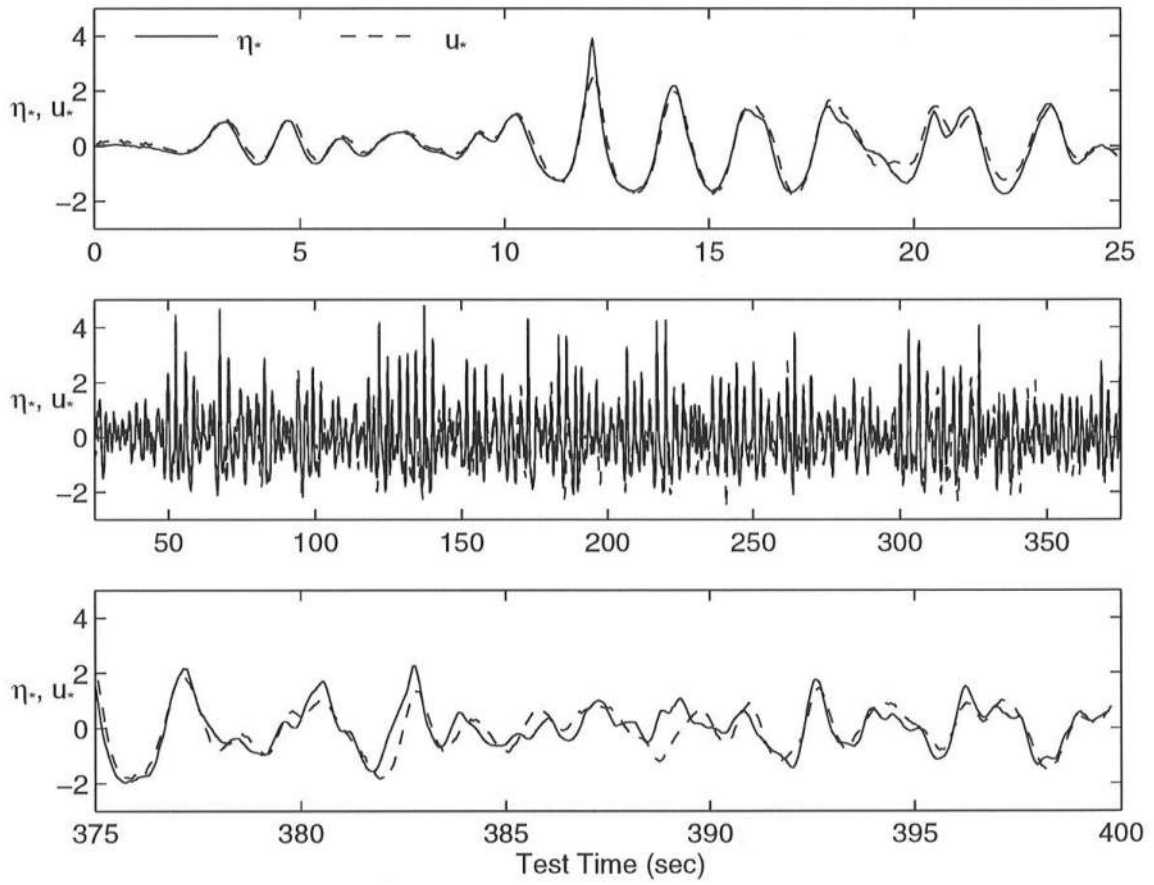
Figure 5.10: Corrected Simultaneous Time Series of Normalized Free Surface, η_*, and Normalized Velocity, u_*, Run 1 of Test 1

113

5.6 Measured and Computed Probability Distributions for Horizontal Velocity

In Figures 5.11 – 5.22 the probability distributions of the horizontal velocity are compared with the distributions computed from the exponential gamma distribution at each of the 21 velocity measurement locations for tests 1 and 2. Note that three separate distributions corresponding to different elevations are shown for the locations $x = 7.35$ m and $x = 9.85$ m, where velocity profiles were measured. The probe coordinates, x_u and z_u, used in Tables 5.1 and 5.2 are indicated as xu and zu in each diagram.
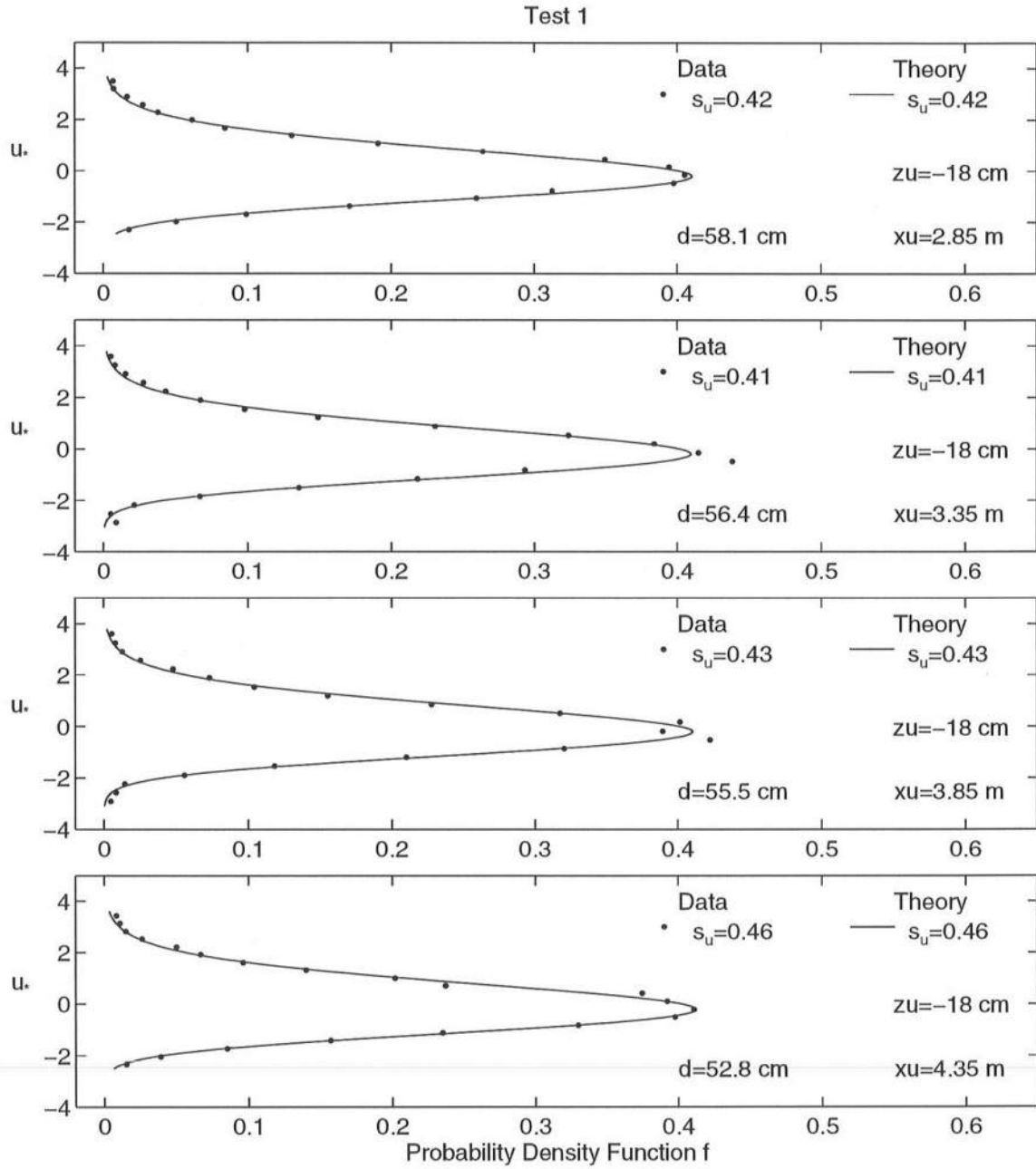
Figure 5.11: Measured and Computed Probability Distributions for Horizontal Velocity at Positions $x = 2.85$, 3.35, 3.85, and 4.35 m for Test 1

115
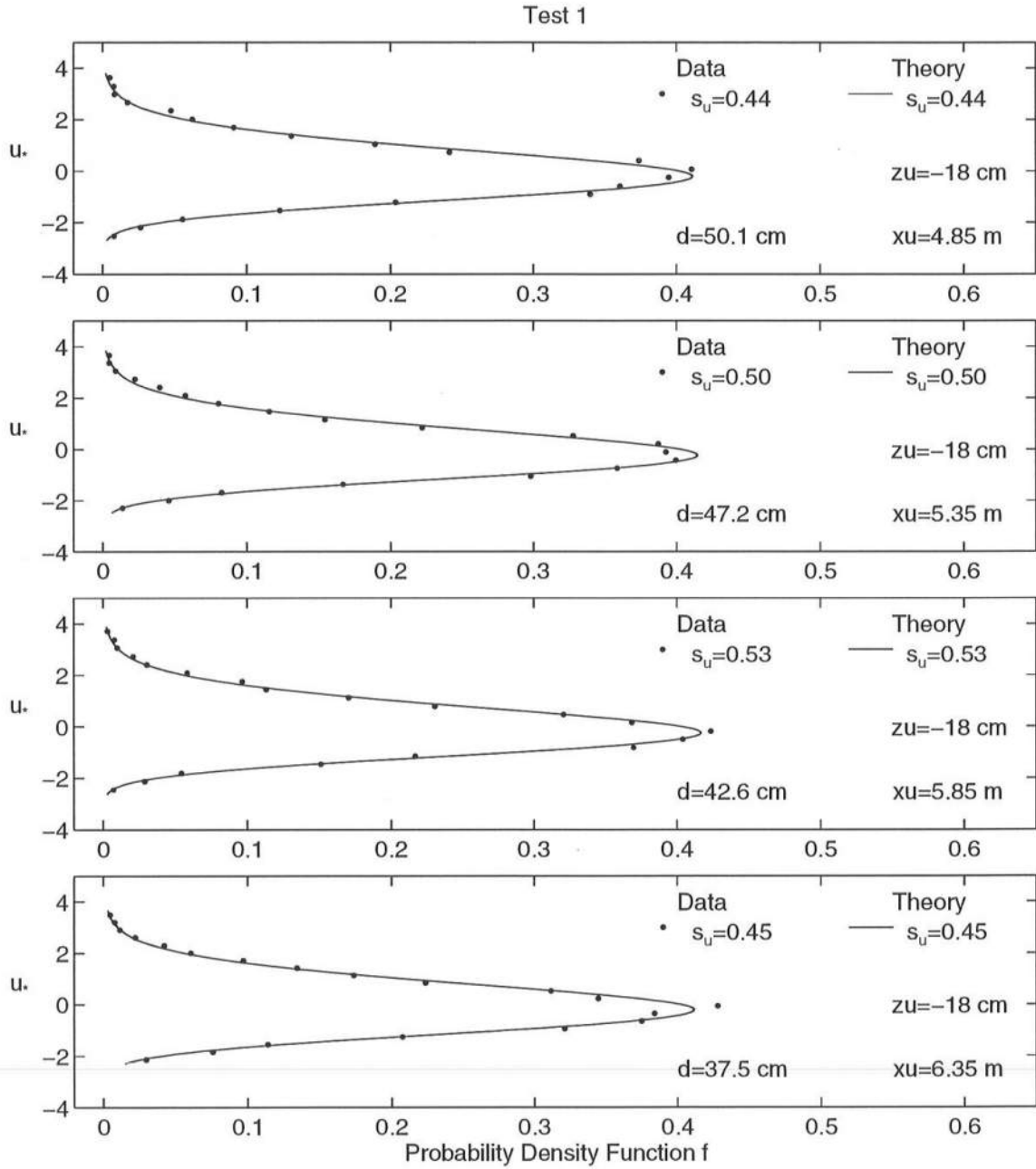
Figure 5.12: Measured and Computed Probability Distributions for Horizontal Velocity at Positions $x = 4.85$, 5.35, 5.85, and 6.35 m for Test 1

116
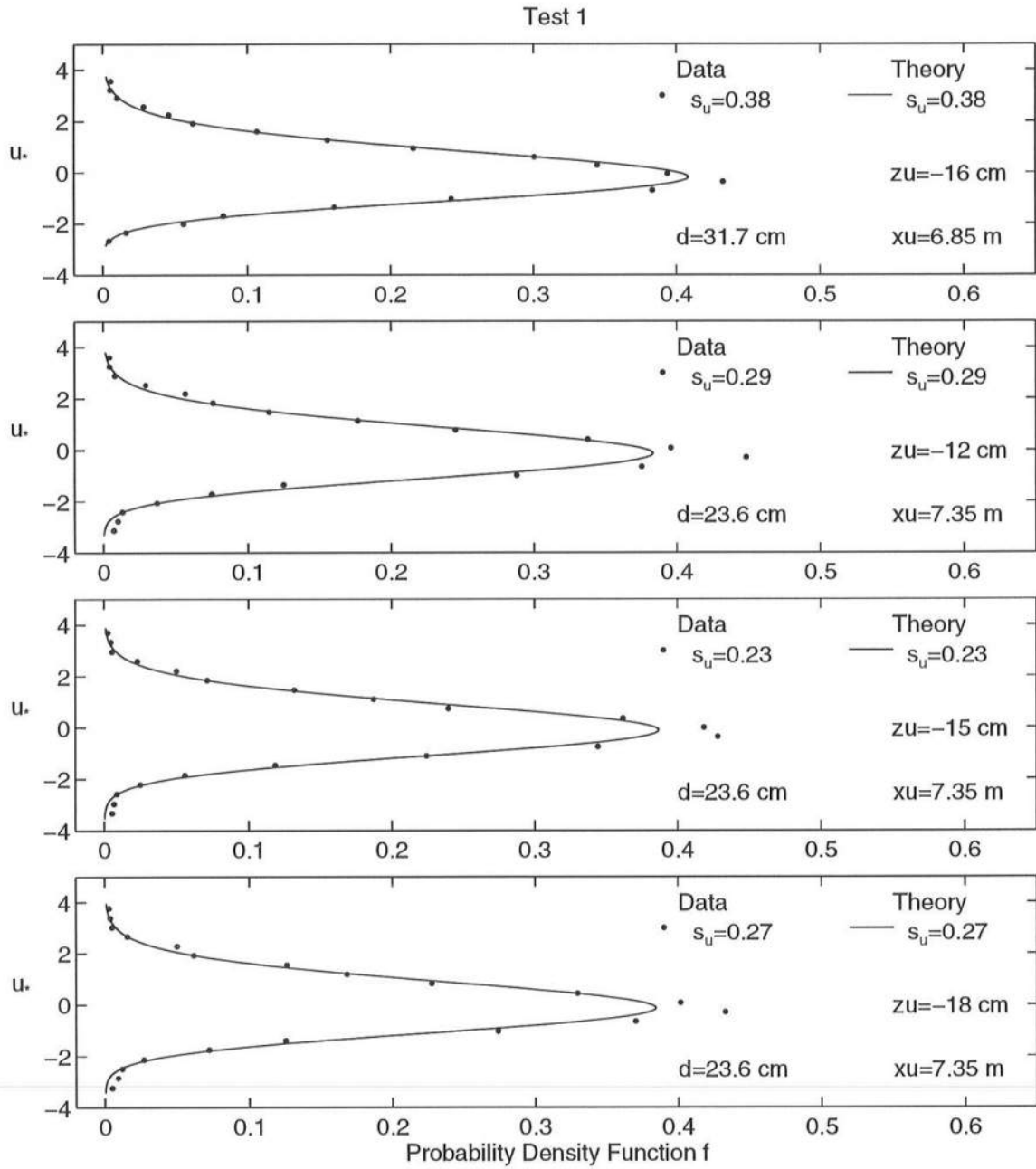
Figure 5.13: Measured and Computed Probability Distributions for Horizontal Velocity at Positions $x = 6.85$ and 7.35 m for Test 1 (Measurements Repeated Due to Three-Point Velocity Profile at 7.35 m)
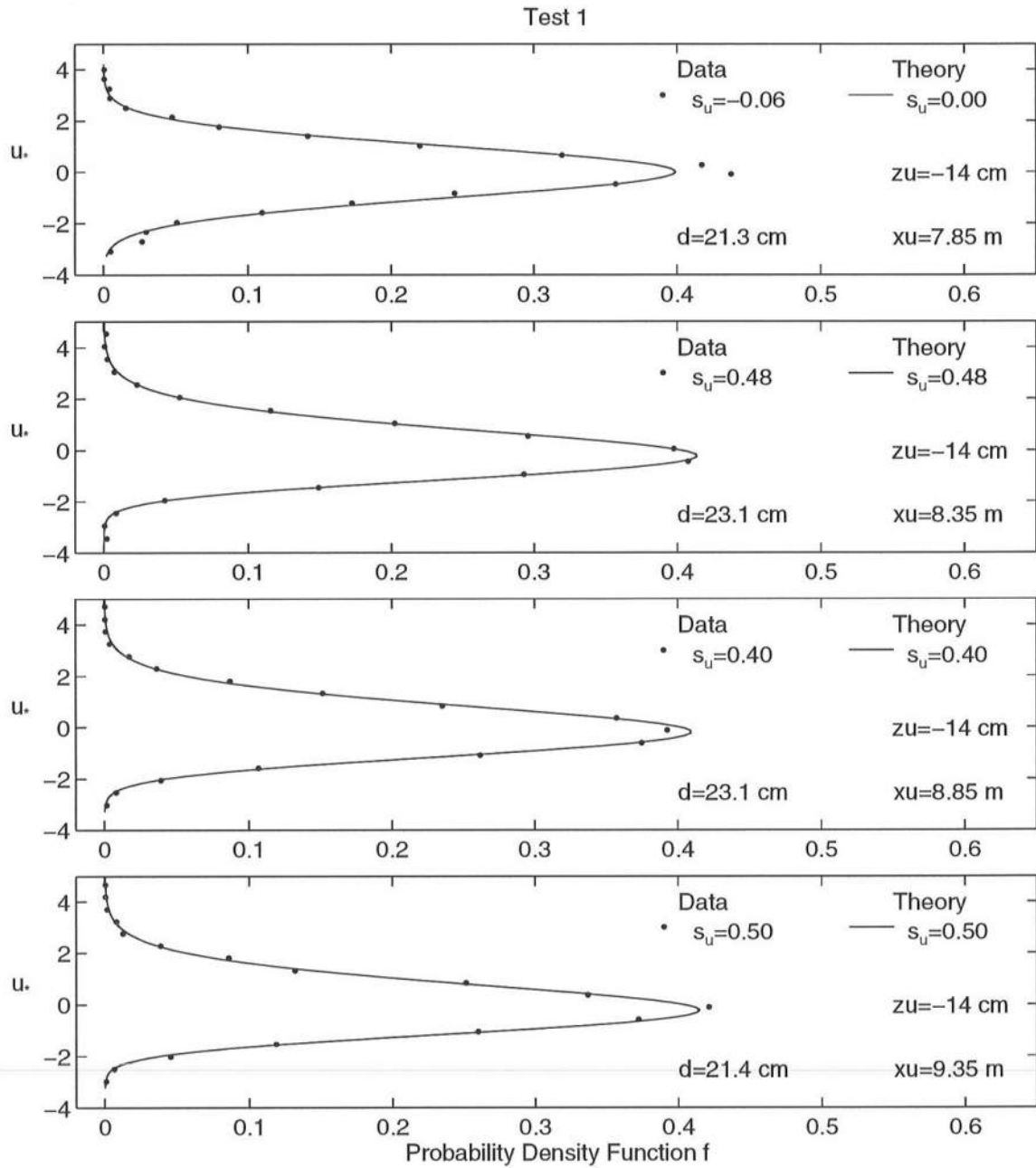
Figure 5.14: Measured and Computed Probability Distributions for Horizontal Velocity at Positions $x = 7.85$, 8.35, 8.85, and 9.35 m for Test 1

118
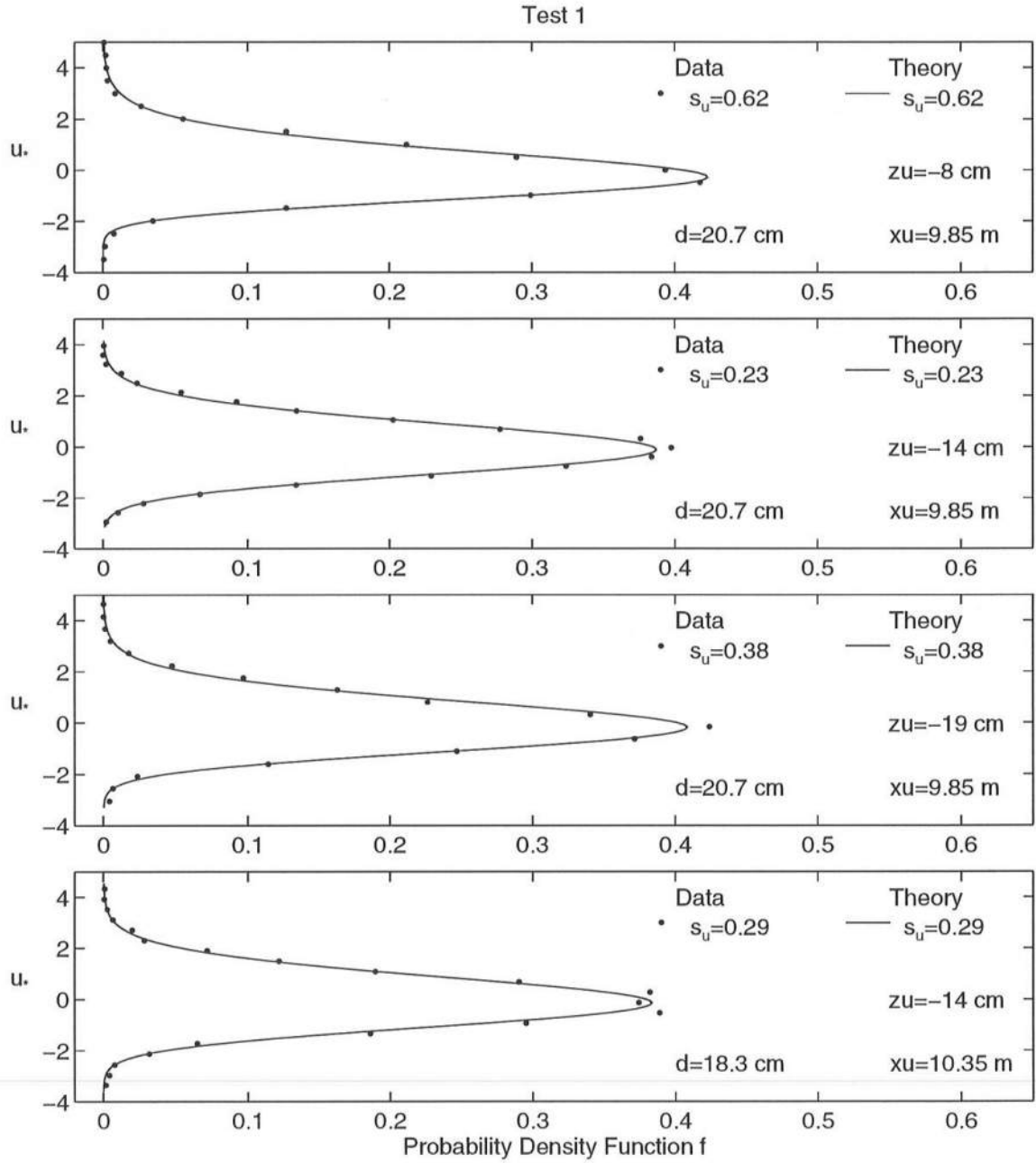
Figure 5.15: Measured and Computed Probability Distributions for Horizontal Velocity at Positions $x = 9.85$ and 10.35 m for Test 1 (Measurements Repeated Due to Three-Point Velocity Profile at 9.85 m)

119
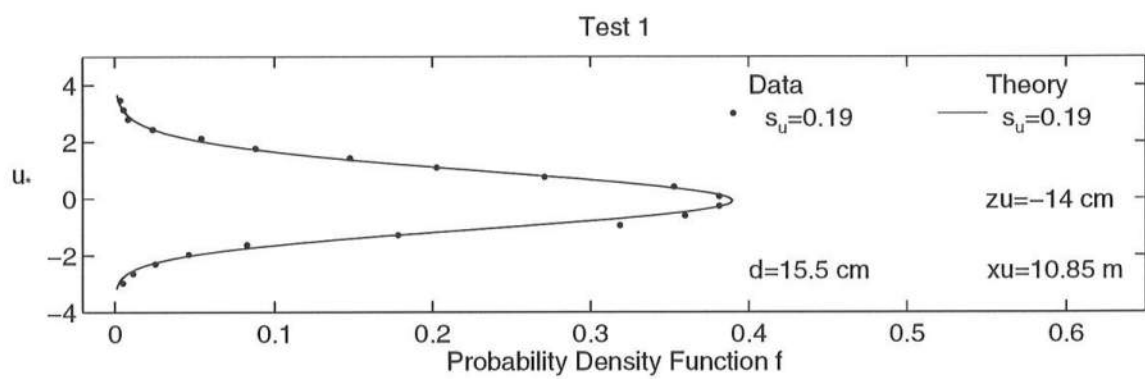
Figure 5.16: Measured and Computed Probability Distributions for Horizontal Velocity at Position $x = 10.85$ m for Test 1
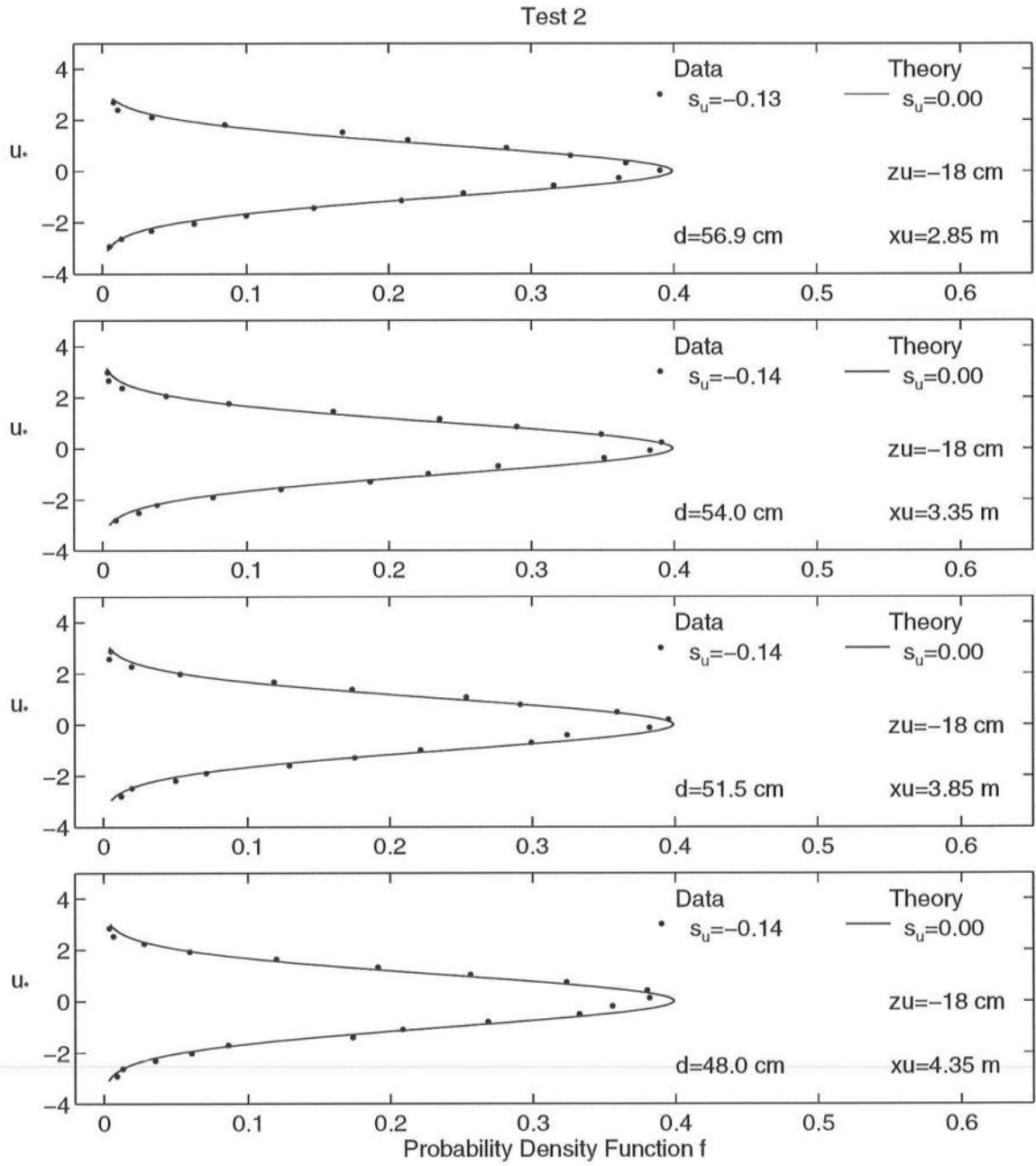
Figure 5.17: Measured and Computed Probability Distributions for Horizontal Velocity at Positions $x = 2.85$, 3.35, 3.85, and 4.35 m for Test 2
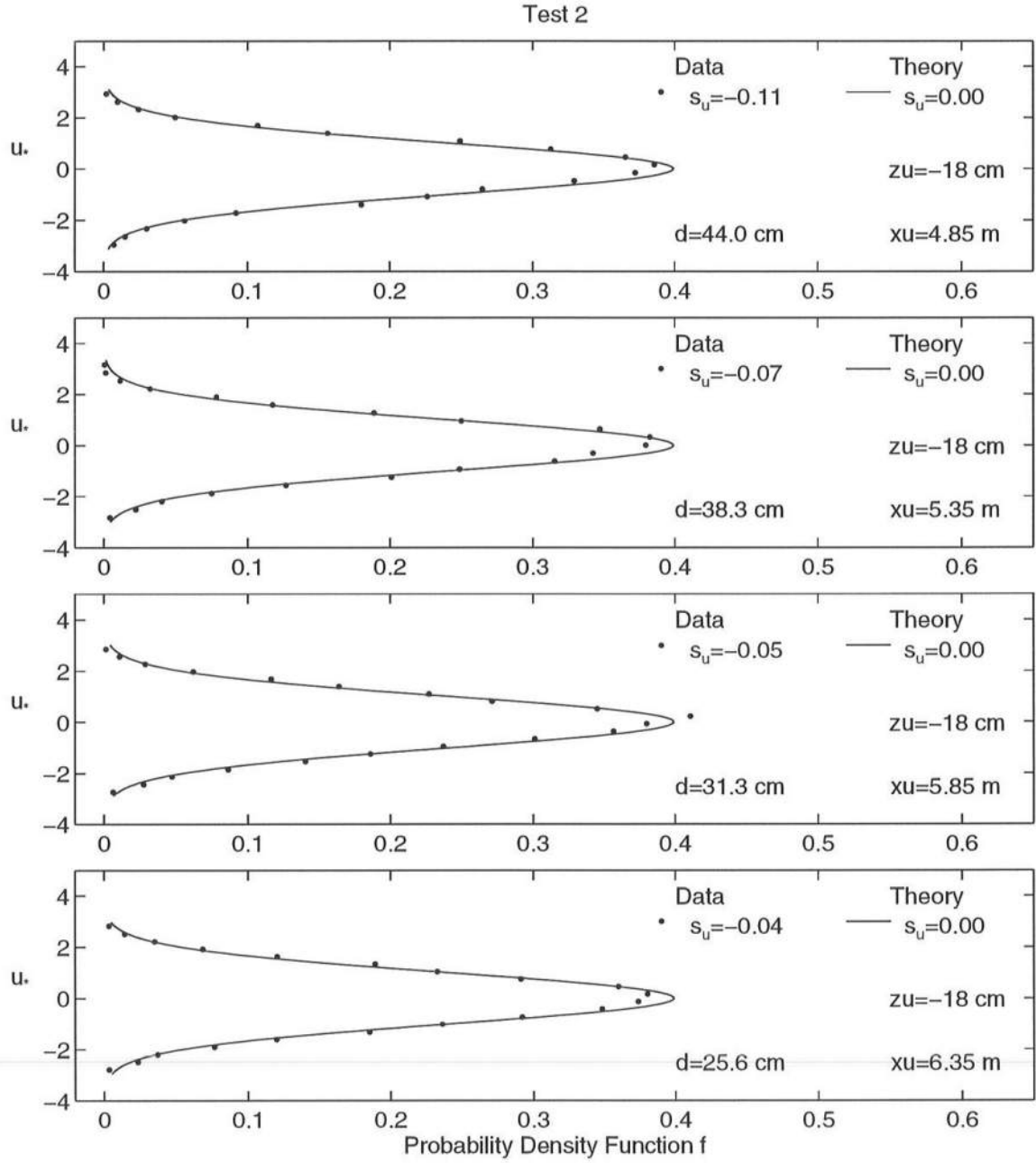
Figure 5.18: Measured and Computed Probability Distributions for Horizontal Velocity at Positions $x = 4.85$, 5.35, 5.85, and 6.35 m for Test 2
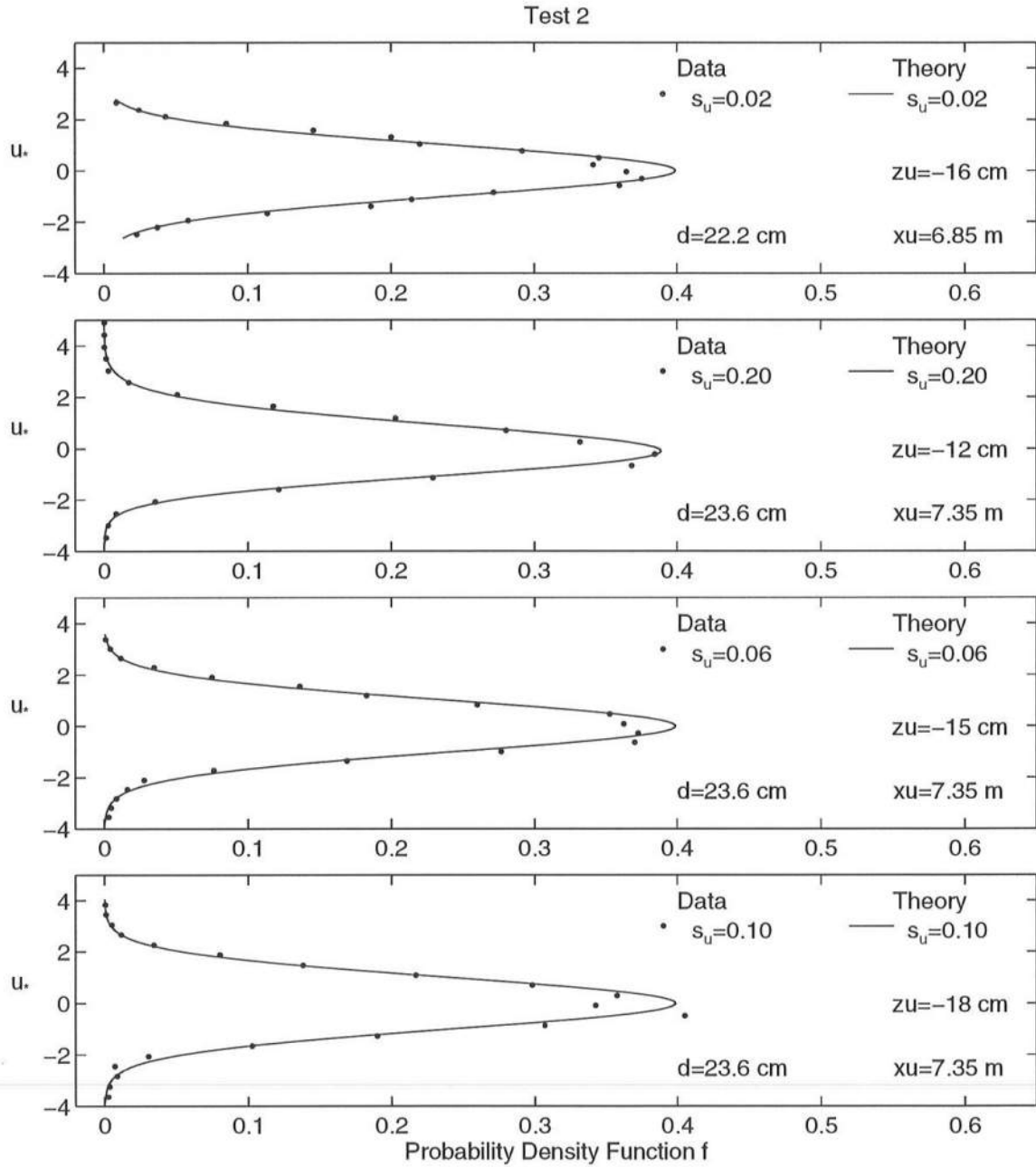
Figure 5.19: Measured and Computed Probability Distributions for Horizontal Velocity at Positions $x = 6.85$ and 7.35 m for Test 2 (Measurements Repeated Due to Three-Point Velocity Profile at 7.35 m)

123
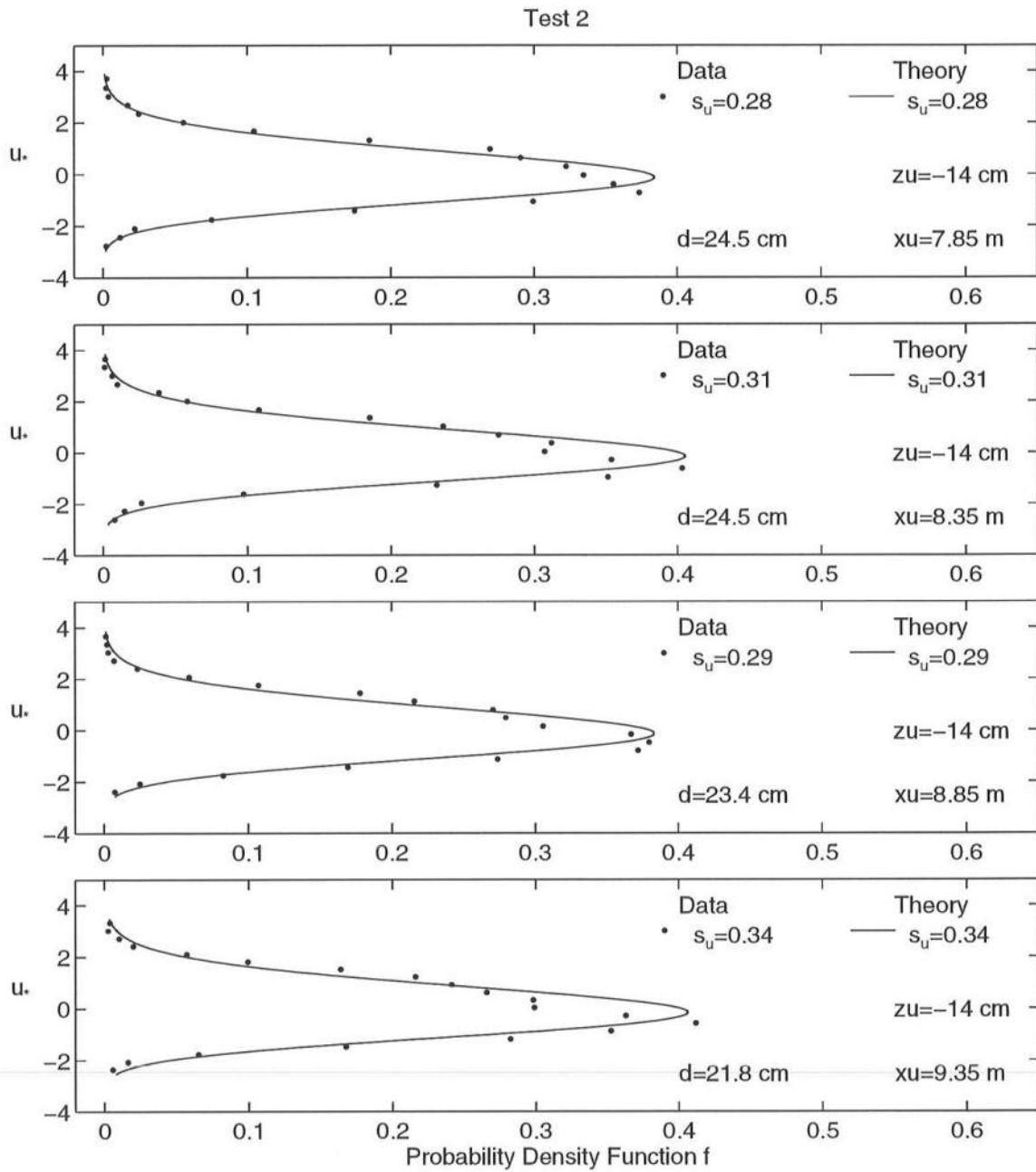
Figure 5.20: Measured and Computed Probability Distributions for Horizontal Velocity at Positions $x = 7.85$, 8.35, 8.85, and 9.35 m for Test 2
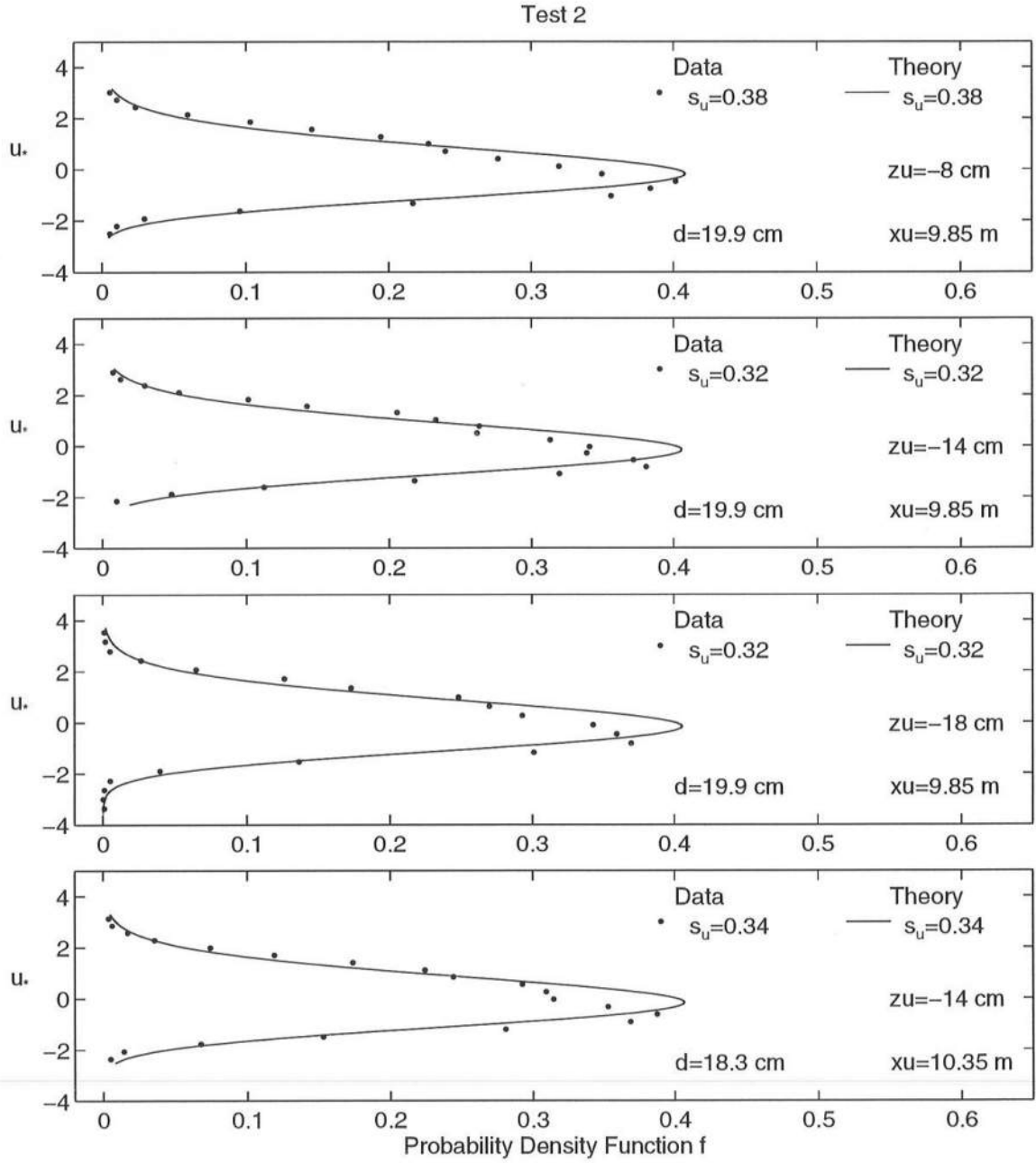
Figure 5.21: Measured and Computed Probability Distributions for Horizontal Velocity at Positions $x = 9.85$ and 10.35m for Test 2 (Measurements Repeated Due to Three-Point Velocity Profile at 9.85 m)
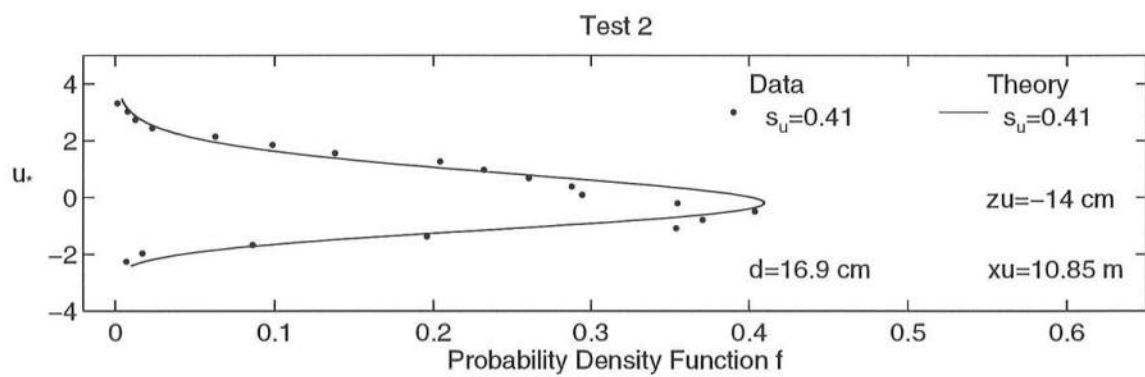
Figure 5.22: Measured and Computed Probability Distributions for Horizontal Velocity at Position $x = 10.85$ m for Test 2

Chapter 6

CROSS-SHORE SEDIMENT TRANSPORT

As mentioned in Chapter 1, perturbations of equilibrium profiles have been observed in the field and the laboratory, but the processes involved in the formation of these perturbed beach profiles are still poorly understood. This chapter will examine the sediment transport models based on the sheet flow approach [Trowbridge and Young (1989)] and the energetics approach [Bowen (1980); Bailard (1981)]. After a summary of theoretical background, the necessary parameters for each model will be calculated using the data from tests 1 and 2. It will be shown that the energetics-based model predicts the equilibrium profile better than the sheet flow model for both tests. Both models overpredict the rate of change of bottom elevation, $\partial z_b / \partial t$, in the region of the bar crest for test 1, but the energetics model predictions are within 1 cm/hr at all locations for test 2. The shortcomings of these two approaches will be used to explore the reasons why existing models cannot predict zero net sediment transport rate on these equilibrium profiles.

6.1 Sheet Flow Model for Onshore Bar Movement

The sheet flow model, developed by Trowbridge and Young (1989), is presently the only model available that attempts to explain onshore bar movement outside the surf zone. For the profiles measured in this study, there may be some regions where the sheet flow model does not apply. While this model is generally limited to smooth beds without ripples, the profiles obtained in these experiments did include

127

rippled sand beds in the offshore and surf zones for both tests. However, both pro-
files were free of ripples in the region over the bar. Hence, it is likely that at least
quasi-sheet flow conditions were achieved in the regions of intense wave breaking.
Consequently, the following comparison will indicate whether this sheet flow model
is applicable in the rippled region outside the surf zone as well as in the sheet flow
and rippled regions inside the surf zone.

6.1.1 Theory

The measured cross-shore velocity is represented here by $u(t)$, and the time-
averaged cross-shore velocity or undertow is represented by $\bar{u}$. The instantaneous
rate of onshore sediment transport, $q(t)$, is assumed to be expressible as

$$\frac{q(t)}{wd} = K \frac{\tau_b(t)}{\rho g d (s - 1)} \tag{6.1}$$

where w = fall velocity, d = diameter of uniform sediment which is taken as $d = d_{50}$,
ρ = density of fluid, $s = \rho_s / \rho$ = specific gravity of sediment with ρ_s = sediment
density, $\tau_b(t)$ = instantaneous bottom shear stress, g = gravitational acceleration,
and K = an empirical coefficient. The time-averaged cross-shore transport rate,
taken to be positive onshore, may thus be written as

$$\bar{q} = K \frac{w \overline{\tau_b}}{\rho g (s - 1)} \tag{6.2}$$

Trowbridge and Young (1989) analyzed the wave boundary layer and derived the
following expression for the mean bottom shear stress, $\overline{\tau_b}$:

$$\overline{\tau_b} = + \frac{\rho f_w}{2} \frac{\overline{|\tilde{u}|^3}}{\sqrt{g \bar{h}}} \tag{6.3}$$

where f_w = friction coefficient and $\tilde{u}$ = oscillatory part of first-order wave velocity
= $(u - \bar{u})$. As this expression only includes $|\tilde{u}|$, it does not explicitly account for
possible undertow, which was significant in the present experiment. Note that while

Trowbridge and Young defined the x-axis as positive offshore, the present analysis defines x as positive onshore. Substituting (6.3) into (6.2):

$$\overline{q}_u = \left(\frac{K f_w}{2}\right) \frac{w\overline{|\tilde{u}|^3}}{g(s-1)\sqrt{g\overline{h}}} \tag{6.4}$$

Trowbridge and Young calibrated the value of $K f_w$ for $d \simeq 0.2$ mm and recommended $K f_w = 0.5$. In the present experiment, $d_{50} = 0.18$ mm as explained in Section 3.1.1, and $K f_w = 0.5$ will be adopted as well. For sheet flow conditions, equation (6.4) may be used to predict the time-averaged cross-shore transport rate, $\overline{q}_u$, based on velocity data as indicated by the subscript u.

Trowbridge and Young used linear long wave theory to relate $\tilde{u}$ to $\tilde{\eta}$:

$$\tilde{u} = (u - \overline{u}) \simeq \sqrt{\frac{g}{h}}(\eta - \overline{\eta}) = \sqrt{\frac{g}{h}}\tilde{\eta} \tag{6.5}$$

with the assumption that $\tilde{\eta}$ is Gaussian. Since velocity data is available here, it will be assumed instead that $\tilde{u}$ is Gaussian and expressible as

$$\overline{|\tilde{u}|^3} \simeq \sqrt{\frac{8}{\pi}}(\overline{|\tilde{u}|^2})^{1.5} \tag{6.6}$$

This assumption is better than that of Trowbridge and Young because the skewness, s_u, of the velocity is generally smaller than the skewness, s, of the free surface. Equation (6.5) then implies

$$\overline{|\tilde{u}|^2} \simeq \frac{g}{h}\overline{|\tilde{\eta}|^2} \tag{6.7}$$

which can be rewritten as

$$\sigma_u^2 \simeq \frac{g}{h}\sigma^2 \tag{6.8}$$

Combining (6.6) and (6.7), one obtains

$$\overline{|\tilde{u}|^3} \simeq \sqrt{\frac{8}{\pi}}\left(\frac{g}{h}\overline{|\tilde{\eta}|^2}\right)^{1.5} = \sqrt{\frac{8}{\pi}}\frac{g}{h}\sqrt{\frac{g}{h}}(\overline{|\tilde{\eta}|^2})^{1.5} \tag{6.9}$$

This expression for $\overline{|\tilde{u}|^3}$ may be substituted into equation (6.4) to obtain, after some algebra:

$$\overline{q} = \sqrt{\frac{2}{\pi}}K f_w \frac{w(\overline{|\tilde{\eta}|^2})^{1.5}}{(s-1)\overline{h}^2} \tag{6.10}$$

Given $(\overline{|\tilde{\eta}|^2})^{1.5} = (\sigma^2)^{1.5} = \sigma^3$ and $\sigma = H_{\rm rms}/\sqrt{8}$, as in equation (2.8), one finally obtains

$$\bar{q}_\eta = \frac{K f_w}{16\sqrt{\pi}} \frac{w H_{\rm rms}}{(s-1)} \left(\frac{H_{\rm rms}}{\bar{h}}\right)^2 \tag{6.11}$$

Equation (6.11) may be used to predict the time-averaged cross-shore transport rate, $\bar{q}_\eta$, using free surface data as indicated by the subscript η.

An expression for the predicted rate of change of the sand bottom elevation may be derived by applying the conservation equation of sediment to a small sand volume of depth Δz_b, length Δx, and unit width. The increase in sand volume over time Δt is equal to the net influx of sand during that time:

$$(1 - n_p)\Delta z_b \Delta x = \left[\bar{q} - \left(\bar{q} + \frac{\partial \bar{q}}{\partial x}\Delta x\right)\right]\Delta t \tag{6.12}$$

In the limit as $\Delta t \to 0$, (6.12) may be rearranged to express the erosion (negative) or accretion (positive) rate $\partial z_b/\partial t$ in terms of the gradient of the cross-shore transport rate $\bar{q}$:

$$\frac{\partial z_b}{\partial t} = \frac{-1}{(1 - n_p)}\frac{\partial \bar{q}}{\partial x} \tag{6.13}$$

in which n_p = porosity. Equation (6.13) may be combined with equation (6.4) or (6.11) to determine the erosion/accretion rate based on velocity data or free surface data, respectively, where $(\partial z_b/\partial t)_u$ and $(\partial z_b/\partial t)_\eta$ are used for the computed values of $(\partial z_b/\partial t)$ corresponding to $\bar{q}_u$ and $\bar{q}_\eta$, respectively.

6.1.2 Analysis of Experimental Results

The velocity and free surface data from tests 1 and 2 are analyzed to obtain the quantities necessary for the evaluation of equations (6.4) and (6.11) at the 17 cross-shore locations at which velocity time series were measured. At the locations of the three point velocity profiles the time series from only the middle position are used; the vertical variations will be discussed in Section 6.2.2. This analysis uses the results of sand tests summarized in Section 3.1: $w = 1.9$ cm/s, $d = d_{50} = 0.18$ mm,
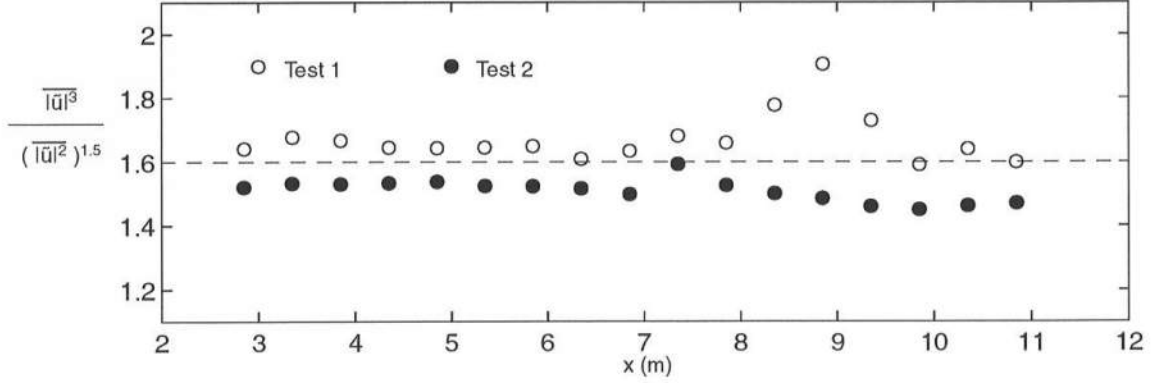
Figure 6.1: Ratio $(\overline{|\tilde{u}|^3})/(\overline{|\tilde{u}|^2})^{1.5}$ for Tests 1 and 2

$s = 2.66$, and $n_p = 0.4$. A cubic spline interpolation is performed on each set of $\overline{q}$ values to obtain the corresponding derivatives, $\partial \overline{q}/\partial x$. Equation (6.13) is then used to calculate $\partial z_b/\partial t$ at each location. The results of these calculations are displayed graphically in Figures 6.1 – 6.3 and summarized in Tables 6.1 and 6.2 at the end of this section.

Figure 6.1 provides a check on equation (6.6), which was based on the assumption that $\tilde{u}$ is Gaussian. This equation may be rewritten as

$$\frac{\overline{|\tilde{u}|^3}}{(\overline{|\tilde{u}|^2})^{1.5}} = \sqrt{\frac{8}{\pi}} \simeq 1.60 \tag{6.14}$$

Figure 6.1 shows that the ratio is indeed quite close to this Gaussian prediction for both tests at nearly all locations, with some minor deviation in test 1 in the region of broken waves.

As mentioned above, the preconditions of the sheet flow model may be satisfied over only part of these equilibrium profiles because of the ripples that were present. The sheet flow conditions occurred from about $x = 5$ m to $x = 9$ m.

Figures 6.2 and 6.3, along with Tables 6.1 and 6.2, predict large onshore transport rates and rapid profile change in the surf zone, especially for test 1. For perfectly equilibrium profiles, $\partial z_b/\partial t = 0$, but the measured equilibrium profiles for

131
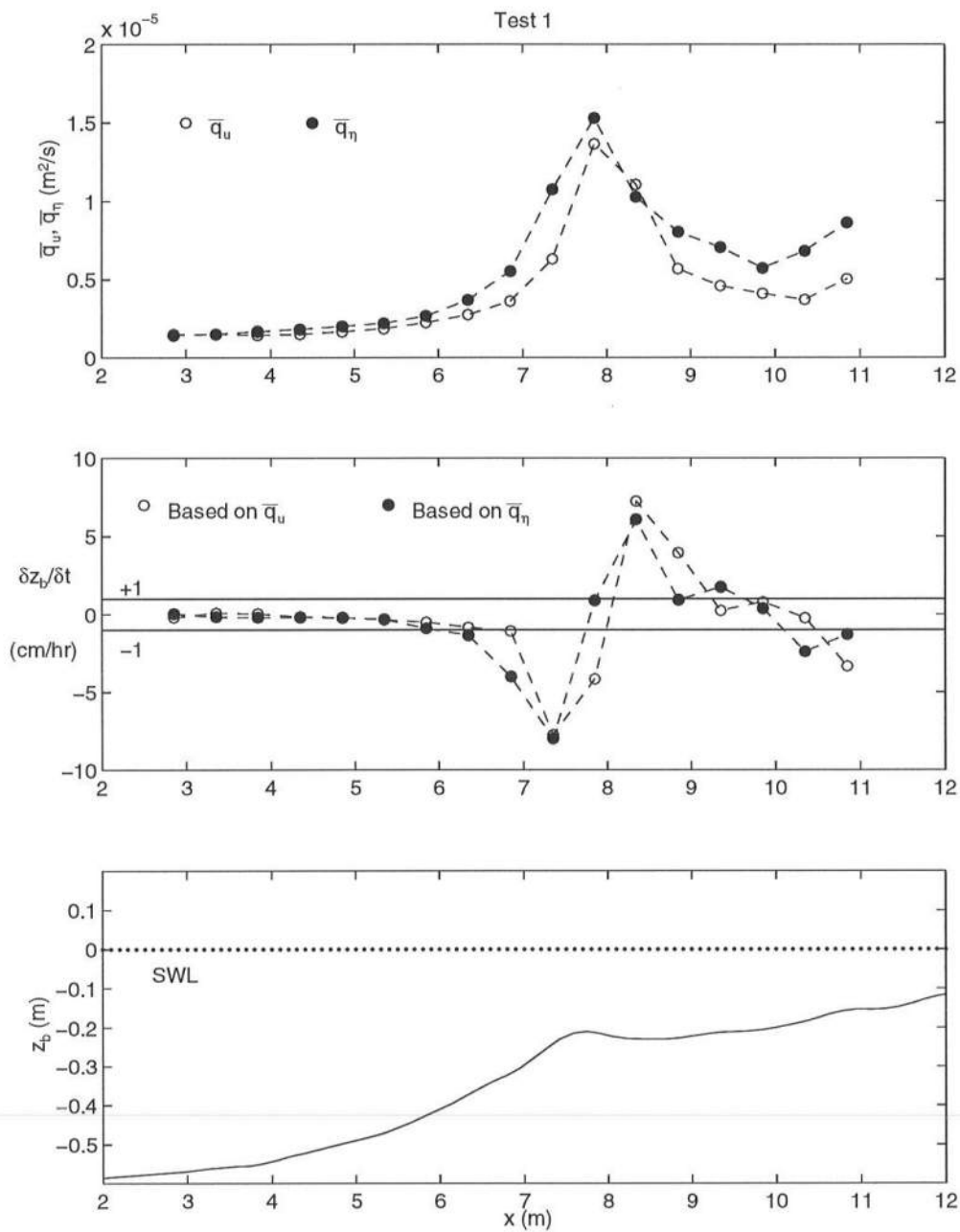
Figure 6.2: Net Transport Predictions $\overline{q}_u$, $\overline{q}_\eta$ and Bottom Elevation Change Rates $(\partial z_b/\partial t)_u$, $(\partial z_b/\partial t)_\eta$, Over Test 1 Profile (Sheet Flow Model)
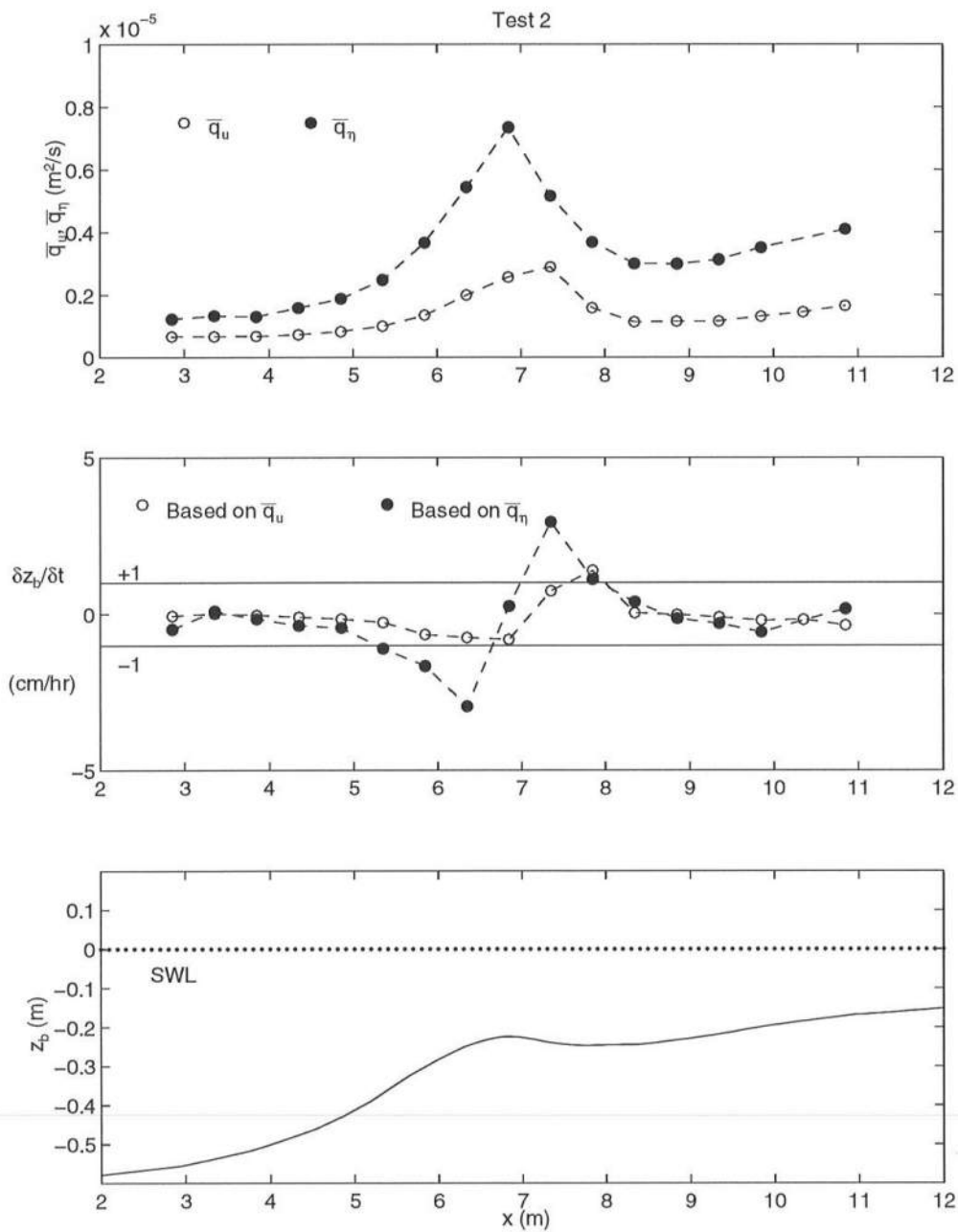
Figure 6.3: Net Transport Predictions $\overline{q}_u$, $\overline{q}_\eta$ and Bottom Elevation Change Rates $(\partial z_b/\partial t)_u$, $(\partial z_b/\partial t)_\eta$, Over Test 2 Profile (Sheet Flow Model)

133

Table 6.1: Total Sediment Loads With Sheet Flow Model, Test 1

x_u (m)	z_u (m)	$\bar{h}$ (m)	H_{rms} (m)	$\overline{\|\bar{u}\|^3}$ (m^3/s^3)	$\dfrac{\overline{\|\bar{u}\|^3}}{(\overline{\|\bar{u}\|^2})^{1.5}}$	$\bar{q}_u \times 10^7$ (m^2/s)	$(\partial z_b/\partial t)_u$ (cm/hr)	$\bar{q}_\eta \times 10^7$ (m^2/s)	$(\partial z_b/\partial t)_\eta$ (cm/hr)
2.85	-0.18	0.579	0.134	0.0121	1.64	14.810	-0.201	14.365	0.028
3.35	-0.18	0.563	0.133	0.0121	1.68	15.077	0.081	15.077	-0.170
3.85	-0.18	0.554	0.136	0.0115	1.67	14.394	0.029	16.718	-0.194
4.35	-0.18	0.525	0.136	0.0117	1.64	14.976	-0.163	18.261	-0.199
4.85	-0.18	0.501	0.136	0.0127	1.64	16.681	-0.200	20.059	-0.214
5.35	-0.18	0.468	0.134	0.0137	1.64	18.631	-0.349	22.082	-0.316
5.85	-0.18	0.425	0.134	0.0157	1.65	22.483	-0.495	26.723	-0.914
6.35	-0.18	0.372	0.136	0.0179	1.61	27.404	-0.832	36.856	-1.351
6.85	-0.16	0.314	0.139	0.0217	1.63	36.067	-1.069	55.376	-4.001
7.35	-0.15	0.234	0.143	0.0328	1.68	63.140	-7.757	107.290	-8.000
7.85	-0.14	0.212	0.151	0.0677	1.66	136.741	-4.145	152.914	0.887
8.35	-0.14	0.225	0.137	0.0564	1.78	110.627	7.238	102.788	6.070
8.85	-0.14	0.231	0.129	0.0293	1.91	56.859	3.946	80.432	0.924
9.35	-0.14	0.215	0.117	0.0229	1.73	46.002	0.248	70.813	1.749
9.85	-0.14	0.211	0.109	0.0202	1.59	40.943	0.794	57.401	0.374
10.35	-0.14	0.189	0.106	0.0173	1.64	37.096	-0.222	68.396	-2.377
10.85	-0.14	0.160	0.103	0.0217	1.60	50.468	-3.337	86.383	-1.299

134

Table 6.2: Total Sediment Loads With Sheet Flow Model, Test 2

x_u (m)	z_u (m)	$\bar{h}$ (m)	$H_{\rm rms}$ (m)	$\overline{\lvert\bar{u}\rvert^3}$ (m^3/s^3)	$\dfrac{\overline{\lvert\bar{u}\rvert^3}}{(\overline{\lvert\bar{u}\rvert^2})^{1.5}}$	$\bar{q}_u \times 10^7$ (m^2/s)	$(\partial z_b/\partial t)_u$ (cm/hr)	$\bar{q}_\eta \times 10^7$ (m^2/s)	$(\partial z_b/\partial t)_\eta$ (cm/hr)
2.85	-0.18	0.567	0.125	0.0053	1.52	6.612	-0.055	12.269	-0.480
3.35	-0.18	0.537	0.124	0.0053	1.53	6.734	0.009	13.340	0.087
3.85	-0.18	0.513	0.120	0.0052	1.53	6.748	-0.031	13.075	-0.162
4.35	-0.18	0.479	0.122	0.0054	1.53	7.321	-0.096	15.899	-0.363
4.85	-0.18	0.438	0.121	0.0059	1.54	8.333	-0.153	18.777	-0.437
5.35	-0.18	0.381	0.121	0.0066	1.52	10.010	-0.262	24.808	-1.095
5.85	-0.18	0.311	0.121	0.0081	1.52	13.473	-0.648	36.752	-1.654
6.35	-0.18	0.254	0.120	0.0108	1.52	20.002	-0.741	54.429	-2.953
6.85	-0.16	0.219	0.121	0.0129	1.50	25.727	-0.803	73.434	0.262
7.35	-0.15	0.235	0.112	0.0151	1.59	28.939	0.737	51.561	2.943
7.85	-0.14	0.245	0.103	0.0085	1.53	15.927	1.385	36.931	1.107
8.35	-0.14	0.246	0.096	0.0061	1.50	11.365	0.048	30.014	0.386
8.85	-0.14	0.236	0.094	0.0060	1.49	11.591	-0.015	29.948	-0.140
9.35	-0.14	0.220	0.091	0.0059	1.46	11.660	-0.093	31.305	-0.295
9.85	-0.14	0.201	0.089	0.0064	1.45	13.224	-0.199	35.196	-0.568
10.35	-0.14	—	—	0.0066	1.46	14.588	-0.167	—	—
10.85	-0.14	0.172	0.084	0.0074	1.47	16.607	-0.352	40.907	0.167

test 1 and 2 discussed in Section 3.4 had uncertainties on the order of 1 cm/hr or less. For test 2, $\partial z_b/\partial t$ based on u is somewhat smaller than $\partial z_b/\partial t$ based on η, though still greater than 1.0 cm/hr over the bar. For both tests the bar is predicted to move further shoreward. Rapid change of this sort was of course not observed in any part of either profile. However, it should be stated that this sheet flow model actually predicts the values of $\partial z_b/\partial t$ well below the data uncertainty of 1 cm/hr outside the surf zone, even though ripples were present outside the surf zone.

To apply the model of Trowbridge and Young (1989) in the surf zone, the effects of wave breaking and undertow will need to be included. These played an important part in surf zone dynamics in the experiment and were illustrated in Figure 5.3. The inclusion of such effects would act to oppose the purely wave-induced onshore transport of this model and would result in the prediction of a more equilibrium profile.

6.2 Energetics-Based Model for Offshore Bar Movement

Unlike the sheet flow model, the energetics-based model developed by Bowen (1980) and Bailard (1981) attempts to account for both onshore transport due to wave skewness and offshore transport due to undertow, as well as slope effects due to gravity. This model separates sediment transport into bed load and suspended load components, including separate terms for each of the above transport mechanisms. Most recently, Thornton *et al.* (1996) used the energetics-based model to predict bar movement in the field at Duck, North Carolina. Sediment size ranged from 0.12–0.20 mm, and significant wave height reached 2.0–2.5 m. Their results indicated that the model could predict correctly the bar movement during storms to first order, but that it underpredicted the development of a trough and performed poorly in mild wave conditions. They found that the effects of bottom slope on sediment load were negligible, while the suspended load was calculated to be an order of magnitude greater than the bed load.

In the present experiment, the fine sand ($d_{50} = 0.18$ mm) was approximately the same size as that present at Duck, while the waves ($H_s \simeq 0.2$ m) were an order of magnitude smaller, though still relatively large for laboratory tests. The terraced and barred beaches for tests 1 and 2 were similar to the beach profiles measured in Duck, except that the offshore slope in these tests was much steeper. Because the experiments were conducted in a wave flume there was no longshore current to contribute to sediment transport. The following analysis will refrain from separating the oscillatory velocity into high and low frequency components and will examine only the unfiltered velocity time series.

6.2.1 Theory

In the energetics model, the time-averaged cross-shore sediment transport rate per unit width can generally be expressed by equation (2) in Thornton *et al.*

(1996). For the present analysis with zero longshore velocity, however, the net onshore sediment transport rate $\bar{q}$ is given by:

$$\bar{q} = K_b \left(\overline{|u(t)|^2 \tilde{u}(t)} \right) + K_b \left(\overline{|u(t)|^2 \bar{u}} \right) - K_{bg} \left(\overline{|u(t)|^3} \right)$$
$$+ K_s \left(\overline{|u(t)|^3 \tilde{u}(t)} \right) + K_s \left(\overline{|u(t)|^3 \bar{u}} \right) - K_{sg} \left(\overline{|u(t)|^5} \right) \qquad (6.15)$$
$$\equiv \bar{q}_{bw} + \bar{q}_{bu} + \bar{q}_{bg} + \bar{q}_{sw} + \bar{q}_{su} + \bar{q}_{sg}$$

where $u(t) = $ cross-shore horizontal velocity, which is positive shoreward in this analysis. In equation (6.15), the first three terms represent bed load (subscript b) produced by wave asymmetry (subscript w), undertow (subscript u), and the effects of gravity (subscript g) on the bottom slope, respectively. The final three terms represent suspended load (subscript s) produced by the same three respective effects. The coefficients in equation (6.15) are expressed as

$$K_b = \frac{1}{(s-1)g} C_f \frac{\varepsilon_b}{\tan(\phi)} \quad ; \quad K_{bg} = K_b \frac{\tan(\beta)}{\tan(\phi)}$$

$$K_s = \frac{1}{(s-1)g} C_f \frac{\varepsilon_s}{w} \quad ; \quad K_{sg} = K_s \frac{\varepsilon_s}{w} \tan(\beta)$$

where $s = \rho_s/\rho = $ specific gravity of sand, $C_f = $ bed drag coefficient, $\phi = $ internal friction angle of sand, $\varepsilon_b = $ bed load efficiency factor, $\varepsilon_s = $ suspended load efficiency factor, $\tan(\beta) = $ local bed slope $= dz_b/dx$, and $w = $ fall velocity. In the following analysis, $s = 2.66$ and $w = 1.9$ cm/s, and other parameters are given the same values as those used in Thornton et $al.$ (1996): $C_f = 0.003$, $\tan(\phi) = 0.63$, $\varepsilon_b = 0.135$, and $\varepsilon_s = 0.015$. The local slope, $\tan(\beta)$, is computed using the equilibrium bottom profile, $z_b(x)$, for each test.

After $\bar{q}$ is obtained using equation (6.15), the predicted erosion or accretion rate, $\partial z_b/\partial t$, for the profile at given locations is found by use of equation (6.13). This corresponds to equation (1) in Thornton et $al.$, except that here the value of $\mu = (1 - n_p)$ is taken as 0.6 rather than 0.7 because the measured porosity $n_p = 0.4$ in these experiments.

138

Table 6.3: Mean Velocity Statistics, Test 1

x_u (m)	z_u (m)	$\tan(\beta)$ (slope)	$\overline{\lvert u\rvert^2\tilde{u}}$ (m^3/s^3)	$\overline{\lvert u\rvert^2\overline{u}}$ (m^3/s^3)	$\overline{\lvert u\rvert^3}$ (m^3/s^3)	$\overline{\lvert u\rvert^3\tilde{u}}$ (m^4/s^4)	$\overline{\lvert u\rvert^3\overline{u}}$ (m^4/s^4)	$\overline{\lvert u\rvert^5}$ (m^5/s^5)
2.85	-0.18	0.016	0.00134	-0.000897	0.0121	0.001068	-0.000282	0.00186
3.35	-0.18	0.017	0.00149	-0.000737	0.0121	0.001059	-0.000235	0.00199
3.85	-0.18	0.041	0.00180	-0.000576	0.0114	0.001154	-0.000180	0.00182
4.35	-0.18	0.045	0.00219	-0.000524	0.0115	0.001401	-0.000163	0.00177
4.85	-0.18	0.054	0.00217	-0.000611	0.0126	0.001458	-0.000196	0.00206
5.35	-0.18	0.085	0.00279	-0.000678	0.0135	0.001872	-0.000222	0.00233
5.85	-0.18	0.097	0.00373	-0.000671	0.0155	0.002520	-0.000231	0.00300
6.35	-0.18	0.117	0.00286	-0.001076	0.0178	0.002175	-0.000380	0.00346
6.85	-0.16	0.119	0.00114	-0.001997	0.0218	0.001348	-0.000758	0.00488
7.35	-0.12	0.151	-0.00006	-0.003191	0.0361	0.000280	-0.001467	0.01253
7.35	-0.15	0.151	-0.00219	-0.003447	0.0334	-0.001332	-0.001544	0.01110
7.35	-0.18	0.151	-0.00175	-0.003366	0.0297	-0.000815	-0.001440	0.00901
7.85	-0.14	-0.033	-0.02548	-0.012479	0.0760	-0.022046	-0.007410	0.04209
8.35	-0.14	-0.009	-0.00196	-0.010273	0.0596	0.008193	-0.005615	0.04927
8.85	-0.14	0.016	0.00035	-0.005611	0.0315	0.013430	-0.002575	0.05312
9.35	-0.14	0.010	-0.00299	-0.005583	0.0254	0.000479	-0.002231	0.00840
9.85	-0.08	0.036	0.00233	-0.004027	0.0290	0.004857	-0.001739	0.01343
9.85	-0.14	0.036	-0.00619	-0.005123	0.0232	-0.003167	-0.001938	0.00487
9.85	-0.19	0.036	-0.00139	-0.004332	0.0242	0.003057	-0.001721	0.01496
10.35	-0.14	0.056	-0.00434	-0.004187	0.0196	-0.001942	-0.001515	0.00406
10.85	-0.14	0.028	-0.00519	-0.004179	0.0237	-0.002743	-0.001610	0.00544

6.2.2 Analysis of Experimental Results

Each of the time-averaged velocity expressions in equation (6.15) was evaluated for the 21 velocity measurements where the middle point at the locations of the three-point velocity profiles is used for plotting the cross-shore variations. These values are tabulated for tests 1 and 2 in Tables 6.3 and 6.4. The values of the six sediment load components are plotted over the test 1 and test 2 equilibrium profiles in Figures 6.4 and 6.5 and listed in Tables 6.5 and 6.6. In both tests the largest

139

Table 6.4: Mean Velocity Statistics, Test 2

x_u (m)	z_u (m)	$\tan(\beta)$ (slope)	$\overline{|u|^2\tilde{u}}$ (m^3/s^3)	$\overline{|u|^2\overline{u}}$ (m^3/s^3)	$\overline{|u|^3}$ (m^3/s^3)	$\overline{|u|^3\tilde{u}}$ (m^4/s^4)	$\overline{|u|^3\overline{u}}$ (m^4/s^4)	$\overline{|u|^5}$ (m^5/s^5)
2.85	-0.18	0.024	-0.00143	-0.000496	0.0056	-0.000528	-0.000117	0.00045
3.35	-0.18	0.048	-0.00145	-0.000495	0.0055	-0.000526	-0.000117	0.00046
3.85	-0.18	0.062	-0.00131	-0.000419	0.0054	-0.000482	-0.000098	0.00043
4.35	-0.18	0.076	-0.00151	-0.000507	0.0057	-0.000571	-0.000121	0.00048
4.85	-0.18	0.101	-0.00131	-0.000450	0.0061	-0.000506	-0.000110	0.00054
5.35	-0.18	0.145	-0.00145	-0.000587	0.0069	-0.000556	-0.000148	0.00064
5.85	-0.18	0.119	-0.00197	-0.000861	0.0084	-0.000803	-0.000233	0.00088
6.35	-0.18	0.073	-0.00250	-0.001145	0.0113	-0.001119	-0.000340	0.00142
6.85	-0.16	-0.003	-0.00293	-0.001616	0.0136	-0.001360	-0.000505	0.00188
7.35	-0.12	-0.033	-0.00334	-0.002786	0.0162	-0.001477	-0.000930	0.00299
7.35	-0.15	-0.033	-0.00403	-0.002438	0.0162	-0.002262	-0.000834	0.00316
7.35	-0.18	-0.033	-0.00261	-0.001600	0.0162	-0.001892	-0.000554	0.00405
7.85	-0.14	0.004	-0.00218	-0.002069	0.0096	-0.000699	-0.000569	0.00107
8.35	-0.14	0.004	-0.00189	-0.001816	0.0071	-0.000593	-0.000444	0.00061
8.85	-0.14	0.030	-0.00169	-0.001618	0.0069	-0.000514	-0.000391	0.00057
9.35	-0.14	0.035	-0.00130	-0.001477	0.0066	-0.000362	-0.000345	0.00049
9.85	-0.08	0.034	0.00003	-0.000940	0.0073	0.000105	-0.000230	0.00061
9.85	-0.14	0.034	-0.00102	-0.001317	0.0068	-0.000275	-0.000312	0.00051
9.85	-0.18	0.034	-0.00074	-0.001111	0.0065	-0.000185	-0.000259	0.00049
10.35	-0.14	0.024	-0.00022	-0.000929	0.0068	0.000024	-0.000221	0.00053
10.85	-0.14	0.027	-0.00045	-0.001334	0.0077	-0.000026	-0.000329	0.00065

values predicted for all types of sediment transport occur around the location of the bar or terrace edge, in the vicinity of $x \simeq 7\text{--}8$ m. The more intense breaking of test 1 is clearly visible from a comparison of sediment loads in this region. The effects of bottom slope on sediment transport ($\overline{q}_{sg}$, $\overline{q}_{bg}$) are most clear seaward of the bar, where the bottom slope is relatively steep and positive. Both bed and suspended sediment fluxes due to slope effects are consistently negative (*i.e.*, offshore transport). Shoreward of the bar, where the bottom slope is negative for a short distance, sediment fluxes due to slope effects are noticeably positive, especially in test 2. One additional effect illustrated by Figures 6.4 and 6.5 is also noteworthy. At $x = 7.85$ m in test 1, a large volume of sediment is transported seaward by both wave and undertow effects; however, just 0.5 m shoreward at $x = 8.35$ m, the wave suspended load $\overline{q}_{sw}$ suddenly reverses and becomes strongly positive onshore.

Tables 6.5 and 6.6 list three sets of values calculated at the locations $x = 7.35$ m and $x = 9.85$ m, where three-point velocity profiles were taken. The predicted total bed load, $\overline{q}_b = (\overline{q}_{bw} + \overline{q}_{bu} + \overline{q}_{bg})$, and the predicted total suspended load, $\overline{q}_s = (\overline{q}_{sw} + \overline{q}_{su} + \overline{q}_{sg})$, are also tabulated. In general, the predicted suspended load values are larger than the corresponding bed load terms, as would be expected from the relatively large waves and fine sand used in these experiments. However, unlike Thornton *et al.* (1996), suspended load, $\overline{q}_s$, is rarely an entire order of magnitude larger than bed load, $\overline{q}_b$, in these laboratory experiments.

The largest suspended sediment fluxes computed in these experiments are about 0.4 m^2/day, while those obtained by Thornton *et al.* approached 50 m^2/day. The largest bed load fluxes in these experiments were approximately 0.1 m^2/day, while the field experiments showed values no larger than 4 m^2/day. Large amounts of sediment were predicted to have been suspended by a strong longshore current in the field experiments. Also, because of the relatively steeper offshore slope in the laboratory, the effects of bottom slope were probably proportionately greater in the

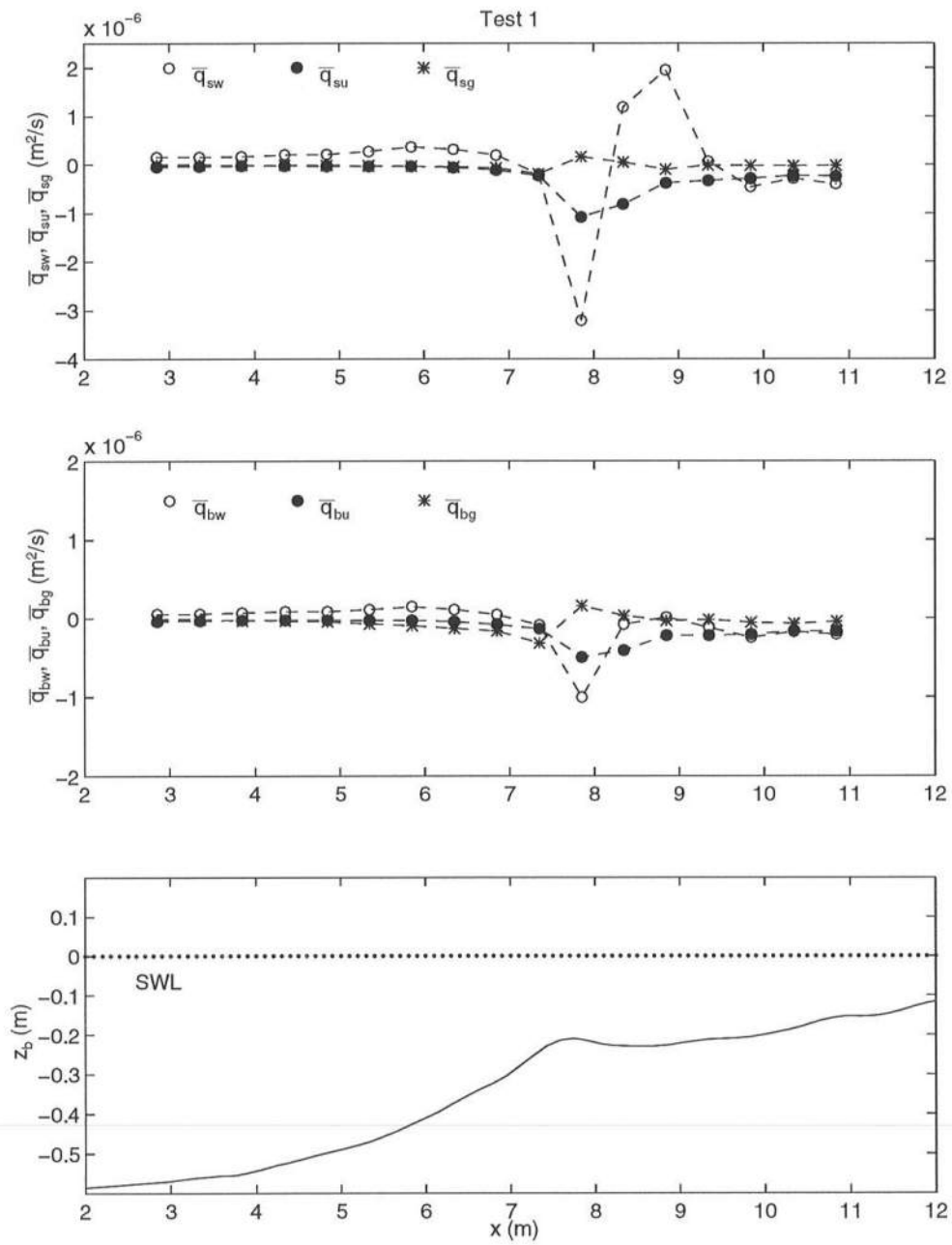141

Figure 6.4: Cross-Shore Variation of Suspended Load and Bed Load Quantities Over Test 1 Profile (Energetics Model)
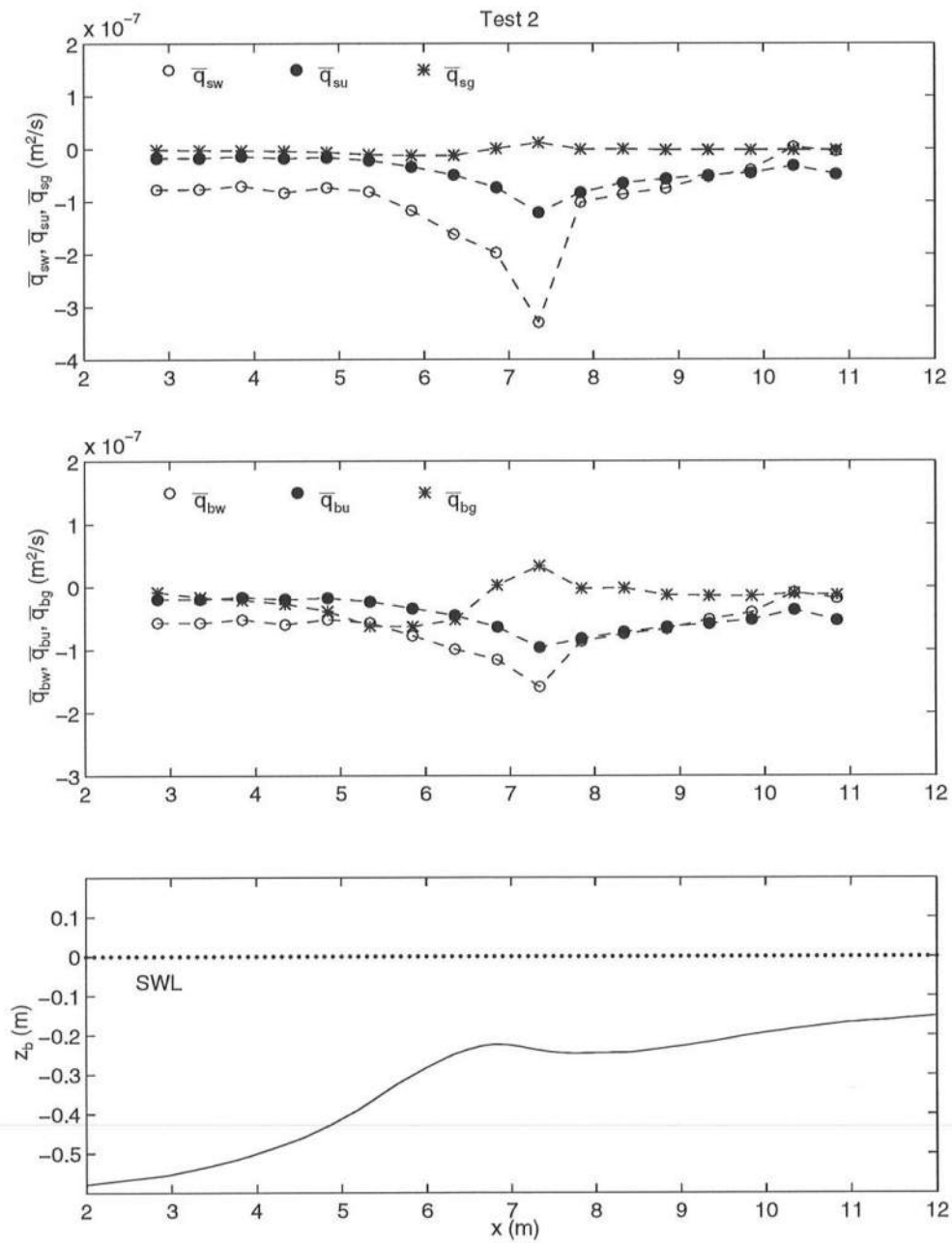
Figure 6.5: Cross-Shore Variation of Suspended Load and Bed Load Quantities Over Test 2 Profile (Energetics Model)

143

Table 6.5: Partial Sediment Loads With Energetics Model, Test 1

x_u (m)	z_u (m)	Bed Load ×10^7 (m²/s)				Suspended Load ×10^7 (m²/s)			
		$\bar{q}_{bw}$	$\bar{q}_{bu}$	$\bar{q}_{bg}$	$\bar{q}_b$	$\bar{q}_{sw}$	$\bar{q}_{su}$	$\bar{q}_{sg}$	$\bar{q}_s$
2.85	-0.18	0.527	-0.354	-0.122	0.051	1.553	-0.409	-0.034	1.109
3.35	-0.18	0.587	-0.291	-0.130	0.166	1.541	-0.342	-0.039	1.159
3.85	-0.18	0.711	-0.228	-0.291	0.192	1.678	-0.262	-0.085	1.331
4.35	-0.18	0.864	-0.207	-0.324	0.334	2.038	-0.237	-0.091	1.709
4.85	-0.18	0.856	-0.241	-0.425	0.190	2.121	-0.284	-0.128	1.709
5.35	-0.18	1.100	-0.268	-0.717	0.115	2.723	-0.323	-0.226	2.174
5.85	-0.18	1.473	-0.265	-0.945	0.262	3.665	-0.335	-0.335	2.995
6.35	-0.18	1.127	-0.425	-1.300	-0.597	3.164	-0.552	-0.463	2.149
6.85	-0.16	0.451	-0.788	-1.620	-1.957	1.960	-1.103	-0.665	0.193
7.35	-0.12	-0.024	-1.260	-3.420	-4.704	0.408	-2.133	-2.173	-3.898
7.35	-0.15	-0.864	-1.361	-3.164	-5.389	-1.938	-2.245	-1.925	-6.108
7.35	-0.18	-0.692	-1.329	-2.812	-4.833	-1.186	-2.094	-1.562	-4.842
7.85	-0.14	-10.057	-4.926	1.578	-13.405	-32.063	-10.777	1.602	-41.238
8.35	-0.14	-0.773	-4.055	0.340	-4.489	11.916	-8.167	0.515	4.265
8.85	-0.14	0.137	-2.215	-0.316	-2.394	19.533	-3.746	-0.976	14.811
9.35	-0.14	-1.180	-2.204	-0.160	-3.545	0.697	-3.245	-0.097	-2.645
9.85	-0.08	0.918	-1.590	-0.650	-1.322	7.064	-2.529	-0.551	3.984
9.85	-0.14	-2.442	-2.022	-0.520	-4.985	-4.606	-2.818	-0.200	-7.624
9.85	-0.19	-0.548	-1.710	-0.542	-2.800	4.446	-2.503	-0.614	1.329
10.35	-0.14	-1.713	-1.653	-0.684	-4.050	-2.824	-2.203	-0.260	-5.287
10.85	-0.14	-2.051	-1.650	-0.422	-4.122	-3.989	-2.341	-0.178	-6.508

Table 6.6: Partial Sediment Loads With Energetics Model, Test 2

x_u (m)	z_u (m)	Bed Load $\times 10^7$ (m^2/s)				Suspended Load $\times 10^7$ (m^2/s)			
		$\overline{q}_{bw}$	$\overline{q}_{bu}$	$\overline{q}_{bg}$	$\overline{q}_b$	$\overline{q}_{sw}$	$\overline{q}_{su}$	$\overline{q}_{sg}$	$\overline{q}_s$
2.85	-0.18	-0.566	-0.196	-0.085	-0.847	-0.768	-0.170	-0.013	-0.951
3.35	-0.18	-0.571	-0.195	-0.167	-0.934	-0.765	-0.171	-0.025	-0.961
3.85	-0.18	-0.516	-0.165	-0.208	-0.889	-0.701	-0.143	-0.031	-0.875
4.35	-0.18	-0.596	-0.200	-0.269	-1.065	-0.830	-0.176	-0.042	-1.048
4.85	-0.18	-0.517	-0.178	-0.386	-1.080	-0.736	-0.160	-0.063	-0.959
5.35	-0.18	-0.571	-0.232	-0.624	-1.426	-0.809	-0.216	-0.106	-1.131
5.85	-0.18	-0.776	-0.340	-0.630	-1.746	-1.168	-0.339	-0.120	-1.627
6.35	-0.18	-0.988	-0.452	-0.520	-1.959	-1.627	-0.495	-0.120	-2.242
6.85	-0.16	-1.157	-0.638	0.029	-1.766	-1.978	-0.735	0.007	-2.706
7.35	-0.12	-1.317	-1.100	0.333	-2.084	-2.148	-1.352	0.113	-3.387
7.35	-0.15	-1.589	-0.962	0.334	-2.218	-3.289	-1.213	0.119	-4.383
7.35	-0.18	-1.029	-0.632	0.334	-1.327	-2.752	-0.806	0.153	-3.404
7.85	-0.14	-0.862	-0.817	-0.026	-1.705	-1.016	-0.827	-0.005	-1.849
8.35	-0.14	-0.745	-0.717	-0.018	-1.481	-0.863	-0.646	-0.003	-1.512
8.85	-0.14	-0.667	-0.639	-0.128	-1.434	-0.748	-0.568	-0.019	-1.335
9.35	-0.14	-0.514	-0.583	-0.144	-1.241	-0.527	-0.502	-0.020	-1.048
9.85	-0.08	0.013	-0.371	-0.153	-0.511	0.153	-0.334	-0.023	-0.205
9.85	-0.14	-0.404	-0.520	-0.144	-1.068	-0.401	-0.454	-0.020	-0.874
9.85	-0.18	-0.291	-0.439	-0.136	-0.866	-0.270	-0.377	-0.019	-0.666
10.35	-0.14	-0.089	-0.367	-0.104	-0.559	0.035	-0.322	-0.015	-0.302
10.85	-0.14	-0.179	-0.527	-0.129	-0.835	-0.038	-0.478	-0.020	-0.536

lab than in the field. In tests 1 and 2 the bed load due to slope effects, $\overline{q}_{bg}$, is larger than the suspended load, $\overline{q}_{sg}$, for most locations. Moreover, the total bed load $\overline{q}_b$ is actually comparable to the total suspended load, $\overline{q}_s$, at most test 2 locations. This may be reasonable under the milder wave conditions of the second test.

As velocity time series were measured at three elevations at two cross-shore locations in these experiments, it is also possible to examine whether the cross-shore sediment transport rate $\overline{q}$ in equation (6.15) is sensitive to the elevation of the cross-shore velocity, $u(t)$, used for its prediction. This variation is illustrated in Figures 6.6 – 6.9. While predicted sediment loads due to undertow and bottom slope remain relatively constant over the depth, predictions of wave-induced loads $\overline{q}_{sw}$ and $\overline{q}_{bw}$ vary somewhat, especially at $x = 9.85$ m for test 1. It may thus be possible to predict sediment load due to undertow and bottom effects by measuring velocities at mid-depth instead of immediately outside the bottom boundary layer as specified by the theory of Bailard (1981). However, for predictions of wave-induced load $\overline{q}_{sw}$ and $\overline{q}_{bw}$, the use of mid-depth velocity measurements may cause some errors when compared to velocity measurements made near the bottom.

The total sediment loads predicted by the energetics model at each cross-shore location are plotted over the equilibrium profiles in Figures 6.10 and 6.11. The values in these figures are summarized in Tables 6.7 and 6.8, along with the ratio of total suspended load to total bed load, $\overline{q}_s/\overline{q}_b$, and the predicted erosion or accretion rate, $\partial z_b/\partial t$. As indicated earlier, the ratio $\overline{q}_s/\overline{q}_b$ rarely reaches the order of 10 in test 1 and remains fairly close to the order of unity for all locations in test 2. This may be reasonable compared to the field data of Thornton *et al.* (1996) because wave heights in the laboratory were much smaller. In test 1, the net sediment transport, $\overline{q}$, is predicted to be weakly onshore at locations seaward of the breaker zone but strongly offshore at almost all locations on the terrace. The magnitude of the parameter $\partial z_b/\partial t$ is not greater than 1 cm/hr, except in the
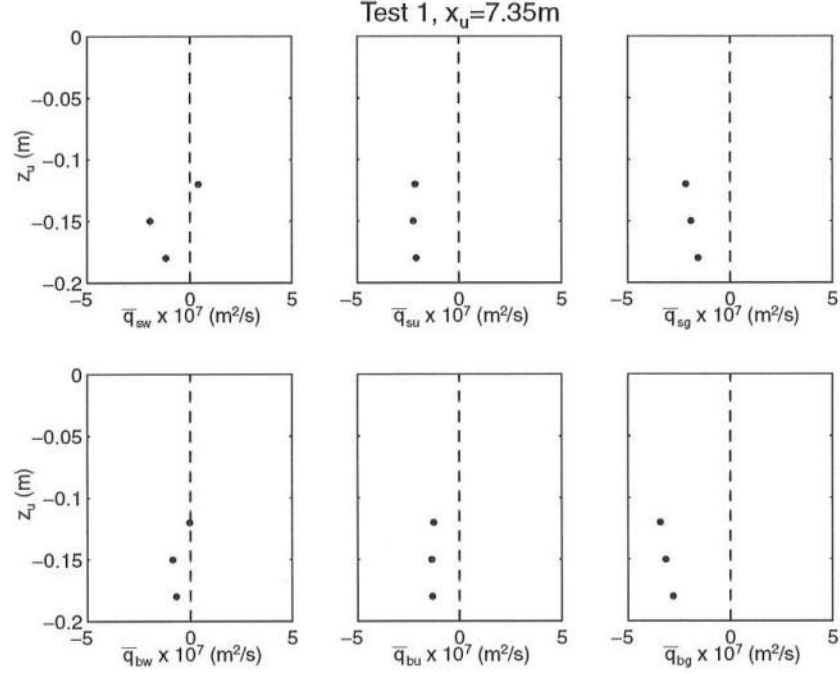
Figure 6.6: Variation of Suspended Load and Bed Load Quantities Over Depth at $x = 7.35$ m, Test 1 (Energetics Model)

region of intense breaking. In test 2, all locations are predicted to have a weak offshore transport, with $\partial z_b / \partial t$ consistently small. These values are smaller than those in test 1 because waves broke less intensely, leading to slower profile changes. Energetics theory thus may be said to be capable of predicting equilibrium in test 2 within measurement errors of 1 cm/hr.

For both tests the energetics model predicts the growth of a bar near x = 7 m and a trough near $x = 8$ m at rates greater than those observed in the laboratory. It should be noted that Bailard (1981) limits the applicability of his model to a plane, sloping beach and does not mention the presence of ripples or bars. The dominant mechanism for the development and movement of the bar in measurements conducted by Thornton *et al.* (1996) was strong longshore current and undertow, yet in the experiments it has been shown that barred and terraced

147

Figure 6.7: Variation of Suspended Load and Bed Load Quantities Over Depth at $x = 9.85$ m, Test 1 (Energetics Model)

profiles may develop and stabilize without longshore current but with relatively large undertow. While the energetics model underpredicted trough development for Thornton *et al.*, it overpredicts both the trough and bar development for the tests in this study.

The energetics model is more accurate than the sheet flow model in both tests 1 and 2, largely because of the inclusion of a greater number of sediment transport mechanisms in the former model. However, both models assume the instantaneous response of both bed load and suspended load particles to the horizontal velocity immediately outside the bottom boundary layer. The water was observed to be consistently very cloudy during both tests, and the assumption of the instantaneous response of suspended load appears to be questionable.

148
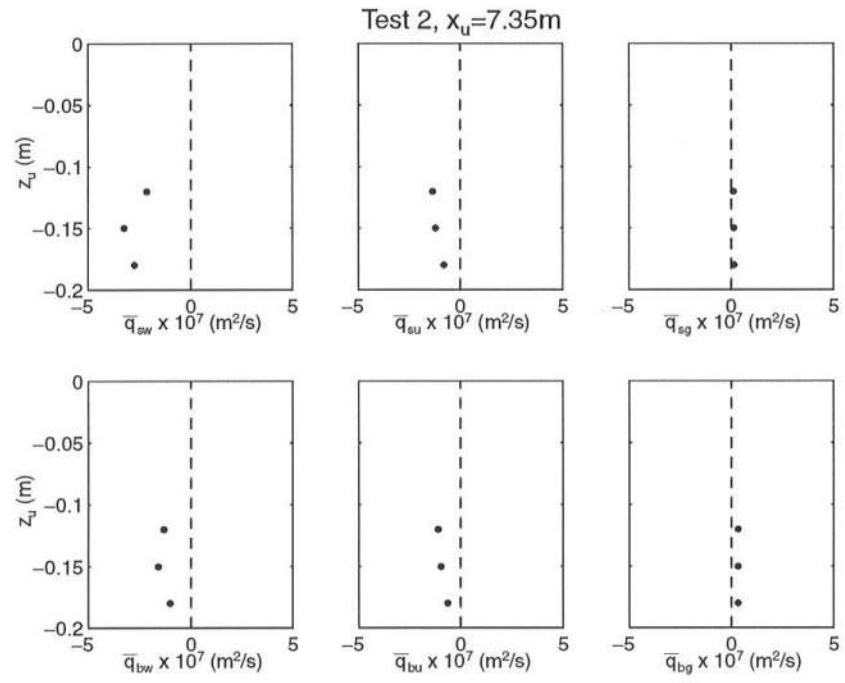
Figure 6.8: Variation of Suspended Load and Bed Load Quantities Over Depth at $x = 7.35$ m, Test 2 (Energetics Model)

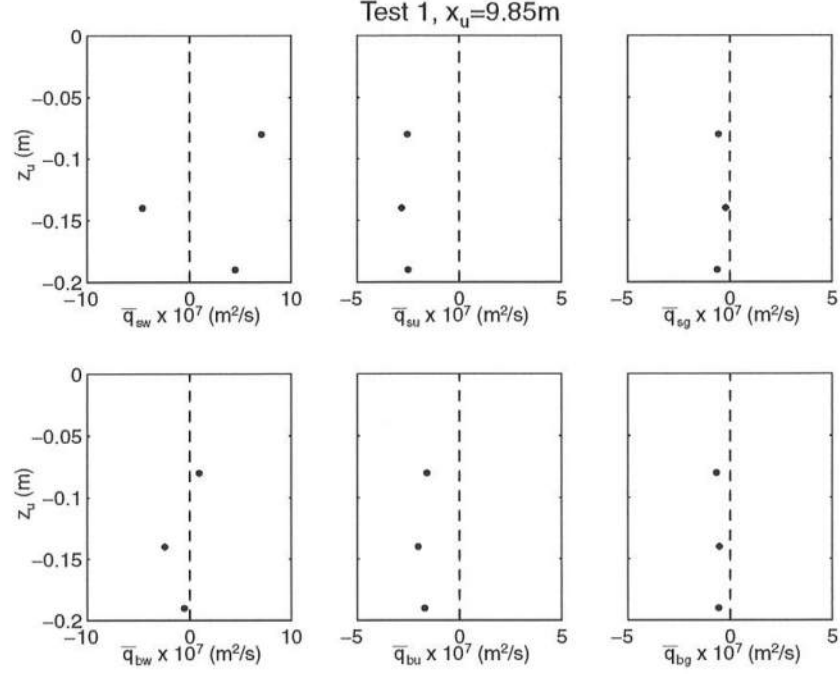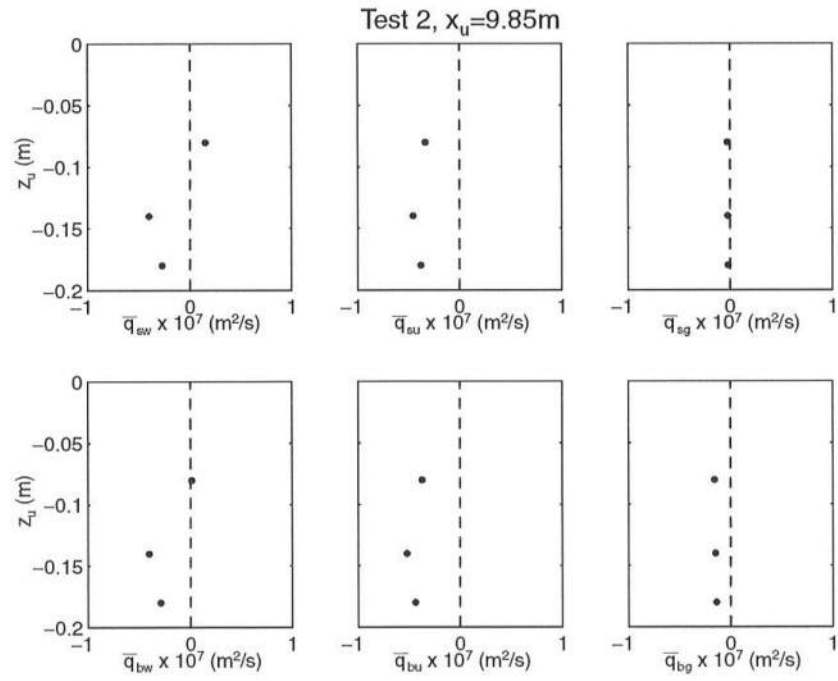**Figure 6.9:** Variation of Suspended Load and Bed Load Quantities Over Depth at $x = 9.85$ m, Test 2 (Energetics Model)
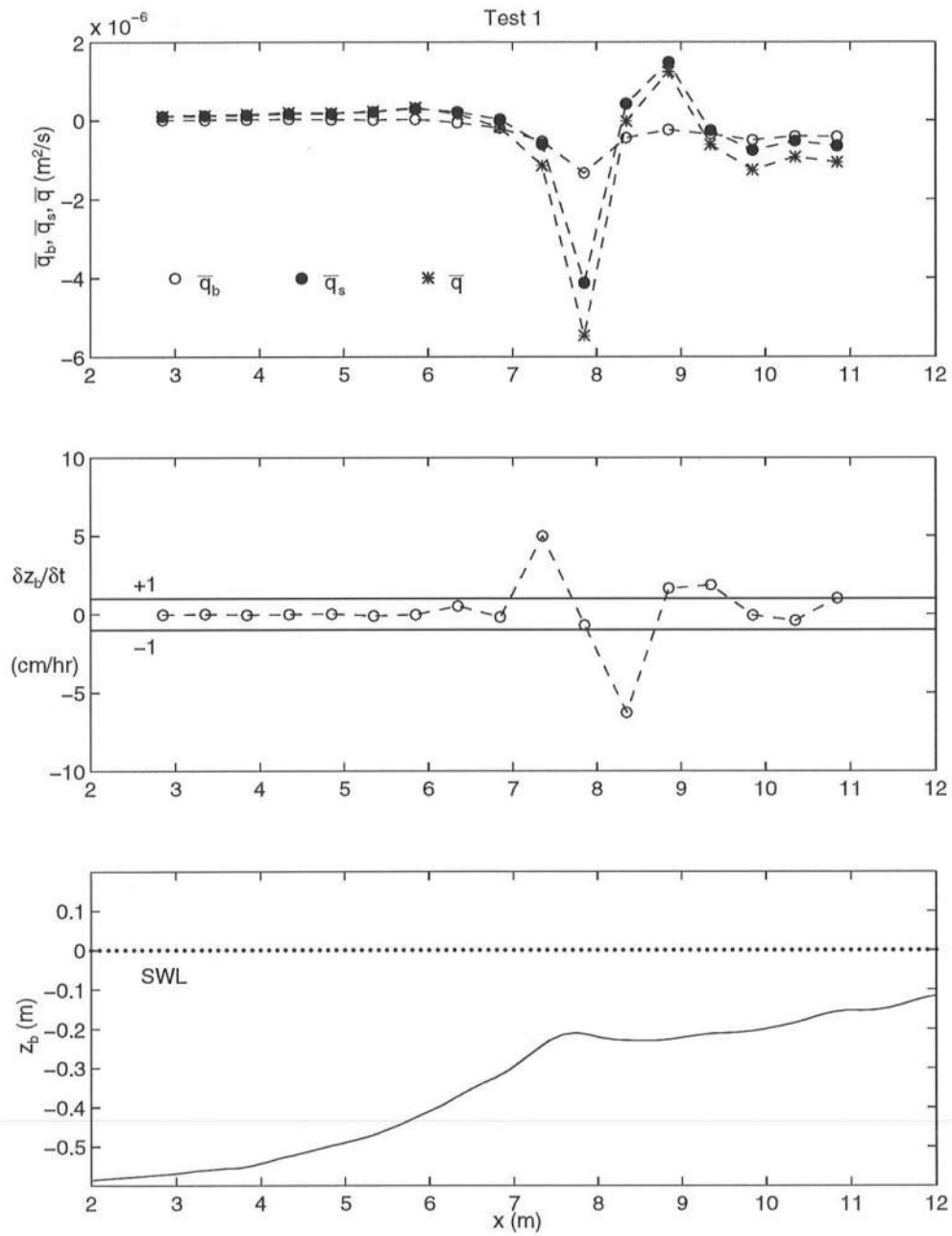
Figure 6.10: Predicted Bed Load $\overline{q}_b$, Suspended Load $\overline{q}_s$, and Total Load $\overline{q}$ with $\partial z_b / \partial t$ Over Test 1 Profile (Energetics Model)
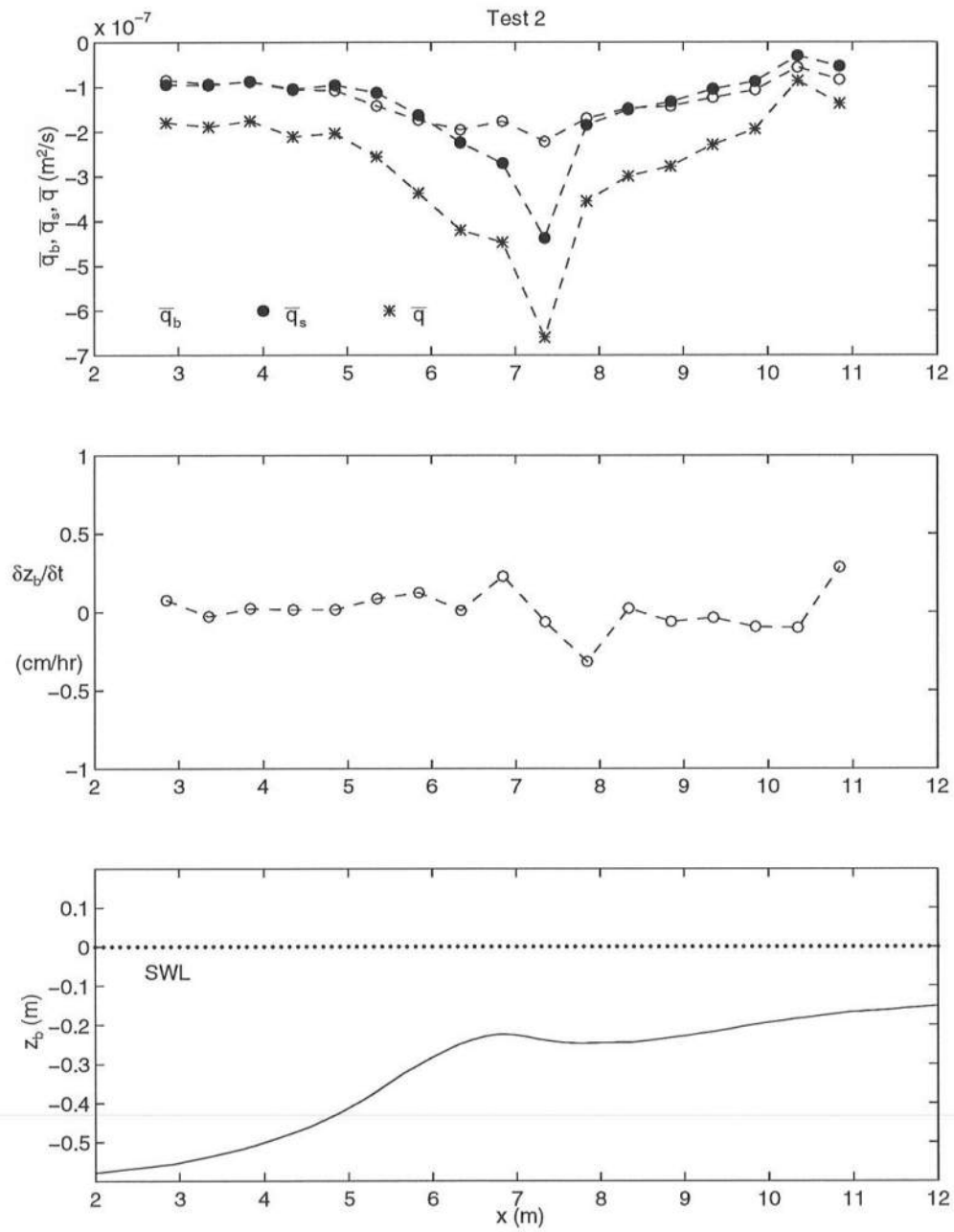
Figure 6.11: Predicted Bed Load $\overline{q}_b$, Suspended Load $\overline{q}_s$, and Total Load $\overline{q}$ with $\partial z_b/\partial t$ Over Test 2 Profile (Energetics Model)

Table 6.7: Total Sediment Loads With Energetics Model, Test 1

x_u (m)	z_u (m)	$\overline{q}_b \times 10^7$ (m^2/s)	$\overline{q}_s \times 10^7$ (m^2/s)	$\overline{q}_s/\overline{q}_b$	$\overline{q} \times 10^7$ (m^2/s)	$\partial z_b/\partial t$ (cm/hr)
2.85	-0.18	0.051	1.109	21.61	1.160	-0.050
3.35	-0.18	0.166	1.159	6.98	1.326	-0.006
3.85	-0.18	0.192	1.331	6.91	1.523	-0.057
4.35	-0.18	0.334	1.709	5.13	2.043	-0.023
4.85	-0.18	0.190	1.709	8.99	1.899	0.013
5.35	-0.18	0.115	2.174	18.88	2.289	-0.118
5.85	-0.18	0.262	2.995	11.41	3.257	-0.032
6.35	-0.18	-0.597	2.149	-3.60	1.551	0.509
6.85	-0.16	-1.957	0.193	-0.10	-1.764	-0.198
7.35	-0.15	-5.389	-6.108	1.13	-11.497	4.982
7.85	-0.14	-13.405	-41.238	3.08	-54.643	-0.692
8.35	-0.14	-4.489	4.265	-0.95	-0.223	-6.272
8.85	-0.14	-2.394	14.811	-6.19	12.417	1.639
9.35	-0.14	-3.545	-2.645	0.75	-6.190	1.862
9.85	-0.14	-4.985	-7.624	1.53	-12.609	-0.079
10.35	-0.14	-4.050	-5.287	1.31	-9.337	-0.412
10.85	-0.14	-4.122	-6.508	1.58	-10.630	1.016

Table 6.8: Total Sediment Loads With Energetics Model, Test 2

x_u (m)	z_u (m)	$\bar{q}_b \times 10^7$ (m^2/s)	$\bar{q}_s \times 10^7$ (m^2/s)	$\bar{q}_s/\bar{q}_b$	$\bar{q} \times 10^7$ (m^2/s)	$\partial z_b/\partial t$ (cm/hr)
2.85	-0.18	-0.847	-0.951	1.12	-1.798	0.077
3.35	-0.18	-0.934	-0.961	1.03	-1.895	-0.028
3.85	-0.18	-0.889	-0.875	0.98	-1.764	0.023
4.35	-0.18	-1.065	-1.048	0.98	-2.114	0.015
4.85	-0.18	-1.080	-0.959	0.89	-2.040	0.015
5.35	-0.18	-1.426	-1.131	0.79	-2.556	0.085
5.85	-0.18	-1.746	-1.627	0.93	-3.373	0.124
6.35	-0.18	-1.959	-2.242	1.14	-4.202	0.011
6.85	-0.16	-1.766	-2.706	1.53	-4.472	0.228
7.35	-0.15	-2.218	-4.383	1.98	-6.601	-0.061
7.85	-0.14	-1.705	-1.849	1.08	-3.553	-0.315
8.35	-0.14	-1.481	-1.512	1.02	-2.992	0.023
8.85	-0.14	-1.434	-1.335	0.93	-2.769	-0.060
9.35	-0.14	-1.241	-1.048	0.85	-2.289	-0.036
9.85	-0.14	-1.068	-0.874	0.82	-1.942	-0.095
10.35	-0.14	-0.559	-0.302	0.54	-0.861	-0.099
10.85	-0.14	-0.835	-0.536	0.64	-1.371	0.287

Chapter 7

CONCLUSION

Two irregular wave tests were conducted on a movable sand beach after allowing the beach to shape itself into equilibrium profiles. The first objective of these tests was to supplement the results of Herrman *et al.* (1997), further investigating the cross-shore variations of the probability distributions and statistics of the free surface elevation and horizontal velocity in the shoaling, surf and swash zones. In addition, velocity statistics were analyzed over depth at two cross-shore locations. The second objective, only partially achieved, was the synchronization of velocity and free surface time series for the separation of incident and reflected waves. The final objective involved the application of the sheet flow and energetics sediment transport models to the equilibrium profiles obtained in this study, in an effort to identify shortcomings of the models.

The exponential gamma distribution was again adopted in this study, which examined its application to more realistic beach profiles. The distribution with the measured mean, standard deviation, and skewness has again been shown to be capable of describing all the measured probability distributions, though uncertainties in measurements of bottom elevation make verification more difficult in very shallow water with the mean water depth $\overline{h} \leq 1$ cm. It was assumed that the lower limit of the exponential distribution of the free surface elevation, η, was imposed by the bottom elevation in the swash zone. This assumption implies that $H_{\mathrm{rms}}/\overline{h} = \sqrt{8}$, where $\overline{h} =$ mean water depth, and $H_{\mathrm{rms}} =$ root-mean-square wave height, defined

155

as $H_{\text{rms}} = \sqrt{8}\sigma$ with σ = standard deviation of η. The measured values of $H_{\text{rms}}/\overline{h}$ in this experiment increased in the swash zone and approached an upper limit of approximately three. With some irregularity in Test 1, the measured skewness, s, of η generally increased landward, then decreased as waves approached the still water shoreline, and finally increased again in the swash zone to an upper limit near the predicted $s = 2$. The trend in measured kurtosis, K, of η was predicted by the relation between K and s derived from the exponential gamma distribution, but actual data may require an empirical fit.

The undertow, $\overline{u}$, and the standard deviation, σ_u, of the horizontal velocity, u, were again measured near the approximate mid-depth below SWL in the shoaling and surf zones. In addition, these velocity statistics were measured in two vertical profiles. The undertow and standard deviation were expressed in terms of $\overline{h}$ and H_{rms} using linear progressive long-wave theory. These simple relationships, together with the measured values of $\overline{h}$ and H_{rms}, were again found to predict the measured cross-shore variations of $\overline{u}$ and σ_u fairly accurately in deeper water. Overprediction of these values in shallower water shoreward of the bar was likely to have resulted from a roller effect due to water carried onto the terrace by breaking waves. The velocity profiles showed little variation in $\overline{u}$ or σ_u over the depth for these irregular wave tests. The skewness, s_u, of u was again found to be consistently smaller than the corresponding skewness, s, of η, indicating the vertical decrease of nonlinearity. The vertical variation of s_u was relatively minimal below the wave trough level and above the bottom boundary layer. The kurtosis, K_u, of u exhibited a similar cross-shore trend to s_u and also appeared to remain fairly constant over depth.

As part of a plan to examine incident and reflected wave spectra in shallower water, simultaneous measurements were made of the free surface elevation and the horizontal velocity, and the combined incident and reflected spectra were calculated at 17 cross-shore locations. Because of slightly different timing rates on computers

156

measuring velocity and free-surface time series, sychronization of the time series became much more difficult and uncertain. Furthermore, the combined wave spectra showed little evidence of long standing waves generated in the shallow region of the profile, indicating that the terraced and barred beach profiles were not caused by low-frequency standing waves.

Finally, the sheet flow and energetics sediment transport models were applied to the equilibrium sand profiles. The energetics model, which attempts to account for effects of wave asymmetry, undertow, and bottom slope, predicted smaller profile change than the sheet flow model, which did not include the effects of wave breaking and undertow. The sheet flow model is currently capable of predicting only onshore transport outside the surf zone and may have been applicable only to a portion of the profiles measured in these tests. Both models predicted significant changes in profile shape, especially around the region of wave breaking, and neither model was able to predict correctly a stable equilibrium profile using the velocity and free surface data, except that the energetics model was within measurement errors for test 2.

In summary, the statistical results of these tests indicate that further development of a time-averaged model incorporating the exponential gamma distribution will be worthwhile, although such a model would be best verified by detailed field data. The model will need to predict the cross-shore variations of $\overline{h}$, σ, s, and s_u. Although they effectively describe $\overline{u}$ and σ_u in deeper water, the simple linear relationships discussed in this study are not sufficient for prediction of these quantities in shallower water or for prediction of s_u and K_u in any depth.

The failure of state-of-the-art sediment transport models to predict the equilibrium profiles illustrates the strict limitations on such models at the present time. The sheet flow model may be improved by the inclusion of additional terms to

157

account for the offshore transport effects of undertow. The energetics model over-predicted profile change in mild wave conditions both for Thornton *et al.* (1996) and for test 1; it, too, will need to describe the suspended load in a physically more realistic manner.

REFERENCES

Abramowitz, M., and Stegun, I.A. (1972). *Handbook of Mathematical Functions*, Dover, New York, N.Y.

Al-Khafaji, A.W., and Andersland, O.B. (1992). *Geotechnical Engineering and Soil Testing*, Saunders College Publishing, Ft. Worth.

Bailard, J.A. (1981). "An Energetics Total Load Sediment Transport Model For a Plane Sloping Beach," *J. Geophys. Res.*, 86(C11), 10,938–10,954.

Battjes, J.A., and Janssen, J.P.F.M. (1978). "Energy loss and set-up due to breaking of random waves," *Proc. 16th Coast. Engrg. Conf.*, ASCE, 1, 569–587.

Battjes, J.A., and Stive, M.J.F. (1985). "Calibration and verification of a dissipation model for random breaking waves," *J. Geophy. Res.*, 90(C5), 9159–9167.

Bitner, E.M. (1980). "Non-linear effects of the statistical model of shallow-water wind waves," *J. Applied Ocean Res.*, 2(2), 63–73.

Bouws, E., Gunther, H., Rosenthal, W., and Vincent, C.L. (1985). "Similarity of the wind wave spectrum in finite depth water. 1: Spectral form," *J. Geophys. Res.*, 90(C1), 975–986.

Bowen, A.J. (1980). "Simple Models of Nearshore Sedimentation; Beach Profiles and Longshore Bars," *The Coastline of Canada*, Geological Survey of Canada, Paper 80-10, 1-11.

Bruun, P. (1954) "Coast Erosion and the Development of Beach Profiles," U.S. Army Corps of Engineers, Beach Erosion Board, Tech. Memo. No. 44.

Cox, D.T., Kobayashi, N., and Kriebel, D.L. (1994). "Numerical model verification using SUPERTANK data in surf and swash zones," *Proc. Coast. Dynamics '94*, ASCE, 248–262.

Cox, D.T., and Kobayashi, N. (1997). "A Kinematic Undertow Model with a Logarithmic Boundary Layer," *J. Wtrwy., Port, Coast. and Oc. Engrg.*, ASCE (in press).

Dally, W.R., and Dean, R.G. (1986). "Transformation of random breaking waves on surf beat," *Proc. 20th Coast. Engrg. Conf.*, ASCE, 1, 109–123.

Dean, R.G. (1991). "Equilibrium Beach Profiles: Principles and Applications," *J. Coastal Res.*, 7, 1, 53–84.

Douglas, S.L. (1992). "Estimating extreme values of run-up on beaches," *J. Wtrwy. Port, Coast., and Oc. Engrg.*, ASCE, 118(2), 220–224.

Goda, Y. (1985). *Random Seas and Design of Maritime Structures*, Univ. of Tokyo Press. Tokyo, Japan.

Gran, S. (1992). *A Course in Ocean Engineering*. Elsevier, New York, N.Y.

Guza, R.T., and Thornton, E.B. (1980). "Local and shoaled comparisons of sea surface elevations, pressures, and velocities," *J. Geophys. Res.*, 85(C3), 1524–1530.

Guza, R.T., and Thornton, E.B. (1982). "Swash oscillations on a natural beach," *J. Geophys. Res.*, 87(C1), 483–491.

Guza, R.T., and Thornton, E.B. (1985). "Velocity moments in nearshore," *J. Wtrwy. Port, Coast., and Oc. Engrg.*, ASCE, 111(2), 235–256.

Herrman, M.N., Kobayashi, N., Johnson, B.D., and Orzech, M.D. (1997). "Experiments on surface elevation probability distribution and statistics in surf and swash zones," Research Report No. CACR-97-01, Center for Applied Coastal Research, Univ. of Delaware, Newark, Del.

Holman, R.A., and Sallenger, A.H. (1985). "Setup and swash on a natural beach," *J. Geophys. Res.*, 90(C1), 945–953.

Huang, N.E., and Long, S.R. (1980). "An experimental study of the surface elevation probability distribution and statistics of wind-generated waves," *J. Fluid Mech.*, 101(1), 179–200.

Kobayashi, N., DeSilva, G.S., and Watson, K.D. (1989). "Wave transformation and swash oscillation on gentle and steep slopes," *J. Geophys. Res.*, 94(C1), 951–966.

Kobayashi, N., and Karjadi, E.A. (1996). "Obliquely incident irregular waves in surf and swash zones," *J. Geophys. Res.*, 101(C3), 6527–6542.

Kobayashi, N., and Raichle, A.W. (1994). "Irregular wave overtopping of revetments in surf zones," *J. Wtrwy. Port, Coast. and Oc. Engrg.*, ASCE, 120(1), 56–73.

Kobayashi, N., and Wurjanto, A. (1992). "Irregular wave setup and run-up on beaches," *J. Wtrwy. Port, Coast., and Oc. Engrg.*, ASCE, 118(4), 368–386.

Kraus, N.C., Lohrmann, A., and Cabrera, R. (1994). "New acoustic meter for measuring 3D laboratory flows," *J. Hydraulic Engrg.*, ASCE, 120(3), 406–412.

Kraus, N.C., and Mason, J.M. (1993). "Discussion of 'Prediction of Storm/Normal Beach Profiles,' *J. Waterway, Port, Coastal, and Ocean Engrg*, ASCE, 119, 4.

Kriebel, D.L. (1994). "Swash zone wave characteristics from SUPERTANK," *Proc. 24th Coast. Engrg. Conf.*, ASCE, 2, 2207–2221.

Longuet-Higgins, M.S. (1963). "The effect of non-linearities on statistical distributions in the theory of sea waves," *J. Fluid Mech.*, 17, 459–480.

Mase, H., and Kobayashi, N. (1991). "Transformation of random breaking waves and its empirical numerical model considering surf beat," *Proc. Coast. Sediments '91*, ASCE, 1, 688–702.

Raubenheimer, B., Guza, R.T., Elgar, S., and Kobayashi, N. (1995). "Swash on a gently sloping beach," *J. Geophys. Res.*, 100(C5), 8751–8760.

Svendsen, I.A. (1984). "Mass flux and undertow in a surf zone," *Coast. Engrg.*, 8, 347–365.

Tayfun, M.A. (1980). "Narrow-band nonlinear sea waves," *J. Geophys. Res.*, 85(C3), 1548–1552.

Thornton, E.B., and Guza, R.T. (1982). "Energy saturation and phase speeds measured on a natural beach," *J. Geophys. Res.*, 87(C12), 9499–9508.

Thornton, E.B., and Guza, R.T. (1983). "Transformation of wave height distribution," *J. Geophys. Res.*, 88(C10), 5925–5938.

Thornton, E.B., Humiston, R.T., and Birkemeier, W. (1996). "Bar/trough generation on a natural beach," *J. Geophys. Res.*, 101(C5), 12,097–12,110.

Trowbridge, J., and Young, D. (1989). "Sand Transport by Unbroken Water Waves Under Sheet Flow Conditions," *J. Geophys. Res.*, 94(C8), 10,971-10,991.

Wolfram, S. (1991). *Mathematica*, 2nd ed., Addison-Wesley, Redwood City, CA.

Yalin, M.S. (1976). *Mechanics of Sediment Transport*, 2nd ed., Oxford, New York, NY.